Dilaton-induced dark matter and long-lived particle recasting

Manuel Utsch

SORBONNE UNIVERSITÉ

LPTHE
LABORATOIRE DE PHYSIQUE THEORIQUE ET HAUTES ENERGIES

THÈSE DE DOCTORAT DE SORBONNE UNIVERSITÉ

Spécialité : Physique Théorique

École doctorale nº564: Physique en Île-de-France

réalisée

au Laboratoire de Physique Théorique et Hautes Énergies

sous la direction de Benjamin FUKS

présentée par

Manuel UTSCH

pour obtenir le grade de :

DOCTEUR DE SORBONNE UNIVERSITÉ

Sujet de la thèse :

Dilaton-induced dark matter and long-lived particle recasting

soutenue le 13 octobre 2021

devant le jury composé de :

M^{me}	Geneviève BÉLANGER	Examinatrice
M.	Benjamin FUKS	Directeur de thèse
M^{me}	Marie-Hélène GENEST	Rapporteuse
M.	Mark GOODSELL	Membre invité
M.	Bertrand LAFORGE	Examinateur
M.	Andre LESSA	Rapporteur

Acknowledgements

First of all, I would like to thank my supervisors Benjamin Fuks and Mark Goodsell for having accepted me as a Ph.D. student, for their continuous support and assistance during the last years, and for their invaluable and sincere advice. For their patience and their helpful answers to all kinds of questions, including the less intelligent ones, as well as for their helpful comments and suggestions concerning this thesis. For their availability even in these unusual and complicated times disturbed by a pandemic, and for the friendly discussions we had at lunch time or during coffee breaks. I am also grateful to Benjamin for having given me the opportunity to travel to Korea.

In addition, I would like to express my gratitude to the members of the jury, Marie-Hélène Genest and Andre Lessa, for the time invested in reading and reviewing this thesis, and for their useful suggestions to improve it. Likewise, I am grateful to Geneviève Bélanger and Bertrand Laforge for their participation in my thesis defense.

Moreover, I would like to thank my mentor Benoît Douçot and my scientific tutor Adam Falkowski for the feedback and recommendations they gave me during the monitoring committee meetings, and for the time they spent in order to fulfil their roles as members of my monitoring committee.

Thanks also to Pyungwon Ko, Dong Woo Kang and Seung J. Lee for the nice and constructive collaboration on the dilaton-dark-matter project and the friendly discussions we had in Jeju, as well as to Jack Araz, who helped me a great deal in understanding MadAnalysis 5 and was always available whenever I needed help.

I also wish to express my gratitude to a number of people of the LPTHE. In particular I would like to thank Françoise Got, Isabelle Nicolaï and Marjorie Stievenart-Ammour for their assistance in administrative tasks, their availability and their help with all sorts of different questions. Thanks to Sebastian Passehr and Karim Benakli for interesting discussions during lunch time. I am especially grateful to the former and current Ph.D. students I met at the LPTHE, Alessandro, Andrei, Andriani, Anthony, Benjamin, Carlo, Charles, Colin, Constantin, Damien, Elena, Enrico, Francesco (3x), François, Gaëtan, Giovanni, Grégoire, Guillaume, Johannes, Kang, Osmin, Ruben, Simon, Sophie, Pierre, Maximilian, Rhea, Thomas, Vincent, Wenqi, Yann, Yehudi, Yoan, Yifan, some of whom helped me with their experience concerning the Ph.D. Thanks for the great atmosphere, for all the nice and funny moments in the lab, in the cantine and outside of Jussieu.

Furthermore, I want to thank some of my friends who studied with me at the University of Siegen, Anna-Lena, Hendrik, Lisa, Magnus, Marius, Markus, Patrick and Simon, for the enjoyable moments we spent together and for the help they provided me during my

undergraduate and graduate studies.

I would like to express my deepest gratitude to my parents, who allowed me to grow up in a good environment, for their love and their continuous support during my entire life, including their mental and fincancial support during my studies. In the same way, I want to thank my brothers for their presence, their help and support as well as good discussions and helpful advice on various topics.

Finally, it is important for me to thank Olga, who has been by my side from the very beginning of this Ph.D., and even long before. I am grateful for the uncountable wonderful moments we shared together and for the constant support throughout the entire Ph.D., even in difficult times.

Dilaton-induced dark matter and long-lived particle recasting

Abstract:

In 2012, Large Hadron Collider (LHC) experiments have been able to confirm the existence of a scalar particle compatible with the Standard Model (SM) Higgs boson, the last missing particle of the theory. Since then, no convincing signals of new physics beyond the SM have been provided by the LHC, despite the various known shortcomings of the SM leading to the conclusion that it is no complete description of nature. To maximise the discovery and exclusion potential of the collider experiments, the full arsenal of possible search strategies should be exploited, including unconventional ones. Also other, non-collider experiments can provide valuable complementary input for probing the viability of new physics models.

One of the unresolved puzzles in particle physics is the nature of dark matter. Within this work, an effective theory is considered, in which dark matter is coupled to the SM via the dilaton portal, which results from spontaneously broken scale invariance. Two different scenarios of Higgs-dilaton mixing are studied: the minimal mixing scenario and a scenario that includes additional terms which restore gauge invariance. The allowed model parameter space is probed trough a combination of constraints from collider searches and dark matter direct detection experiments, as well as the dark matter relic density and partial wave unitarity bounds.

The second part of this work focuses on collider signatures of long-lived particle (LLP) decays, including in particular displaced tracks and vertices with respect to the primary vertex and the collission axis. New particles might be revealed by these signatures, which could so far have remained undetected in prompt searches. In recent years, a number of searches for LLP signatures has been conducted at the LHC. The present work puts an emphasis on the re-interpretation of such searches in the context of a different BSM physics model via *recasting*. This technique relies on the re-implementation of a physics analysis into a computer program, which can be used for analysing simulated event samples of a different signal model than the one which was originally targeted. The analysis results for the simulated samples can be used, in comparison with the experimental search results, to constrain the model. In this work, two existing LLP searches performed by the ATLAS and CMS collaborations have been implemented in the recasting framework MadAnalysis 5. One of these searches, which targets displaced vertices of oppositely charged leptons, has been used to place constraints on a vector-like leptons model. This thesis also describes a

contribution to a new module of MadAnalysis 5, which simulates the effects of a magnetic field in a detector and calculates quantities relevant for LLP studies.

Keywords:

dilaton, dark matter, long-lived particles, recasting, Large Hadron Collider, vector-like leptons

Dilaton-induced dark matter and long-lived particle recasting

Résumé :

En 2012, des expériences au Grand collisionneur de hadrons (LHC) ont confirmé l'existence d'une particule scalaire compatible avec le boson de Higgs du modèle standard (MS), la dernière particule manquante de la théorie. Depuis, aucun signal convaincant de nouvelle physique au-delà du MS n'a pu être apporté par le LHC, malgré un bon nombre de lacunes connues du MS indiquant qu'il doit être une description incomplète de la nature. Afin de maximiser le potentiel de découverte et d'exclusion des expériences au LHC, l'intégralité des stratégies de recherche possibles devraient être exploitées, y compris celles qui sont moins courantes. De plus, d'autres données complémentaires venant d'expériences non-liées à des collisionneurs peuvent être utiles.

Une des questions persistantes en physique des particules est celle de la nature de la matière noire. Dans le cadre de ce travail, une théorie effective est examinée, dans laquelle la matière noire est couplée au MS via la portail du dilaton, qui résulte de l'invariance d'échelle spontanément brisée. Deux scénarios de mixage entre le boson de Higgs et le dilaton sont étudiés, dont le scénario minimal ainsi qu'un scénario incluant des termes supplémentaires qui réinstaurent l'invariance de jauge. L'espace des paramètres est sondé en prenant en compte des contraintes basées sur des expériences de collisionneur et de détection directe de matière noire, la densité relique de matière noire et l'unitarité.

La deuxième partie de ce travail se concentre aux signatures de désintégration de particules à longue vie (PLV), en particulier les traces et vertex déplacés par rapport au vertex premier, où se déroule la collision, et l'axe de collision. De nouvelles particules pourraient se manifester par ces signatures, alors qu'elles auraient pu, jusqu'à présent, avoir échappé aux recherches plus courantes limitées aux particules dont l'intégration est imminente. Durant les dernières années, des recherches ont été menées au LHC afin d'identifier des événements présentant ces signatures. Ce travail met l'accent sur la réinterprétation de ces recherches dans le contexte d'un autre modèle de physique au-delà du MS avec la technique de *recasting*. Cette dernière vise à reproduire la logique de l'analyse d'événements de ces recherches telle qu'elle est appliquée aux événements observés experimentalement dans un code qui peut être appliqué à des événements simulés. En appliquant cette analyse à des événements simulés, les résultats peuvent être utilisés, en comparaison avec les résultats de l'analyse expérimentale, à contraindre le modèle. Deux recherches existantes des collaborations ATLAS et CMS ont ainsi été implémentées dans

le logiciel MadAnalysis 5. Une de ces recherches, ciblant des vertex déplacés impliquant des leptons de charges opposées, a été utilisée pour restraindre un modèle de leptons de type vecteur. Cette thèse porte également sur la contribution à un nouveau module de MadAnalysis 5. Celui-ci permet une simulation des effets d'un champ magnétique présent dans le volume d'un détecteur, calculant en même temps des grandeurs pertinentes dans le cadre d'études impliquant des PLV.

Mots clés :

dilaton, matière noire, particules à longue vie, recasting, Grand collisionneur de hadrons, leptons de type vecteur

Contents

Introduction

Particle physics has celebrated one of its biggest successes in 2012 at the Large Hadron Collider (LHC) with the discovery of a 125 GeV scalar particle that is in harmony with the predicted Standard Model (SM) Higgs boson. Close to 40 years after the completed theoretical elaboration of this model [1], its particle content has finally been confirmed. But even before the Higgs boson was discovered, it was already clear that the SM could not be the final theory of all fundamental particles and their interactions. In spite of its extraordinary success in past and current collider experiments, there are solid arguments for its incompleteness, which include but are not limited to the absence of a suitable candidate for dark matter (DM) and the fact that it does not incorporate quantum gravity. Needless to say, the LHC was not just built for discovering the missing Higgs boson, but it continued and will continue operating with the aim of finding some clear signal of physics beyond the SM. Now, after Run 2, it can be said that it has so far failed to do so.

A plethora of different models of physics Beyond the SM (BSM) exist, which typically adress at least one, if not more of the unanswered questions of the SM in a theoretically well-motivated way. A very prominent example of a BSM theory is the Minimal Supersymmetric Standard Model (MSSM), which is an extension of the SM that is based on Supersymmetry (SUSY), a symmetry which connects bosonic and fermionic degrees of freedom. At the beginning of the LHC, the MSSM was one of the favoured candidate models for new physics [2], as it provides a very elegant solution for the hierarchy problem of the SM as well as a DM candidate, the lightest supersymmetric particle (LSP). However, until now, the LHC has not been able to confirm the existence of any of the supersymmetric particles predicted by the theory, and searches for SUSY have continuously pushed the limits towards higher masses. This has in some sort dampened the former enthusiasm about SUSY, even if it is far from being dead. But also among the other BSM physics models there is currently no candidate that is strongly favoured by the available LHC data.

A somewhat pessimistic, but natural question to ask is: Could it be that new physics enters only at energy scales which are not accessible to contemporary high-energy collider experiments? Another imaginable option is that new physics manifests itself via very rare processes, which have therefore not been observed in the past, or at least not in a sufficient number to draw any conclusions. Both of these possibilities will be addressed in the future via an increase in the energy and luminosity through upgrades and possibly at different colliders. Nonetheless, this should not be the only way to deal with the non-observation of new physics. One should also consider the option that new physics could be in reach of the existing experiments, but is not observed due to inadequate search strategies. Given

the high amount of financial and human ressources necessary to generate experimental data, it is important to make use of it to the best of our knowledge [3]. Seeing that the collider signatures studied so far did not unveil any clear manifestation of new physics, it is about time to seriously consider also more exotic signatures. On the other hand, the experimental signatures are not uniquely linked to a specific model, but can in most instances be generated by a larger class of signal models. Therefore, it is sensible not to restrict the use of search results to the study of a particular signal model of interest, but also examine the implications of the searches on other models. Furthermore, in addition to using data from high energy collisions, it can be useful to include also complementary data measured by other, non-collider experiments.

To some extent, the work presented in this thesis encompasses all of these aspects. It essentially covers two main topics. The first one is the phenomenological study of a particular SM extension, which accomodates DM via the introduction of an additional scalar particle, the dilaton, which is embedded into the SM Lagrangian by assuming spontaneously broken scale invariance. This results in an effective theory, in which the dilaton serves as a mediator for interactions between the DM candidate and the SM particle content. For this model, various constraints on the parameter space are determined by means of recent experimental results from collider searches, which include Higgs and heavy scalar searches as well as DM searches, but also via the observed DM relic density and bounds from direct detection together with partial wave unitarity. Also prospects of DM production at future colliders are estimated.
The second major topic is the search for long-lived particles (LLPs) at the LHC, and in particular the re-interpretation of existing LLP searches of the ATLAS and CMS collaborations. Two selected LLP searches have been implemented within the MadAnalysis 5 recasting framework. In this work, the details of the implementation and validation are documented and the challenges and difficulties of these tasks as well as the limitations of the re-implemented analyses are explained. One of these analyses is used to probe the excluded parameter space of a vector-like lepton (VLL) model. Additionally, a technical enhancement of MadAnalysis 5 for the simulation of particle trajectories under the influence of a magnetic field in a detector and the calculation of displacement variables for LLP searches is presented.

The present thesis is organised in the following way: In chapter 1, the fundamental aspects of the construction of the SM will be reviewed. Both its successes and its deficiencies, from the theoretical and experimental point of view, will be pointed out in order to advert to the necessity of new physics beyond the SM. The chapter will also include a short presentation of two examples of BSM theories. Chapter 2 gives an introduction to the concept of recasting, a technique for the re-interpretation of existing physics analyses at collider experiments with a different signal hypothesis. It will also discuss some important technical elements of this technique and give an overview about the different existing recasting approaches and tools. Chapter 3 is devoted to the construction of a theory involving the dilaton, which is systematically introduced into an existing theory, guided by the principle of spontaneous broken scale invariance. This is first explained for a generic Lagrangian, before it is applied to the SM Lagrangian, augmented by kinetic and mass terms of a DM candidate, leading to the above-mentioned effective theory. The study of this theory is the matter of chapter 4, where the model parameter space is limited with the

previously mentioned collider and complementary non-collider bounds. Different scenarios of Higgs-dilaton mixing are investigated. Finally, chapter 5 illustrates the interest in LLP searches and It then explains the new particle propagator module of MadAnalysis 5, before documenting the re-implementation and validation of two LLP searches of the CMS and ATLAS collaborations. As mentioned earlier, the parameter space of the VLL model will then be constrained by application of the ATLAS analysis. Ultimately, some concluding remarks about the presented work will end this thesis.

The contents of chapters 3 and 4 are based on the article

> Benjamin Fuks, Mark D. Goodsell, Dong Woo Kang, Pyungwon Ko, Seung J. Lee and Manuel Utsch; *Heavy dark matter through the dilaton portal*; JHEP **10** (2020) 44; `arXiv:2007.08546`,

whereas the work of chapter 5 is part of a larger project about LLP recasting in collaboration with Jack Y. Araz, Benjamin Fuks and Mark D. Goodsell, for which an article is planned to be published in the near future.

Chapter 1

The Standard Model, its successes and its shortcomings

Our current knowledge about the existing particles, their properties and their interactions is to a wide extent incorporated in the Standard Model of particle physics, hereafter simply referred to as *the Standard Model* (SM). Its predictions are in remarkable agreement with an immense number of measurements in contemporary experimental high-energy physics research [4–7]. Yet, various arguments from both the theoretical and experimental point of view lead to the conclusion that the SM is an incomplete description of nature and can at best represent a low-energy description of a more fundamental theory. This explains why tremendous efforts are being made to find theoretically well-motivated and experimentally viable candidate models to eventually replace the SM some day.

Before evoking any ideas and models for physics beyond the Standard Model (BSM) or strategies to test them experimentally, it is worthwhile recalling the essential aspects which make up the SM, which is the purpose of section 1.1. A number of arguments for qualifying the SM as a successful theory is given in section 1.2, while the most striking deficits of the SM are discussed in section 1.3. They encourage the search for new physics and are addressed by diverse BSM theories. Two examples of models, which extend the SM, will be introduced in section 1.4 and will be relevant as signal models in chapter 5. This chapter uses explanations, formulæ and references from refs. [1, 8–32].

1.1 A short review of the Standard Model

There are certainly numerous possible ways to present the Standard Model. The motivation of this section is to give an idea of the main concepts and model specific constituents involved in the SM, present its particles and shed light on the possible interactions. Some basic derivations will be given or sketched to clarify the origin of the most fundamental features of the SM, in particular gauge invariance and the allowed interactions, the mechanism behind the particle masses and flavour mixing. No detailed and more advanced calculations will be given though, such as the computation of beta functions via loop diagrams. The outline of this section is as follows: It starts with a summary of the main ideas going into the construction of the SM and a presentation of the field and particle

content in section 1.1.1. Section 1.1.2 will recapitulate the concept of gauge symmetries and the construction of gauge theories. In section 1.1.3, the gauge theory of the electroweak interactions and the mechanism of electroweak symmetry breaking will be studied. Section 1.1.4 on the other hand discusses Quantum Chromodynamics, which is the gauge theory of the strong interactions.

1.1.1 Building blocks of the Standard Model

As a theory of fundamental particles and their interactions, the Standard Model is constructed based on some rather general principles, which regulate the practice of model building in particle physics. On the other hand, it involves a number of specific ingredients, which distinguish this particular model from other theories of particle physics. Both of these aspects will briefly be recapitulated here using refs. [13, 33] and a list of the SM particles will be given.

The formulation of theories in particle physics usually makes use of the framework of quantum field theory, that builds upon quantum mechanics and the theory of special relativity as well as on classical field theory. There is no room in this work for an in-depth introduction to the concepts of quantum field theory (QFT), so it is assumed that the reader is familiar with these. In QFT, a model is formulated as a Lagrangian, written in terms of fields, which transform under different representations of the Lorentz group. For a fundamental theory, such a Lagrangian must be Poincaré invariant and may feature a certain number of additional symmetries.

In particular, the Lagrangian can be constructed by requiring it to be symmetric under a set of gauge transformations, which apply to the different fields in the Lagrangian. On the other hand, continuous *global* symmetries are not enforced in the same way, since they cause problems in theories of quantum gravity. Still, they can exist as accidental symmetries of the Lagrangian, which is the case when all symmetry breaking operators are non-renormalisable and therefore not included. Such symmetries turn out to be only approximate, since they get violated by higher order terms in perturbation theory [34]. An important concept in quantum field theory is spontaneous symmetry breaking, where the symmetry is not broken on the level of the Lagrangian, but by the vacuum state. The Goldstone theorem [35, 36] states that the spontaneous breakdown of a continuous *global* symmetry implies the existence of a massless boson (Goldstone boson) for each broken generator. In contrast, there are no physical Goldstone bosons in spontaneously broken *gauge* symmetries: the Goldstone modes are "eaten" by the gauge bosons, where they show up as longitudinal helicity states, and the gauge bosons acquire a mass [37–43]. Finally, a QFT becomes only predictive, once its independent parameters have been determined by means of experimental measurements.

The actual construction of a specific model, i.e. in particular its Lagrangian, then usually involves the following steps:

1. A gauge group is chosen.
2. The field content of the model is specified, and correspondingly also the representations under which the fields transform under gauge transformations.
3. A Lagrangian is composed from the field contents such that it respects the gauge

symmetry, i.e. the action must be invariant under gauge transformations. All renormalisable, gauge invariant operators are included. Renormalisability is important, since it makes the theory predictive after a finite number of measurements, since it requires only a finite number of counterterms in order to absorb all divergences appearing in the calculation of observables. Note that effective theories, in contrast to fundamental theories, may contain non-renormalisable operators, as they are not expected to by valid at arbitrary energy scales.

4. Part of the gauge symmetry is spontaneously broken according to a pattern, which needs to be provided.

The concept of gauge symmetries will be revised very briefly in section 1.1.2, where also the specification of the representations will be clarified. However, beforehand, the basic ingredients of the SM will be presented.

Following the above principles, the Standard Model is obtained after making the following choices: The SM gauge group is a product of three gauge groups,

$$G_{\text{SM}} = SU(3)_C \times SU(2)_L \times SU(1)_Y \,.$$

These gauge groups introduce $8 + 3 + 1$ associated vector fields (gauge bosons) into the theory, namely the gluon fields G^a_μ with $a = 1, \ldots, 8$ as well as the vector fields W^j_μ with $j = 1, 2, 3$ and B_μ, which will be discussed more later on. For the gauge bosons, it is not necessary to explicitly specify the representation, c.f. section 1.1.2.

The remaining field content is given in table 1.1 together with the corresponding representations of the SM gauge group. They are specified in terms of two bold numbers, indicating whether the fields transform under the singlet or triplet (doublet) representation of $SU(3)_C$ ($SU(2)_L$), and a third number corresponding to the charge under $U(1)_Y$, the *hypercharge*[1]. What exactly this means will become clear in section 1.1.2. The SM contains the $SU(2)_L$ doublets Q_i, L_i of left-handed fermion fields and $SU(2)_L$ singlets $u_{i,R}$, $d_{i,R}$, $e_{i,R}$, which are right-handed counterparts to these fields, as well as a complex scalar $SU(2)_L$ doublet H (*Higgs* doublet). Here, the index i is a generation index with possible values $i = 1, 2, 3$. More precisely, in the first place, the left- and right-handed fermion fields are independent fields, but they mix through mass terms generated by spontaneous symmetry breaking, c.f. section 1.1.3.5. Note that the left-handed lepton fields $\nu_{i,L}$ do not have a right-handed counterpart. The fermions, which transform non-trivially under $SU(3)_C$ are called *quarks*, the remaining ones *leptons*; their names in the different generations will be given below. Each of the quark fields exists in three different colours, so they carry an additional colour index $a = 1, 2, 3$ indicating the corresponding component of the $SU(3)$ triplet, which has been omitted here to simplify the notation. Concerning the notation of the Higgs doublet components, the field ϕ^+ carries positive electric charge ($+e$), while ϕ^0 is electrically neutral, which will become clear in section 1.1.3.2.

In the SM, spontaneous symmetry breaking occurs in the electroweak gauge symmetry $SU(2)_L \times U(1)_Y$, which is broken down to the group $U(1)_{\text{EM}}$, the gauge symmetry of the electromagnetic interactions, while the $SU(3)_C$ group remains intact:

$$G_{\text{SM}} \quad \to \quad SU(3)_C \times U(1)_{\text{EM}} \,. \tag{1.1.1}$$

1. Note that this number depends on the conventions used in the definition of the gauge transformations and the covariant derivative. It is quite frequent in the literature that it occurs with a factor of 2. More details about the different conventions can be found in [44].

	fields	representation
quark sector	$Q_i = \begin{pmatrix} u_{i,L} \\ d_{i,L} \end{pmatrix}$	$(\mathbf{3}, \mathbf{2}, 1/6)$
	$u_{i,R}$	$(\mathbf{3}, \mathbf{1}, 2/3)$
	$d_{i,R}$	$(\mathbf{3}, \mathbf{1}, -1/3)$
lepton sector	$L_i = \begin{pmatrix} \nu_{i,L} \\ e_{i,L} \end{pmatrix}$	$(\mathbf{1}, \mathbf{2}, -1/2)$
	$e_{i,R}$	$(\mathbf{1}, \mathbf{1}, -1)$
Higgs sector	$H = \begin{pmatrix} \phi^+ \\ \phi^0 \end{pmatrix}$	$(\mathbf{1}, \mathbf{2}, 1/2)$

Table 1.1: List of fields and representations of the SM fermion and scalar sectors. The index $i = 1, 2, 3$ is a generation index, whereas the quark fields carry an additional colour index $a = 1, 2, 3$, which has been omitted here to simplify the notation.

This symmetry pattern is achieved through a scalar potential $V(H)$ of a form that allows the Higgs doublet to acquire a vacuum expectation value (vev) at the minimum of V,

$$\langle H \rangle = \begin{pmatrix} 0 \\ v/\sqrt{2} \end{pmatrix} . \tag{1.1.2}$$

As will be illustrated in section 1.1.3.2, it is the sign of one of the parameters appearing in $V(H)$ which provokes this minimum and hence a non-zero vev.

Table 1.1 has provided a list of scalar and fermion fields of the SM, and it has been mentioned that each gauge group of G_{SM} implies a certain number of vector fields. Before reviewing the fundamental aspects of this quantum field theory, a complete list of the fundamental physical particles in the SM shall be given in table 1.2, which has been inspired by ref. [45]. The connection between these particles and the fields in table 1.1 will be clarified in the following subsections.

1.1.2 Gauge symmetries

Section 1.1.1 has shown the relevance of gauge symmetries in the SM and other models of particle physics. The SM gauge group G_{SM} consists of an abelian group $U(1)$ and two non-abelian groups of the type $SU(N)$. The construction of abelian and non-abelian gauge theories will be reviewed here based on ref. [1] for these particular types of groups in anticipation of sections 1.1.3 and 1.1.4, where these concepts will find application.

1.1.2.1 Abelian gauge theories

To illustrate the construction of an abelian gauge theory with a simple example, a Lagrangian involving just one complex scalar field ϕ will be considered, which contains a kinetic term and a potential that only depends on the modulus of ϕ:

$$\mathcal{L} = \partial_\mu \phi^* \partial^\mu \phi - V(|\phi|) , \tag{1.1.3}$$

Gauge bosons	Strong interactions:		8 gluons
	Weak interactions:		$W^{\pm}$, Z bosons
	Electromagnetic interactions:		γ (photon)
leptons	1st generation	2nd generation	3rd generation
neutrinos	ν_e electron neutrino	ν_μ muon neutrino	ν_τ tau neutrino
charged leptons	e^- electron	μ^- muon	τ^- tauon/tau lepton
quarks (3 colours)	1st generation	2nd generation	3rd generation
up-type quarks	u up	c charm	t top
down-type quarks	d down	s strange	b bottom
Higgs boson H^0			

Table 1.2: Listing of all Standard Model particles, inspired by [45]. Their anti-particles are not explicitly included. The anti-particle of the electron is also called *positron*, whereas the other anti-particles are usually simply denoted by the particle's name together with the prefix *anti* or the indication of the charge.

A $U(1)$ transformation acting on ϕ is just a phase transformation

$$\phi \to \phi' = e^{i\alpha}\phi\,, \qquad \phi^* \to (\phi^*)' = e^{-i\alpha}\phi^*\,, \tag{1.1.4}$$

under which the potential $V(|\phi|)$ is obviously invariant, so that it does not need to be discussed any further. The same would be the case for the kinetic term, if α was just a constant parameter. However, what makes this transformation a *gauge* transformation is the fact that it is local, i.e. the transformation parameter $\alpha(x)$ is dependent on the position in space-time x^μ. This has no consequences on the transformation of the potential, so the variation of $\mathcal{L}$ emanates entirely from the transformation of the kinetic term. For infinitesimal values of α it is given by

$$\delta\mathcal{L} = i(\partial_\mu\alpha)(\phi\,\partial^\mu\phi^* - \phi^*\partial^\mu\phi)\,. \tag{1.1.5}$$

The strategy to construct a gauge invariant Lagrangian is the following: One introduces a vector field $A_\mu(x)$ into the Lagrangian, which transforms under the gauge transformations in the following way:

$$A_\mu(x) \to A'_\mu(x) = A_\mu(x) - \frac{1}{e}\partial_\mu\alpha(x)\,. \tag{1.1.6}$$

Here, the constant e is the gauge coupling related to the gauge group. In order to make the Lagrangian gauge invariant, it is introduced via the *covariant derivative* D_μ,

$$D_\mu\phi = (\partial_\mu + ieA_\mu)\phi\,. \tag{1.1.7}$$

The term *covariant* refers to the behaviour under gauge transformations, which is just the same as for the field ϕ:

$$\begin{aligned} D_\mu\phi \to (D_\mu\phi)' &= (\partial_\mu + ieA'_\mu)\phi' \\ &= \partial_\mu(e^{i\alpha(x)}\phi) + ie\left(A_\mu - \frac{1}{e}\partial_\mu\alpha(x)\right)e^{i\alpha(x)}\phi \\ &= e^{i\alpha(x)}D_\mu\phi\,. \end{aligned} \tag{1.1.8}$$

Here, only the x-dependence of α has been written explicitly to show that the transformation is a local one, but of course the fields ϕ and A_μ also depend on x. From eq. (1.1.8) it is clear that by replacing the ordinary space-time derivative in the initial Lagrangian by the covariant derivative one obtains a gauge-invariant version of the Lagrangian

$$\mathcal{L} \supset (D_\mu \phi)^* (D^\mu \phi) - V(|\phi|)\,. \tag{1.1.9}$$

However, now that the Lagrangian contains an additional vector field A_μ, it should also provide a corresponding kinetic term in order for A_μ to be a dynamical field, which must be gauge invariant as well. It is constructed from the field strength tensor $F_{\mu\nu}$, which can be expressed in terms of the commutator of two covariant derivatives as follows:

$$F_{\mu\nu} = -\frac{i}{e}[D_\mu, D_\nu] = \partial_\mu A_\nu - \partial_\nu A_\mu\,. \tag{1.1.10}$$

It is straightforward to show from the transformation of A_μ according to eq. (1.1.6) that $F_{\mu\nu}$ is gauge invariant:

$$\begin{aligned} F'_{\mu\nu} &= \partial_\mu A'_\nu - \partial_\nu A'_\mu \\ &= \partial_\mu \left(A_\nu - \frac{1}{e}\partial_\nu \alpha(x) \right) - \partial_\nu \left(A_\mu - \frac{1}{e}\partial_\mu \alpha(x) \right) \\ &= \partial_\mu A_\nu - \partial_\nu A_\mu \\ &= F_{\mu\nu}\,. \end{aligned} \tag{1.1.11}$$

Therefore the kinetic term to include into the Lagrangian, given by

$$\mathcal{L} \supset -\frac{1}{4} F_{\mu\nu} F^{\mu\nu}\,, \tag{1.1.12}$$

is also gauge invariant.

The Lagrangian of a complex scalar field given in eq. (1.1.3) has been chosen for its simplicity to illustrate how gauge invariance of the kinetic term can be restored via the covariant derivative. This principle is however also applicable in the same way to fermions. Furthermore, gauge invariant interaction terms of different fields can be composed, which are not discussed here. The introduction of a vector field via the covariant derivative has phenomenological consequences since it generates new interaction terms. In the above example of a scalar field, these are $\phi^*\phi A$ and $\phi^*\phi AA$ interactions. For a fermion field ψ, since the kinetic term only involves one derivative, the covariant derivative only leads to a $\overline{\psi}\psi A$ interaction.

There is one more important point to be discussed, which is the subject of representations. Fields can transform under different representations of the same gauge symmetry, i.e. they can have different *charges* under the gauge group. If the constant e in the above example is identified with the electric charge of the scalar ϕ, then the example describes a gauge theory of scalar Quantum Electrodynamics (QED). Suppose now that the charge of ϕ is instead Qe, then the gauge transformation of ϕ and its covariant derivative are given by

$$\phi \to \phi' = e^{iQ\alpha(x)}\phi\,, \qquad D_\mu \phi = (\partial_\mu + ieA_\mu Q)\,\phi\,, \tag{1.1.13}$$

and the covariant derivative transforms as

$$D_\mu \phi \to e^{iQ\alpha(x)} D_\mu \phi \,. \tag{1.1.14}$$

To come back to the specification of the representations in table 1.1, the third number represents the *hypercharge* Y, which is the generator of the group $U(1)_Y$, and the transformation of the fields under this group can be obtained in analogy to eqs. (1.1.13) and (1.1.14). The representations of the different fields determine which operators, apart from the kinetic terms, respect the gauge symmetry and are hence allowed in the Lagrangian.

1.1.2.2 Non-abelian gauge theories

Non-abelian gauge theories are based on groups with non-commuting group elements (non-abelian groups). In the SM, the non-abelian gauge groups are of the type $SU(N)$ ($SU(2)$ and $SU(3)$), which will be considered here.

$SU(N)$ transformations can be expressed in terms of $N^2 - 1$ Hermitian matrices T^a and real parameters α^a,

$$U = \exp(i\alpha^a T^a) \equiv \exp(i\alpha) \qquad \text{with} \quad \alpha \equiv \alpha^a T^a \,. \tag{1.1.15}$$

As usual, the summation of the index a is implicit with $a = 1, \ldots, N^2 - 1$. The matrices T^a are the *generators* of the group and satisfy the Lie algebra relation

$$[T^a, T^b] = i f^{abc} T^c \,, \tag{1.1.16}$$

where f^{abc} are totally anti-symmetric structure constants. Furthermore, the generators will be required to be normalised according the convention $\mathrm{Tr}(\mathrm{T^a T^b}) = \frac{1}{2}\delta^{\mathrm{ab}}$.

Again, a simple example of a theory with scalar fields will be studied, where the transformation acts on an N-component vector [2] Φ of scalar fields ϕ_i:

$$\Phi \to \Phi' = U\Phi \,, \qquad \Phi^\dagger \to (\Phi^\dagger)' = \Phi^\dagger U^\dagger \,, \qquad \text{with} \quad \Phi = \begin{pmatrix} \phi_1 \\ \vdots \\ \phi_N \end{pmatrix} . \tag{1.1.17}$$

A similar Lagrangian to eq. (1.1.3) will be taken, which is symmetric under global $SU(N)$ transformations:

$$\mathcal{L} = (\partial_\mu \Phi)^\dagger (\partial^\mu \Phi) - V(\Phi^\dagger \Phi) \,. \tag{1.1.18}$$

However, it violates the symmetry when the transformations are local, i.e. for x^μ-dependent parameters $\alpha^a(x)$. The space-time derivative transforms as

$$\partial_\mu \Phi \to \partial_\mu \Phi' = \partial_\mu (U\Phi) = U \partial_\mu \Phi + (\partial_\mu U)\Phi \,, \tag{1.1.19}$$

and therefore the kinetic term in eq. (1.1.18) is not invariant under $SU(N)$ transformations. As in the abelian case, it can be made invariant by replacing the usual space-time derivative by a gauge-covariant derivative, which now involves N different gauge fields A^a_μ. It will be

2. Such a vector of fields, transforming under some representation of a symmetry group, is commonly called *multiplet*, or more specifically *singlet*, *doublet*, *triplet*, *sextet*, *octet*, ... for 1, 2, 3, 6, 8, ... components.

convenient to write $A_\mu \equiv A_\mu^a T^a$. Assuming the same form of the covariant derivative as in the abelian case, the requirement that it transforms in the same way as Φ determines the transformation of the gauge fields:

$$\begin{aligned}(D_\mu\Phi)' &= [(\partial_\mu + igA^\mu)\Phi]' \\ &= (\partial_\mu + igA'_\mu)(U\Phi) \\ &= U(\partial_\mu + U^\dagger(\partial_\mu U) + igU^\dagger A'_\mu U)\Phi \\ &\stackrel{!}{=} U(D_\mu\Phi) \\ &= U(\partial_\mu + igA^\mu)\Phi\,.\end{aligned} \tag{1.1.20}$$

Here the expression of the transformed ordinary derivative $\partial_\mu U$ from eq. (1.1.19) was used. By comparing the third and the last line of eq. (1.1.20), one obtains:

$$igA_\mu = U^\dagger(\partial_\mu U) + igU^\dagger A'_\mu U \quad \Leftrightarrow \quad A'_\mu = UA_\mu U^\dagger - \frac{i}{g}U\partial_\mu U^\dagger\,. \tag{1.1.21}$$

As before, the Lagrangian should also provide kinetic terms for the gauge fields in a gauge invariant way. To this end, a field strength tensor can be constructed, proceeding like in the abelian case:

$$\begin{aligned}F_{\mu\nu} &= -\frac{i}{g}[D_\mu, D_\nu] \\ &= \partial_\mu A_\nu - \partial_\nu A_\mu + ig[A_\mu, A_\nu] \\ &= \partial_\mu A_\nu - \partial_\nu A_\mu + igA_\mu^b A_\nu^c [T^b, T^c] \\ &= \partial_\mu A_\nu - \partial_\nu A_\mu - gf^{abc}A_\mu^b A_\nu^c T^a \\ &= F_{\mu\nu}^a T^a\,,\end{aligned} \tag{1.1.22}$$

where

$$F_{\mu\nu}^a \equiv \partial_\mu A_\nu^a - \partial_\nu A_\mu^a - gf^{abc}A_\mu^b A_\nu^c\,. \tag{1.1.23}$$

Its form is manifestly different from the one in the abelian case. Moreover, it is not invariant under the $SU(N)$ transformations, but its transformation is given by

$$F_{\mu\nu} \to F'_{\mu\nu} = UF_{\mu\nu}U^\dagger\,. \tag{1.1.24}$$

It is easy to see that also the combination $F_{\mu\nu}F^{\mu\nu}$ is not gauge invariant. Taking the trace however makes it gauge invariant, because the cyclic permutation property of the trace can be used to combine the surrounding U and $U^\dagger$ matrices to the identity matrix. Therefore, the gauge boson kinetic terms are embedded in

$$\mathcal{L} \supset -\frac{1}{2}\mathrm{Tr}\,(F_{\mu\nu}F^{\mu\nu}) = -\frac{1}{4}F_{\mu\nu}^a F^{a,\mu\nu}\,, \tag{1.1.25}$$

where the standard normalisation convention was used.

As opposed to abelian gauge theories, the kinetic term in non-abelian gauge theories is accompanied by interaction terms involving three or four gauge boson fields A_μ^a of different indices a, which one can see by expanding eq. (1.1.25) after inserting the expression of eq. (1.1.23). Like in the abelian case, the covariant derivative induces $\Phi^\dagger\Phi A$ and $\Phi^\dagger\Phi AA$ interactions in the scalar case and $\overline{\Psi}\Psi A$ interactions in the fermion case (where Ψ is like Φ a *vector* of fields, but here fermionic ones).

1.1.2.3 The fundamental representations of $SU(2)$ and $SU(3)$

The relevant fermion representations in the SM are the fundamental representations of $SU(2)$ and $SU(3)$. Here, the generators in these representations will be given, together with the structure constants, which do not depend on the representation.

In the fundamental representation of $SU(2)$, the generators can be chosen proportional to the Pauli matrices, $T^i = \sigma^i/2$, and the structure constants are the values of the totally anti-symmetric tensor ϵ^{ijk}, so that the Lie algebra relation is given by

$$\left[\frac{\sigma^i}{2}, \frac{\sigma^j}{2}\right] = i\epsilon^{ijk}\frac{\sigma^k}{2}\,, \qquad i,j,k \in \{1,2,3\}\,, \tag{1.1.26}$$

with

$$\sigma^1 = \begin{pmatrix} 0 & 1 \\ 1 & 0 \end{pmatrix}\,, \qquad \sigma^2 = \begin{pmatrix} 0 & -i \\ i & 0 \end{pmatrix}\,, \qquad \sigma^3 = \begin{pmatrix} 1 & 0 \\ 0 & -1 \end{pmatrix}\,. \tag{1.1.27}$$

For the generators in the fundamental representation of $SU(3)$, instead of Pauli matrices, the Gell-Mann matrices λ^a are used, i.e. $T^a = \lambda^a/2$, with

$$\lambda^1 = \begin{pmatrix} 0 & 1 & 0 \\ 1 & 0 & 0 \\ 0 & 0 & 0 \end{pmatrix}\,, \quad \lambda^2 = \begin{pmatrix} 0 & -i & 0 \\ i & 0 & 0 \\ 0 & 0 & 0 \end{pmatrix}\,, \quad \lambda^3 = \begin{pmatrix} 1 & 0 & 0 \\ 0 & -1 & 0 \\ 0 & 0 & 0 \end{pmatrix}\,, \quad \lambda^4 = \begin{pmatrix} 0 & 0 & 1 \\ 0 & 0 & 0 \\ 1 & 0 & 0 \end{pmatrix}\,,$$

$$\lambda^5 = \begin{pmatrix} 0 & 0 & -i \\ 0 & 0 & 0 \\ i & 0 & 0 \end{pmatrix}\,, \quad \lambda^6 = \begin{pmatrix} 0 & 0 & 0 \\ 0 & 0 & 1 \\ 0 & 1 & 0 \end{pmatrix}\,, \quad \lambda^7 = \begin{pmatrix} 0 & 0 & 0 \\ 0 & 0 & -i \\ 0 & i & 0 \end{pmatrix}\,, \quad \lambda^8 = \frac{1}{\sqrt{3}}\begin{pmatrix} 1 & 0 & 0 \\ 0 & 1 & 0 \\ 0 & 0 & -2 \end{pmatrix}\,. \tag{1.1.28}$$

They fulfill

$$\left[\frac{\lambda^i}{2}, \frac{\lambda^j}{2}\right] = if^{ijk}\frac{\lambda^k}{2}\,, \tag{1.1.29}$$

where the non-zero structure constants are given by

$$\begin{aligned} &f^{123} = 1\,, \quad f^{147} = \frac{1}{2}\,, \quad f^{156} = -\frac{1}{2}\,, \quad f^{246} = \frac{1}{2}\,, \quad f^{257} = \frac{1}{2}\,, \\ &f^{345} = \frac{1}{2}\,, \quad f^{367} = -\frac{1}{2}\,, \quad f^{458} = \sqrt{\frac{3}{2}}\,, \quad f^{678} = \sqrt{\frac{3}{2}}\,. \end{aligned} \tag{1.1.30}$$

1.1.3 Electroweak theory and spontaneous symmetry breaking

The electroweak theory is the part of the SM related to the electroweak gauge symmetry, which is the symmetry under $SU(2)_L \times U(1)_Y$ gauge transformations. This symmetry is related to a number of interaction terms of the corresponding gauge bosons with the fermion and scalar (or Higgs) sectors of the SM, but in addition, its breakdown to $U(1)_{\mathrm{EM}}$ in spontaneous symmetry breaking generates the masses of the SM gauge bosons $W^\pm$ and Z. As for the SM fermions, they acquire their masses via Yukawa interactions with

the Higgs field. The electroweak interactions, the mechanism of spontaneous symmetry breaking in the SM, the masses and mixing shall be reviewed in the following, using for the most part formulæ and explanations of ref. [14], but with some changes on the notation inspired by ref. [33].

1.1.3.1 The electroweak Lagrangian

Different sorts of terms contribute to the electroweak Lagrangian

$$\mathcal{L}_{\text{EW}} = \mathcal{L}_{\text{gauge}} + \mathcal{L}_H + \mathcal{L}_f + \mathcal{L}_{\text{Yukawa}} \,. \tag{1.1.31}$$

The first term $\mathcal{L}_{\text{gauge}}$ involves the field strength tensors of the gauge boson fields W^i_μ and B_μ,

$$W^i_{\mu\nu} = \partial_\mu W^i_\nu - \partial_\nu W^i_\mu - g\epsilon^{ijk} W^j_\mu W^k_\nu \,, \quad i = 1,2,3 \,, \tag{1.1.32}$$

$$B_{\mu\nu} = \partial_\mu B_\nu - \partial_\nu B_\mu \,, \tag{1.1.33}$$

where g is the gauge coupling of the $SU(2)_L$ group, and is given by

$$\mathcal{L}_{\text{gauge}} = -\frac{1}{4} W^i_{\mu\nu} W^{i,\mu\nu} - \frac{1}{4} B_{\mu\nu} B^{\mu\nu} \,. \tag{1.1.34}$$

The $U(1)_Y$ coupling will be denoted by g', but does not appear in the field strength tensor. While these terms include the kinetic terms of the gauge bosons, the last term in eq. (1.1.32) gives rise to self-interactions of the different $SU(2)_L$ gauge bosons W^i_μ, which will not be given explicitly here.

The second contribution $\mathcal{L}_H$ consists of the scalar kinetic and gauge interaction terms, generated by the gauge covariant derivative applied on the scalar $SU(2)_L$ doublet H, and the scalar potential $V(H)$:

$$\mathcal{L}_H = \left(D^\mu H\right)^\dagger \left(D_\mu H\right) - V(H) \,. \tag{1.1.35}$$

Given that H transforms under the $(\mathbf{1}, \mathbf{2}, 1/2)$ representation of the SM gauge group, its covariant derivative reads

$$D_\mu H = \left(\partial_\mu + ig\frac{\sigma^i}{2} W^i_\mu + \frac{ig'}{2} B_\mu\right) \begin{pmatrix} \phi^+ \\ \phi^0 \end{pmatrix} \,. \tag{1.1.36}$$

As mentioned earlier, the form of the scalar potential plays a crucial role in the breakdown of the electroweak symmetry. Its form is given by

$$V(H) = \mu^2 H^\dagger H + \lambda \left(H^\dagger H\right)^2 \tag{1.1.37}$$

with real parameters $\mu^2 < 0$ and $\lambda > 0$, leading to the required symmetry pattern. This scalar potential causes cubic and quartic scalar self-interactions, which will be further specified after considering the spontaneous symmetry breaking in more detail in section 1.1.3.2.

The third term $\mathcal{L}_f$ concerns the fermion interaction terms with the electroweak gauge bosons. Here, the different fermion representations imply different forms of the covariant

derivative. In the following, an additional zero will be added as superscript in the fermion field notation, since they are not in the mass eigenstate basis, but there is mixing between fermions of different generations. This will also be done for the fields of the massless neutrinos, for which a different basis of fields will be chosen as well. The details are discussed in section 1.1.3.5. For the lepton fields, the covariant derivatives are

$$D_\mu L_i^0 = \left(\partial_\mu + \frac{ig}{2} W_\mu^j \sigma^j - \frac{ig'}{2} B_\mu\right) \begin{pmatrix} \nu_{i,L}^0 \\ e_{i,L}^0 \end{pmatrix}, \qquad D_\mu e_{i,R}^0 = \left(\partial_\mu - ig' B_\mu\right) e_{i,R}^0, \tag{1.1.38}$$

and for the quark fields

$$D_\mu Q_i^0 = \left(\partial_\mu + \frac{ig}{2} W_\mu^j \sigma^j + \frac{ig'}{6} B_\mu\right) \begin{pmatrix} u_{i,L}^0 \\ d_{i,L}^0 \end{pmatrix}, \qquad \begin{aligned} D_\mu u_{i,R}^0 &= \left(\partial_\mu + \tfrac{2ig'}{3} B_\mu\right) u_{i,R}^0, \\ D_\mu d_{i,R}^0 &= \left(\partial_\mu - \tfrac{ig'}{3} B_\mu\right) d_{i,R}^0, \end{aligned} \tag{1.1.39}$$

where in both cases the indices j are implicitly summed over. Concerning the quark fields, it should be noticed that the given expressions are not the complete covariant derivatives of the SM gauge symmetry group, but only the part related to the electroweak gauge group $SU(2)_L \times U(1)_Y$. The $SU(3)_C$ covariant derivative will be considered separately in section 1.1.4 and involves colour indices, which are disregarded here. The Lagrangian $\mathcal{L}_f$, in which the above covariant derivatives appear, is given by

$$\mathcal{L}_f = \sum_{i=1}^{3} \left(\overline{Q}_i^0 i\not{D} Q_i^0 + \overline{L}_i^0 i\not{D} L_i^0 + \overline{u}_{i,R}^0 i\not{D} u_{i,R}^0 + \overline{d}_{i,R}^0 i\not{D} d_{i,R}^0 + \overline{e}_{i,R}^0 i\not{D} e_{i,R}^0\right), \tag{1.1.40}$$

where the symbol i appearing in front of $\not{D}$ is not the index used for the summation over the generations, but the imaginary unit.

Finally, there are also Yukawa interaction terms between the fermion and scalar fields, which are invariant under the electroweak gauge group. As will be shown in section 1.1.3.2, these terms also generate the mass terms of the fermions when the symmetry is spontaneously broken, i.e. the field H acquires a non-zero vacuum expectation value in its second component ϕ_0. In order to give also masses to the up-type quarks, the field $\tilde{H}$ is used, which is related to H through the similarity transformation

$$\tilde{H} \equiv i\sigma^2 H^* . \tag{1.1.41}$$

Neutrino mass terms cannot be generated through Yukawa interaction terms, since there are no right-handed neutrino fields. The possible Yukawa interactions are then given by

$$\mathcal{L}_{\text{Yukawa}} = -\sum_{i,j=1}^{3} \left(y_{ij}^u \overline{Q}_i^0 \tilde{H} u_{j,R}^0 + y_{ij}^d \overline{Q}_i^0 H d_{j,R}^0 + y_{ij}^e \overline{L}_i^0 H e_{j,R}^0\right) + \text{h.c.}. \tag{1.1.42}$$

1.1.3.2 Electroweak symmetry breaking

The spontaneous breaking of the electroweak symmetry is particularly important in the SM, since it provides a mechanism (the *Brout-Englert-Higgs mechanism* [37–43]) to generate mass terms for the gauge bosons, which cannot be constructed otherwise without

violating the gauge symmetry. Indirectly, this also leads to fermion masses via the Yukawa couplings to the Higgs field. For the SM fermions, explicit mass terms are not allowed due to their representations: Since they involve left- and right-handed spinor fields, they should have a Dirac mass term, which mixes the left- and right-handed fields. However, since these transform under different representations of the electroweak gauge group, such a Dirac mass term would not be gauge invariant and is therefore forbidden. In the contrary, so-called *vector-like* fermions with left- and right-handed parts which transform under the same representation *do* allow for a Dirac mass term, c.f. section 1.4.1.

The mechanism which breaks the electroweak symmetry follows the assumption that the lowest energy state, i.e. the vacuum, does not share the symmetry. This becomes manifest in a non-zero vacuum expectation value in the Higgs doublet H at the minimum of the potential, corresponding to the lowest-energy state. In order for this scenario to occur, the scalar potential must have an appropriate shape. As pointed out in section 1.1.1, in the SM scalar potential in eq. (1.1.37) this will result from a proper choice of the signs of the parameters:

$$\mu^2 < 0\,, \qquad \lambda > 0\,. \tag{1.1.43}$$

It is the sign of μ^2 which causes the minimum of the potential to be displaced from the zero field configuration.

The Higgs doublet, consisting of two complex fields ϕ^+ and ϕ^0, or alternatively four real fields ϕ_i, can be written as

$$H = \begin{pmatrix} \phi^+ \\ \phi^0 \end{pmatrix} = \frac{1}{\sqrt{2}} \begin{pmatrix} \phi_1 - i\phi_2 \\ \phi_3 - i\phi_4 \end{pmatrix}\,. \tag{1.1.44}$$

Inserting this parameterisation into the Higgs potential, it takes the form

$$V(H) = \frac{1}{2}\mu^2 \left(\sum_{i=1}^{4} \phi_i^2 \right) + \frac{1}{4}\lambda \left(\sum_{i=1}^{4} \phi_i^2 \right)^2\,. \tag{1.1.45}$$

It is obvious that this potential is symmetric under $SO(4)$ transformations rotating the fields ϕ_i among each other [10]. One is therefore free to choose the field ϕ_3 as the one that acquires the non-zero vev [3] $\langle \phi_3 \rangle = v$, while it is zero for the remaining fields, i.e. $\langle \phi_i \rangle = 0$ for $i = 1, 2, 4$. Hence, as announced in section 1.1.1, one has

$$\langle H \rangle = \begin{pmatrix} 0 \\ v/\sqrt{2} \end{pmatrix}\,. \tag{1.1.46}$$

The value of the potential at the vev of H is given by

$$V(\langle H \rangle) = \frac{1}{2}\mu^2 v^2 + \frac{1}{4}\lambda v^4\,. \tag{1.1.47}$$

From the requirement that this is a minimum of the potential, the vev can be expressed in terms of the parameters of the Lagrangian:

$$v = \sqrt{-\frac{\mu^2}{\lambda}}\,. \tag{1.1.48}$$

3. For the vacuum expectation value, the notation $\langle ... \rangle \equiv \langle 0|...|0\rangle$ is used, where $|0\rangle$ is the vacuum state.

To see how the gauge boson and fermion masses are generated, it will be convenient to write the field H in terms of an $SU(2)$ gauge transformation $U(x)$ and a real scalar field $h(x)$ as [46]

$$H(x) = U(x)\frac{1}{\sqrt{2}}\begin{pmatrix} 0 \\ v + h(x) \end{pmatrix} . \tag{1.1.49}$$

With the degrees of freedom embodied by the three x-dependent parameters $\alpha^a(x)$ in $U(x)$ and the real scalar field $h(x)$, any two-component complex scalar field can be composed in this way. On the other hand, the matrix U can be removed due to gauge invariance via a gauge transformation, so that H takes the simple form

$$H = \frac{1}{\sqrt{2}}\begin{pmatrix} 0 \\ v + h \end{pmatrix} , \tag{1.1.50}$$

and there is only one physical degree of freedom left in H. This gauge fixing is known as the *unitary gauge*. Note that the physical degrees of freedom, which have disappeared from the Higgs field, show up again as the longitudinal modes of the gauge boson fields, which at the same time become massive. Of course, the SM does not rely on this gauge, but the Lagrangian is simplest with this gauge fixing. Other gauges shall not be discussed here.

A way to check that the symmetry is broken by the vacuum expectation value is to see how it behaves when a gauge transformation is applied to it. If it respects the electroweak symmetry, then an arbitrary $SU(2)_L$ or $U(1)_Y$ transformation should have no effect on $\langle H \rangle$. This is the case, if the group generators acting on $\langle H \rangle$ give zero (in both components), which in the following will be checked explicitly:

$$\begin{aligned}
T^1\langle H\rangle &= \frac{1}{2}\begin{pmatrix} 0 & 1 \\ 1 & 0 \end{pmatrix}\begin{pmatrix} 0 \\ v/\sqrt{2} \end{pmatrix} = \frac{1}{2}\begin{pmatrix} v/\sqrt{2} \\ 0 \end{pmatrix} \neq 0\,, \\
T^2\langle H\rangle &= \frac{1}{2}\begin{pmatrix} 0 & -i \\ i & 0 \end{pmatrix}\begin{pmatrix} 0 \\ v/\sqrt{2} \end{pmatrix} = -\frac{i}{2}\begin{pmatrix} v/\sqrt{2} \\ 0 \end{pmatrix} \neq 0\,, \\
T^3\langle H\rangle &= \frac{1}{2}\begin{pmatrix} 1 & 0 \\ 0 & -1 \end{pmatrix}\begin{pmatrix} 0 \\ v/\sqrt{2} \end{pmatrix} = -\frac{1}{2}\begin{pmatrix} 0 \\ v/\sqrt{2} \end{pmatrix} \neq 0\,, \\
Y\langle H\rangle &= \frac{1}{2}\begin{pmatrix} 0 \\ v/\sqrt{2} \end{pmatrix} \neq 0\,.
\end{aligned} \tag{1.1.51}$$

Since none of these results vanishes, all four generators are broken. However, these results also show that the sum $Q \equiv T^3 + Y$ applied on $\langle H \rangle$ vanishes, so this combination is a new unbroken generator. This confirms the pattern of spontaneous symmetry breaking of eq. (1.1.1), where Q is the generator of the group $U(1)_{\mathrm{EM}}$ and corresponds to the electric charge. The invariance of the Lagrangian under this group implies that the associated gauge boson, the photon, has to remain massless, which is indeed the case, c.f. section 1.1.3.4. Having identified the operator Q as the sum of T^3 and Y, the notation of the Higgs doublet components ϕ^+ and ϕ^0 related to the electric charge can now be understood via the eigenvalues of these fields to Q, which are $+1$ and 0.

1.1.3.3 Higgs boson mass and self interactions

Besides leading to the spontaneous symmetry breaking in the electroweak theory, the potential in eq. (1.1.37) is also the source for a mass term and self interactions for the physical scalar h. Inserting the expression for H of eq. (1.1.50) into this potential, one obtains

$$V(h) = -\frac{\mu^4}{4\lambda} - \mu^2 h^2 + \lambda v h^3 + \frac{\lambda}{4} h^4 \,. \tag{1.1.52}$$

The first term is just constant and is irrelevant in the SM, but represents a problematic term in the context of gravity. However, this shall not be discussed here. A mass term for the Higgs boson is provided by the second term, where the tree level mass can be identified as

$$m_h = \sqrt{-2\mu^2} = \sqrt{2\lambda} v \,. \tag{1.1.53}$$

The remaining two terms are cubic and quartic interaction terms of the Higgs boson.

1.1.3.4 Gauge boson masses and interactions with the Higgs boson

The mass terms of the electroweak gauge bosons can easily be derived, using the parameterisation of H in eq. (1.1.50), by considering its gauge invariant kinetic term $(D_\mu H)^\dagger D^\mu H$, which is the only term in the SM Lagrangian that couples H to these gauge bosons. The only terms relevant for these mass terms are the ones proportional to v^2, which are at the same time free of the field h. Using that the matrices σ^i are Hermitian, one obtains

$$\begin{aligned}(D_\mu H)^\dagger D^\mu H &= \frac{1}{2}\begin{pmatrix}0 & v\end{pmatrix}\left(\frac{g}{2}\sigma^i W_\mu^i + \frac{g'}{2}B_\mu\right)^2\begin{pmatrix}0\\ v\end{pmatrix} + h \text{ terms} \\ &= \frac{g^2 v^2}{4}\frac{W_\mu^1 - iW_\mu^2}{\sqrt{2}}\frac{W^{1\mu} + iW^{2\mu}}{\sqrt{2}} + \frac{v^2}{2}\left(\frac{g'}{2}B_\mu - \frac{g}{2}W_\mu^3\right)^2 \\ &\quad + h \text{ terms} \,.\end{aligned} \tag{1.1.54}$$

This expression contains mixed terms of the different gauge bosons. A basis of vector fields, in which the mass terms are diagonal, is given by

$$W_\mu^\pm = \frac{1}{\sqrt{2}}\left(W_\mu^1 \mp i W_\mu^2\right) \,, \qquad \begin{pmatrix}Z_\mu\\ A_\mu\end{pmatrix} = \begin{pmatrix}\cos\theta_W & -\sin\theta_W\\ \sin\theta_W & \cos\theta_W\end{pmatrix}\begin{pmatrix}W_\mu^3\\ B_\mu\end{pmatrix} \,. \tag{1.1.55}$$

Here, the weak mixing angle θ_W is defined in terms of the coupling constants g and g' via the relation

$$\tan\theta_W \equiv \frac{g'}{g} \,. \tag{1.1.56}$$

In the new basis, the expression in eq. (1.1.54) becomes

$$(D_\mu H)^\dagger D^\mu H = m_W^2 W_\mu^+ W^{-\mu} + \frac{m_Z^2}{2} Z_\mu Z^\mu + h \text{ terms} \tag{1.1.57}$$

with

$$m_W = \frac{gv}{2} \,, \qquad m_Z = \frac{v}{2}\sqrt{g^2 + g'^2} = \frac{m_W}{\cos\theta_W} \,. \tag{1.1.58}$$

As expected, there is one gauge boson without mass term, the photon field A^μ that corresponds to the unbroken generator Q, i.e. it belongs to the symmetry group $U(1)_{\mathrm{EM}}$.

Eq. (1.1.57) also includes interaction terms of h, which have not been written explicitly. The whole expression in unitary gauge contains a kinetic term (the other terms involving a derivative cancel each other) as well as interaction terms, which according to the form of H in eq. (1.1.50) can be obtained by replacing v by $v+h$ in the mass terms. The result is

$$(D_\mu H)^\dagger D^\mu H = \frac{1}{2}\partial_\mu h\,\partial^\mu h + m_W^2 W_\mu^+ W^{-\mu}\left(1+\frac{h}{v}\right)^2 + \frac{m_Z^2}{2} Z_\mu Z^\mu \left(1+\frac{h}{v}\right)^2 , \quad (1.1.59)$$

which includes WWh, $WWhh$, ZZh and $ZZhh$ couplings.

1.1.3.5 Fermion masses and interactions with the Higgs boson

Finally, as argued in section 1.1.3.1, the spontaneous symmetry breaking also generates fermion masses due to the Yukawa couplings given in eq. (1.1.42). As before, inserting the field H in unitary gauge from eq. (1.1.50) into the Lagrangian, one obtains both fermion mass terms and corresponding interactions with the field h:

$$\mathcal{L}_{\text{Yukawa}} = -\sum_{i,j=1}^{3}\left(\overline{u}^0_{i,L} M^u_{ij} u^0_{j,R} + \overline{d}^0_{i,L} M^d_{ij} d^0_{j,R} + \overline{e}^0_{i,L} M^e_{ij} e^0_{j,R}\right)\left(1+\frac{h}{v}\right) + \text{h.c.}\,. \quad (1.1.60)$$

Here, the mass matrices are given by

$$M^f_{ij} = \frac{y^f_{ij} v}{\sqrt{2}} \qquad \text{for} \quad f = u, d, e\,. \quad (1.1.61)$$

There is no reason for the mass matrices to be diagonal. Therefore, in order to switch to the mass eigenstate basis, each mass matrix is transformed using two unitary transformations U^f_L and U^f_R such that

$$U^{f\dagger}_L M^f U^f_R = M^f_D \qquad \text{for} \quad f = u, d, e \quad (1.1.62)$$

is diagonal. For example, for the up-type quarks one has

$$U^{u\dagger}_L M^u U^u_R = M^u_D = \begin{pmatrix} m_u & 0 & 0 \\ 0 & m_c & 0 \\ 0 & 0 & m_t \end{pmatrix} . \quad (1.1.63)$$

Correspondingly, the fermion fields $f_L = (f_{1,L}, f_{2,L}, f_{3,L})$ and $f_R = (f_{1,R}, f_{2,R}, f_{3,R})$ for $f = u, d, e$ in the mass eigenstate basis are obtained from f^0_L and f^0_R as follows:

$$f_L = U^{f\dagger}_L f^0_L\,, \qquad f_R = U^{f\dagger}_R f^0_R\,, \qquad \text{for} \quad f = u, d, e\,. \quad (1.1.64)$$

These transformations can be used not only for the diagonalisation of the mass matrices, but also of the corresponding Yukawa couplings of h to the same fermion fields, which according to eq. (1.1.60) are proportional to the mass matrices. Even though there is no

neutrino mass matrix to diagonalise, the neutrino fields $\nu^0_{i,L}$ can also be transformed via a unitary transformation. Here, the same transformation as for the fields $e^0_{i,L}$ is chosen [46], i.e.

$$\nu_L = U_L^{e\dagger} \nu_L^0 \tag{1.1.65}$$

with $\nu_L = (\nu_{1,L}, \nu_{2,L}, \nu_{3,L})$. With this choice, both components of the lepton doublets L_i^0 are transformed in the same way. In contrast, the components of the quark doublet Q_i^0 are transformed via two independent matrices U_L^u and U_L^d due to independent Yukawa couplings y^u and y^d. The above transformations have consequences beyond the diagonalisation of the mass matrices, which will be discussed in section 1.1.3.6.

1.1.3.6 Gauge interactions of the fermions

The gauge interactions of the SM fermion fields have already been provided via the covariant derivatives in eqs. (1.1.38) and (1.1.39) and the Lagrangian in eq. (1.1.40). Since then, both the vector bosons and the fermions have been transformed to the mass basis. Therefore, these expressions shall be reconsidered here in the mass basis.

Applying first the replacements for the vector boson fields, one obtains the following structure [46]:

$$\begin{aligned}\mathcal{L}_f = &\sum_{i=1}^{3} \left(\overline{Q}_i^0 i\partial\!\!\!/ Q_i^0 + \overline{L}_i^0 i\partial\!\!\!/ L_i^0 + \overline{u}_{i,R}^0 i\partial\!\!\!/ u_{i,R}^0 + \overline{d}_{i,R}^0 i\partial\!\!\!/ d_{i,R}^0 + \overline{e}_{i,R}^0 i\partial\!\!\!/ e_{i,R}^0 \right) \\ &+ g \left(W_\mu^+ J_W^{+\mu} + W_\mu^- J_W^{-\mu} + Z_\mu^0 J_Z^\mu \right) + e A_\mu J_{\mathrm{EM}}^\mu \,.\end{aligned} \tag{1.1.66}$$

Here, the different charged and neutral currents are defined as

$$\begin{aligned}
J_W^{+\mu} &= \frac{1}{\sqrt{2}} \sum_{i=1}^{3} \left(\overline{\nu}_{i,L}^0 \gamma^\mu e_{i,L}^0 + \overline{u}_{i,L}^0 \gamma^\mu d_{i,L}^0 \right) , \\
J_W^{-\mu} &= \frac{1}{\sqrt{2}} \sum_{i=1}^{3} \left(\overline{e}_{i,L}^0 \gamma^\mu \nu_{i,L}^0 + \overline{d}_{i,L}^0 \gamma^\mu u_{i,L}^0 \right) , \\
J_Z^\mu &= \frac{1}{\cos\theta_W} \sum_{i=1}^{3} \Bigg[\frac{1}{2} \overline{\nu}_{i,L} \gamma^\mu \nu_{i,L} \\
&\qquad + \left(-\frac{1}{2} + \sin^2\theta_W \right) \overline{e}_{i,L}^0 \gamma^\mu e_{i,L}^0 + \left(\sin^2\theta_W \right) \overline{e}_{i,R}^0 \gamma^\mu e_{i,R}^0 \\
&\qquad + \left(\frac{1}{2} - \frac{2}{3}\sin^2\theta_W \right) \overline{u}_{i,L}^0 \gamma^\mu u_{i,L}^0 + \left(-\frac{2}{3}\sin^2\theta_W \right) \overline{u}_{i,R}^0 \gamma^\mu u_{i,R}^0 \\
&\qquad + \left(-\frac{1}{2} + \frac{1}{3}\sin^2\theta_W \right) \overline{d}_{i,L}^0 \gamma^\mu d_{i,L}^0 + \left(\frac{1}{3}\sin^2\theta_W \right) \overline{d}_{i,R}^0 \gamma^\mu d_{i,R}^0 \Bigg] , \\
J_{\mathrm{EM}}^\mu &= \sum_{i=1}^{3} \left[(-1)\, \overline{e}_i^0 \gamma^\mu e_i^0 + \left(\frac{2}{3} \right) \overline{u}_i^0 \gamma^\mu u_i^0 + \left(-\frac{1}{3} \right) \overline{d}_i^0 \gamma^\mu d_i^0 \right] .
\end{aligned} \tag{1.1.67}$$

In the last current J_{EM}^μ, the Dirac spinor notation was used to combine the left- and right-handed fermion fields:

$$e_i = \begin{pmatrix} e_{i,L} \\ e_{i,R} \end{pmatrix} , \qquad u_i = \begin{pmatrix} u_{i,L} \\ u_{i,R} \end{pmatrix} , \qquad d_i = \begin{pmatrix} d_{i,L} \\ d_{i,R} \end{pmatrix} , \qquad \text{for} \quad i = 1, 2, 3 \,. \tag{1.1.68}$$

The values in J^{μ}_{EM}, which are written in parentheses, correspond to the electric charge of the fermions.

Proceeding now with the fermion field transformations in eqs. (1.1.64) and (1.1.65), one could first notice that most of the terms are unaffected by the transformations. These are all terms involving the same chiralities and fermion flavours, which transform as [46]

$$\begin{aligned}\overline{f}^{0}_{i,L}\gamma^{\mu}f^{0}_{i,L} &= \left(\overline{f}_{j,L}U^{\dagger f}_{L,ji}\right)\gamma^{\mu}\left(U^{f}_{L,ik}f_{k,L}\right)\\ &= \left(U^{\dagger f}_{L}U^{f}_{L}\right)_{jk}\overline{f}_{j,L}\gamma^{\mu}f_{k,L}\\ &= \delta_{jk}\overline{f}_{j,L}\gamma^{\mu}f_{k,L}\\ &= \overline{f}_{j,L}\gamma^{\mu}f_{j,L}\,,\end{aligned} \tag{1.1.69}$$

where the summation over repeated indices was left implicit, and analogously

$$\overline{f}^{0}_{i,R}\gamma^{\mu}f^{0}_{i,R} = \overline{f}_{i,R}\gamma^{\mu}f_{i,R}\,. \tag{1.1.70}$$

This applies also to the terms of J^{μ}_{EM}, where the corresponding left- and right-handed terms are just combined into Dirac spinors.

Therefore, only the charged currents $J^{\pm\mu}_{W}$ get affected by the transformation of the fermion field basis. However, the leptonic terms remain invariant as well, because the transformation matrix of the neutrino fields has been chosen to be equal to the one of the left-handed lepton field of the same $SU(2)_L$ doublet, such that the transformations cancel each other just like in eq. (1.1.69). After all, only the charged quark currents are different in the mass basis, where the transformation leads to

$$\begin{aligned}\overline{u}^{0}_{i,L}\gamma^{\mu}d^{0}_{i,L} &= \left(\overline{u}_{j,L}U^{u\dagger}_{L,ji}\right)\gamma^{\mu}\left(U^{d}_{L,ik}d_{k,L}\right)\\ &= \left(U^{u\dagger}_{L}U^{d}_{L}\right)_{jk}\overline{u}_{j,L}\gamma^{\mu}d_{k,L}\\ &= \left(V_{\mathrm{CKM}}\right)_{jk}\overline{u}_{j,L}\gamma^{\mu}d_{k,L}\,,\end{aligned} \tag{1.1.71}$$

with $V_{\mathrm{CKM}} \equiv U^{u\dagger}_{L}U^{d}_{L}$, and similarly

$$\overline{d}^{0}_{i,L}\gamma^{\mu}u^{0}_{i,L} = \left(V^{\dagger}_{\mathrm{CKM}}\right)_{jk}\overline{d}_{j,L}\gamma^{\mu}u_{k,L}\,. \tag{1.1.72}$$

The matrix V_{CKM} is referred to as the *Cabibbo-Kobayashi-Maskawa* (CKM) matrix, which is observed to be approximately of the form

$$V_{\mathrm{CKM}} = \begin{pmatrix} V_{ud} & V_{us} & V_{ub}\\ V_{cd} & V_{cs} & V_{cb}\\ V_{td} & V_{ts} & V_{tb}\end{pmatrix} \approx \begin{pmatrix} 1 & \lambda & \lambda^{3}\\ \lambda & 1 & \lambda^{2}\\ \lambda^{3} & \lambda^{2} & 1\end{pmatrix}\,, \tag{1.1.73}$$

where $\lambda = \sin\theta_c \approx 0.22$. The angle θ_c is the *Cabibbo angle*. It should be mentioned that the CKM matrix can in general be parameterised in terms of three mixing angles and one phase; the latter is responsible for the CP violation in the SM [47].

1.1.4 Quantum Chromodynamics

The gauge theory of strong interactions, called *Quantum Chromodynamics*, is based on the gauge group $SU(3)_C$ of the SM gauge group G_{SM}. The name of this gauge theory is related to the illustrative picture that each quark flavour exists in three different colours (red, blue, green and their anti-colours), but the observable particles in nature are always colour singlets, i.e. bound states, in which the colours add up to white.

1.1.4.1 The QCD Lagrangian

The QCD Lagrangian has a relatively simple structure. It only involves 8 gauge bosons, the gluons, as well as both left- and right-handed quarks, which transform under the same representations of $SU(3)_C$. Here, it is therefore most convenient to work with the Dirac spinor notation. The relevant Lagrangian terms in QCD are [9, 14]

$$\mathcal{L}_{\text{QCD}} = -\frac{1}{4} F^a_{\mu\nu} F^{a,\mu\nu} + \sum_{r=1}^{n_f} \overline{q}^{\alpha}_r \left(i \not{D}^{\alpha\beta} - m_r \delta^{\alpha\beta} \right) q^{\beta}_r \,. \tag{1.1.74}$$

This time, the colour indices $\alpha, \beta \in \{1, 2, 3\}$ of the quarks are written explicitly and as usual, they are implicitly summed over, when they appear repeatedly. The index r is a flavour index, where the number of flavours in the SM is $n_f = 6$. All quark fields are given in the mass basis with masses m_r, which are just the diagonal matrix elements of the diagonalised mass matrices M^u_D and M^d_D in eq. (1.1.62). The expression of the covariant derivative, which includes only the $SU(3)_C$ part, is given by

$$D^{\alpha\beta}_{\mu} = \delta^{\alpha\beta} \partial_\mu + i g_s G^a_\mu \left(T^a\right)^{\alpha\beta} \,, \tag{1.1.75}$$

with $a = 1, ..., 8$ being summed over, where $T^a = \lambda^a/2$ are the Gell-Mann matrices provided in eq. (1.1.28). The fields G^a_μ are the gluon fields and g_s is the strong coupling constant. Finally, according to eq. (1.1.23), the components of the field strength tensor read

$$F^a_{\mu\nu} = \partial_\mu G^a_\nu - \partial_\nu G^a_\mu - g_s f^{abc} G^b_\mu G^c_\nu \,, \tag{1.1.76}$$

with $b, c \in \{1, ..., 8\}$ being summed over and the non-zero structure constants f^{abc} being given by eq. (1.1.30).

As discussed in section 1.1.2.2, the interactions following from $\mathcal{L}_{\text{QCD}}$ are on the one hand interactions of gluons to quarks of the same flavour but possibly different colours, and on the other hand three- or four-gluon self-interactions.

1.1.4.2 Asymptotic freedom and confinement

A topic which has so far been neglected is *renormalisation*. The different parameters in the Lagrangians given so far are tree-level quantities which in renormalised perturbation theory receive corrections from loop diagrams. The technical details of the renormalisation program are not of interest in this chapter. However, in QCD the renormalisation of g_s has phenomenological implications, which are far too important to be ignored. The value of the renormalised coupling depends on a renormalisation scale μ. Typically, this scale can be

put into relation with a momentum scale Q involved in the process under consideration [48]. The scale dependence of the coupling is then governed by a *beta-function* via

$$\beta = \mu \frac{\partial g_s}{\partial \mu} \,. \tag{1.1.77}$$

In the case of the strong coupling, the beta function for $\alpha_s = \frac{g_s^2}{4\pi}$ is given by

$$\beta = \mu \frac{\partial \alpha_s}{\partial \mu} = -\frac{\beta_0}{2\pi}\alpha_s^2 - \frac{\beta_1}{4\pi^2}\alpha_s^3 - \frac{\beta_2}{64\pi^3}\alpha_s^4 - \dots \tag{1.1.78}$$

with

$$\begin{aligned} \beta_0 &= 11 - \frac{2}{3} n_f \,, \\ \beta_1 &= 51 - \frac{19}{3} n_f \,, \\ \beta_2 &= 2857 - \frac{5033}{9} n_f + \frac{325}{27} n_f^2 \,. \end{aligned} \tag{1.1.79}$$

Keeping only the leading term in α_s of the beta function, one finds the following scale dependence:

$$\alpha_s(\mu) = \frac{4\pi}{\beta_0 \ln\left(\frac{\mu^2}{\Lambda_{\mathrm{QCD}}^2}\right)} \,. \tag{1.1.80}$$

Here, the scale Λ_{QCD} is a scale of the order of 200 MeV, at which perturbation theory breaks down: One can see that the expression in eq. (1.1.80) diverges for $\mu \to \Lambda_{\mathrm{QCD}}$ (this is called the *Landau pole* [49,50], giving the impression that the coupling becomes infinitely strong around this scale. If that is the case, then perturbation theory breaks down, since it relies on small couplings. This in turn implies that the expression in eq. (1.1.80) does not correctly describe the behaviour of α_s in this regime, since it is itself the result of a perturbative calculation.

Nevertheless, this equation gives an impression of the *running* of the strong coupling constant: The coupling becomes small for high momenta (or small distances). This property of QCD is called *asymptotic freedom*. In contrast, for small momenta near or below the scale Λ_{QCD} (or high distances), the coupling becomes strong and perturbative calculations become impossible. Therefore, quarks and gluons are not observable as asymptotic states but are always *confined* into colour-neutral states (hadrons).

1.2 Successes of the theory

The way in which the Standard Model is presented in the previous section does not reflect the historical development of the theory. Obviously, the SM has been formulated under the influence of experimental observations and discoveries, but is also the fruit of the development of new theoretical concepts, such as non-abelian gauge theories or the spontaneous breakdown of these [1]. A historical review of the development of the SM can be found in ref. [51], which points out that there were also some misunderstandings

on the way to the complete theory. Nonetheless, the SM as we know it today is an extraordinarily successful theory. Some of the particularly satisfactory features of the SM are the following [48, 52]:

— It is both renormalisable and unitary [53, 54].

— The electromagnetic and weak forces are unified via the electroweak gauge group $SU(2)_L \times U(1)_Y$.

— It contains a reasonable number of 18 free parameters, which need to be determined in experimental measurements, until the theory becomes fully predictive. There are three coupling constants, six quark masses, three lepton masses, three mixing angles and one phase for the CKM matrix, the Higgs mass and the mass of either the W or the Z boson.

— The ratio between the W and Z boson masses is predicted at tree level by $\cos\theta_W$.

— All particles of the Standard Model are by now known to exist. After the completion of the SM, gluons were discovered in 1979, the W and Z bosons in 1983, the third family quarks and leptons between 1975 and 2000, and finally the Higgs boson in 2012 [1, 45].

— In comparison with experimental data, e.g. cross section measurements at the LHC [5–7] or electroweak precision data [4], the SM turns out to be extremely robust, i.e. the vast majority of the predictions are in good agreement with measurements in consideration of the respective uncertainties.

1.3 Theoretical and experimental puzzles

Despite the undeniable success of the SM, it is not capable of explaining all observations in nature. These deficiencies reveal the incompleteness of the SM and clearly indicate that there should be some sort of new physics that the theory does not take into consideration. Also, some persisting experimental tensions could be hints for new physics. Further doubts about the completeness of the model arise on the theoretical level, in particular due to the necessity of unnatural fine-tuning in order to match physical observables. In addition, one can ask more philosophical questions about the architecture of the SM and the values of its parameters, which could in principle remain unanswered without causing any trouble, even though it might seem more satisfactory from the theoretical point of view to have a precise explanation. This can motivate the search for mechanisms which naturally generate the observed patterns of parameter values present in the SM while reducing the number of free parameters. This section gives a brief overview of the most important, and some less important unanswered questions related to particle physics and the SM.

— **Quantum gravity:** A complete theory of nature should successfully describe all forces, which is clearly not the case for the SM, since it does not include gravity [8]. Even though it is completely irrelevant at the energy scales which are achievable in collider experiments, the ultimate goal should be to find a theory that properly takes it into account. A classical description of gravity is given by the theory of General Relativity, but in constructing a quantum theory the renormalisability represents a major problem.

— **Dark matter:** The first observerations in favour of the existence of dark matter (DM) were made in the 1930s, in particular by Zwicky who found that galaxies in the COMA cluster have an excessively high velocity dispersion, leading to the conclusion that the cluster should have a much higher mass than expected from the luminosities of the galaxies [55, 56]. Similarly, it was observed that rotation curves of objects in galaxies, more precisely their velocities as a function of the radius R from the center of the galaxy, did not match the naive expectations [57–69]: Instead of decreasing with the radius from the galactic center, they were observed to be nearly constant over a wide range of radii. Since the mass distribution of the visible objects could not explain the observed curves, it was suggested that there should be additional mass belonging to some invisible form of matter, which is referred to as *dark matter*, that must be included into the calculations to obtain the correct velocities of the objects. Later on, this hypothesis has been consolidated through a number of independent observations such as gravitational lensing [68–83], hot gas in galaxy clusters [84], and the cosmic microwave background [85–91]. According to the standard model of cosmology (also called ΛCDM, where CDM stands for *cold dark matter* and Λ is the cosmological constant that will be discussed below [92–94]), the quota of DM in the universe is about 26 %, compared to 69 % of dark energy and only 5 % of ordinary baryonic matter. While it is nowadays widely believed that DM exists, there is still no precise answer to the question what it is made of. The general expectations on the properties of DM are the following: It should be massive and non-relativistic, electrically and possibly colour neutral as well as stable or very long-lived, with a longer lifetime than the age of the universe. None of the elementary SM particles satisfies all of these criteria. Therefore, the DM problem is mostly addressed by various BSM physics models, even though there are also some attempts to explain dark matter without extending the SM, such as hexaquarks or primordial black holes [95]. A more unconventional and controversial proposal to explain the observed phenomena without dark matter, known as *Modified Newtonian dynamics* (MOND) [96–102], relies on a modification of the gravitational acceleration [103]. These alternative options are beyond the scope of this work and shall not be discussed any further. Instead, an extension of the SM with new particles, including DM, will be studied in chapters 3 and 4.

— **Cosmological constant:** Einstein originally introduced the cosmological constant Λ into the field equation of General Relativity in order to obtain a static universe [104], which is what he later called his "greatest blunder". Since the universe was found to be expanding, it became unnecessary at first sight, but setting it to zero would be inconsistent with the later observation that the expansion is accelerating. The cosmological constant is therefore positive and can be related to the total energy density of the vacuum ρ_Λ, which has a measured value given in Planck units by [25, 105]

$$\rho_\Lambda = (1.35 \pm 0.15) \times 10^{-123} \,. \tag{1.3.1}$$

In contrast, the theory prediction in the SM includes different loop and effective scalar potential contributions, which exceed the experimental value by 60 to 120 orders of magnitude. The vacuum energy/cosmological constant problem is this drastic disagreement, which raises the question how theory and observation can be

reconciled.

— **Baryogenesis:** The proportion of antimatter compared to matter in the universe is significantly smaller, in other words, there is an important matter-antimatter asymmetry [106–108]. This asymmetry can be explained by a process called *baryogenesis*, that occurred in the early universe, in which the asymmetry is dynamically generated from an initially symmetric state. The conditions for baryogenesis to take place were established by Sakharov [109], which are

1. baryon number (B) violation,
2. C and CP violation and
3. a thermal non-equilibrium.

The standard models in particle physics and cosmology (SM and ΛCDM) are *a priori* compatible with all of these conditions [47, 110–118]: Anomalous B violation happens through so-called *sphaleron processes*, which are efficient at temperatures $T \gtrsim 130\,\text{GeV}$, both C and CP are violated in weak interactions, and the departure from the thermal equilibrium results from the expansion of the universe. However, the amount of CP violation caused by the complex phase in the CKM matrix is not sufficient to explain the observed asymmetry, and there is no other source of CP violation in the SM, so that new physics is needed to successfully explain baryogenesis. Also the deviation from thermal equilibrium is insufficient, as pointed out in ref. [106].

— **Neutrino masses:** The observation of oscillations between the neutrino flavours implies that the neutrinos must have masses, which are however experimentally found to be extremely small [119–131]. In fact there are currently only upper limits, the most recent value reported by KATRIN being 1.1 eV [132]. However, the origin of these masses is not explained by the SM. It is not clear, whether they result from Majorana or Dirac mass terms, and if there are right-handed neutrinos, which are necessary in some models explaining the neutrino masses.

— **Muon anomalous magnetic moment:** The magnetic moment of the muon is typically written as

$$\vec{\mu}_\mu = g_\mu \left(\frac{q}{2m_\mu} \right) \vec{s}\,, \qquad \text{with} \quad g_\mu = 2(1 + a_\mu)\,, \tag{1.3.2}$$

where the anomalous contribution is parameterised via a_μ, i.e. the tree-level prediction is given by $g_\mu = 2$. Here q and m_μ are the charge and mass of the muon and $\vec{s}$ is the spin vector. In ref. [26], it was found that the SM prediction of the muon anomalous magnetic moment deviates from the combined result of measurements by the BNL E821 experiment in 2006 [133] and the more recent value measured in 2021 by the Fermilab $g-2$ experiment [26] by 4.2 standard deviations, which confirms and reinforces the tension already reported in 2006. This is clearly an exciting result and potentially a manifestation of new physics.

— **Flavour anomalies:** Other tensions have also been identified in B-hadron decays [134–153], where the results indicate that lepton flavour universality (LFU) could be violated. LFU means that the coupling strength of the electroweak gauge

bosons is identical among the three lepton generations and is an approximate symmetry that is only broken by the different Yukawa couplings of the leptons. Deviations at the level of four standard deviations from SM results were observed in different observables relating branching fractions of decays with the quark flavour transitions $b \to c\ell\nu$ and $b \to s\ell\ell$ as well as angular observables. These can be interpreted as hints for violation of LFU that might be caused by new particles which contribute to the quark flavour transitions and couple differently to the different lepton flavours.

— **The Hierarchy Problem:** The Planck scale $M_P \sim 10^{19}\,\text{GeV}$, at which gravity becomes important, is about 17 orders of magnitude higher than the electroweak scale, which is of the order of $10^2\,\text{GeV}$, the scale at which electroweak symmetry breaking occurs [154, 155]. The hierarchy between these scales becomes relevant when corrections to the Higgs mass are calculated, which are quadratically divergent. Assuming that the theory is valid up to some cutoff scale Λ, the corrections to the squared Higgs mass δm_h^2 are quadratically sensitive to this scale [156–159]. Consequently, if the cutoff scale is fixed to the Planck scale, this correction is of the order $\delta m_h^2 \sim (10^{19}\,\text{GeV})^2$. The physical mass of the Higgs boson is however found at the electroweak scale at $m_h \approx 125\,\text{GeV}$, which is then again about 17 orders of magnitude smaller than the loop correction. Therefore, there must be a very precise cancellation between two parameters, the bare mass parameter and the corrections, in order to obtain the comparatively tiny Higgs mass. This is called a *fine-tuning problem* [155], since such a precise cancellation (*tuning*) seems highly unnatural. It is related to the question, why the Higgs boson has such a small mass compared to M_P, which is referred to as the *hierarchy problem*. More generally, it goes back to the sensitivity to the Higgs mass to new physical scales, as for example the mass of a new particle. For this reason, one can hope that new physics will be found at a significantly lower scale, justifying a correspondingly lower cutoff Λ, in which case the problem would be less dramatic. In any case, it can be debated to what extent there is really a problem: The SM is a renormalisable theory, so the quadratic divergence will not show up in physical quantities, and the lack of naturalness could be considered as a rather philosophical issue, but does not represent a profound problem of the theory [160].

— **The strong *CP* problem:** The $SU(3)_C$ gauge symmetry allows for an additional term that is given by [29, 161–163]

$$\mathcal{L}_{\text{QCD}} = \theta \frac{g_s^2}{32\pi^2} G^a_{\mu\nu} \tilde{G}^{a,\mu\nu}\,, \qquad \text{with} \quad \tilde{G}^{a,\mu\nu} = \frac{1}{2}\epsilon^{\mu\nu\rho\sigma} G^a_{\rho\sigma}\,. \tag{1.3.3}$$

This term is a surface term, i.e. a total space-time derivative, and therefore does not have any consequences on the classical equations of motion. For this reason, it has been omitted so far, but it is important in a *quantum* theory. Furthermore, it has the property that it violates CP. The term in eq. (1.3.3) is not the only term that has been omitted: the chiral transformations $U^q_{L/R}$ of the quarks $q = u, d$ lead to an anomaly term (i.e. it results from the transformation of the path integral measure) of the same form, with θ replaced by $\arg(\det M_q)$. Here, M_q is the combined mass matrix of the up- and down-type quarks. The physical parameter is therefore not θ, but

$$\tilde{\theta} = \theta + \arg(\det M_q)\,. \tag{1.3.4}$$

As a result of the additional terms, the neutron acquires an electric dipole moment (EDM) given by

$$d_n \simeq \left(10^{-16} \times \tilde{\theta}\right) \mathrm{e} \times \mathrm{cm}\,, \tag{1.3.5}$$

which is experimentally bound from above by $d_n < 10^{-26}\,\mathrm{e}\times\mathrm{cm}$, so that the physical parameter in eq. (1.3.4) must obey $\tilde{\theta} < 10^{-10}$.

Naturally, one would expect $\tilde{\theta}$ to be an order one parameter, just as for the two contributions θ and $\arg(\det M_q)$. However, according to the experiment the two contributions should be very close to cancelling each other, i.e. there should be a *fine-tuning* between the two independent values. There is in principle no problem with $\tilde{\theta}$ being small, but it is a serious issue that the SM does not give any explanation of *why* it should be so small. This would not be a matter of concern, if CP were a symmetry of the theory, but since it is known to be violated in the weak interaction, it cannot just be imposed in QCD.

— **Fermion mass matrices:** The masses of SM particles have very different values in the range from about $5 \times 10^{-4}\,\mathrm{GeV}$ (electron) to roughly $170\,\mathrm{GeV}$ (top quark), with a somewhat arbitrary hierarchy between the masses, and the CKM matrix looks nearly diagonal, i.e. its off-diagonal elements are comparatively small. Can this pattern be explained?

— **Charge quantisation:** Why are all the observed electric charges integer multiples of $\frac{1}{3}e$, although the $U(1)_Y$ charges could in principle take arbitrary values?

— **Number of fermion families:** Is there a reason why quarks and leptons appear in three families?

— **Gauge coupling unification:** The gauge couplings g, g' and g_s have very different values at low energies. Is there a way to unify them?

1.4 BSM physics candidates

This section will show two possible ways to extend the SM. First, a very simple modification of the SM will be considered in some detail, which is the introduction of vector-like fermions in two different representations. The second example given in this section is Supersymmetry (SUSY), and in particular the case of the Minimal Supersymmetric Standard Model (MSSM) [164–167], which is a much more extensive extension of the SM. A thorough introduction into supersymmetric theories including complete derivations or an in-depth introduction into the superfield notation or the possible SUSY breaking mechanisms is definitely far beyond the scope of this thesis. Therefore, this section will only give a very brief explanation of SUSY and sketch the most important features of the MSSM in the shortest possible manner.

1.4.1 Vector-like fermions

The electroweak interaction is described within the Standard Model as a chiral gauge theory, i.e. the left- and right-handed parts of the SM fermion fields transform differently

under $SU(2)_L \times U(1)_Y$ gauge transformations. Extending the Standard Model with additional fermion fields, which transform non-trivially under the SM gauge group is possible, but the way in which they can be added is governed by experimental constraints.

The embedding of a fourth generation of *chiral* fermions into the minimal [4] Standard Model has been excluded via Higgs measurements, since the extra fermions have substantial impact on the Higgs production and decay processes [173–177]. The issue with a fourth chiral family of fermions is that their masses would arise solely from the Higgs Yukawa couplings, since a Dirac mass term would violate gauge invariance. On the other hand, they should have high masses to justify that they were not detected directly until now, and consequently come with large Yukawa couplings. In this way, they strongly affect the Higgs production and decay processes through their presence in loop diagrams.

Alternatively, the Standard Model could be supplemented with fermion fields which transform identically in their left- and right-handed parts. In this way, a Dirac mass term is compatible with the gauge symmetry and can contribute to the fermion masses. In particular, it may provide arbitrarily high fermion masses independently of the Yukawa couplings to the Higgs boson. This circumstance gives rise to an important difference between vector-like and chiral fermions, as pointed out in refs. [173, 174], which is the following:
Increasing the mass of the vector-like fermions via the Dirac mass parameter leads to *decoupling*, i.e. predictions for observables in which the vector-like fermions are involved via loops tend to be in better agreement with the Standard Model. This means that the experimental bounds on vector-like fermions become weaker, provided that the Standard Model predictions of the relevant observables are themselves consistent with experimental data. Additional chiral fermions, on the contrary, do not benefit from such a decoupling, because the Yukawa couplings inevitably scale with the fermion masses. For this reason, they cannot be kept alive by simply raising their mass, as long as direct detection fails.

This subsection gives an introduction to vector-like leptons (VLLs) based on refs. [173, 174], by reviewing the theoretical aspects of two different simple extensions of the Standard Model. These models are referred to as the *singlet VLL* and *doublet VLL* models, according to the different representations under which the vector-like leptons transform under the electroweak gauge group. It will be of particular interest in section 5.5, where the scenario of a long-lived VLL is investigated. Other ways to realise vector-like leptons exist, and vector-like fermions can in addition be strongly interacting, in which case they are vector-like quarks, but these possibilities are not discussed in this section. Note that vector-like fermions also arise naturally in various well-motivated, more sophisticated BSM physics models. Examples are Little Higgs models [178–180], composite Higgs models [181, 182] and Quiver theories [183, 184].

Within this subsection, the relevant Lagrangian pieces are exclusively written in terms of two-component left-handed spinorial fields τ, $\overline{\tau}$, τ', $\overline{\tau}'$, ν', $\overline{\nu}'$. The decomposition of the corresponding four-component Dirac spinors in terms of the two-component fields is given

4. A fourth chiral fermion generation could still be allowed in models with an extended scalar sector, as considered e.g. in refs. [168–172]. This is however not the subject of this subsection, which focuses on adding vector-like fermions without any further modifications of the Standard Model.

by

$$\Psi_\tau = \begin{pmatrix} \tau \\ \overline{\tau}^\dagger \end{pmatrix}, \qquad \Psi_{\tau'} = \begin{pmatrix} \tau' \\ \overline{\tau}'^\dagger \end{pmatrix}, \qquad \Psi_{\nu'} = \begin{pmatrix} \nu' \\ \overline{\nu}'^\dagger \end{pmatrix}. \tag{1.4.1}$$

These fields describe the SM tau lepton and the new vector-like tau-lepton and Dirac neutrino. The latter is part of the doublet VLL model, but not the singlet VLL model. Note that the two-component spinors τ, $\overline{\tau}$, τ', $\overline{\tau}'$, ν', $\overline{\nu}'$ are all *left-handed*, i.e. Hermitian conjugation is needed to obtain the right-handed parts of the Dirac spinors. A basic introduction to the two-component spinor notation is given in appendix A. Some elements of the derivations related to the mixing between the SM leptons and the vector-like leptons as well as the different interaction terms are given in appendix B with the purpose of illustrating the construction of the model, without however playing the role of a complete derivation.

1.4.1.1 Singlet vector-like lepton model

The singlet VLL model contains, in addition to all the SM particles, one vector-like lepton associated with two left-handed spinors: τ' transforms under the $(\mathbf{1}, \mathbf{1}, -1)$ representation of the SM gauge group and $\overline{\tau}'$ under the $(\mathbf{1}, \mathbf{1}, +1)$ representation. It is obvious that with these representations, the left-handed part τ' of the VLL and its right-handed part $\overline{\tau}'^\dagger$ have the same quantum numbers and hence transform in the same way. Recall that fields associated with the SM third-generation leptons transforms under the $(\mathbf{1}, \mathbf{2}, -1/2)$ representation for $L = (\nu, \tau)$ and $(\mathbf{1}, \mathbf{1}, +1)$ for $\overline{\tau}$, and likewise for the first two lepton generations, and so the new vector-like lepton carries the same electric charge as the SM leptons.

Lepton masses and mixing

For this choice of particle content and representations, the possible Lagrangian terms consistent with the gauge symmetry, which give rise to mass and mixing terms of the SM lepton τ and the vector-like lepton τ', are the following:

$$\mathcal{L} \supset -y_\tau H L \overline{\tau} - m_{\tau'} \tau' \overline{\tau}' - \epsilon H \cdot L \overline{\tau}' + \text{h.c.}\ . \tag{1.4.2}$$

Here it is assumed that there is only mixing with the third generation SM lepton, which is a deliberate choice; it could instead or in addition occur with the leptons of the first two generations. The first term is the usual Yukawa coupling of the tau lepton that involves the Higgs doublet H and lepton doublet $L = (\nu, \tau)$ with a coupling constant y_τ and is also present in the Standard Model (c.f. eq. (1.1.42)). The second term, together with its Hermitian conjugate, form a Dirac mass term of the vector-like lepton with mass parameter $m_{\tau'}$. The third term leads to mixing between the tau lepton and the vector-like lepton to the amount specified by the parameter ϵ, which will assumed to be small.

Electroweak symmetry breaking is responsible for both the SM τ mass term and the mass mixing term, which arise from the vacuum expectation value v in the second component of the Higgs doublet field H. This results in a non-diagonal mass matrix:

$$\mathcal{L} \supset -\begin{pmatrix} \tau & \tau' \end{pmatrix} \mathcal{M} \begin{pmatrix} \overline{\tau} \\ \overline{\tau}' \end{pmatrix} + \text{h.c.} \qquad \text{with} \qquad \mathcal{M} = \begin{pmatrix} \frac{y_\tau v}{\sqrt{2}} & \frac{\epsilon v}{\sqrt{2}} \\ 0 & m_{\tau'} \end{pmatrix}. \tag{1.4.3}$$

A diagonal mass matrix is then obtained using two unitary matrices L and R via $\mathbf{m} = \mathrm{diag}(M_\tau, M_{\tau'}) = L^T \mathcal{M} R$, which corresponds to a change of the basis of fields

$$\begin{pmatrix} \tau \\ \tau' \end{pmatrix} = L \begin{pmatrix} \tilde{\tau} \\ \tilde{\tau}' \end{pmatrix} , \qquad \begin{pmatrix} \overline{\tau} \\ \overline{\tau}' \end{pmatrix} = R \begin{pmatrix} \tilde{\overline{\tau}} \\ \tilde{\overline{\tau}}' \end{pmatrix} , \tag{1.4.4}$$

where the fields carrying an extra tilde symbol correspond to the mass eigenstate basis. The derivation of the matrices L and R in the approximation of small mixing ($\epsilon \ll 1$) is sketched in appendix B.1. They take the form

$$L = \begin{pmatrix} 1 & -\alpha_L \\ \alpha_L & 1 \end{pmatrix} , \qquad R = \begin{pmatrix} 1 & -\alpha_R \\ \alpha_R & 1 \end{pmatrix} , \tag{1.4.5}$$

with

$$\alpha_L = -\frac{\sqrt{2}\epsilon m_{\tau'} v}{2m_{\tau'}^2 - v^2 y_\tau^2} , \qquad \alpha_R = -\frac{\epsilon v^2 y_\tau}{2m_{\tau'}^2 - v^2 y_\tau^2} . \tag{1.4.6}$$

Neglecting $\mathcal{O}(\epsilon^2)$ terms, the diagonalised mass matrix is just

$$\mathbf{m} = \begin{pmatrix} \frac{y_\tau v}{\sqrt{2}} & 0 \\ 0 & m_{\tau'} \end{pmatrix} , \tag{1.4.7}$$

so the tree-level masses are $M_\tau = \frac{y_\tau v}{\sqrt{2}}$ and $M_{\tau'} = m_{\tau'}$. For the sake of readability, the interaction Lagrangian, which will be presented in the following, will be written in the mass eigenbasis, but without the additional tilde symbol. In each case, it will be indicated how the expressions are obtained from the Lagrangian in the interaction basis.

Interactions

The interaction terms of the vector-like leptons with the electroweak gauge bosons in the zero mixing case ($\epsilon = 0$) follow entirely from the gauge-covariant derivative, the form of which depends on the chosen representations. The individual gauge interaction terms of τ' and $\overline{\tau}'$ are given in appendix B.2.2 and sum up to

$$\mathcal{L}_{\mathrm{int}}^{\tau'} \supset -\frac{g s_W^2}{c_W} Z_\mu (\tau'^\dagger \overline{\sigma}^\mu \tau' - \overline{\tau}'^\dagger \overline{\sigma}^\mu \overline{\tau}') + e A_\mu (\tau'^\dagger \overline{\sigma}^\mu \tau' - \overline{\tau}'^\dagger \overline{\sigma}^\mu \overline{\tau}') \tag{1.4.8}$$

with $\overline{\sigma}^\mu = (\mathbb{1}_{2\times 2}, -\sigma^i)$, where σ^i are the Pauli matrices. Note that in contrast to refs. [173, 174], the sign convention of the metric tensor used in this thesis is $(+,-,-,-)$. These interactions are also present when the mixing parameter ϵ is non-zero, but the vector-like lepton acquires additional interaction terms, which emerge from the interaction terms of the SM lepton fields τ and $\overline{\tau}$ in the interaction basis, given in appendix B.2.1, but also their Higgs Yukawa coupling terms contained in eq. (1.4.2), once the mixing is switched on (i.e. $\epsilon \neq 0$). These terms, together with the mass mixing term of eq. (1.4.2) are given in the interaction basis by

$$\begin{aligned} \mathcal{L}_{\mathrm{int}}^{\tau,\tau'} \supset & -\frac{g}{\sqrt{2}} W_\mu^+ \nu^\dagger \overline{\sigma}^\mu \tau - \frac{g}{\sqrt{2}} W_\mu^- \tau^\dagger \overline{\sigma}^\mu \nu + e A_\mu \tau^\dagger \overline{\sigma}^\mu \tau - \frac{g}{c_W} \left(s_W^2 - \frac{1}{2} \right) Z_\mu \tau^\dagger \overline{\sigma}^\mu \tau \\ & - \left(e A_\mu - g \frac{s_W^2}{c_W} Z_\mu \right) \overline{\tau}^\dagger \overline{\sigma}^\mu \overline{\tau} \\ & - \frac{h}{\sqrt{2}} (y_\tau \tau \overline{\tau} + \epsilon \tau \overline{\tau}' + \mathrm{h.c.}) . \end{aligned} \tag{1.4.9}$$

Taking all terms of eqs. (1.4.8) and (1.4.8) and going to the mass basis via the replacements

$$\begin{aligned} \tau &\to \tau - \alpha_L \tau' , \qquad & \tau' &\to \tau' + \alpha_L \tau , \\ \overline{\tau} &\to \overline{\tau} - \alpha_R \overline{\tau}' , \qquad & \overline{\tau}' &\to \overline{\tau}' + \alpha_R \overline{\tau} , \end{aligned} \tag{1.4.10}$$

one obtains at $\mathcal{O}(\epsilon)$, and under the assumption that $y_\tau v \ll m_{\tau'}$, the following mixed interaction terms of the SM and vector-like lepton fields [173]:

$$\begin{aligned} \mathcal{L}^{\tau,\tau'}_{\text{int},\epsilon} \supset \; & -\epsilon \frac{M_W}{M_{\tau'}} \left[W^+_\mu (\nu^\dagger \overline{\sigma}^\mu \tau') + W^-_\mu (\tau'^\dagger \overline{\sigma}^\mu \nu) \right] \\ & + \epsilon \frac{M_Z}{\sqrt{2} M_{\tau'}} Z_\mu \left(\tau^\dagger \overline{\sigma}^\mu \tau' + \tau'^\dagger \overline{\sigma}^\mu \tau \right) \\ & + \left(\frac{\epsilon}{\sqrt{2}} h \tau \overline{\tau}' + \text{h.c.} \right) . \end{aligned} \tag{1.4.11}$$

Among the above interaction terms, the lepton flavour conserving interactions are the most important ones for the VLL production at proton colliders, with the prevailing production mode being

$$pp \to \tau'^+ \tau'^- . \tag{1.4.12}$$

Mixed production modes involving both SM and vector-like leptons are in principle possible with the flavour-changing interactions, but suppressed by the small mixing parameter ϵ. The decay modes of the vector-like lepton are

$$\tau' \to W\nu , \qquad \tau' \to Z\tau , \qquad \tau' \to h\tau , \tag{1.4.13}$$

which are induced by the non-zero mixing.

1.4.1.2 Doublet vector-like lepton model

The doublet VLL model extends the SM particle content with two left-handed fermion doublets under $SU(2)_L$:

$$L' = \begin{pmatrix} \nu' \\ \tau' \end{pmatrix} , \qquad \overline{L}' = \begin{pmatrix} \overline{\tau}' \\ \overline{\nu}' \end{pmatrix} . \tag{1.4.14}$$

L' transforms under the $(\mathbf{1}, \mathbf{2}, -1/2)$ representation and $\overline{L}'$ under the $(\mathbf{1}, \mathbf{2}, +1/2)$ representations.

Lepton masses and mixing

Here, the possible mass and mixing terms, supposing again mixing with the third generation of SM leptons, originate from the terms

$$\mathcal{L} \supset -m_{\tau'} L' \overline{L}' - \epsilon H \cdot L' \overline{\tau} - y_\tau H \cdot L \overline{\tau} + \text{h.c.} , \tag{1.4.15}$$

and correspond to

$$\mathcal{L} \supset - \begin{pmatrix} \tau & \tau' \end{pmatrix} \mathcal{M} \begin{pmatrix} \overline{\tau} \\ \overline{\tau}' \end{pmatrix} \qquad \text{with} \qquad \mathcal{M} = \begin{pmatrix} \frac{y_\tau v}{\sqrt{2}} & 0 \\ \frac{\epsilon v}{\sqrt{2}} & m_{\tau'} \end{pmatrix} . \tag{1.4.16}$$

The similarity with the mass matrix in the singlet case is obvious, and the procedure to diagonalise it is identical. The same matrices are obtained, but L and R are interchanged. One obtains, by again neglecting $\mathcal{O}(\epsilon^2)$ terms, the tree-level masses

$$M_\tau = \frac{y_\tau v}{\sqrt{2}} \quad \text{and} \quad M_{\tau'} = M_{\nu'} = m_{\tau'} \,, \tag{1.4.17}$$

so the electrically charged and neutral VLLs have identical mass. Including 1-loop corrections would generate a small mass splitting, which can safely be neglected for the purposes in this work.

Interactions

The derivation of the interaction terms of the VLLs and third-generation SM leptons is carried out along the same lines as in the singlet VLL model, with some differences due to the different representations and different number of fermion fields. In the absence of mixing (or in the interaction basis), the gauge interactions read

$$\begin{aligned}
\mathcal{L}_{\text{int}}^{\tau',\nu'} \supset & -\frac{g}{\sqrt{2}} W_\mu^+ \left(\nu'^\dagger \overline{\sigma}_\mu \tau' + \overline{\tau}'^\dagger \overline{\sigma}^\mu \overline{\nu}' \right) - \frac{g}{\sqrt{2}} W_\mu^- \left(\tau'^\dagger \overline{\sigma}_\mu \nu' + \overline{\nu}'^\dagger \overline{\sigma}^\mu \overline{\tau}' \right) \\
& - e A_\mu \left(\overline{\tau}'^\dagger \overline{\sigma}^\mu \overline{\tau}' - \tau'^\dagger \overline{\sigma}^\mu \tau' \right) \\
& + \frac{g}{c_W} \left(s_W^2 - \frac{1}{2} \right) Z_\mu \left(\overline{\tau}'^\dagger \overline{\sigma}^\mu \overline{\tau}' - \tau'^\dagger \overline{\sigma}^\mu \tau' \right) \\
& + \frac{g}{2 c_W} Z_\mu \left(\overline{\nu}'^\dagger \overline{\sigma}_\mu \overline{\nu}' - \nu'^\dagger \overline{\sigma}^\mu \nu' \right) \,,
\end{aligned} \tag{1.4.18}$$

which are composed from the contributions listed in appendix B.2.3. As before, to obtain the mixed interaction terms including the SM leptons and the VLLs in the non-zero mixing case, these terms are combined with the gauge interactions of the SM third generation leptons and the Lagrangian in eq. (1.4.15), and the change to the mass basis gives the following $\mathcal{O}(\epsilon)$ terms [173]:

$$\begin{aligned}
\mathcal{L}_{\text{int},\epsilon}^{\tau,\tau',\nu'} \supset \; & \epsilon \frac{M_W}{M_{\tau'}} \left[W_\mu^+ (\overline{\tau}^\dagger \overline{\sigma}^\mu \overline{\nu}') + W_\mu^- (\overline{\nu}'^\dagger \overline{\sigma}^\mu \overline{\tau}) \right] \\
& + \epsilon \frac{M_Z}{\sqrt{2} M_{\tau'}} Z_\mu \left(\overline{\tau}^\dagger \overline{\sigma}^\mu \overline{\tau}' + \overline{\tau}'^\dagger \overline{\sigma}^\mu \overline{\tau} \right) \\
& + \left(\frac{\epsilon}{\sqrt{2}} h \tau' \overline{\tau} + \text{c.c.} \right) \,.
\end{aligned} \tag{1.4.19}$$

Here, the dominant production modes for the VLLs at proton colliders, induced by the given interaction terms, are

$$pp \to \tau'^+ \tau'^- \,, \qquad pp \to \nu' \overline{\nu}' \,, \qquad pp \to \nu' \tau'^+ \,, \qquad pp \to \overline{\nu}' \tau'^- \,, \tag{1.4.20}$$

where the mixed production modes are again neglected, and the VLL decay modes are

$$\tau' \to Z \tau \,, \qquad \tau' \to h \tau \,, \qquad \tau' \to W \tau \,, \tag{1.4.21}$$

which also go back to the non-zero mixing.

1.4.2 Supersymmetry and the Minimal Supersymmetric Standard Model

Supersymmetry (SUSY) is the symmetry of a theory under certain transformations, which relate fermionic and bosonic degrees of freedom. This subsection will give a very short overview about the most important features and elements in the construction of supersymmetric theories, and in particular the Minimal Supersymmetric Standard Model (MSSM), using mainly ref. [185], but also ref. [186]. The latter is a far more detailed pedagogical introduction to SUSY, which is recommended for further reading.

1.4.2.1 Supersymmetry transformations and supersymmetric Lagrangians

Supersymmetry circumvents a no-go theorem found by Coleman and Mandula [187], which states that it is not possible to build a consistent quantum field theory by non-trivially combining internal symmetries and space-time symmetries using Lie-algebras, i.e. the commutator of their generators must be zero. A way to combine these different types of symmetry has been found by Haag, Lopuszanski and Sohnius [188], which consists in using instead a *graded* Lie algebra that includes fermionic generators satisfying anti-commutation relations. By introducing the fermionic two-component generator Q (*supercharge*) and its Hermitian conjugate $Q^\dagger$, the Poincaré algebra can be extended in the following way

$$\begin{aligned}
[M^{\mu\nu}, M^{\rho\sigma}] &= i(M^{\mu\sigma}g^{\nu\rho} + M^{\nu\rho}g^{\mu\sigma} - M^{\mu\rho}g^{\nu\sigma} - M^{\nu\sigma}g^{\mu\rho})\,, \\
[P^\mu, P^\nu] &= 0\,, \\
[M^{\mu\nu}, P^\sigma] &= i(P^\mu g^{\nu\sigma} - P^\nu g^{\mu\sigma})\,, \\
\{Q_\alpha, Q^\dagger_{\dot\beta}\} &= 2P_\mu \sigma^\mu_{\alpha\dot\beta}\,, \\
\{Q_\alpha, Q_\beta\} &= 0\,, \\
[Q_\alpha, M^{\mu\nu}] &= (\sigma^{\mu\nu})_\alpha{}^\beta Q_\beta\,, \\
[Q_\alpha, P^\mu] &= 0\,.
\end{aligned} \tag{1.4.22}$$

This corresponds to the most basic case, that is referred to as $\mathcal{N} = 1$ Supersymmetry, since there is only one supercharge Q together with its Hermitian conjugate $Q^\dagger$. The fermionic generators act on bosonic and fermionic states as

$$Q\,|\text{Boson}\rangle = |\text{Fermion}\rangle \qquad \text{and} \qquad Q\,|\text{Fermion}\rangle = |\text{Boson}\rangle\ . \tag{1.4.23}$$

The MSSM incorporates $\mathcal{N} = 1$ SUSY and involves at most spin-1 fields, so that the only relevant SUSY representations are chiral and gauge supermultiplets, which have the following physical field content:

— chiral supermultiplet: one complex scalar field and one two-component fermion field,

— vector supermultiplet: one two-component fermion field and one gauge boson field.

For a precise matching between the bosonic and fermionic on-shell and off-shell degrees of freedom, they further contain non-propagating auxiliary fields, which are a complex scalar field F in the chiral supermultiplet and real scalar field D in the vector supermultiplet. These multiplets can be combined in a chiral superfield Φ or vector superfield V

respectively, the form of which will be given below. There can also be anti-chiral supermultiplets/superfields, as defined below, but they will not be considered separately here, since they can be traded for a chiral one.

A useful concept in the description of theories with $\mathcal{N} = 1$ supersymmetry is the *superspace* formalism. The superspace is an extension of the usual four-dimensional spacetime with coordinates x^μ , that includes additional two-component spinor coordinates θ_α and $\theta^{\dagger\dot{\alpha}}$. An infinitesimal SUSY transformation is then interpreted as a translation in superspace of the form

$$(x, \theta, \theta^\dagger) \to (x^\mu + i\theta\sigma^\mu\epsilon^\dagger, \theta + \epsilon, \theta^\dagger + \epsilon^\dagger)\,, \tag{1.4.24}$$

where the transformation parameter ϵ is itself a two-component spinor object with anti-commuting components. In order to understand how this leads to SUSY transformations, the expressions for the chiral and vector superfields will be needed. The general expression for a superfield is an expansion in the fermionic coordinates θ and $\theta^\dagger$, which has the form

$$\begin{aligned} F(x, \theta, \theta^\dagger) =& f(x) + \theta\psi(x) + \theta^\dagger\chi^\dagger(x) + \theta\theta M(x) + \theta^\dagger\theta^\dagger N(x) \\ &+ \theta\sigma^\mu\theta^\dagger v_\mu(x) + \theta\theta\theta^\dagger\lambda^\dagger(x) + \theta^\dagger\theta^\dagger\theta\xi(x) + \theta\theta\theta^\dagger\theta^\dagger D(x) \end{aligned} \tag{1.4.25}$$

and is an exact expansion, since the components of the spinors θ and $\theta^\dagger$ are anti-commuting, i.e. products of the same components vanish. Note that the products of two-spinors have to be understood as a contraction with the anti-symmetric epsilon symbol, as explained in appendix A. For instance, $\theta\theta = \theta^\alpha\theta_\alpha = \epsilon^{\alpha\beta}\theta_\beta\theta_\alpha = 2\theta_2\theta_1$ is a product of *different* spinor components and is therefore non-vanishing. From the generic superfield $F(x, \theta, \theta^\dagger)$, the (anti-)chiral and vector superfields can be obtained with the superspace covariant derivatives [5]

$$D_\alpha = \frac{\partial}{\partial\theta^\alpha} + i\sigma^\mu_{\alpha\dot{\alpha}}\theta^{\dagger\dot{\alpha}}\partial_\mu\,, \qquad D^\dagger_{\dot{\alpha}} = -\frac{\partial}{\partial\theta^\dagger_{\dot{\alpha}}} - i\theta^\alpha\sigma^\mu_{\alpha\dot{\alpha}}\partial_\mu\,. \tag{1.4.26}$$

The expansion $F(x, \theta, \theta^\dagger)$ can be identified with a chiral, anti-chiral or vector superfield (i.e. $F = \Phi$ or $F = \Phi^\dagger$ or $F = V$), if it fulfills one of the following conditions:

$$\begin{aligned} \text{chiral superfield:} \qquad & D^\dagger_\alpha\Phi = 0\,, \\ \text{anti-chiral superfield:} \qquad & D_{\dot{\alpha}}\Phi^\dagger = 0\,, \\ \text{vector superfield:} \qquad & V = V^\dagger\,. \end{aligned} \tag{1.4.27}$$

In the case of the chiral superfield, one obtains the explicit expression

$$\Phi(y, \theta) = \phi(y) + \sqrt{2}\theta\psi(y) + \theta\theta F(y)\,, \tag{1.4.28}$$

which contains a complex scalar field ϕ, a two-component fermion field ψ and the auxiliary field F, as announced above. Applying the superspace transformation of eq. (1.4.24), one obtains the SUSY transformation of the individual fields:

$$\begin{aligned} \delta_\epsilon\phi(x) &= \sqrt{2}\epsilon\psi(x)\,, \\ \delta_\epsilon\psi(x) &= i\sqrt{2}\sigma^\mu\epsilon^\dagger\partial_\mu\phi(x) + \sqrt{2}\epsilon F(x)\,, \\ \delta_\epsilon F(x) &= i\sqrt{2}\epsilon^\dagger\overline{\sigma}^\mu\partial_\mu\psi(x)\,. \end{aligned} \tag{1.4.29}$$

5. Details about differentiation and integration with anti-commuting numbers, as for the components of θ and $\theta^\dagger$, can be found in ref. [186].

The Lagrangian of an $\mathcal{N} = 1$ supersymmetric theory that involves several chiral supermultiplets Φ_i is given in its most general form by

$$\mathcal{L} = \int \mathrm{d}^4\theta\, K(\Phi, \Phi^\dagger) + \left(\int \mathrm{d}^2\theta\, W(\Phi) + \mathrm{h.c.} \right) . \tag{1.4.30}$$

Here, $K(\Phi, \Phi^\dagger)$ is the *Kähler potential*, a real function of the chiral superfields with mass dimension $[K] \leq 2$ in renormalisable theories and due to gauge invariance typically just given by $K = \Phi_i^\dagger \Phi_i$. The function $W(\Phi)$ is a holomorphic function of the chiral superfields and is referred to as the *superpotential*. The compact notation of the integral measure corresponds to $\mathrm{d}^4\theta = \mathrm{d}^2\theta \mathrm{d}^2\theta^\dagger$. With the above form of K and after integrating out the auxiliary fields, the Lagrangian is of the form

$$\mathcal{L} = \partial_\mu \phi_i^* \partial^\mu \phi_i + i\psi_i^\dagger \overline{\sigma}^\mu \partial_\mu \psi_i - \frac{\partial^2 W}{\partial\phi_i \partial\phi_j} \psi_i \psi_j - \sum_i \left| \frac{\partial W}{\partial \phi_i} \right|^2 , \tag{1.4.31}$$

with W being evaluated at ϕ_i instead of Φ_i.

In the next step, gauge interactions will be included. The form of a vector superfield in *Wess-Zumino gauge* is

$$V = -\theta\sigma^\mu\theta^\dagger V_\mu(x) + i\theta\theta\theta^\dagger\lambda^\dagger(x) - i\theta^\dagger\theta^\dagger\theta\lambda(x) + \frac{1}{2}\theta\theta\theta^\dagger\theta^\dagger D(x) \tag{1.4.32}$$

and contains as physical degrees of freedom the gauge field $V_\mu(x)$ and the gauginos $\lambda(x)$ and $\lambda^\dagger(x)$. Both the chiral and the vector superfields transform under gauge transformations with transformation parameters, which depend on the chiral superfield $y = x^\mu + i\theta\sigma^\mu\theta^\dagger$ (instead of just x^μ for gauge transformations of ordinary fields). Under non-abelian gauge transformations, they transform as

$$\Phi \to e^{-gT^a\Lambda^a}\Phi\,, \qquad e^{T^aV^a} \to e^{T^a\Lambda^{a\dagger}} e^{T^aV^a} e^{T^a\Lambda^a} . \tag{1.4.33}$$

The gauge interactions are then included into the previous Lagrangian via the introduction of the gauge superfields into the Kähler potential and the addition of kinetic terms involving the chiral superfields

$$\begin{aligned} W_\alpha^a &= -\frac{1}{4} D^{\dagger\dot\alpha} D_{\dot\alpha}^\dagger D_\alpha V^a \\ &= -i\lambda_\alpha^a(y) + \theta_\beta \left[\delta_\alpha^\beta D^a(y) - \frac{i}{2} (\sigma^\mu\overline{\sigma}^\nu)_\alpha^\beta F_{\mu\nu}^a(y) \right] + \theta\theta\sigma_{\alpha\dot\alpha}^\mu \lambda^{a\dagger\dot\alpha}(y)\,. \end{aligned} \tag{1.4.34}$$

The modified Lagrangian reads

$$\mathcal{L} = \int \mathrm{d}^4\theta\, \Phi_i^\dagger e^{gT^aV^a} \Phi_i + \int \mathrm{d}^2\theta \left(\frac{1}{4} W_\alpha^a W^{a\alpha} + \mathrm{h.c.} \right) + \int \mathrm{d}^2\theta \left(W(\Phi) + \mathrm{h.c.} \right) . \tag{1.4.35}$$

1.4.2.2 Features of the Minimal Supersymmetric Standard Model

The MSSM is a supersymmetric theory that is constructed based on the field content that is already present in the SM. These fields are however not sufficient. In fact, the SM does not contain any particles, which belong to the same supermultiplet. This implies that

the missing superpartner fields must be introduced as new particles. The matter content of the model is embedded in the chiral superfields

$$Q\,, \quad U\,, \quad D\,, \quad L\,, \quad E\,, \quad H_d\,, \quad H_u\,.$$

With the exception of the Higgs doublets H_d and H_u they are in one-to-one correspondence with the SM fermion fields listed in table 1.1, i.e. for both left- and right-handed SM fermion fields, corresponding complex scalar superpartners are introduced. These are called *sfermions*, or more specifically *squarks* and *sleptons*. The presence of two Higgs doublets can be justified with requirement of the superpotential to be holomorphic, which is incompatible with the term $\tilde{H} = i\sigma^2 H^*$ that was introduced to give a mass to the up-type quarks, c.f. eq. (1.1.42). Furthermore, the MSSM contains fermionic superpartners for the gauge bosons, which are referred to as *gauginos*. One should expect these additional particles, which are commonly called *sparticles*, to have the same masses as their SM superpartners due to the vanishing commutator of Q_α and P^μ in eq. (1.4.22), since the square of the mass is the eigenvalue to the operator $P^2 = P^\mu P_\mu$. If this were the case, the superpartners to some of the SM fermions would have been found long ago. Therefore, if Supersymmetry is to be taken seriously, it must be broken, as will be discussed below.

The superpotential of these fields is given by

$$\begin{aligned} W =& y_u^{ij} Q^i H_u U^{j\dagger} + y_d^{ij} Q^i H_d D^{j\dagger} + y_e^{ij} L^i H_d E^{j\dagger} + \mu H_u H_d \\ &+ \lambda_1^{ijk} Q^i L^j D^{k\dagger} + \lambda_2^{ijk} L^i L^j E^{k\dagger} + \lambda_3^i L^i H_u + \lambda_4^{ijk} D^{i\dagger} D^{j\dagger} U^{k\dagger}\,. \end{aligned} \tag{1.4.36}$$

The λ-terms in the second line of the equation are problematic since they violate baryon and lepton number, which in the SM are accidental symmetries. If these terms are present, the λ-coefficients must be very small in order for the model to be phenomenologically viable. It is possible to get rid of these terms by introducing R-parity, i.e. a sign is assigned to each field, depending on the baryon and lepton number and the spin:

$$P_R = (-1)^{3(B-L)+2s}\,. \tag{1.4.37}$$

It turns out that the R-parity is $+1$ for all SM fields and -1 for their superpartners. R-parity is then required to be multiplicatively conserved, i.e. the product of R-parities of all the fields participating in an interaction vertex must be $+1$. This additional symmetry, if it is realised, eliminates the problematic terms in the superpotential. R-parity conservation has the following implications:

1. The lightest supersymmetric particle (LSP) is stable, which makes it a good DM candidate, if it is electrically neutral and a colour singlet.
2. All other supersymmetric particles are unstable.
3. Colliders can only produce even numbers of sparticles, as the initial state has $P_R = +1$. According to the previous points, the sparticles should decay, except for the LSP. If it is the DM candidate, it escapes undetected and carries away momentum.

Supersymmetry relates the interactions of particles belonging to the same supermultiplet. This gives rise to an important feature of the MSSM, which is one of the main motivations for SUSY: As explained in section 1.3, the Higgs boson mass receives loop corrections, which generate quadratic divergences. These result from fermion loops in

Higgs self-energy diagrams. Supersymmetry relates the couplings of the SM fermions to the Higgs boson to the ones of their superpartners, in such a way that additional diagrams from the scalar loops lead to an exact cancellation of the quadratic divergence. This makes SUSY a particularly elegant solution to the hierarchy problem. However, it has been argued before that SUSY must be broken in order to explain the non-observation of sparticles at equal masses as those of the SM particles. There are different mechanisms to explain SUSY breaking, none of which shall be discussed here. However, in order for SUSY to remain a good solution to the hierarchy problem, it should be broken *softly*, which means that the SUSY breaking terms should have couplings of positive mass dimension in order to avoid reintroducing quadratic divergences into loop corrections to scalar masses.

Chapter 2

Aspects of collider physics and recasting

A particle physics model is only of interest as long as it does not contradict the available experimental data. Collider experiments, and nowadays in particular those at the Large Hadron Collider (LHC), constitute the main source of experimental data that is used to test the validity of the SM or search for signatures of new physics, which are expected in different BSM models. The purpose of this chapter is to recapitulate briefly in section 2.1 the way in which relevant information is collected from the collision activity at the LHC experiments and processed in order to draw conclusions on the possible signal hypotheses, i.e. place limits on the parameter space of the models. Furthermore, it will explain in section 2.2 the concept of *recasting*, an approach to exploit the results of existing physics analyses for the study of a larger number of physics scenarios in addition to the one that was originally targeted. First, it will explain the purpose of recasting and different approaches to realise it in praxis. Also some technical aspects relevant to the recasting process will be addressed and the chain of tools, which typically comes into play, will be discussed. The contents of this chapter are mainly relevant for chapter 5, which deals with the recasting of long-lived particle searches at the LHC. In addition to the references which are given explicitly, this chapter uses ideas and formulæ from refs. [189–193].

2.1 Experiments at the Large Hadron Collider

The Large Hadron Collider is presently the biggest existing collider on earth with a circumference of about 26.7 km [194]. It belongs to the accelerator complex of the European Organization for Nuclear Research (CERN), that is situated in Geneva. In the past it had two data taking periods, Run 1 from 2010 to 2012 and Run 2 from 2015 to 2018, and at the time of this writing it is in preparation for Run 3, which is scheduled for the years 2022 to 2024.

2.1.1 Characteristics of the Large Hadron Collider

As suggested by its name, the LHC generates high energy collisions of hadrons, mostly protons (pp), but occasionally also heavy ions [195]. Only proton-proton collisions shall be discussed in the following. The proton beams consist of bunches, which are accelerated in different stages by other accelerators, before they are injected into the two LHC accelerator rings, where they circulate in opposite directions. At four different locations (interaction points), beam crossings lead to collisions of the proton bunches, where the four LHC main detectors ATLAS, CMS, ALICE and LHCb are installed for the purpose of reconstructing the final states of the collision events.

The approximately circular shape of the trajectory is generated with 1232 dipole magnets (other sorts of magnets are used for focalisation and to ensure a high beam quality), which generate a deflecting Lorentz force acting on the positively charged protons. This deflection causes energy loss through synchrotron radiation, which is compensated through periodical acceleration via radio frequency (RF) cavities. The maximum center-of-mass energy $\sqrt{s}$ of the colliding protons is limited primarily by the maximum magnetic field strength B achievable with the magnets and the bending radius ρ [196]:

$$\sqrt{s} \propto \rho B \,. \tag{2.1.1}$$

The available center-of-mass energy is obviously an important figure-of-merit of a collider, since it determines which particles can be produced, so a high energy is desirable for the search of new heavy particles. During Run 1, the LHC had an energy of 7 and 8 TeV (energy in one proton-proton collision), which has been further increased to 13 TeV in Run 2 [197].

Another important characteristic quantity of a particle collider is the (instantaneous) luminosity $\mathcal{L}(t)$, which indicates how many events N_{events} for a process with cross section σ_{events} will occur in a given time [198, 199]. It has been increasing over the data taking periods of the LHC. The expected number of events in a dataset is obtained from the *integrated* luminosity L_{int}:

$$N_{\text{events}} = \sigma_{\text{events}} L_{\text{int}} \qquad \text{with} \quad L_{\text{int}} = \int \mathrm{d}t\, \mathcal{L}(t) \,. \tag{2.1.2}$$

The proton beams consisted of about 1400 (2500) bunches per beam in Run 1 (Run 2), with a bunch spacing of about 50 ns (25 ns) [200]. In Run 2, the LHC has reached a peak luminosity of $2 \times 10^{34}\,\mathrm{cm}^{-2}\mathrm{s}^{-1}$, which is going to be further increased in the future, in particular with the high-luminosity upgrade of the LHC (HL-LHC). A high luminosity is important to allow for the observation of rare processes (with a small cross section).

2.1.2 Collision activity at the main detectors

As previously mentioned, the LHC has four main experiments: ATLAS and CMS are general purpose experiments, whereas ALICE focuses on heavy-ion physics and LHCb on B meson physics [198]. Only ATLAS and CMS shall be relevant the following. These detectors infer information about the final state particles of the pp collisions from their interactions with the various detector components in order to reconstruct the events. Both

detectors have a cylindrical shape and consist of the following subdetectors (from smaller to larger radii with respect to the beam line) [201–203]: An inner detector (ID) for the observation of charged particle *tracks*, an electromagnetic calorimeter (ECAL) for measuring predominantly the energies of electrons and photons, a hadronic calorimeter (HCAL) for the energies of both charged and neutral hadrons and a muon detector. Neutrinos escape the detector without being detected, but carry away momentum. The IDs of both experiments consist of different parts, e.g. silicon microstrip and pixel trackers as well as transition radiation trackers in the case of ATLAS [204]. They have the highest resolution in the innermost regions. With the tracks determined by the ID, *vertices* can be determined via suitable reconstruction algorithms, from which the tracks originate. Furthermore, in both detectors a magnetic field is generated (4 T in CMS and 2 T in ATLAS) to bend the trajectories of charged particles, which is used for measuring their momenta. Figure 2.1 shows final state particles of a simulated event passing through the ATLAS detector, in the cross-sectional view.

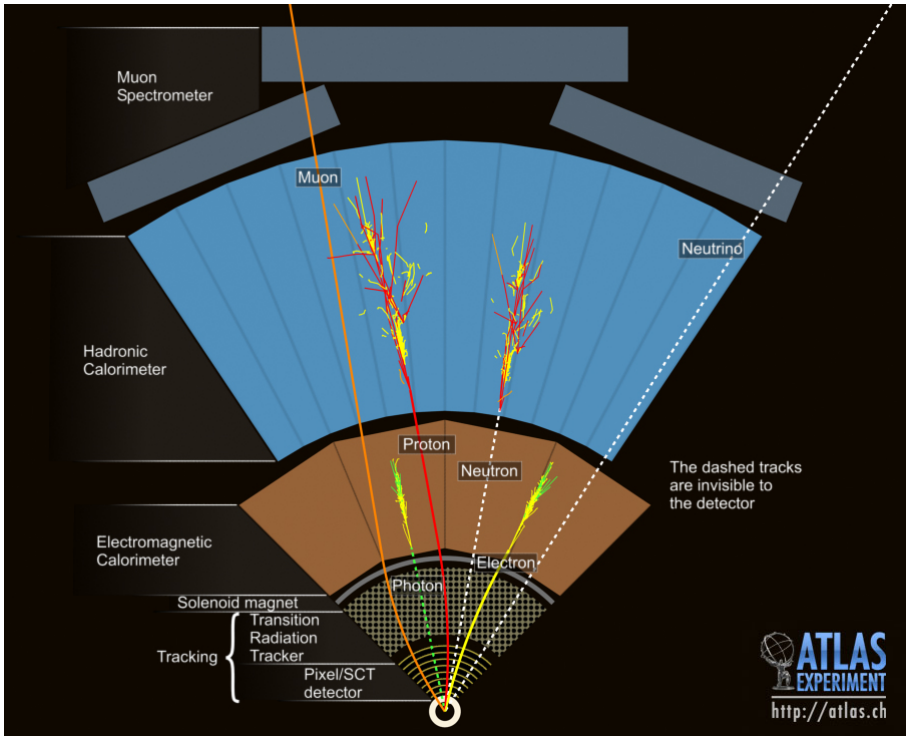

Figure 2.1: Cross-sectional view on final state particles of a simulated event passing through the ATLAS detector. The figure has been provided by CERN [205].

The number of collision events at the LHC is of the order 1 billion per second. Given the storage size required to record one event, which is about 1 MB, it is impossible to keep all events and to process them. For this reason, triggers need to be used, requiring for example a certain number of jets with a given transverse momentum. Only events which pass such a set of trigger requirements will be recorded.

A further complication is *pile-up*, which is the fact that several events occur in a single bunch crossing. The average number of pile-up events $\langle N_{\mathrm{PU}} \rangle$ in bunch crossings at the

LHC was about 20 in Run 1 and 30 at the beginning of Run 2 [206]. If one is interested in observing a particular process (*hard event*), the effect of pile-up is to add mostly soft hadrons to the final state, resulting from the pp collision events which are unrelated to the hard event. At the LHC, the number of additional soft hadrons is of the order 100 to 1000, which makes the event reconstruction more involved.

The physics objects used in analyses by ATLAS and CMS, which are reconstructed using the different subdetectors and algorithms, are the following [207]: As mentioned above, *tracks* are reconstructed from hits of charged particles in the ID, as well as *vertices*, which correspond to intersecting tracks. *Electrons*[1] and *photons* are identified via clusters of energy deposit in the ECAL and ID tracks in the case of electrons. *Muons* can be recognised via tracks in both the ID and the muon detector. *Jets* result from clustering together particles with a specific jet algorithm [208] that respects infrared and collinear safety. Various different algorithms exist, but jet clustering and the matter of infrared/collinear safety shall not be discussed here. CMS combines calorimeter and tracking information via a particle flow algorithm, whereas ATLAS used only calorimeter information in the first instance, but started to make use of particle flow as well [209, 210]. Tau leptons have a short lifetime (c.f. table 5.1), leading to the observation of *hadronic τ decays* into narrow jets consisting of charged and neutral pions or kaons, reconstructed using ID, ECAL and HCAL. If jets contain a B or D hadron, they can be tagged as *flavoured* jets, i.e. b or c jets. They can be distinguished from other jets via displaced vertices of the decaying b or c hadrons, i.e. vertices at a measurable distance from the primary vertex related to the hard event, where the hadron has a high mass and eventually decays semi-leptonically. Ideally, the net momentum of all particles should be zero. Therefore, particles which are not identified lead to an observable *missing transverse momentum* (c.f. section 2.1.3), calculated as the negative of the vector sum of all transverse momenta belonging to the identified objects.

2.1.3 Particle kinematics and observables

Kinematic quantities are important in the description of an event and shall therefore be reviewed briefly based on ref. [189]. Usually, for the description of a collision event (e.g. in event records) a coordinate system is used with a z axis that is directed as the beam axis and with the origin located at the interaction point, where the collision takes place. In this system, the four-momenta P_1^μ and P_2^μ of the colliding protons are:

$$P_1^\mu = \begin{pmatrix} \sqrt{s}/2 \\ 0 \\ 0 \\ \sqrt{s}/2 \end{pmatrix}, \qquad P_2^\mu = \begin{pmatrix} \sqrt{s}/2 \\ 0 \\ 0 \\ -\sqrt{s}/2 \end{pmatrix}. \tag{2.1.3}$$

This is however not the momentum of the partons (i.e. quarks and gluons) involved in the hard event, which instead carry only a fraction x_1 and x_2 of the protons' momenta,

$$p_1^\mu = x_1 P_1^\mu, \qquad p_2^\mu = x_2 P_2^\mu. \tag{2.1.4}$$

1. Note that the term *electron* in this context generically refers to electrons and their anti-particles (positrons). This applies also to other particles, such as muons.

Here, x_1 and x_2 are independent, so the z component of the sum $p_1 + p_2$ has generally some arbitrary non-zero value in the laboratory frame. The probability for the partons to take a momentum fraction $x_{1,2}$ is described by *parton distribution functions* [211].

If the momentum of a final state particle $p^\mu = (E, p_x, p_y, p_z)$ in the laboratory frame is boosted into the rest frame of the colliding partons, only the transverse momentum, i.e. the vectorial and scalar quantities

$$\vec{p}_T \equiv (p_x, p_y)\,, \qquad p_T = |\vec{p}_T| \tag{2.1.5}$$

as well as the azimutal angle

$$\phi \equiv \arctan\left(\frac{p_x}{p_y}\right) \tag{2.1.6}$$

remain invariant. In contrast, the angle θ between the momentum and the x-y-plane changes under the boost. Boost invariant quantities are obviously more meaningful, since the necessary boost to convert to the rest frame is not known. A boost invariant quantity is the difference of two *rapidities* $\Delta y = y_2 - y_1$, with the rapidity for a given particle momentum p^μ being defined as

$$y = \frac{1}{2}\ln\left(\frac{E + p_z}{E - p_z}\right)\,. \tag{2.1.7}$$

Using in addition the difference between their azimutal angles $\Delta\phi = \phi_2 - \phi_1$, another boost invariant quantity can be defined, the *angular separation*

$$\Delta R = \sqrt{(\Delta\phi)^2 + (\Delta y)^2}\,. \tag{2.1.8}$$

The rapidity y is a kinematic quantity and is barely used in high energy physics [212]. In contrast, the *pseudorapidity* η is a very common geometric quantity, which is defined via the angle θ as

$$\eta = \ln\cot\left(\frac{\theta}{2}\right) \tag{2.1.9}$$

and is therefore not boost invariant. However, it is identical to the rapidity for massless particles and a good approximation for it, when the mass is low compared to the momentum. The difference between pseudorapidities is only boost invariant for massless particles. Both ATLAS and CMS cover the range between ± 5, which is nearly the entire θ range. Usually, the angular separation ΔR in eq. (2.1.8) is also calculated with η rather than y.

To conclude this section, a few standard observables will be listed: As previously explained, undetected particles are responsible for a *missing transverse momentum*, defined via the transverse momenta of the observed particles as

$$\vec{\not{p}}_T \equiv -\sum \vec{p}_T\,, \tag{2.1.10}$$

which is a two-vector. Missing momentum implies that also energy must be missing. The *missing transverse energy* (MET) is defined as

$$\not{E}_T \equiv |\vec{\not{p}}_T|\,. \tag{2.1.11}$$

The *invariant mass* of a set of objects is obtained from squaring the sum of all four momenta,

$$m^2_{\text{objects}} = \left(\sum_{\text{objects } i} p_i^\mu \right)^2 . \tag{2.1.12}$$

The *transverse energy* of a particle is given by

$$E_T \equiv \sqrt{m^2 + p_T^2} \tag{2.1.13}$$

and the *transverse mass* of two particles is given in terms of their transverse momenta and energies by

$$m_T = \sqrt{(E_T^1 + E_T^2)^2 - (p_T^1 + p_T^2)^2} \, . \tag{2.1.14}$$

2.2 Recasting: purpose and strategies

Collider searches for specific signatures, which could indicate the presence of new physics, usually test one or several particular signal hypotheses, i.e. it is assumed that processes of a selected BSM model contribute a certain number of events to the signal regions defined in the analysis, in addition to the SM background events. Confronting the event numbers of the signal regions expected under the signal hypothesis with the corresponding experimentally observed event numbers, conclusions can be drawn on the viability of the signal model or a point in its parameter space. By simulating signal processes and determining the signal efficiencies of the different regions, i.e. the ratio of selected to generated events, it is possible to draw an upper limit on the cross section of the processes using appropriate statistical methods. If the relevant quantities for constraining a model are just the event numbers of signal regions, it should in principle be possible to test in the same way a different signal hypothesis, i.e. a different model or parameter configuration. This principle is exploited in the *recasting* approach, which will be introduced in the following based on ref. [213], before a few important aspects will be discussed in some more detail.

2.2.1 The purpose of recasting

Given the immense effort on the experimental side to undertake a physics analysis, it is highly desirable to get as much benefit as possible from the results, even after the completion of the analysis. It is not unusual that processes of different BSM models lead to the same experimental signatures. Therefore it is natural to ask what are the implications of the search results on other models of interest. Recasting addresses this question in a systematic way by making the event selection process and the search results of existing analyses available within a computer program.

There is a number of good reasons to follow this approach. Obviously, using existing analyses has the advantage that a considerable part of the work necessary to confront theories with nature has already been accomplished. An analysis is typically designed in such a way that its event selection criteria lead to a high sensitivity to signals of new physics with low background contamination. To recast an existing analysis, it is "only"

necessary to correctly implement the existing event selection process, since all criteria have already been fixed. Processing experimental data is not necessary, since only the published search results for the different signal regions are needed, provided that this information is available. Also the estimates of the contributions from SM background can be re-used, if available. In this way, an existing analysis can become useful to constrain a whole class of models instead of just the one(s) considered by the experimental collaboration.

The principle of recasting may seem rather straightforward, but the success of the approach depends on how it is realised (and realisable) in praxis: For the implementation of a selected analysis, it is first necessary to understand how the event selection of the original analysis is performed. In principle, the published article of the analysis should contain all the indispensable information concerning the event selection. A re-implemented analysis is supposed to be applicable to Monte-Carlo generated event samples of the presumed signal process in the model under consideration. These are commonly referred to as *Monte-Carlo truth* events, because they are ideal in the sense that the particles and their properties are perfectly identified and the information about the particle properties is not altered by detector effects. In reality, the experimental part of the analysis uses imperfect detectors and reconstruction algorithms, which attempt to reconstruct different objects and their kinematics based on interactions with detector elements. A perfect reconstruction of all particles in an event, comparable to the Monte-Carlo truth, is not possible. The detector effects affect the number of observed events selected in the signal regions and are in general not negligible. Therefore they should be taken into account in some way in the analysis of the Monte-Carlo truth events. Different possibilities to do this are discussed in section 2.2.3. In any case, this is only possible if sufficient information about the performance of detectors and reconstruction algorithms is available. This kind of information is frequently provided as supplementary material to the analyses.
Provided that all the information needed for the re-implementation of an analysis is available, the technical details of the implementation in a computer program need to be sorted out. In the whole recasting process, a certain number of tasks are not analysis specific, but are essential parts of the workflow for every analysis. Examples are the handling of input files (especially event records), methods for book-keeping, statistical functions to determine exclusion limits and the generation of output files containing the results of an analysis. Instead of realising every single analysis as a separate program, it is more sensible to embed them into a framework that takes care of these tasks in a unified way and ideally provides a large number of functionalities which could be useful in the implementation of the different analyses. This is convenient not only since the effort in the implementation of an analysis gets reduced, but also because event samples can possibly be confronted with more than one different physics analyses simultaneously. The work presented in chapter 5 makes use of the MadAnalysis 5 [193, 193, 214–218] framework that will be introduced in section 2.2.5, where also some other recasting tools shall be enumerated and briefly commented on.
In order for a re-implemented analysis or a recasting framework to be useful, it should be public, user-friendly, efficient both in performance and memory consumption and support commonly used standards for event records. Before using it to constrain a selected model, its validity must be verified by reproducing published results of the analysis. This aspect will be discussed in more detail in section 2.2.4. Depending on the complexity of the analysis, the performance might also play a role, since for achieving a reasonably small

statistical uncertainty on the theoretical results of the selection efficiencies, it can be necessary to analyse hundreds of thousands of events. This becomes even more important when analyses are used for dense parameter scans, where a high number of different event samples need to be analysed.

Re-interpreting an existing analysis under a different signal hypothesis in order to test its phenomenological viability has some limitations that one should be aware of. Even by carefully following the description of the event selection procedure provided for the analysis under consideration, it may not be possible to implement it in full detail in exactly the same way as it was performed by the experimental collaboration. For example, some criteria could depend on the quality of the reconstruction of some particles and therefore be related to details of the reconstruction algorithms which are not publicly available. The same is the case for the simulation of the detector response, which can in praxis only be done in a simplified way compared to the full simulation of the experimental collaboration, as discussed in section 2.2.3. Therefore, it can in general not be expected that the re-implementation of an analysis reproduces exactly the same results. Although it might be possible to check the validity of the re-implementation against the original analysis by reproducing published results with good agreement, this does still not guarantee that the re-implementation would agree in equal measure with the original analysis for every other signal process, especially if the re-implementation relies on model-dependent information. It is therefore important to cautiously evaluate whether a re-implemented analysis is applicable to a given signal process and to make sure that the exclusion limits will be conservative rather than aggressive. The results obtained via recasting can be very useful to probe the allowed parameter space of various models, but for the before-mentioned reasons they do not have the same value as a dedicated physics analysis which explicitly targets a particular signal model and process.

The focus of this section as well as chapter 5 is on the re-implementation of *existing* analyses and the re-interpretation of their results for different signal hypotheses. A somewhat different application of the methods and tools used for recasting is the implementation of physics analyses, which have not been performed in the past, but could on the contrary be realised *in the future*. Instead of constraining a model via the analysis of simulated event samples of some signal process through comparison of the signal events with experimentally observed ones, one determines instead *hypothetical* constraints by assuming that there is no signal, i.e. the signal regions are only populated with background events. In this way, it is possible to determine the reach in parameter space that could be excluded by the analysis, if the experimental observations are indeed consistent with the background-only hypothesis. An example of such a prospective study is presented in section 4.4 for a monojet/multijet+MET search that could be performed at a possible future 100 TeV collider.

2.2.2 Recasting approaches

In section 2.2.1, a recasting strategy is described, which relies on a complete description of the event selection procedure in the analysis under consideration, such that it can be re-implemented in a computer code, and it uses the experimentally observed number of events in the different signal regions. The re-implementation of the analysis can then be

used for the analysis of event samples in some user-selected signal model to determine limits on the cross section of the simulated process via comparison with the observed number of signal events. These limits can finally be used to constrain the parameter space of the model.

As explained in refs. [193, 216, 219], there exists a another, different approach that has the same purpose but some important differences. It relies on so-called *Simplified Model Spectra*, i.e. it uses search results which are provided by the experimental collaborations in terms of limits on cross sections of processes in *simplified models*. These models extend the SM with only a few additional particles and interactions, and are often a simplified version of a more complete model with a reduced particle content, since the other particles have been integrated out [220]. In this case, the experimentally determined limits on the cross sections of the considered processes are also applicable to processes of other models, if they have the same topologies. Therefore, the recasting process reduces to the calculation of cross sections times braching ratios ($\sigma \times \mathrm{Br}$) and does not require the simulation and subsequent analysis of event samples. This has the advantage of being much faster, but is in turn less general, since it restricts the use of the search results to signal hypotheses, which involve the same topologies. Furthermore, this principle allows for an efficient confrontation with a higher number of search results of different analyses via the calculation of $\sigma \times \mathrm{Br}$ for different topologies of the selected signal model, which can then be compared to upper limits on cross sections of processes with matching topologies, provided in various different analyses, c.f. ref. [219]. This approach will however not be further considered in this work.

2.2.3 Detector simulation

It was pointed out in section 2.2.1 that incorporating detector effects into simulated events is important to allow for a comparison of the numbers of simulated signal events with the experimentally observed ones. At least in principle, the imperfections of the detectors and the related algorithms can have impacts on the results of the event selection. For instance, particles can be misidentified or not reconstructed at all, and measurements of quantities such as the energy of a particle can differ from the true value due to a finite resolution.

Naively, one could consider two options to handle detector effects: Either the knowledge about the detector is used to infer the true event information of the observed reconstructed events, i.e. one performs an *unfolding* of the detector effects, so that a direct comparison with simulated events becomes possible. There is however no guarantee that this leads to the right results, as the reversion of the detector effects cannot be expected to give a unique result. For this reason, unfolding is practically not applied for BSM searches. The safer and easier possibility is to do the comparison between simulated and observed events on the reconstructed level, i.e. mimic the reconstruction of the simulated events including the known effects of the detector, which corresponds to a *folding*.

Simulating the detector response can be done at different levels of complexity, which should correspond to the accuracy needed for the application in which it is used. The more sophisticated a detector simulation is, the higher the requirements on the computational ressources, i.e. the memory and performance of the machine on which the simulation is

performed, or the longer the computing time. This determines which effects can and should be taken into account. Even though a unique classification of different approaches does not exist, a short review of existing approaches, based essentially on refs. [191, 218, 221] shall be given here, where the contrast between the different levels of complexity should become apparent.

The most refined simulation toolkit used by the experimental collaboration is GEANT [222], which emulates in high detail the interactions of particles with the different detector parts. In ref. [223], this approach is referred to as *full simulation*, where also the different steps of the simulation are outlined: A very precise modelling of the detector geometry is used, and the transition of particles (including the effect of the magnetic field) through the material of both the sensitive and non-sensitive detector parts is simulated. Within the sensitive parts, i.e. the ones which are indeed useful for measurements, hits are generated, where different electromagnetic and hadronic interactions including the production of additional particles is iteratively considered, as long as the energy of the particles exceeds a certain threshold. This is followed by triggering (*online* event reconstruction) and *offline* event reconstruction for the actual physics analysis.

The GEANT approach reproduces the various effects very accurately, but is also very time-consuming and therefore not particularly suitable for a recasting program, if a very large number of events need to be analysed. Therefore, the experimental collaborations of the LHC have also elaborated various simpler *fast-simulation* techniques [224–228]. These use different simplifications, such as a simplified detector geometry or simplifying assumptions about the material distribution, or Gaussian smearing of the hit position in the subdetector for reproducing its finite resolution and hit reconstruction efficiencies, parameterised in different quantities, e.g. the incident angle of the particle. These simplified techniques have been validated against the full simulation with GEANT and are about 2-3 orders of magnitude faster. Still, they require a high amount of know-how as well as computational power.

For many phenomenological applications, such sophisticated simulation techniques as the above-mentioned ones are not necessary and a lower accuracy can be accepted. In these cases, a simplified but faster and easy-to-use method is preferable. Such a method is provided by the DELPHES package [221, 229], which includes the simulation of a magnetic field in the tracker, the application of user-specified parameterised energy and momentum resolutions as well as efficiencies, which depend on the particle species, and a simple modelation of the calorimeters. Tracks of charged particles have a certain probability to be reconstructed. The calorimeters are divided into cells, i.e. uniform segments in (η, ϕ), with a size that can be specified. These segments are identical for both the electromagnetic and the hadronic calorimeters and the fraction deposited in the ECAL and HCAL cells is fixed, either via default or user-defined values for each kind of stable particle (or with a sufficiently long lifetime to traverse the detector). Gaussian smearing is applied to the energy deposit in the calorimeter cells, independently for the ECAL and HCAL. DELPHES also applies a simple particle-flow algorithm to combine tracking and calorimeter information. In the object reconstruction, it applies a certain number of approximations, e.g. it neglects photon conversions in the ECAL. Furthermore, there are different options to reconstruct jets from different sorts of input, including the use of the FASTJET [230] package, and it has some capabilities to include pile-up effects. However, these techniques are fairly

simple and considerably faster compared to the full or fast simulation of the experimental collaborations of the LHC and simple to use.

An even simpler approach is to account for the detector effects only via the application of smearing of the kinematic variables and reconstruction or tagging efficiencies to the MC truth objects (in addition to a jet clustering algorithm). This option has been considered in refs. [191, 218] and can be sufficient for many applications.

2.2.4 Validation

The validation of an analysis is an essential part of the re-implementation process. It is important to ensure that the analysis is correctly implemented in order to generate physically meaningful results, whereas a wrong implementation could lead to wrong conclusions about the phenomenological viability of some new physics model or parameter space. It is therefore crucial to check the correctness of an analysis re-implementation, i.e. validate it, before advocating its use. This means that it must be able to reproduce with reasonable agreement results obtained by the experimental collaboration, which can in some cases be difficult to achieve [213, 231]. Usually, (part of) the validation is done simultaneously with the the process of implementing the analysis, in particular when intermediate results (e.g. cutflows) are available. In this way, the implications of the different steps in the event analysis can be directly observed and used as a sort of feedback, which can provide hints about whether a specific part of the analysis has been implemented correctly. Besides programming mistakes, this can reveal misunderstandings of the analysis description or an incomplete simulation of detector effects.

The exact validation procedure to follow depends on the publicly available results in the published analysis note or the corresponding auxiliary material. Examples are results of parameter scans, i.e. plots of excluded parameter space, upper limits on cross sections or selection efficiencies. The provided material might also contain histograms, e.g. p_T distributions of relevant particles after event selection. More precise information can be provided via tabulated cutflows, i.e. a listing of the event numbers after the application of the individual selection criteria (cuts), or the efficiencies of these cuts. The validation procedure consists in reproducing these results with reasonable agreement, where corresponding event samples for the cases under consideration need to be simulated. A disagreement can sometimes give a concrete indication about the origin of the discrepancy in the implementation.

2.2.5 MadAnalysis 5 and other recasting tools

The work presented in chapter 5 concerns the re-implementation of searches for long-lived particles within the MadAnalysis 5 framework, which will briefly be introduced here based on ref. [193, 218], followed by an enumeration of some other existing recasting tools, which are more briefly commented on based on the information from refs. [213, 232, 233].

MadAnalysis 5 is a software package for the analysis of event records for simulated events. It can handle events in the Monte-Carlo truth, which may contain only the hard scattering process or include also parton showering and hadronisation, or reconstructed

events. For this purpose, it supports a number of different event formats, which are used by the various existing Monte-Carlo event generators, but also ROOT [234] files obtained from DELPHES for reconstructed events. Its abilities to analyse events and generate histograms can also be used directly from the event generator MADGRAPH5_aMC@NLO [235]. MADANALYSIS 5 can be used via a command line interface written in PYTHON, whereas its core is written in C++. The user can therefore provide instructions for the analysis in a user-friendly way using the command-line interface, or implement analyses in a more flexible way as C++ code using the *expert mode*. MADANALYSIS 5 has interfaces to different other codes, which include FASTJET for jet clustering and DELPHES for a fast simulation of detector effects and event reconstruction. The analysis is internally carried out by the SAMPLEANALYZER library and generates output in its own format, the SAF format, which is a set of directories and files. MADANALYSIS 5 has also some abilities for the generation of figures and reports provided in the formats HTML and PDF. Alternatively to the DELPHES package for detector simulation and reconstruction, MADANALYSIS 5 comes with a more lightweight alternative, concerning both the execution speed and the storage size of output files. It is referred to as *Simplified Fast detector simulation* (SFS) [218] and is based on smearing functions and reconstruction efficiencies, as mentioned in section 2.2.3. A number of existing LHC Run 1 and 2 analyses are available in the Public Analysis Database (PAD), which can be accessed directly via the command line interface of MADANALYSIS 5 [216].

Like MADANALYSIS 5, the tools CheckMATE [236, 237], Rivet [238, 239] and the GAMBIT module ColliderBit [240, 241] follow a relatively general approach for LHC searches involving the analysis of simulated event samples, where detector effects are either simulated with DELPHES or in a smearing/efficiencies approach. They all come with a certain number of BSM analyses by ATLAS and CMS. The tool CONTUR [242, 243] uses Rivet to eliminate unviable BSM theories with differential measurements corresponding to SM signatures. SModelS [233, 244–246] follows the approach mentioned in section 2.2.2 using Simplified Model Spectrum topologies obtained for BSM models with a $\mathbb{Z}_2$ symmetry. A very similar approach is adopted by the program HiggsBounds [247–251] that determines exclusion limits using results of Higgs searches. As mentioned earlier, in this approach event generation is not necessary, but only cross section times branching ratios need to be computed. SModelS contains more than 60 SUSY searches by ATLAS and CMS. Two other tools, which also follow similar approaches in using pre-computed efficiency maps are XQCAT [252] for models with additional heavy quarks and Fastlim for the MSSM [253]. Furthermore, `HiggsSignals` [254–256] and `Lilith` [257, 258] constrain BSM models based on a set of Higgs signal strength measurements, and in the case of `HiggsSignals` also mass measurements. Furthermore, one could also mention RECAST [259, 260], which is however not a publicly available tool, but an experiment-owned analysis reinterpretation framework.

2.2.6 Typical tool chain for recasting with MadAnalysis 5

Assuming that a selected analysis has been implemented within MADANALYSIS 5 and successfully validated, it will now be reviewed which different tools come into play (and in which order) in order to investigate the implications of the analysis results on a

chosen BSM model. The purpose of this review, which is inspired by refs. [193, 261, 262], is to give an impression of the workflow and the relevance of the different tools, rather than explaining technical details or giving a complete list of specific computer programs.

As a first step, one should either select an existing BSM model or work out a new one. Once the theoretical ideas of the model of interest are established, i.e. the Lagrangian of the new model is known, the aim is to check the viability of the model by confronting its predictions to experimental results. To do this with the re-implementation of the analysis in MadAnalysis 5, it is necessary to generate event samples of processes which could contribute to the signal events.

Before generating events, it is necessary to make the information about the model available to the selected event generator. The way in which this can be done depends in general on the generator itself: Some event generators contain hard-coded processes for specific models. Otherwise, the model information is usually provided in some model file(s), in which the particles of the model, their properties and their interactions are specified in a well-defined format. Doing this implementation by hand is a cumbersome and error-prone task. A convenient tool for the correct implementation of a model for the use with a Monte-Carlo event generator is the `Mathematica` [263] package FeynRules [262]. Using FeynRules, the model is implemented by specifying, among other things, the field contents, gauge groups, parameters, indices and the Lagrangian. The Lagrangian is written in a certain syntax, which makes use of pre-defined expressions such as the gauge covariant derivative of a field. Supersymmetric theories can be directly implemented in the superspace notation. FeynRules provides a number of useful functions, including sanity checks to ensure the correctness of the implementation. In particular, for a correctly implemented model it is able to determine all Feynman rules and generate model files in formats for the different event generators. One particular format is the *Universal FeynRules Output* (UFO) [264], which can be used with several event generators. Besides FeynRules, other packages with the purpose of generating correct model files for event generators are LanHep [265, 266] and Sarah [267, 268].

The simulation of event samples can be done at different levels [269]: Parton level events are obtained via matrix element generation of the hard process at leading or next-to-leading order (LO/NLO) as well as phase-space Monte-Carlo integration and sampling. Also parton distribution functions are relevant at this stage. Parton level events can for example be generated with MadGraph5_aMC@NLO [235, 270], Sherpa [271–273] or `WHIZARD` [274–276]. Parton showers and hadronisation can be simulated for the given parton level events using e.g. Herwig [277, 278], Pythia [279–281] or Sherpa.

The simulated events are then passed to the MadAnalysis 5 re-implementation of the analysis. However, before the actual analysis of the event sample comes the simulation of detector effects and event reconstruction. This happens, depending on the implementation of the analysis, either with Delphes or SFS. Then, the application of the selection criteria of the analysis to the event sample takes place. In this process, an event is rejected if it fails to fulfill one of the selection criteria (cuts). MadAnalysis 5 takes care of the book-keeping by counting the number of surviving events after each cut and adding up their weights. The cutflow, which contains these numbers, is part of the output and is generated for each signal region. Upper limits on the cross section of the simulated process are then computed for each signal region based on the corresponding signal efficiency, i.e.

the ratio of the sum of weights belonging to the signal events in this region to the sum of weights of all simulated events, using the CL_s method [282].

Chapter 3

Heavy dark matter through the dilaton portal

Any theory can be made scale invariant by coupling it to a dilaton. The scale invariance can then be softly broken, giving the dilaton a mass and self-interactions, and this becomes a popular proposal [283–296] for solving the hierarchy problem of the SM. Such SM plus dilaton theories can either be thought of as fundamental, or as the low-energy limit of composite theories, where the dilaton becomes the pseudo-Goldstone boson associated with the spontaneous breaking of scale invariance. It therefore couples to the SM fields through the trace of the energy-momentum tensor.

The dilaton portal is also an extremely economic way of coupling the SM to a dark matter particle: a massive dark matter field automatically couples to the dilaton, so that there is no need to add any additional interactions with the SM. Such models are very economical in terms of new parameters: one has effectively just the dilaton mass, dark matter mass, and the dilaton decay constant/symmetry breaking scale as extra degrees of freedom relative to the SM.

Models of dilaton portal dark matter have also been well studied in the literature [291, 297–300]. Both the fermionic and vector dark matter cases will be studied in detail in this work, where the connection between the dilaton portal and models of vector dark matter based on effective field theory will be pointed out. Different scenarios of Higgs-dilaton mixing shall be considered, the simplest one being the vanilla dilaton scenario without mixing with the Higgs boson. Additionally, once mixing is included, two different formulations of the theory will be distinguished (in section 3.4): the model is not uniquely defined, and the simplest way to include mixing is not gauge invariant; as a second option, the Lagrangian will therefore be written in a gauge-invariant way. The aim is to revisit and update the constraints on the main parameters of the model, via dark matter constraints, the latest Higgs-like particle searches for the dilaton itself, collider constraints from direct searches for the dark matter particle at the LHC, and perturbative unitarity of scattering amplitudes. Then, also projections for future colliders will be provided. The focus of this work is in particular on a heavy dilaton above about 300 GeV (see ref. [296] for a detailed recent examination of constraints on the dilaton in the low-mass window) where diboson searches push the dilaton to large masses and weak couplings. However, a vector dark

matter candidate is produced much more copiously at the LHC than a fermion candidate, assuming the same parameter values, and thus this model is more promising for future searches. Due to the low production rate of scalars, they are not be considered in this work.

This chapter illustrates the construction of the model as an extension of the SM, motivated by scale invariance and the introduction of dark matter. It is organised as follows: Section 3.1 explains scale transformations and a procedure to compose a scale invariant theory by systematically incorporating the dilaton field into a generic Lagrangian. In section 3.2, the form of the dilaton potential will be worked out. Then, in section 3.3, the concepts of the previous sections are applied to explicitly construct the Lagrangian of the model, which will thereafter be studied in detail. The possibilities of the dilaton to mix with the SM Higgs boson and the consequences on the interactions in the mass eigenbasis will be discussed in section 3.4. Section 3.5 explains the choice of the dark matter candidates as well as discrete symmetries of the dark matter Lagrangian, and compares the Higgs and dilaton portals to dark matter.

Perturbative unitarity bounds, experimental constraints and future collider prospects for the model will be presented in the next chapter. The work presented in this and the following chapter has been published in [301].

3.1 Constructing a scale-invariant theory

This section illustrates the underlying principles to derive from some existing model Lagrangian a new model in a way that is guided by the ambition to establish scale-invariance. First, the form of scale transformations (*dilatations*) and their implications on the Lagrangian as well as conditions on the Lagrangian for scale invariance are reviewed. It is then shown that the Lagrangian can be turned into a formally scale-invariant one with the help of an additional field. In the next step, the resulting expression is expanded in the new field, giving rise to an effective Lagrangian suitable for perturbative calculations. Finally, additional self-interaction terms are discussed. This section is based to a large extent on the explanations and equations from ref. [302].

3.1.1 Scale transformations

The starting point for the following considerations is a generic Lagrangian, written in terms of operators $\mathcal{O}_i$ with corresponding couplings g_i which depend on the renormalisation scale μ:

$$\mathcal{L}_0 = \sum_i g_i(\mu)\mathcal{O}_i(x)\,. \tag{3.1.1}$$

The classical scaling dimensions of the operators will be denoted as $[\mathcal{O}_i] = d_i$. The effect of dilatations on this Lagrangian follows from the transformation prescriptions

$$\begin{aligned} x^\mu &\to e^\lambda x^\mu\,, \\ \mathcal{O}_i(x) &\to e^{\lambda d_i}\,\mathcal{O}_i(e^\lambda x)\,, \\ \mu &\to e^{-\lambda}\mu\,, \end{aligned} \tag{3.1.2}$$

where λ is the transformation parameter of this continuous transformation. Following the usual procedure, i.e. taking this parameter to be small and expanding to first order, the transformations are

$$\begin{aligned} x^\mu &\to (1+\lambda)x^\mu\,, \\ \mathcal{O}_i(x) &\to (1+\lambda d_i)\mathcal{O}_i(x) + \lambda x^\mu \partial_\mu \mathcal{O}_i(x)\,, \\ \mu &\to (1-\lambda)\mu\,, \end{aligned} \tag{3.1.3}$$

and the variation of the Lagrangian reads

$$\delta\mathcal{L}_0 = \lambda \sum_i \left[g_i(\mu)(d_i \mathcal{O}_i(x) + x^\mu \partial_\mu \mathcal{O}_i(x)) - \mu \frac{\partial g_i}{\partial \mu} \mathcal{O}_i(x) \right] . \tag{3.1.4}$$

The second term of this expression can be partially integrated, which generates a total space-time derivative term. The last term describes the variation of the Lagrangian due to the renormalisation scale dependence of the couplings, which is governed by their beta functions $\mu \frac{\partial g_i}{\partial \mu} \equiv \beta(g_i)$, and the variation $\delta\mathcal{L}_0$ can thus be written as

$$\delta\mathcal{L}_0 = \lambda \sum_i \left[(d_i - 4) g_i(\mu) - \beta(g_i) \right] \mathcal{O}_i(x) + \lambda \partial_\mu \left(x^\mu \mathcal{L}_0 \right) . \tag{3.1.5}$$

One can see that, in order for the Lagrangian $\mathcal{L}_0$ to describe a scale invariant theory, which is realised when $\delta\mathcal{L}_0$ is a total space-time derivative, the classical scaling dimensions of all operators must be equal to four and the couplings independent of the renormalisation scale μ. Under this condition, the divergence of the associated *scale current* (or *dilatation current*) S^μ vanishes, so the current is conserved. It is related to the symmetric [1] energy-momentum tensor via $S^\mu = T^\mu{}_\nu x^\nu$ and its divergence reads

$$\partial_\mu S^\mu = T^\mu{}_\mu = \sum_i \left[(d_i - 4) g_i(\mu) - \beta(g_i) \right] \mathcal{O}_i(x)\,. \tag{3.1.6}$$

3.1.2 Restoring scale invariance

Given a Lagrangian as the one in eq. (3.1.1) that is not scale-invariant, i.e. the variation $\delta\mathcal{L}$ under the above dilation is non-vanishing, it is possible to modify the Lagrangian in a way that recovers scale-invariance. This requires the introduction of a *conformal compensator field*, an additional real scalar field $\chi(x)$ that transforms itself under scale transformations,

$$\chi(x) \to e^\lambda \chi(e^\lambda x)\,. \tag{3.1.7}$$

Incorporating this field systematically into the Lagrangian allows it to compensate for the terms which appear in the variation of the original Lagrangian, making it formally

1. The energy-momentum tensor involved in the scale current differs from the *canonical* energy-momentum tensor by an extra term which makes it *symmetric*. This symmetric version remains conserved if this is the case for the canonical version, and the additional term does not affect the global momentum four-vector

$$P^\mu = \int \mathrm{d}^3x\, T^{0\mu}\,.$$

For more information, I refer the interested reader to [46, ch. 19.5] and [303].

scale invariant. This is achieved by the replacement of the couplings g_i according to the prescription

$$g_i(\mu) \quad \to \quad g_i\left(\mu\frac{\chi(x)}{f}\right)\left(\frac{\chi(x)}{f}\right)^{4-d_i}\,, \tag{3.1.8}$$

i.e. the field χ not only appears to some convenient power as a new factor in each term, but also in the dependence of the couplings g_i on the renormalisation scale μ. With this replacement, the new Lagrangian takes the form

$$\mathcal{L} = \sum_i g_i\left(\mu\frac{\chi(x)}{f}\right)\left(\frac{\chi(x)}{f}\right)^{4-d_i}\mathcal{O}_i(x)\,. \tag{3.1.9}$$

Carrying out the same program, i.e. applying the scale transformation to the new Lagrangian, it is straightforward to check that the variation $\delta\mathcal{L}$ is indeed vanishing:

$$\begin{aligned}\mathcal{L} \quad \to \quad & \sum_i g_i\left(e^{-\lambda}\mu\frac{e^\lambda\chi(e^\lambda x)}{f}\right)\left(\frac{e^\lambda\chi(e^\lambda x)}{f}\right)^{4-d_i} e^{\lambda d_i}\mathcal{O}_i(x) \\ = & \sum_i e^{4\lambda} g_i\left(\mu\frac{\chi(e^\lambda x)}{f}\right)\left(\frac{\chi(e^\lambda x)}{f}\right)^{4-d_i}\mathcal{O}_i(e^\lambda x)\,.\end{aligned} \tag{3.1.10}$$

In summary, the transformation contributes a global factor $e^{4\lambda}$ and substitutes x^μ by $e^\lambda x^\mu$. Therefore, to first order in the transformation parameter λ, these two types of modification can be written as two separate terms:

$$\delta\mathcal{L}(x) = 4\lambda\mathcal{L}(x) + \lambda x^\mu\partial_\mu\mathcal{L}(x)\,. \tag{3.1.11}$$

After partial integration, using $\partial_\mu x^\mu = 4$, one obtains

$$\begin{aligned}\delta\mathcal{L}(x) &= 4\lambda\mathcal{L}(x) + \lambda\partial_\mu(x^\mu\mathcal{L}(x)) - \lambda(\partial_\mu x^\mu)\mathcal{L}(x) \\ &= \lambda\partial_\mu(x^\mu\mathcal{L}(x))\,,\end{aligned} \tag{3.1.12}$$

which is a total space-time derivative that leaves the action integral invariant. Therefore, one can conclude that the modified Lagrangian is symmetric under the above dilatations.

3.1.3 Dilaton interaction terms

It has been shown how a Lagrangian has to be modified to turn it into a new, *formally* scale invariant Lagrangian. On the one hand, terms with dimensionful couplings are multiplied with some power of $\chi(x)/f$, which then together form an operator of classical scaling dimension 4, that consequently appears with a dimensionless coupling. On the other hand, also the scale-dependence of the couplings g_i is modified through the introduction of a factor $\chi(x)/f$ to compensate for the variation of the renormalisation scale μ under scale transformations.

Along with the additional field χ, these changes also introduce a new parameter, the cut-off scale $f = \langle\chi\rangle$, which is an artefact of the spontaneous breaking of scale symmetry, i.e. the vacuum expectation value of χ. A possible parameterisation of χ involving the associated Goldstone boson σ, namely the *dilaton* field, is given by

$$\chi(x) = f e^{\sigma(x)/f}\,. \tag{3.1.13}$$

This is clearly a sensible expansion around f, as the value of $\chi(x)$ for vanishing $\sigma(x)$ is f. However, since the aim is to expand the Lagrangian in σ/f, a different parameterisation is instead chosen, where the relation between χ and σ is given by

$$\chi(x) = f + \sigma(x)\,. \tag{3.1.14}$$

With this parameterisation, the expansion in σ/f takes the form:

$$\begin{aligned}\mathcal{L} &= \sum_i g_i \left(\mu\left(1+\frac{\sigma(x)}{f}\right)\right)\left(1+\frac{\sigma(x)}{f}\right)^{4-d_i}\mathcal{O}_i(x)\\ &= \mathcal{L}_0 - \frac{\sigma(x)}{f}\sum_i\left[(d_i-4)g_i(\mu)\mathcal{O}_i(x) - \beta(g_i)\mathcal{O}_i(x)\right]\\ &\quad + \frac{\sigma(x)^2}{2f^2}\sum_i\left[(4-d_i)(3-d_i)g_i(\mu)\mathcal{O}_i(x)\right]\\ &\quad + \dots\,.\end{aligned} \tag{3.1.15}$$

Here, only the leading terms in σ/f are shown explicitly, and the ellipsis stands for any (potentially relevant) higher-order contributions. In comparison with eq. (3.1.6) one can easily see that at leading order the dilaton couples to the trace of the symmetric energy-momentum tensor.

While the chosen parameterisation should not impact the physics, the form of the expanded Lagrangian at a given order in σ/f depends on this choice. Note that in the limit of very high values of f, i.e. $\sigma/f \ll 1$, the higher order terms become negligible, so that eq. (3.1.13) coincides with eq. (3.1.14). This also explains, why the expansion of $\mathcal{L}$ is identical at first order in σ/f. The advantage of the chosen parameterisation is that for appropriate values of d_i, the term $\chi^{4-d_i} = (1+\sigma/f)^{4-d_i}$ is just a polynomial, corresponding to a finite number of terms, in which case only the couplings g_i need to be expanded explicitly.

3.2 Dilaton self-interactions

In the interaction terms considered so far, in which the dilaton is involved, it only couples to the fields of the original Lagrangian. For the purpose of establishing scale-invariance in a given model, this might seem sufficient. However, apart from these terms, a kinetic and a mass term for the dilaton should also be present, as well as its potential self-interaction terms.

This model includes a dilation potential that is constructed under the assumption that the conformally-invariant field theory, for which this model represents an effective theory, is explicitly broken due to the addition of an operator with a scaling dimension $\Delta_\mathcal{O} \neq 4$ [290],

$$\mathcal{L}^{\text{CFT}}_{\text{breaking}} = \lambda_\mathcal{O}\mathcal{O}(x)\,. \tag{3.2.1}$$

This yields a potential $V(\chi)$ [286, 290],

$$V(\chi) = \chi^4 \sum_{n=0}^{\infty} c_n(\Delta_\mathcal{O})\left(\frac{\chi}{f}\right)^{n(\Delta_\mathcal{O}-4)}\,, \tag{3.2.2}$$

that will be added to the effective Lagrangian. At the minimum of the potential at which $\langle\chi\rangle = f$, the coefficients c_n can be related to the parameters of the underlying conformal field theory [2]. This potential is supposed to be at the origin of the dilaton mass m_σ, which translates into the condition

$$m_\sigma^2 = \left.\frac{\mathrm{d}^2 V(\chi)}{\mathrm{d}\chi^2}\right|_{\langle\chi\rangle=f} > 0\,. \tag{3.2.3}$$

With the assumption that $|\Delta_\mathcal{O} - 4| \ll 1$, i.e. the operator $\mathcal{O}$ in eq. (3.2.1) is nearly marginal, it is possible to expand the potential in $|\Delta_\mathcal{O} - 4|$ such that the explicit $\Delta_\mathcal{O}$-dependence of the different coefficients c_n disappears [290],

$$V(\chi) = \frac{1}{16}\frac{m^2}{f^2}\chi^4\left[4\ln\frac{\chi}{f} - 1\right] + \mathcal{O}(|\Delta_\mathcal{O} - 4|^2)\,. \tag{3.2.4}$$

A derivation of this expression is given in appendix C. By applying the parameterisation of eq. (3.1.14), one obtains, after adding the dilaton kinetic term [298],

$$\mathcal{L}_\sigma^{\text{self}} = \frac{1}{2}\partial_\mu\sigma\partial^\mu\sigma - \frac{m_\sigma^2}{2}\sigma^2 - \frac{5}{6}\frac{m_\sigma^2}{f}\sigma^3 - \frac{11}{24}\frac{m_\sigma^2}{f^2}\sigma^4 + \dots\,, \tag{3.2.5}$$

where the dots stand for higher-dimensional interactions.

3.3 Extending the Standard Model with the dilaton and dark matter

The effective theory studied in the following is constructed from the SM Lagrangian and the mass term of a dark matter candidate, either a Majorana fermion or a vector boson, using eq. (3.1.15) to derive the interactions of the dilaton with the remaining field content. This also establishes interactions between the SM and dark matter, with the dilaton as mediator.

As pointed out earlier, the interactions resulting from dimensionful couplings are obtained via the multiplication of the terms by $(1 + \sigma/f)^{4-d_i}$, with d_i being the classical scaling dimension of the operator involved in the term. For instance, the mass terms of the fermions and electroweak gauge bosons, induce the following interaction terms:

$$\begin{aligned}
-m_f\bar{\psi}_f\psi_f \quad &\to \quad -m_f\bar{\psi}_f\psi_f\frac{\sigma}{f}\,,\\
m_W^2 W_\mu^+ W^{-\mu} \quad &\to \quad m_W^2 W_\mu^+ W^{-\mu}\left(2\frac{\sigma}{f} + \frac{\sigma^2}{f^2}\right)\,,\\
\frac{1}{2}m_Z^2 Z_\mu Z^\mu \quad &\to \quad \frac{1}{2}m_Z^2 Z_\mu Z^\mu\left(2\frac{\sigma}{f} + \frac{\sigma^2}{f^2}\right)\,.
\end{aligned} \tag{3.3.1}$$

The couplings involving the dark matter candidates are found analogously (see below).

2. Note that the exact details of the underlying theory is beyond the scope of this work, which follows an effective theory approach.

The simplest way to obtain the interactions related to the beta-functions of the electromagnetic and strong couplings e and g_s is through a rescaling of the gauge fields, e.g. $A^\mu \to \frac{1}{e}A^\mu$ for the photon field, such that e is only present in the photon kinetic term [46, ch. 19.5]:

$$\mathcal{L} \supset -\frac{1}{4e^2}F_{\mu\nu}F^{\mu\nu}\,. \tag{3.3.2}$$

Once the related dilaton interaction term has been found, the rescaling of A^μ is reversed.

Considering the broken electroweak phase, the interaction terms of the dilaton with the SM sector are given, including all the Lagrangian terms of dimension 6 or below, by

$$\begin{aligned}\mathcal{L}_\sigma =& \frac{\sigma}{f}\Big[2m_W^2 W_\mu^+ W^{-\mu} + m_Z^2 Z_\mu Z^\mu - m_h^2 h^2 - \sum_\psi m_\psi \overline{\psi}\psi \\ &- \frac{m_h^2}{2v}\Big[h^3 + hG^0G^0 + 2hG^+G^-\Big] \\ &+ \frac{gv}{2}\Big[\partial^\mu G^- W_\mu^+ + \partial^\mu G^+ W_\mu^- + \frac{1}{c_W}\partial^\mu G^0 Z_\mu\Big] \\ &+ g m_W h W_\mu^+ W^{\mu-} + \frac{g}{2c_W} m_Z h Z_\mu Z^\mu \\ &+ i g' m_W (G^- W_\mu^+ - G^+ W_\mu^-)(c_W A^\mu - s_W Z^\mu) \\ &+ \frac{11\alpha_{\mathrm{EM}}}{24\pi}F_{\mu\nu}F^{\mu\nu} - \frac{7\alpha_s}{8\pi}G^a_{\mu\nu}G^{a,\mu\nu}\Big] \\ &+ \frac{\sigma^2}{2f^2}\Big[2m_W^2 W_\mu^+ W^{-\mu} + m_Z^2 Z_\mu Z^\mu - m_h^2 h^2\Big]\,,\end{aligned} \tag{3.3.3}$$

where the summation over ψ refers to all the SM fermionic mass-eigenstates of mass m_ψ, and m_h, m_W and m_Z stand for the Higgs boson, W-boson and Z-boson masses. Moreover, v denotes the vacuum expectation value of the Standard Model Higgs field, c_W and s_W the cosine and sine of the electroweak mixing angle, and g, g' and g_s the weak, hypercharge and strong coupling constants. These expressions include the interactions between the physical Higgs (h) and electroweak (A_μ, W_μ, Z_μ) bosons and the three Goldstone bosons (G^0, $G^\pm$). For the corresponding expression in the unbroken electroweak phase, I refer to ref. [297] that additionally includes a complete Higgs-dilaton mixing analysis.

The interactions of the dilaton with the two considered dark matter candidates, namely a Majorana fermion Ψ_X and a real vector field X_μ, read

$$\mathcal{L}_\sigma^{\mathrm{DM}} = \begin{cases} -\frac{\sigma}{2f} m_\Psi \overline{\Psi}_X \Psi_X & \text{(Majorana fermion)}\,, \\ \left(\frac{\sigma}{f} + \frac{\sigma^2}{2f^2}\right) m_V^2 X_\mu X^\mu & \text{(vector boson)}\,, \end{cases} \tag{3.3.4}$$

where m_Ψ and m_V denote the mass of the dark matter state in the fermion and vector case respectively. In order to ensure the stability of the dark matter particle, the setup assumes a $\mathbb{Z}_2$ symmetry.

3.4 Higgs-Dilaton mixing

When two physical neutral scalars are present in the theory (the Higgs field h and the dilaton field σ), they could in principle mix, unless it is forbidden by some symmetry. If

the mixing is allowed, its origins can be found through a UV completion of the effective setup. This option was first studied in ref. [299], and will be re-investigated in the light of the most recent experimental data in section 4.2.

Keeping in mind the effective approach adopted in this work, no assumption will be made about any UV-physics that drives the source, and hence the amount, of mixing. Instead, for studying the possibility of a non-vanishing Higgs-dilaton mixing, a mixing angle α will be introduced as an additional parameter. The original flavour states will be *relabelled* as h_0, σ_0 with mass parameters $m_{h,0}, m_{\sigma,0}$ and are related to the new mass eigenstates h, σ via the rotation

$$\begin{pmatrix} h \\ \sigma \end{pmatrix} = \begin{pmatrix} \cos\alpha & \sin\alpha \\ -\sin\alpha & \cos\alpha \end{pmatrix} \begin{pmatrix} h_0 \\ \sigma_0 \end{pmatrix} \equiv \begin{pmatrix} c_\alpha & s_\alpha \\ -s_\alpha & c_\alpha \end{pmatrix} \begin{pmatrix} h_0 \\ \sigma_0 \end{pmatrix} . \tag{3.4.1}$$

Then, it will be assumed that the (lighter, by assumption) scalar h can be identified as the experimentally confirmed scalar of mass of about 125 GeV, so that it is mostly compatible with the SM Higgs boson. In contrast, the heavier scalar field σ is mostly dilaton-like.

The impact of the non-zero mixing of the Higgs boson and the dilaton can be inferred from the similarity between the couplings of the h_0 and σ_0 states with the remaining particle content in the zero-mixing case. Without mixing and in unitary gauge (i.e. ignoring Goldstone bosons), there is a corresponding dilaton coupling for every Higgs boson coupling. This is not surprising since these dilaton couplings originate from the presence of a dimensionful coupling in the SM Lagrangian after electroweak symmetry breaking, where the dimensionful quantity in the coupling constants is actually the Higgs vacuum expectation value v. In all of these cases, the coupling constants appearing in the dilaton interaction vertices therefore differ by a factor of $r_f = v/f$ for each dilaton participating in the interaction, when compared with the corresponding Higgs-boson interaction. In principle, dilaton couplings involving the Higgs or Goldstone bosons (leaving the unitary gauge) should be discussed as well, but they cannot be related to any SM counterpart by factors of v/f. The discussion below will address those multi-scalar interactions.

For the dilaton and Higgs Yukawa couplings to the SM fermions, this yields the interaction Lagrangian $\mathcal{L}_\sigma^\psi$,

$$\begin{aligned} \mathcal{L}_\sigma^\psi &= \sum_\psi \frac{m_\psi}{v} \Big(h_0 + r_f \sigma_0\Big) \overline{\psi}\psi \\ &= \sum_\psi \frac{m_\psi}{v} \Big[(c_\alpha + r_f s_\alpha) h + (r_f c_\alpha - s_\alpha)\sigma\Big] \, \overline{\psi}\psi \, . \end{aligned} \tag{3.4.2}$$

Similarly, the massive gauge boson interactions read, at leading order in the scalar fields,

$$\mathcal{L}_\sigma^V = \Big[(c_\alpha + r_f s_\alpha) h + (r_f c_\alpha - s_\alpha)\sigma\Big] \times \left(\frac{2m_W^2}{v} W_\mu^+ W^{-\mu} + \frac{m_Z^2}{v} Z_\mu Z^\mu \right) . \tag{3.4.3}$$

The W- and Z-boson couplings to a pair of scalar fields h and/or σ are obtained analogously.

These couplings are potentially relevant for processes addressing both scalar production and decays. For example, in scalar production at hadron colliders through gluon fusion, the leading-order contribution involves triangle diagrams featuring a loop of quarks (the

top quark one being the most relevant by virtue of its largest mass), so that the associated predictions are affected by the modifications of eq. (3.4.2). In case of the light scalar, a factor of $(c_\alpha + r_f s_\alpha)$ is introduced into the amplitude compared to the zero-mixing case. On the contrary, for the production of the heavy scalar, the extra factor is given by $(-s_\alpha + r_f c_\alpha)$. This feature is obviously also present for any other production mode at colliders, like associated production (Vh or $V\sigma$) or vector-boson fusion, that involve the coupling of the scalar to the W- and Z-bosons.

On the other hand, the dark matter mass term is at the origin of a dilaton coupling which obviously does not have an analogue for the Higgs boson due to the absence of the dark matter in the SM and of a Higgs portal relating the dark and the visible sector. Depending on the type of dark matter, the Lagrangian in terms of the scalars h and σ gives

$$\mathcal{L}_\sigma^{\mathrm{DM}} = -\frac{m_\Psi}{2f} s_\alpha h \overline{\Psi}_X \Psi_X - \frac{m_\Psi}{2f} c_\alpha \sigma \overline{\Psi}_X \Psi_X \tag{3.4.4}$$

in the Majorana case and

$$\mathcal{L}_\sigma^{\mathrm{DM}} = \frac{m_V^2}{f}(s_\alpha h + c_\alpha \sigma) X_\mu X^\mu + \frac{m_V^2}{2f^2}(s_\alpha h + c_\alpha \sigma)^2 X_\mu X^\mu \tag{3.4.5}$$

in the vector case. In the latter case, the trilinear couplings are the most relevant ones for Higgs measurements and heavy scalar searches, but the quartic couplings are very important for dark matter searches when $m_V \gg m_\sigma$. Consequently, mixing leads to a coupling of the SM-like Higgs state to the dark-matter candidate that would not exist without mixing.

The same applies to the tree-level couplings of the dilaton to the massless gauge-bosons, which are not induced by dimensionful couplings but by the scale-dependence of the electromagnetic and the strong coupling. Here the contribution to the Lagrangian in the mass eigenbasis $\mathcal{L}_{VVS}$ reads

$$\begin{aligned} \mathcal{L}_{VVS} = &\frac{11\alpha_{\mathrm{EM}}}{24\pi v}\Big(r_f s_\alpha h + r_f c_\alpha \sigma\Big)\, F_{\mu\nu}F^{\mu\nu} \\ &- \frac{7\alpha_s}{8\pi v}\Big(r_f s_\alpha h + r_f c_\alpha \sigma\Big)\, G^a_{\mu\nu} G_a^{\mu\nu}\,. \end{aligned} \tag{3.4.6}$$

Without mixing, the dilaton coupling to photons or gluons must take into account both a tree-level and a one-loop contribution at leading order in the electromagnetic or strong coupling, while the Higgs boson interacts with these bosons only beyond tree-level. Eq. (3.4.6) shows that in the mixing case, the tree level contributions enter into the amplitudes for *both* the light and the heavy scalar with a factor of $\sin\alpha$ or $\cos\alpha$ respectively.

Furthermore, there are also couplings which involve some combination of the two scalars. These result from the Higgs and the dilaton potentials, where couplings between the two scalars h and σ are only present when the mixing is non-zero. On the other hand, the dimensionful couplings of the Higgs potential also give rise to interaction terms involving both the dilaton and the Higgs boson, which are present even in the zero-mixing case. These trilinear couplings are phenomenologically very important, because they allow the dilaton to decay into a pair of Higgs bosons. Unfortunately, they are *not uniquely defined* within this model. Starting from the Lagrangian introduced in the previous subsection,

the cubic couplings come from the terms

$$\mathcal{L}_{\phi^3} = -\frac{1}{2v}m_{h,0}^2 h_0^3 - \xi\frac{m_{\sigma,0}^2}{f}\sigma_0^3 - \frac{m_{h_0}^2}{f}h_0^2\sigma_0\,. \tag{3.4.7}$$

Here ξ is a model-dependent dilaton self-coupling, that has been fixed to 5/6 in eq. (3.2.5). The trilinear couplings between the two mass eigenstates are then found by substituting, in the above equation, the mixing relation of eq. (3.4.1).

Note that the parameter $m_{h,0} \equiv \sqrt{2\lambda_{SM}v^2}$ is *not* equal to the mass of the lightest scalar. The physical masses are instead determined by the diagonalisation of the dilaton-Higgs mass matrix extracted from the bilinear terms of the scalar potential,

$$\mathcal{L}_{\phi^2} = -\frac{1}{2}m_{h,0}^2 h_0^2 - \frac{1}{2}m_{\sigma,0}^2\sigma_0^2 - m_{h\sigma}^2 h_0\sigma_0\,, \tag{3.4.8}$$

where

$$\begin{aligned} m_{h,0}^2 &= m_h^2 c_\alpha^2 + m_\sigma^2 s_\alpha^2\,, \quad m_{\sigma,0}^2 = m_h^2 s_\alpha^2 + m_\sigma^2 c_\alpha^2\,, \\ m_{h\sigma}^2 &= -c_\alpha s_\alpha (m_\sigma^2 - m_h^2)\,. \end{aligned} \tag{3.4.9}$$

Note also that in the work of ref. [299] the parameter $m_{h\sigma}^2$ is not explicitly discussed. However, it is clear that if it is present, then the full Lagrangian of the theory cannot be written in a gauge-invariant way: one has to give up precision calculations for the model and it is harder to make a connection with a UV-completion. On the other hand, in order to write the lowest-dimension effective operator which can yield such a mass and preserve the gauge symmetry, the SM degrees of freedom must be written in terms of a doublet $H \supset H^0 = \frac{1}{\sqrt{2}}[(v + h_0) + iG^0]$, and it follows that the physics that generates a dilaton mass should also generate a new coupling

$$\mathcal{L} \supset -\frac{m_{h\sigma}^2}{v}\sigma|H|^2 \supset -m_{h\sigma}^2 h_0\sigma_0 - \frac{1}{2}\frac{m_{h\sigma}^2}{v}h_0^2\sigma_0\,. \tag{3.4.10}$$

This new trilinear coupling has dramatic consequences for the phenomenology: it allows for unsuppressed decays of the dilaton into two Higgs bosons. Therefore, both scenarios will be investigated: the "minimal mixing scenario" of eq. (3.4.8) and the "gauge invariant mixing scenario" of eq. (3.4.10).

3.5 Fermionic and vector dark matter through the dilaton portal

The dilaton portal is particularly interesting and simple for dark matter models because the dark matter coupling is unique (being determined only by the dark matter mass). The most commonly considered and perhaps simplest dark matter candidate in a dilaton portal model is a Majorana fermion Ψ or a real scalar S, with a $\mathbb{Z}_2$ symmetry. Note that in ref. [299] a *Dirac* fermion was considered, which has instead a continuous unbroken global $U(1)$ symmetry (although this was not explicitly stated). The phenomenology is however very similar up to some factors of 2.

There is little to add to the analysis of dark matter constraints performed in this earlier work (and for the case of zero mixing, in the works of ref. [291, 297, 298]). However, to give an update on those results, limits from recent monojet and multijet searches in the fermionic case are provided in section 4.3.1, as well as projections for a future 100 TeV collider in section 4.4.

A vector boson as the dark matter particle has attracted some interest as an alternative to the more common fermion or scalar candidates. The particular challenge for the vector case is to allow it to remain stable; a $\mathbb{Z}_2$ symmetry forbids conventional gauge interactions. This can either be accepted [291, 304–307], or one can stabilise the vector through another symmetry such as a custodial one [308]. Here the minimal model, which can arise from a Stückelberg $U(1)$ field coupled to the dilaton, shall be considered. This automatically features a $\mathbb{Z}_2$ symmetry provided there is no matter charged under it; and the symmetry also forbids any kinetic mixing term involving the dark vector field, through which it could decay.

Since the dilaton must be rather heavy and couples to all the SM particles including the Higgs boson, it could be considered as generating effective Higgs portal interactions. Indeed, integrating it out generates the effective Lagrangian $\mathcal{L}_{\text{eff}}$,

$$\begin{aligned}\mathcal{L}_{\text{eff}} = \frac{1}{2f^2 m_\sigma^2}\Big[\sum_\psi m_\psi \overline{\psi}\psi - m_V^2 X_\mu X^\mu - m_Z^2 Z_\mu Z^\mu \\ - 2m_W^2 W_\mu^+ W^{-\mu} + m_h^2 h^2\Big]^2 ,\end{aligned} \tag{3.5.1}$$

after neglecting any higher-dimensional operators. This can be compared with the standard Higgs-portal Lagrangian for vector dark matter $\mathcal{L}_{\text{VHPDM}}$ (which has become a popular benchmark scenario) [306, 307],

$$\mathcal{L}_{\text{VHPDM}} = \frac{\lambda_{hv}}{8} h^2 X_\mu X^\mu + \frac{1}{2} m_V^2 X_\mu X^\mu + \frac{\lambda}{4}(X_\mu X^\mu)^2 , \tag{3.5.2}$$

that exhibits the same classes of terms. These types of vector dark matter effective Lagrangians including a mass term generated by the Stückelberg mechanism exhibit a violation of unitarity, in particular at high energy colliders and even for the standard Higgs portal. The Higgs invisible decay width hence diverges when $m_V \to 0$. One simple way to cure these problems consists of introducing a Higgs mechanism in the dark sector [309]. Then, the Higgs invisible decay width becomes finite [310] and unitarity is restored [311–313]. In the following, this complication will not arise.

In the dilaton case, the generic coefficients λ_{hv}, m_V and λ are expressed in terms of m_V and f. While in $\mathcal{L}_{\text{VHPDM}}$ the vector self-coupling λ is rather unimportant, $\mathcal{L}_{\text{eff}}$ instead features additional dimensionless quartic terms $(X_\mu X^\mu)(Z_\mu Z^\mu)$ and $(X_\mu X^\mu)(W_\mu^+ W^{-\mu})$ that are *crucial* for the phenomenology of the model. They indeed provide the principal annihilation channels for the dark matter. Therefore, there is no obvious reason why these couplings should be neglected in a generic vector dark matter effective field theory, and it could be worth reconsidering benchmark scenarios that omit them.

Another interesting feature of a vector coupling to the dilaton is that a heavy dilaton will *predominantly* decay into vectors. The partial width of the dilaton into dark matter

becomes

$$\Gamma(\sigma \to XX) = \frac{m_\sigma^3}{32\pi f^2}\left[1 - 4\frac{m_V^2}{m_\sigma^2} + 3\frac{m_V^4}{m_\sigma^4}\right]\sqrt{1 - \frac{4m_V^2}{m_\sigma^2}} \underset{m_\sigma \gg m_V}{\to} \frac{m_\sigma^3}{32\pi f^2}\,, \tag{3.5.3}$$

which is independent of the vector mass. By fully considering the decay channels into Z and W bosons, one finds that the total width of the dilaton can be well approximated by

$$\Gamma \underset{m_\sigma \gg m_V, m_Z}{\simeq} \frac{m_\sigma^3}{8\pi f^2}\,, \tag{3.5.4}$$

and the branching ratio of the dilaton into dark matter then becomes roughly 0.25. This is much larger than for the scalar or fermionic cases, where the dilaton branching ratio into dark matter tends to zero for small dark matter masses. Consequently, vector dark matter production at colliders could be potentially enhanced via a dilaton resonance.

This width also provides a limit on the size of the dilaton mass from the requirement that it be a narrow state. However, it turns out that this is actually a weaker constraint than perturbative unitarity of scattering amplitudes (c.f. section 4.1).

Chapter 4

Probing the viability of the dilaton-dark-matter model

In this chapter, the effective theory introduced in the previous chapter will be constrained in various different ways. First of all, in section 4.1, the issue of partial wave unitarity will be addressed. Section 4.2, is dedicated to the estimation of the constraints on the Higgs-dilaton mixing using results of Higgs and heavy scalar searches as well as electroweak precision measurements, and section 4.3 to the bounds that can be imposed from dark matter direct detection and LHC searches. Section 4.4 finally focuses on future collider prospects. Some concluding remarks about the study of this model and the different results are given in section 4.5.

4.1 Perturbative partial wave unitarity

Since the effective theory contains non-renormalisable operators, it must have a cutoff *comparable* to the scale f (up to factors of 2π). This should be manifest, even at tree level, as perturbative unitarity constraints on two-body scattering amplitudes. In particular, there are some couplings that could in principle be large compared to f since they come with additional massive factors – such as the masses of vector bosons, and particularly the dark matter (in the vector dark matter scenario). Therefore, the constraints have been calculated originating from imposing the unitarity of two-particle scattering when vector and dilaton fields are involved, as well as the one stemming from the scattering of gluons into heavy vectors via a dilaton exchange. The details are given in appendix D that also includes the derivation of useful approximate formulæ such as an upper bound on the dilaton mass from self-scattering in eq. (D.4) of

$$m_\sigma \lesssim 2f\,, \tag{4.1.1}$$

which gives $\Gamma_\sigma/m_\sigma \lesssim 1/2\pi$.

In particular, the scattering of gluons into vectors via a dilaton places a constraint on the *maximum scattering energy* permissible in this theory. This will be relevant for the LHC and future collider constraints; and also for all other unitarity constraints (which necessarily also involve choosing a scattering momentum).

As shown in appendix D.4, unitarity is violated if

$$s > \frac{8\pi^2 f^2}{7\alpha_s} \,. \tag{4.1.2}$$

In principle, when the process centre-of-mass energy s is above this value (30 TeV for $f = 3$ TeV), the cross section calculation in the theory is not reliable. However, in collider processes, it is of course not the centre-of-mass energy of the proton-proton collision that is relevant, but the partonic one $\hat{s}$. One has instead

$$\hat{s} \equiv x_1 x_2 s < \frac{8\pi^2 f^2}{7\alpha_s} \equiv \hat{s}_{\text{unitarity}} \,, \tag{4.1.3}$$

or equivalently

$$x_1 x_2 < 0.08 \left(\frac{f}{3 \text{ TeV}}\right)^2 \frac{(100 \text{ TeV})^2}{s} \,. \tag{4.1.4}$$

Here $x_{1,2}$ are the momentum fractions carried by the initial-state gluons, the relevant processes being induced by gluon fusion. So provided that the gluon parton distribution function (PDF) is negligible for $x_i > \mathcal{O}(10^{-1})$, calculations for a 100 TeV collider are safe for f greater than about 1 TeV. In the considered processes a single dilaton is resonantly produced. The relevant scale therefore consists of its mass m_σ, and taking into account the dilaton mass range investigated in this work, the typical gluon-gluon parton collision scale is $x_1 x_2 \sim 10^{-4} - 10^{-3}$. This therefore guarantees the suppression of any growth in the cross section coming from high-energy subprocesses.

On the other hand, the above constraint is very important when considering the unitarity of (vector) dark matter scattering. While it is typically convenient to take the high-energy limit for unitarity calculations to simplify matters and avoid resonances, it has become clear that this is not possible in this model. In particular, the scattering of dilaton pairs into longitudinal vectors exhibits (only) a logarithmic growth with energy, so that the cutoff of eq. (4.1.2) also reduces the power of other unitarity constraints. To be safe for $f = 2$ TeV one should take $\sqrt{s} < 20$ TeV and for $f = 1$ TeV one should take $\sqrt{s} < 10$ TeV.

Throughout the rest of the chapter, the above limit shall be used as a guide for fixing the *cutoff* on the theory. This only appears in the unitarity constraints, arising from massive vector/dilaton scattering, where all momentum values up to a maximum centre-of-mass momentum $p_{V,\text{max}}$ of the vector boson are scanned, with $p_V = \sqrt{s/4 - m_V^2}$. Since these other constraints grow logarithmically with $p_{V,\text{max}}$ this is both necessary (to give finite results) and conservative.

4.2 Constraints on the Higgs-dilaton mixing

In order to assess the viable regions of the model parameter space, experimental input is used from Higgs-boson measurements and heavy scalar searches, as well as constraints on the magnitude of the new physics contributions to the Peskin-Takeuchi parameters S and T [314].

For the Higgs and heavy scalar set of constraints, it is enforced that predictions for the signal strengths of various scattering processes (i.e. the ratio of total rates to their Standard Model counterparts) be consistent with observations (within uncertainties). In this context, it is assumed that the light or heavy scalar is resonantly produced. It is therefore allowed to factorise the scattering cross sections into the scalar production cross section times the branching ratio of the considered decay mode.

The Higgs and heavy scalar constraints are determined using LILITH-2.2.0 [257, 258] and HIGGSSIGNALS-2.4.0 [256] for the SM-like Higgs measurements, and HIGGSBOUNDS-5.5.0 [315] for the heavy scalar searches. The input for these codes is generated using a specially written main program for MICROMEGAS-5.0.8 [316, 317] using model files generated with FEYNRULES-2.3.36 [262]. The Higgs and heavy scalar search limits require the computation of ratios of scalar couplings to the ones of a SM-like Higgs particle of the same mass, both for the lighter (observed) state and the heavier one. These are estimated using a modified version of the routines embedded into HIGGSBOUNDS, that calculate tree-level scalar decays into quarks with their masses evaluated at a fixed running scale of 100 GeV, as well as quark-loop-induced couplings to photons and gluons (including some higher-order QCD factors) which are supplemented with the higher-order operators given by eq. (3.4.6). It has been verified that in the limit of small dilaton masses, the loop-induced operators exactly cancel against the dilatonic ones for the dilaton state, as they should.

The Peskin-Takeuchi parameters S, T and U [314] quantify the effects of new physics on the self-energies of the electroweak gauge bosons, which are referred to as *oblique corrections*. Writing the vacuum polarisation functions of the electroweak gauge bosons in the form [318]

$$\Pi_{ab}^{\mu\nu}(q) = \Pi_{ab}(q^2) g^{\mu\nu} + (q^\mu q^\nu \text{ terms}) \tag{4.2.1}$$

and splitting the $g^{\mu\nu}$ coefficient into a SM and a new physics contribution

$$\Pi_{ab}(q^2) = \Pi_{ab}^{\text{SM}}(q^2) + \delta\Pi_{ab}^{\text{NP}}(q^2)\,, \tag{4.2.2}$$

the three parameters are defined in terms of the latter as

$$T \equiv \frac{1}{\alpha(m_Z^2)} \left[\frac{\Pi_{WW}^{\text{NP}}(0)}{m_W^2} - \frac{\Pi_{ZZ}^{\text{NP}}(0)}{m_Z^2} \right], \tag{4.2.3}$$

$$S \equiv \frac{4s^2c^2}{\alpha(m_Z^2)} \left[\frac{\Pi_{ZZ}^{\text{NP}}(m_Z^2) - \Pi_{ZZ}^{\text{NP}}(0)}{m_Z^2} - \Pi_{\gamma\gamma}^{\prime\text{NP}}(0) - \left(\frac{c^2 - s^2}{cs} \right) \frac{\Pi_{Z\gamma}^{\text{NP}}(m_Z^2)}{m_Z^2} \right], \tag{4.2.4}$$

$$U \equiv \frac{4s^2}{\alpha(m_Z^2)} \left[\frac{\Pi_{WW}^{\text{NP}}(m_W^2) - \Pi_{WW}^{\text{NP}}(0)}{m_W^2} - \Pi_{\gamma\gamma}^{\prime\text{NP}}(0) - \left(\frac{c}{s} \right) \frac{\Pi_{Z\gamma}^{\text{NP}}(m_Z^2)}{m_Z^2} \right] - S\,, \tag{4.2.5}$$

with

$$\Pi_{\gamma\gamma}^{\prime\text{NP}}(0) = \left. \frac{\mathrm{d}\Pi_{\gamma\gamma}^{NP}}{\mathrm{d}q^2} \right|_{q^2=0}. \tag{4.2.6}$$

Here, c and s are the sine and cosine of the weak mixing angle θ_W, such that

$$c^2 = \frac{m_W^2}{m_Z^2}\,, \qquad s^2 = 1 - \frac{m_W^2}{m_Z^2}\,. \tag{4.2.7}$$

As pointed out in [314], in most models the predicted value of U is close to zero. Therefore, only S and T will be used to constrain the model. The formulæ can in principle also be evaluated with the SM contributions to the vacuum polarisation functions instead of just Π_{ab}^{NP}, but one is generally interested in the *deviation* from the Standard Model.

Predictions for the electroweak parameters S and T in the dilaton-dark-matter model are obtained by rescaling Standard Model results: For the calculation of the contributions from the h and σ scalars (δS and δT), the SM Higgs-boson contribution X_{SM} (for $X = S_H, T_H$, given below) is used, after replacing the Higgs-boson mass by the corresponding scalar mass and modifying the couplings as explained in section 3.4. This leads to [299]

$$\delta X = \left[(r_f s_\alpha + c_\alpha)^2 - 1\right] X_{\mathrm{SM}}(m_h) + (r_f c_\alpha - s_\alpha)^2 X_{\mathrm{SM}}(m_\sigma)\,. \tag{4.2.8}$$

The results are then compared with the experimental values extracted from the electroweak precision fits [4] according to formulæ taken from ref. [257]. According to ref. [319], the Standard Model Higgs contributions to S is given by

$$S_H = \frac{1}{\pi} H_S\left(\frac{m_h^2}{m_Z^2}\right) \tag{4.2.9}$$

with

$$H_S(x) = \frac{3}{8}x - \frac{1}{12}x^2 + \left(\frac{3-x}{4} + \frac{x^2}{24} + \frac{3}{4(1-x)}\right) x\ln(x) + \left(1 - \frac{x}{3} + \frac{x^2}{12}\right) B(x) \tag{4.2.10}$$

and

$$B(x) = \begin{cases} \sqrt{x(4-x)}\arctan\left(\sqrt{\frac{4}{x}-1}\right) & \text{for} \quad 0 < x < 4\,, \\ \sqrt{x(x-4)}\ln\left(\frac{2}{\sqrt{x}+\sqrt{x-4}}\right) & \text{for} \quad x > 4\,, \end{cases} \tag{4.2.11}$$

and the contribution to T is given by

$$T_H = \frac{G_F m_Z^2}{2\sqrt{2}\pi^2\alpha} H_T\left(\frac{m_H^2}{m_Z^2}\right) \tag{4.2.12}$$

with

$$H_T(x) = \frac{3}{4}x\left(\frac{\ln(x)}{1-x} - \frac{\ln(x/c^2)}{1-x/c^2}\right), \qquad c^2 \equiv \frac{m_W^2}{m_Z^2}\,. \tag{4.2.13}$$

4.2.1 Constraints from the light SM-like Higgs boson

Since a mass-mixing term between the dilaton and the SM-like Higgs scalar must violate the electroweak symmetry, it is natural to assume that this mixing should be small. However, in the absence of complete top-down constraints, all possible bottom-up values for the mixing angle α should be considered. The allowed amount of mixing, depending on the parameter f (or r_f), was examined in ref. [299] for heavy scalar masses of 200, 600 and 900 GeV with the Dirac dark matter mass being fixed to 300 GeV. While the bounds from heavy scalar searches obviously are strongly dependent on the mass of the heavy scalar (having a rather weak dependence on the dark matter mass with some provisos), the constraints on the light Higgs couplings are independent of both the dilaton and the dark

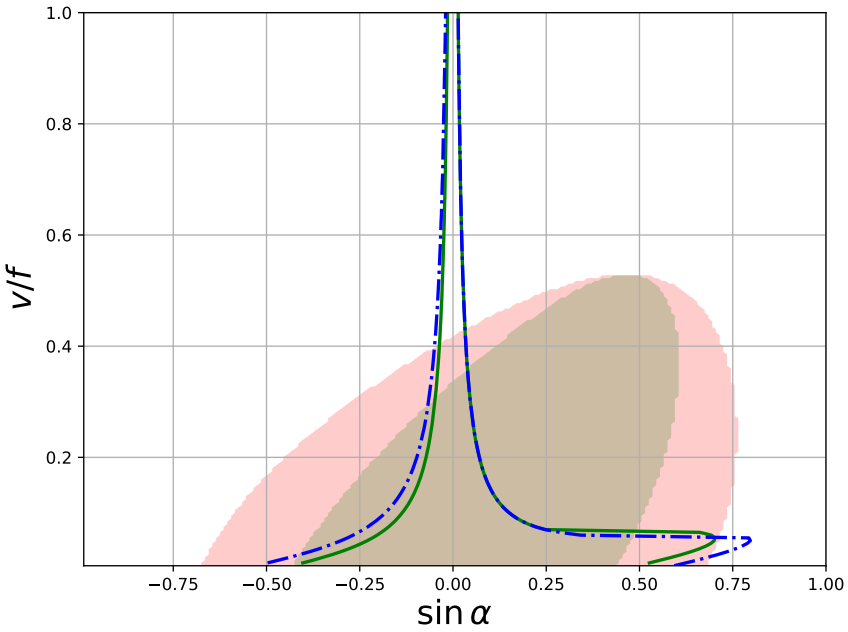

Figure 4.1: Constraints on the mixing angle between the Higgs and dilaton against the ratio $r_f = v/f$, computed using LILITH (solid green contour) and HIGGSSIGNALS (blue dot-dashed contour), where the allowed region is inside the contours. The figure also shows the allowed regions from constraints originating from the electroweak S and T parameters for dilaton masses of 3000 GeV (inner, light brown shaded region) and 500 GeV (outer, light red shaded region).

matter masses (provided that the dark matter is not lighter than half the Higgs-boson mass, opening up invisible decays). The constraints from the S and T parameters are also only relatively weakly dependent on the dilaton mass and have hence not drastically altered since 2014. The possible values are therefore restricted to $|\sin\alpha| \ll 1$ or $r_f \ll 1$ (or both), whereas the combination with electroweak precision measurements imposes an additional upper bound of approximately 0.4 for $|\sin\alpha|$ and r_f.

Figure 4.1 shows the preferred parameter space regions in the $(\sin\alpha, r_f)$ plane, after considering 99% exclusion bounds stemming from the most recent experimental input from Higgs measurements (as implemented in LILITH [258] and HIGGSSIGNALS [256]), as well as values for the S and T parameters extracted from the most up-to-date electroweak fits [4]. The dark matter mass has been chosen sufficiently high such that none of the scalars can decay invisibly, in order to obtain bounds on $\sin\alpha$ and r_f which are not influenced by dark matter. The bounds originating from the electroweak precision fit are presented for heavy scalar masses of 500 and 3000 GeV.

It is found that a large amount of mixing is still permitted by data. Larger mixing however modifies the constraints related to both heavy Higgs searches (see below) and the dark matter sector. For the latter, the effect is to more strongly couple the dark matter to the Higgs boson, which greatly strengthens constraints from direct detection since the Higgs couples much more strongly to light quarks than the dilaton does.

The results additionally allow for a comparison between the LILITH and HIGGSSIGNALS programs, the former requiring slightly more input (the decays needing to be specified) while the latter calculates the decay table based on coupling ratios. The results agree at an excellent level and do not substantially differ from older bounds [299].

4.2.2 Heavy scalar searches

Heavy scalar searches provide rather powerful complementary information, and indeed have been substantially strengthened during the second run of the LHC. These constitute some of the main new results of this work. Here the allowed parameter space for f and m_σ is probed for fixed mixing angles α. The results depend crucially on the treatment of the dilaton-Higgs mixing term, as described below.

The dilaton is considered to be heavy with a mass larger than 300 GeV. Throughout most of the parameter space the main constraint therefore comes from diboson searches since the dilaton predominantly decays to heavy vector bosons. However, there are two notable special cases.

The first is when the dilaton decay constant is not large compared to the dilaton mass. As seen before, the dilaton can become a wide resonance, for large m_σ. Even though unitarity constrains $\Gamma_\sigma/m_\sigma \lesssim 1/2\pi$, the width may be large enough that the standard narrow resonance searches do not apply. This issue shall be avoided by limiting the study of this model to the case of a narrow dilaton.

The second special case, as already pointed out in ref. [299], is when f and α fulfill the condition

$$(-s_\alpha + r_f c_\alpha) = 0 \quad \Leftrightarrow \quad r_f = \tan\alpha\,. \tag{4.2.14}$$

Here the couplings of the heavy scalar σ to fermions and heavy vector bosons in eqs. (3.4.2) and (3.4.3) vanish, *independently of* m_σ. This does not mean that the heavy scalar completely decouples from the Standard Model: the tree-level couplings to photons and especially gluons do not carry the factor $(-s_\alpha + r_f c_\alpha)$ and are therefore non-vanishing (although the contribution from fermion and vector loops vanishes). Moreover, since the dark matter particle does not obtain its mass from the Higgs mechanism, its coupling to the heavy scalar is also non-vanishing at this point. Therefore, in a 'magic window' around $r_f = \tan\alpha$ the most stringent constraints on the heavy scalar disappear, yet it can still be produced by gluon fusion and decay significantly to dark matter.

There are still constraints even exactly at this magic value, notably from diphoton and di-Higgs decays. The details depend crucially on the treatment of the mixing mass term, as described in section 3.4. If the minimal approach to the dilaton-Higgs mixing is taken, without introducing additional interactions, then for small values of the mixing angle the emergence of this 'magic window' can be observed. The width of this window in terms of values of f depends on the mixing and mass m_σ, and so does the *depth*: for sufficiently large mixing the window actually disappears. The appearance of a wide window at small $\sin\alpha = 0.04$ and large $f = 6$ TeV, and its eventual disappearance around $\sin\alpha = 0.13$ are illustrated in figure 4.2. At larger mixing angles, the constraints from the light Higgs measurements and the S/T parameters moreover dominate.

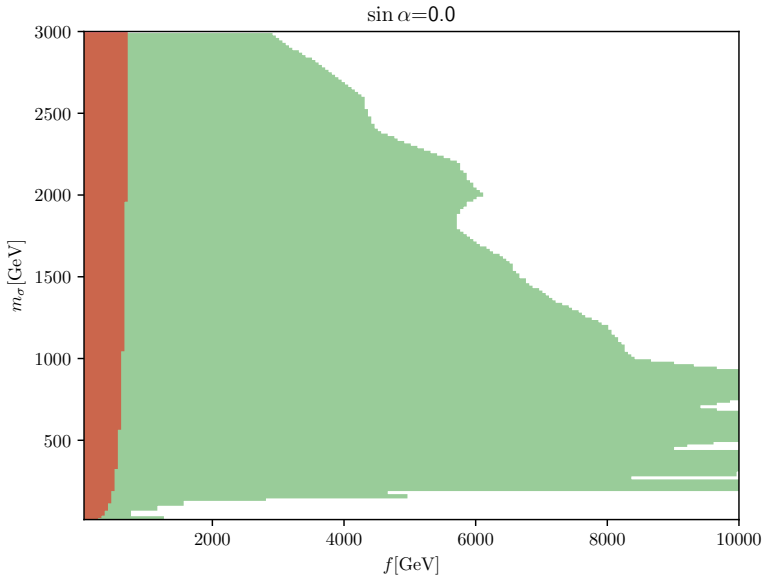

(a) Zero-mixing case

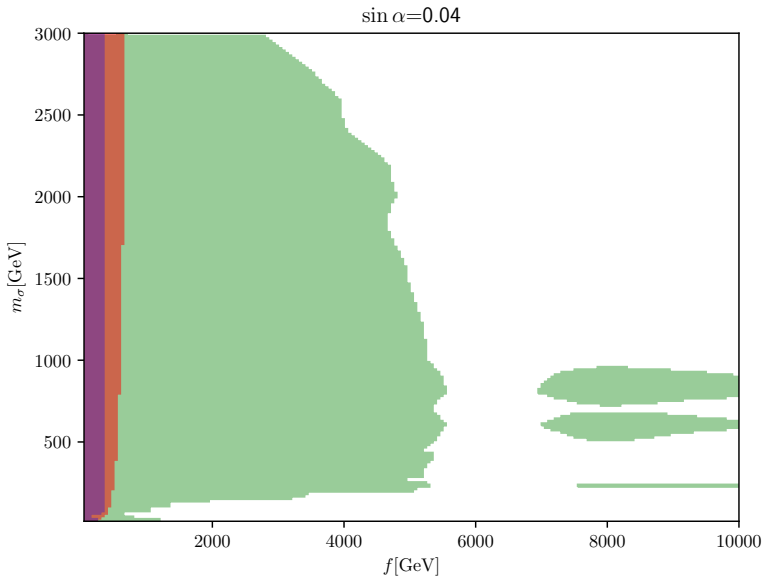

(b) Amount of Higgs-dilaton mixing: $\sin\alpha = 0.04$

Figure 4.2: Excluded regions of the model parameter space, presented in the (f, m_σ) plane for a selection of mixing angles, with the 'minimal mixing term' treatment of the Higgs-dilaton mixing. The figures include 99% confidence level exclusions from Higgs measurements (blue) and the electroweak S and T parameters (red/purple), as well as 95% confidence level bounds from heavy scalar searches (green). The parameter scans were done using Lilith and HiggsBounds. The findings demonstrate that for sufficiently low positive mixing angles, a gap in the exclusion emerges around the value f that satisfies $v/f = \tan\alpha$. In this gap, the couplings of the heavy scalar to the Standard Model fermions and massive gauge bosons are close or equal to zero, so that searches for heavy scalars turn out to be insensitive and arbitrary heavy scalar masses are allowed.

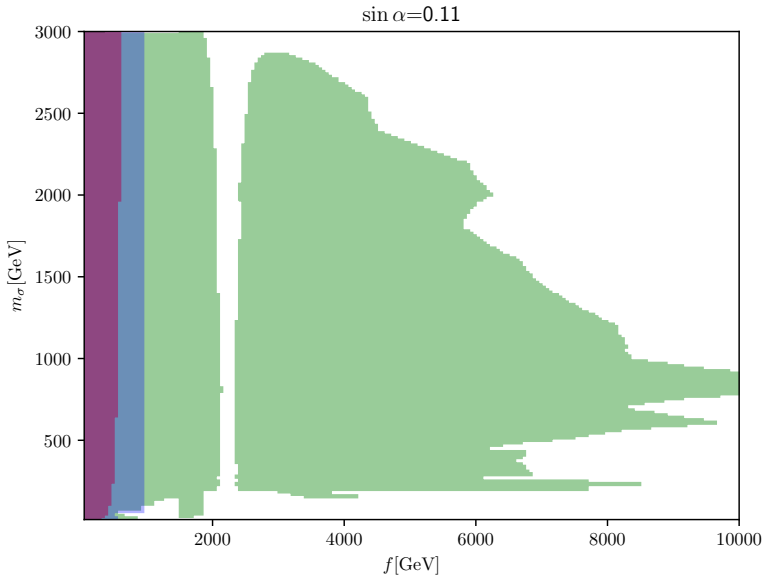

(c) Amount of Higgs-dilaton mixing: $\sin\alpha = 0.11$

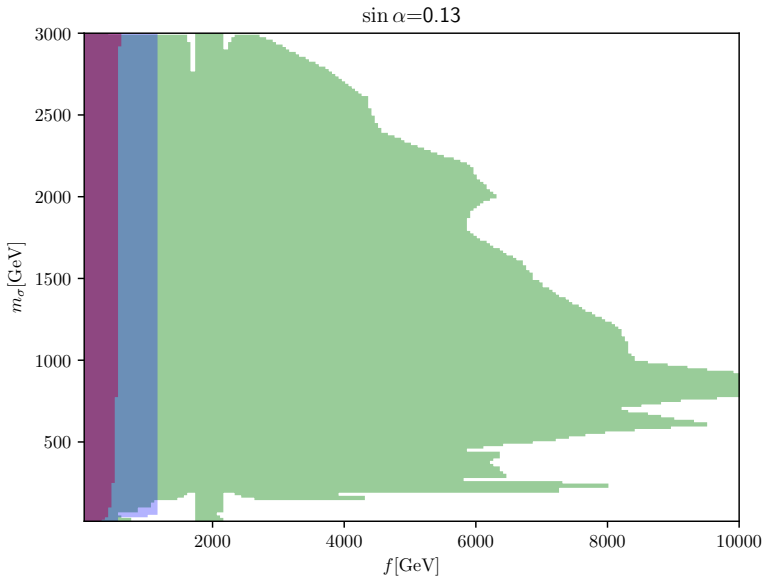

(d) Amount of Higgs-dilaton mixing: $\sin\alpha = 0.13$

Figure 4.2: Excluded regions of the model parameter space, presented in the (f, m_σ) plane for a selection of mixing angles, with the 'minimal mixing term' treatment of the Higgs-dilaton mixing. The figures include 99% confidence level exclusions from Higgs measurements (blue) and the electroweak S and T parameters (red/purple), as well as 95% confidence level bounds from heavy scalar searches (green). The parameter scans were done using Lilith and HiggsBounds. The findings demonstrate that for sufficiently low positive mixing angles, a gap in the exclusion emerges around the value f that satisfies $v/f = \tan\alpha$. In this gap, the couplings of the heavy scalar to the Standard Model fermions and massive gauge bosons are close or equal to zero, so that searches for heavy scalars turn out to be insensitive and arbitrary heavy scalar masses are allowed.

On the other hand, if an additional term is introduced into the Lagrangian to restore gauge invariance, then the results are dramatically different. In particular, the 'magic window' around $v/f = \tan\alpha$ that was found with the minimal treatment of the mixing disappears. In the 'minimal mixing' case and for large dilaton mass, the trilinear σh^2 coupling $\lambda_{\sigma hh}$ becomes

$$\lambda_{\sigma hh} \underset{v/f=s_\alpha/c_\alpha}{\longrightarrow} \frac{m_\sigma^2}{v} c_\alpha^2 s_\alpha^3 (\xi - 2) - 2\frac{m_h^2}{v} c_\alpha^4 s_\alpha + \dots , \tag{4.2.15}$$

where the ellipsis denotes additional terms suppressed by powers of s_α. On the other hand, in the 'gauge invariant mixing' case it becomes

$$\lambda_{\sigma hh} \underset{v/f=s_\alpha/c_\alpha}{\longrightarrow} - c_\alpha^4 s_\alpha \frac{m_\sigma^2}{v} + \dots , \tag{4.2.16}$$

which is dramatically enhanced compared to the previous value, by a factor of order m_σ^2/m_h^2. This leads to dilaton decays into two Higgs fields dominating for much of the parameter space, and has the effect of *completely erasing the 'magic window'*. The constraints in this case are given in figure 4.3, which shows current heavy scalar searches wiping out all of the interesting parameter space. An overview of the most important searches and channels leading to the heavy scalar constraints in figures 4.2 and 4.3 is given in appendix E. In the above figures, a parameter point is considered as excluded, if it is found to be excluded by one channel. Moderate improvements can be expected for these constraints at the HL-LHC. Since they are dominated by di-boson searches, the cross sections scale with the fourth power of $1/f$, while the integrated luminosity of the HL-LHC will be bigger by a factor of the order 10 compared to the LHC, so that the range in f of the excluded parameter space would increase by a factor of about 1.8. Since there is no increase in the energy, the excluded range in m_σ should not increase significantly.

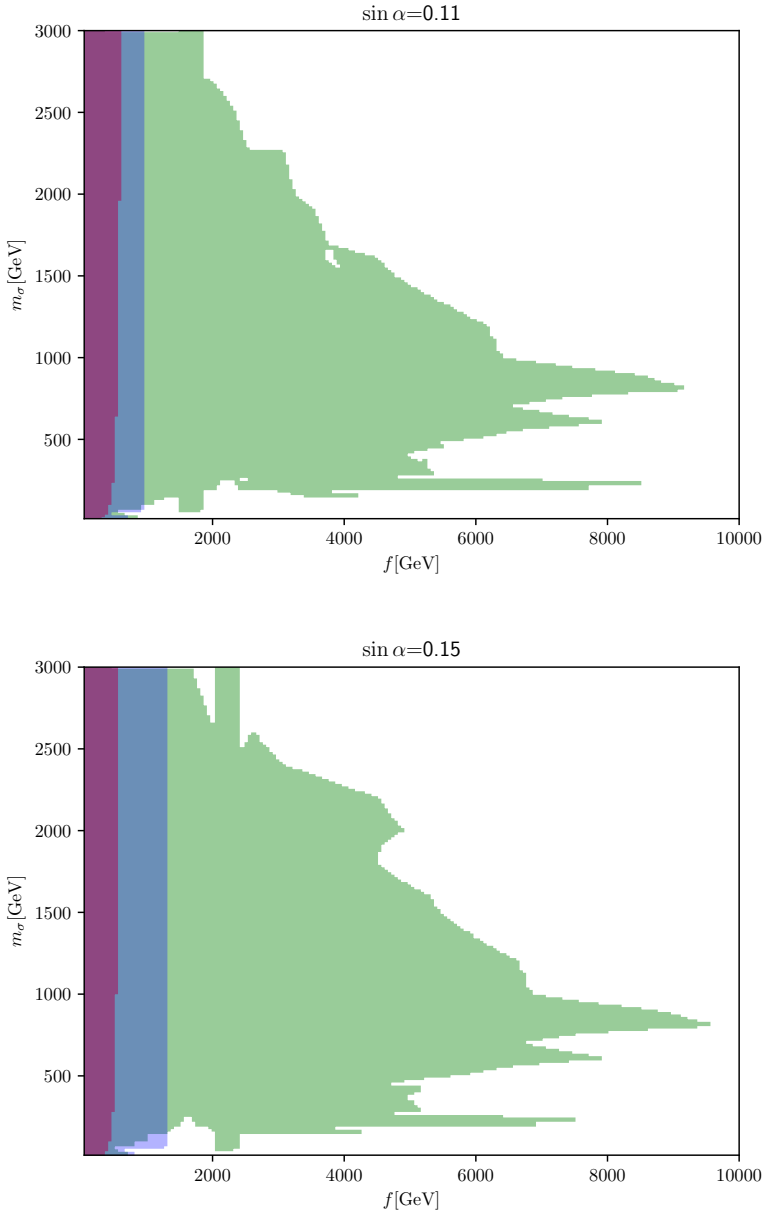

Figure 4.3: Constraints on the parameter space of f and m_σ for $\sin\alpha = 0.11$ (upper) and $\sin\alpha = 0.15$ (lower) with a 'gauge invariant' treatment of the dilaton-Higgs mixing. The colour coding is the same as for figure 4.2.

4.3 Dark matter searches

Next, the constraints on the dilaton dark matter model originating from the relic density, direct detection, and the LHC will be considered. Combined with unitarity constraints, it will be shown which part of the parameter space remains phenomenologically viable, and to what extent the different searches are complementary.

4.3.1 Collider constraints

In order to assess the constraints originating from dark matter searches at the LHC, the implementation of the Lagrangian in eq. (3.3.3) in the FeynRules package [262] (mentioned already in section 4.2) was used to generate a UFO library [264]. Then, the event generator MG5_aMC [235] is employed to generate hard-scattering events relevant for the production of a pair of dark matter particles together with jets,

$$pp \to XXj \ , \tag{4.3.1}$$

where X generically denotes the dark matter particle (a Majorana fermion or a vector boson). In the simulations, leading-order (LO) matrix elements are convoluted with the LO set of NNPDF 3.0 parton densities [320]. Moreover, for every dilaton/dark matter mass configuration, the dilaton width is evaluated with the MadSpin [321] and MadWidth [322] packages and we make sure that the dilaton is narrow (see eq. (3.5.4)). In other words, the ratio m_σ/f in enforced to be small enough.

After matching with parton showers, the above hard process gives rise to a monojet or a multijet plus missing transverse energy (MET) collider signature, that is targeted by numerous dark matter searches undertaken by the ATLAS and CMS collaborations [323, 324]. As those searches usually select events featuring at least one highly-energetic central jet, it is imposed, at the event generator level, that the transverse momentum of the jet satisfies $p_T > 100$ GeV and that its pseudo-rapidity fulfills $|\eta| < 5$.

The simulation of the QCD environment relevant for proton-proton collisions is achieved by matching the hard-scattering events with parton showering and hadronisation as modelled in the Pythia 8 program [280, 281]. The LHC sensitivity to the model is then estimated by re-interpreting the results of the ATLAS-CONF-2019-040 analysis [324] that probes dark matter models through a luminosity of 139 fb^{-1} of LHC data at a centre-of-mass energy of 13 TeV. This analysis targets multijet events featuring a monojet-like topology, *i.e.* it requires events to exhibit a large amount of missing transverse energy, a large number of jets with at least one of them being very hard. As a consequence, it gives a great handle on the model considered in this work and dark matter models in general.

Starting from Monte Carlo simulations of the dilaton-induced dark matter signal, the MadAnalysis 5 program [193, 214, 325] is used to automatically simulate the response of the ATLAS detector through a tune of the Delphes 3 package [221], that internally relies on the FastJet software [230] for event reconstruction on the basis of the anti-k_T jet algorithm [208]. Then, the MadAnalysis 5 framework provides estimates of the efficiencies of the different signal regions of the ATLAS-CONF-2019-040 analysis as it has been implemented in its Public Analysis Database [216]. The sensitivity of the LHC run 2 to the signal is extracted through the CL$_s$ method [282].

In figure 4.4, the obtained constraints for various dark matter and dilaton mass configurations are presented, both for Majorana fermion (upper panel) and vector (lower panel) dark matter. For each mass configuration, the maximum value of the cut-off scale that is excluded by the ATLAS analysis under consideration is evaluated.

This shows that the LHC has no sensitivity to scenarios in which the dilaton cannot be produced on-shell and then decay into a pair of dark matter particles (which corresponds to the parameter space region lying above the blue line). In contrast, when $2m_X \lesssim m_\sigma$ (with m_X generically denoting the dark matter mass), cut-off scales f around the TeV scale can be reached, which closes a part of the small light dilaton window visible allowed by Higgs data (see figure 4.2 for $\sin\alpha = 0.0$). Moreover, as expected from the spin nature, constraints are tighter in the vector dark matter case than in the fermionic one.

Enforcing a naive scaling of both the background and the signal [326], it has been verified that the future high-luminosity operation of the LHC will not substantially affect those conclusions, even with 3000 fb^{-1} of data. Multijet plus missing transverse energy LHC analysis targeting a monojet-like topology within a multijet environment are indeed already limited by the systematics [327] so that mild improvements can only be expected with a larger amount of luminosity. Moreover, in the present case, the limit depends on the fourth power of the cut-off scale, so that a noticeable improvement at the level of the bounds on f would require a huge improvement at the analysis level.

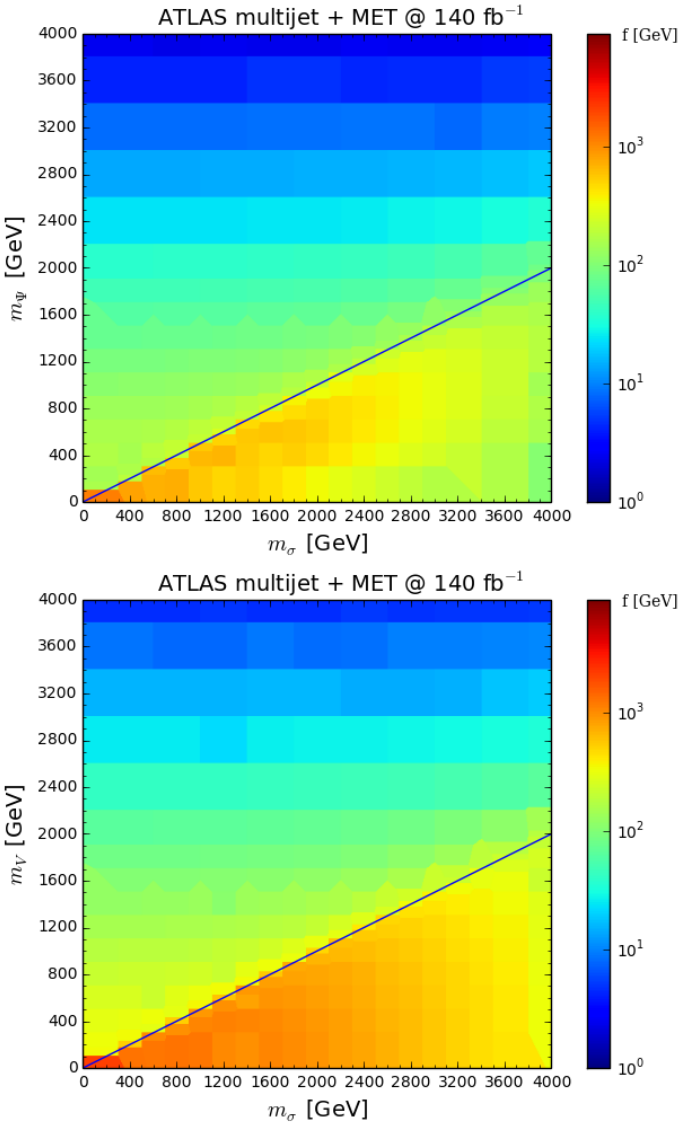

Figure 4.4: Constraints on dilaton-induced dark matter for fermionic dark matter (upper) and vector dark matter (lower), presented in the $(m_\sigma, m_{\Psi,V})$ plane. For each mass configuration, the maximum value of the cut-off scale that can be probed by using 140 fb^{-1} of LHC data and the ATLAS analysis of ref. [324] is evaluated.

4.3.2 Vector dark matter at zero mixing

The dilaton portal for dark matter is very simple, and, as described above, rather special. Its phenomenology in the case of no mixing between the Higgs and the dilaton is therefore rather straightforward: there are two regimes, either near the s-channel resonance where $m_V \simeq m_\sigma/2$, or in the parameter space region where $m_V \gg m_\sigma$ in which there is a combination of t-channel annihilations of the dark matter to dilaton pairs and s-channel annihilation. However, in the previous sections it was found that heavy Higgs searches force $m_\sigma > 3$ TeV for $f < 3$ TeV at zero mixing, and the bound on m_σ is roughly given by

$(3000\,\text{GeV})^2/f$. Clearly this will limit the possibilities for detecting dilaton-induced vector dark matter at colliders or via direct detection.

Figure 4.5 shows the contours of relic density matching the Planck results [328] for fixed f values in the (m_σ, m_V) plane, for values of f upwards of 3 TeV. One can observe that the sensitivity of heavy scalar searches is not noticeably weakened due to the invisible dilaton decays into dark matter, and so the most promising regions for detection corresponds to a resonant configuration. This thus leads to $m_\sigma > 2700$ GeV (rather than 3000 GeV without the presence of dark matter) for $f = 4000$ GeV, but where unfortunately $\sigma_{\text{proton,spin}-\text{independent}} \simeq 10^{-50}\,\text{cm}^2$, well beyond the reach of current and near-future direct-detection experiments. Moreover, the LHC and HL-LHC searches described in the previous section do not limit the parameter space in the figure at all. Alternatively it can be said that this model has a large unexcluded viable parameter space.

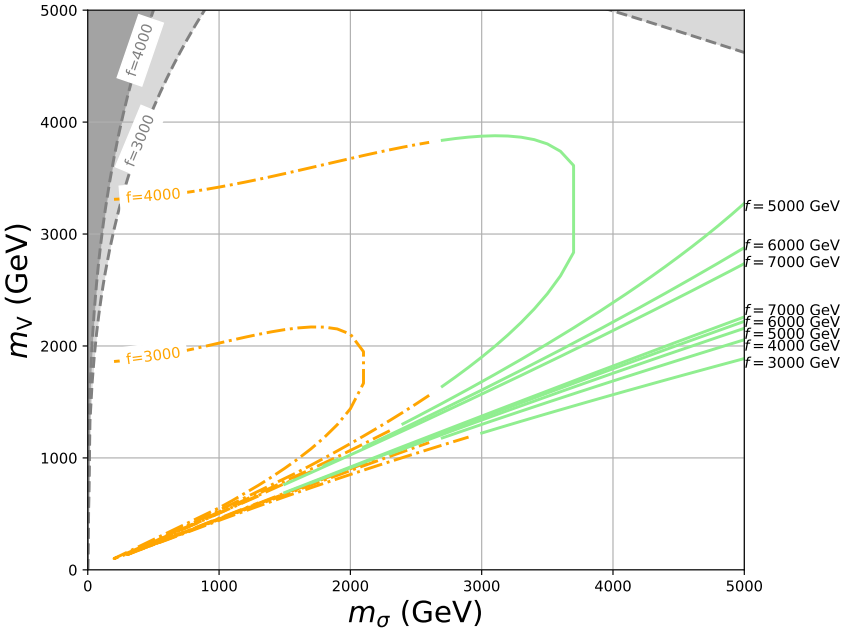

Figure 4.5: Dilaton and vector dark matter masses that saturate the observed dark matter relic density $\Omega h^2 = 0.12$, for differing values of f and no mixing between the dilaton and the Higgs boson. The curves are green and solid when the points are not excluded by any observations; they are orange and dot-dashed when excluded by heavy Higgs searches. The dark matter is *underdense* (and thus allowed if there is another source of dark matter) between the two curves related to a given f value, and *overdense* (hence excluded unless there is some mechanism to dilute the dark matter density) outside them. For the values $f = 3000, 4000$ GeV the underdense region therefore extends above the curves towards $m_V \to \infty$. Unitarity constraints are shown as the shaded grey regions.

Furthermore, limits from unitarity as described in appendix D are presented, which appear at the edges of figure 4.5. The constraints come from dark-matter scattering at low momentum via a dilaton exchange, and at small dilaton masses. This could also be interpreted as the regime where Sommerfeld enhancement should be taken into account in the calculations. In the top right corner of the figure, high-energy scattering constraints become visible, where a maximum centre-of-mass vector momentum of $p_{V,\text{max}} = 20$ TeV

has been taken.

It is legitimate to ask what happens at smaller values of f: can there remain some viable parameter space? For $f = 1$ TeV, a maximum cutoff of $\sqrt{s} = 10$ TeV has to be imposed due to the constraints on the gluon scattering momentum, leading to $p_{V,\mathrm{max}} = 5$ TeV. In the upper panel of figure 4.6, one can see that this excludes $m_\sigma < 2.5$ TeV. However, in a more aggressive approach where a higher cutoff is allowed, the parameter space can be further shrunk. This figure also shows the sensitivity of the collider searches for dark matter, although *the entire* (m_σ, m_V) *plane is excluded by a combination of heavy Higgs search results, dark matter and unitarity constraints.*

On the other hand, as shown in the lower panel of figure 4.6, the unitarity constraints impose an upper bound on the dark matter mass for $f = 2$ TeV. With these results, the considered parameter space regions are naively limited to $m_\sigma > 3$ TeV and $m_V \in [1.1, 2.5]$ TeV. The reason is that at $m_\sigma = 3$ TeV the dilaton is rather *wide*, with $\Gamma_\sigma \simeq 250$ GeV. This means that the dark matter density constraint does not longer result in a funnel, as dark matter is underdense everywhere above the shown curve. Clearly, the choice $f = 2$ TeV is therefore rather borderline in terms of whether the results of the numerical calculations can be trusted.

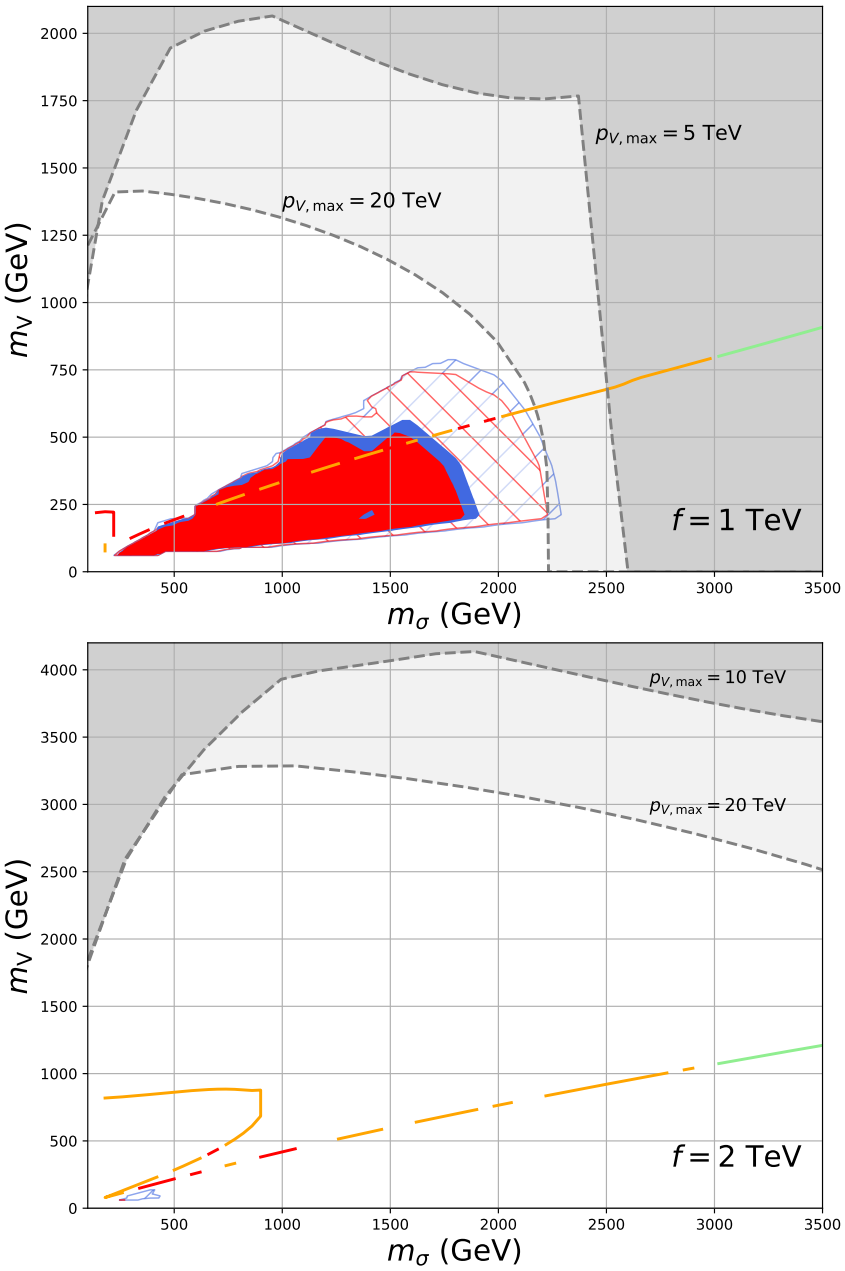

Figure 4.6: Dark matter *curve* as in figure 4.5, but for $f = 1000$ GeV (upper) and 2000 GeV (lower); the red portion of the curve corresponds to regions excluded by both heavy Higgs searches *and* dark matter direct detection experiments. The solid and hatched *regions* show (current) LHC and (future) HL-LHC exclusions from dark-matter-inspired collider searches: the solid blue region is the future exclusion reach at the HL-LHC, after accounting for LO signal cross sections, and the hatched blue region shows the same constraint but with a signal enhanced by a K-factor of 2. Similarly, the red solid and hatched regions depict the current LHC exclusion without and with a K-factor of 2. Unitarity constraints are again shown as shaded grey regions. On the upper figure, the entire parameter space of the model is excluded by a combination of heavy Higgs searches and unitarity. On the lower panel, the monojet/multijet+MET searches are barely visible, and some viable parameter space exists above the reach of heavy Higgs searches.

4.3.3 Collider and vector dark matter constraints at non-zero mixing

The hope of detecting dark matter greatly improves when allowing for dilaton-Higgs boson mixing: the dark matter acquires a coupling to the Higgs, and so interacts much more strongly with nuclei (in principle the model can then accommodate a Higgs portal, which shall not be considered as being very fine-tuned). Moreover, there is also the possibility of sitting in the 'magic window' where $f = v/\tan\alpha$, which should also maximise the reach of dark matter collider searches.

In the 'minimal mixing' case, this would seem to be the ideal situation: the dilaton still has barely suppressed gluon and dark vector couplings, but its couplings to SM bosons and fermions vanish. This means that the dilaton decays only to the dark vector and the SM Higgs boson. Potentially, then, monojet and multijet + MET searches could probe some interesting part of the parameter space of the model. Since the collider searches depend so strongly on f, to have the best sensitivity one should look for the lowest possible value. It has been observed earlier that in the 'minimal mixing' case at the magic window, for $m_\sigma > 300$ GeV, the minimum value of f that survives all constraints was for $\sin\alpha = 0.11$, giving $f = 2.2$ TeV.

For the 'minimal mixing' case, the results are shown for both relic density, direct detection and direct production at the LHC and HL-LHC in figure 4.7, for mixing angles of $\sin\alpha = 0.11$ and $\sin\alpha = 0.15$. The relic density and direct detection cross sections were computed using MicrOMEGAs and compared with the limits summarised in ref. [329]. The LHC limits and projections were inferred from the results in section 4.3.1 by recomputing the production cross sections (for the $pp \to VVj$ process with the same cuts on the hard jet) for the mixing case. Due to the dilaton widths and the relative coupling changes, one could not naively rescale the cross sections. However, the same cutflows/limits on the total rate can be used. It is observed that the (HL-)LHC searches do not overlap with any of the viable regions of the parameter space, so that for $\sin\alpha = 0.11$ the theory could be a viable dark matter model for $m_\sigma < 1$ TeV.

On the other hand, as discussed previously, if the mass mixing term is made gauge invariant, the decays to the SM Higgs boson then dominate, and exclude the dilaton over masses from about 300 GeV up to the limit reached by the LHC searches (currently 3 TeV). The same results are therefore presented for the 'gauge invariant mixing' case in figure 4.8. There is no dark matter parameter space available for $m_\sigma > 300$ GeV, and the LHC/HL-LHC searches are completely wiped out as the production of dark matter greatly diminishes. The 'gauge invariant mixing' scenario is therefore entirely unappealing phenomenologically, and invites other model-building solutions.

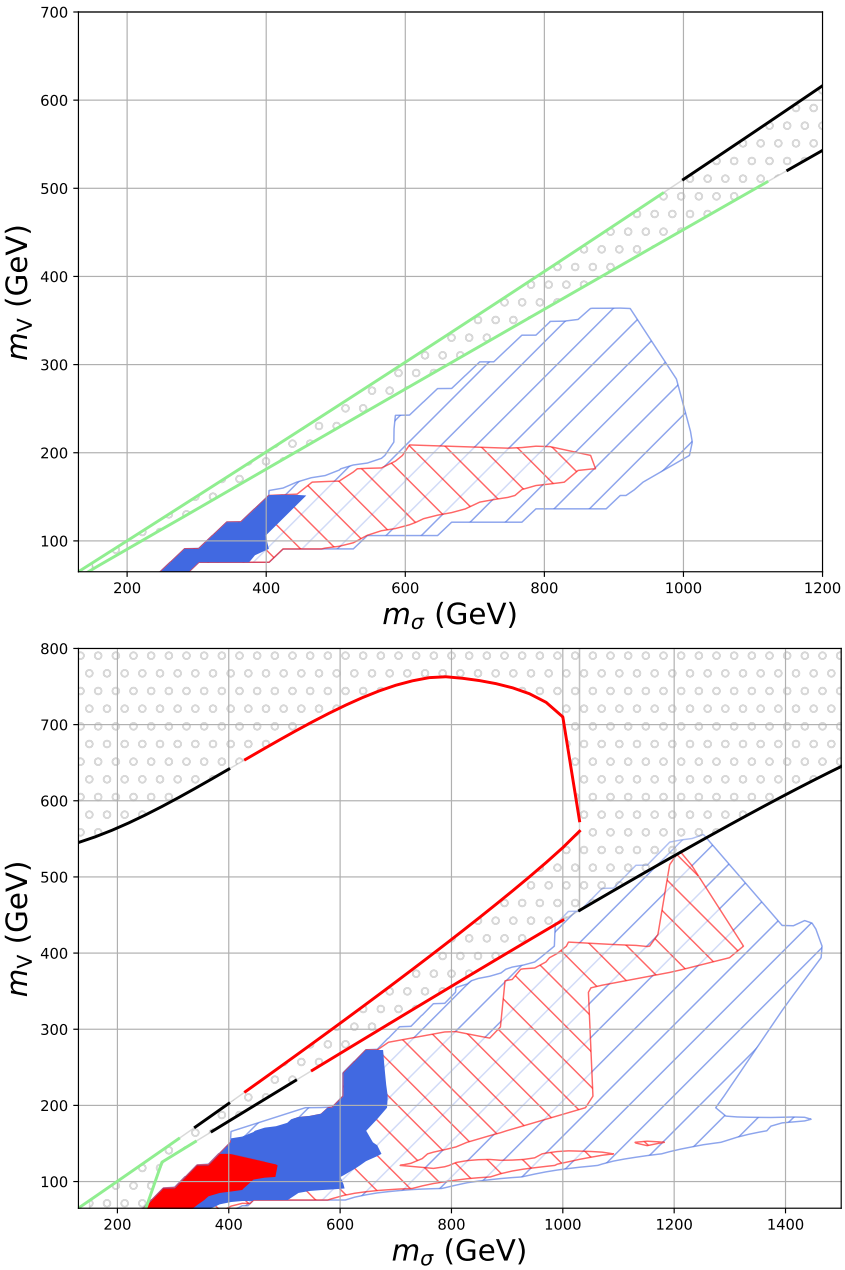

Figure 4.7: Combined dark matter, Higgs and collider constraints on the considered model for $\sin\alpha = 0.11$ (upper) and 0.15 (lower) in the 'magic window' where $f = v/\tan\alpha$ and under the assumption of a 'minimal Higgs-dilaton mixing' treatment. The solid lines show the curves where the dark matter density matches the Planck limit of $\Omega h^2 = 0.12$ with the circular shading between them showing the *underdense* regions. The solid line is green and orange for allowed and excluded by heavy Higgs searches, and black when excluded by dark matter direct detection. The solid and hatched regions show the current and future exclusions from dark matter collider searches: the solid blue region is the future exclusion reach at the HL-LHC after accounting for LO signal cross sections and the hatched blue region is the same constraint but with the signal enhanced by 2σ according to the uncertainty on its total rate. The red solid and hatched region represent the corresponding constraints at the end of the LHC run 2.

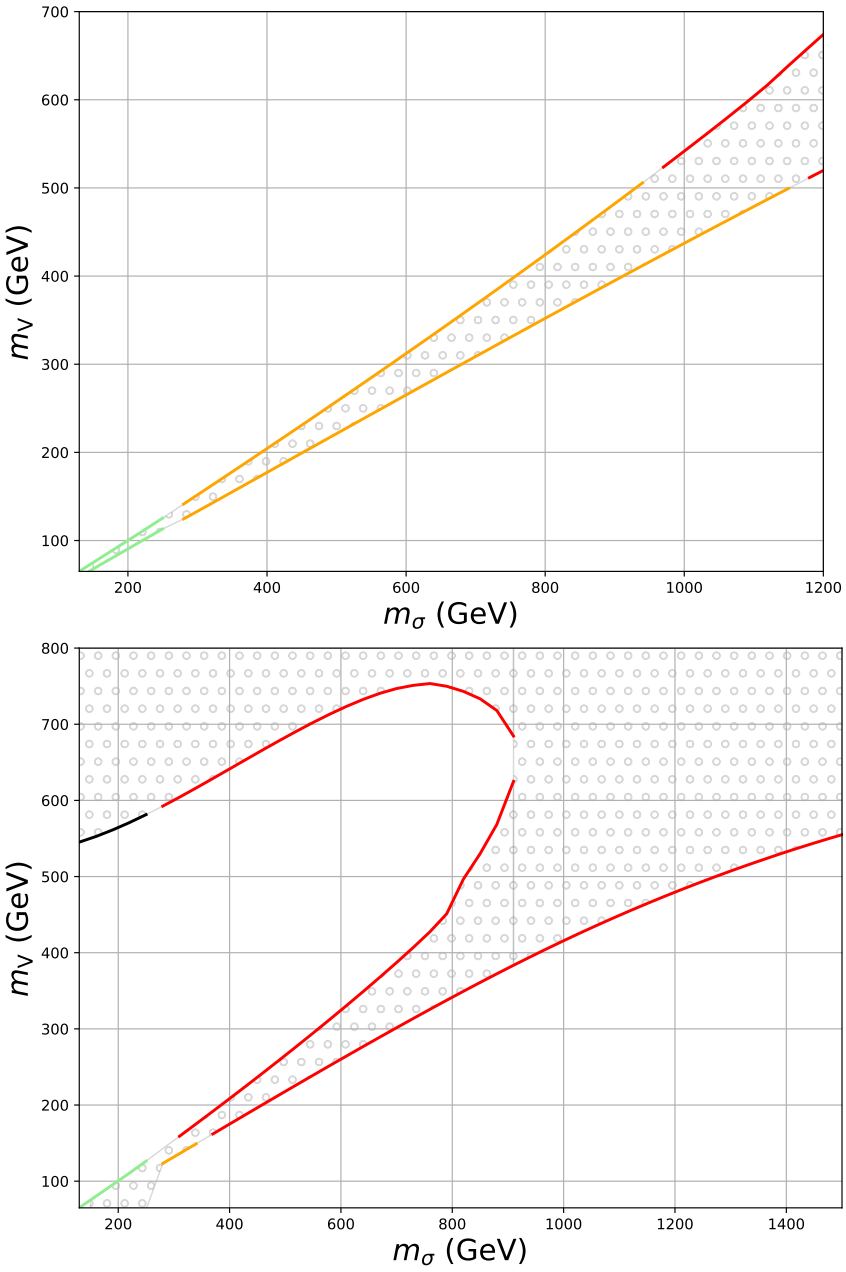

Figure 4.8: Combined dark matter and Higgs constraints for $\sin\alpha = 0.11$ (upper panel) and 0.15 (lower panel) for a 'gauge invariant' treatment of the Higgs-dilaton mixing. The description is similar as in figure 4.7, except that there are no LHC or HL-LHC constraints from monojets or multijet searches, the cross sections being orders of magnitude too small.

4.4 Future collider constraints

The previous sections have shown that searches for dark matter at the LHC and at its future high-luminosity operation are not sensitive to our scenario. In this section, monojet and multijet+MET collider probes at a future 100 TeV collider will instead be investigated. The simulation chain introduced in section 4.3.1 is used for studying the hard-scattering process of eq. (4.3.1). The analysis follows the steps given in ref. [330]. At the generator level, it is imposed that the transverse momentum of the hardest jet satisfies $p_T > 1500$ GeV and that its pseudo-rapidity fulfills $|\eta| < 5$. In addition, the production of an invisible Z-boson with jets is considered as main background to the analysis.

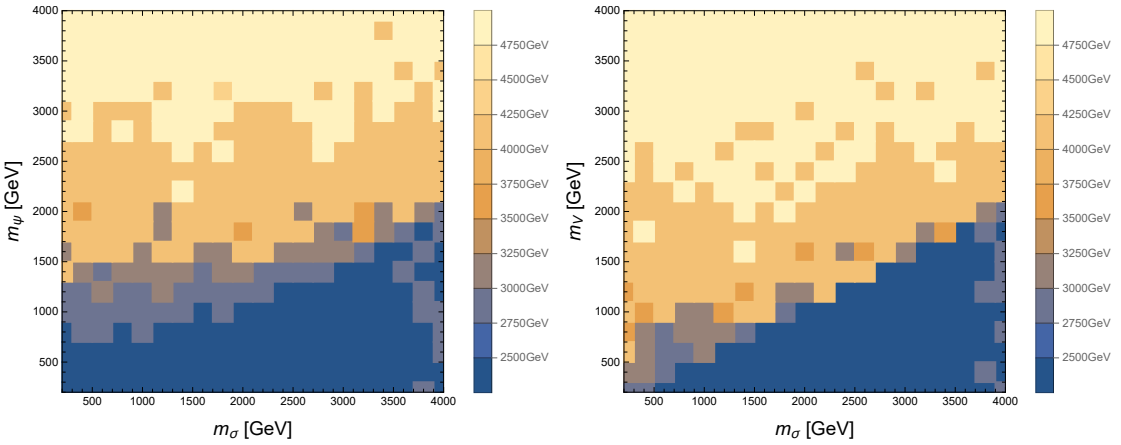

Figure 4.9: Missing energy selection thresholds as a function of the dilaton and fermionic (left panel) and vector (right panel) dark matter masses to achieve the best sensitivity at a future 100 TeV proton-proton collider. In order to avoid any potential unitarity issues at high energies, it is imposed that the threshold value is smaller than 5 TeV.

The analysis first vetoes the presence of charged leptons with a transverse momentum $p_T > 20$ GeV and a pseudo-rapidity $|\eta| < 2.5$ and 2.1 for electrons and muons respectively, and then rejects events featuring at least one hadronic tau with $p_T > 40$ GeV and $|\eta| < 2.3$. Next, it is required that the leading jet is central and very hard, with $p_T(j_1) > 1500$ GeV and $|\eta(j_1)| < 2.4$, while some extra hadronic activity is allowed in the selected events. This hadronic activity is associated with the ensemble of non-leading jets whose $p_T > 30$ GeV and $|\eta| < 4.5$. The leading and all the extra jets satisfying the above requirements are further imposed to be well separated in azimuth from the missing momentum,

$$\Delta\varphi(\not{\mathbf{p}}_T, j_i) > 0.4\,, \tag{4.4.1}$$

and additionally, the second jet is prevented from being back-to-back with the leading jet,

$$\Delta\varphi(j_1, j_2) < 2.5\,. \tag{4.4.2}$$

After this preselection, the analysis relies on various signal regions to estimate the sensitivity of a future 100 TeV proton-proton collider to the dark matter monojet/multijet+MET

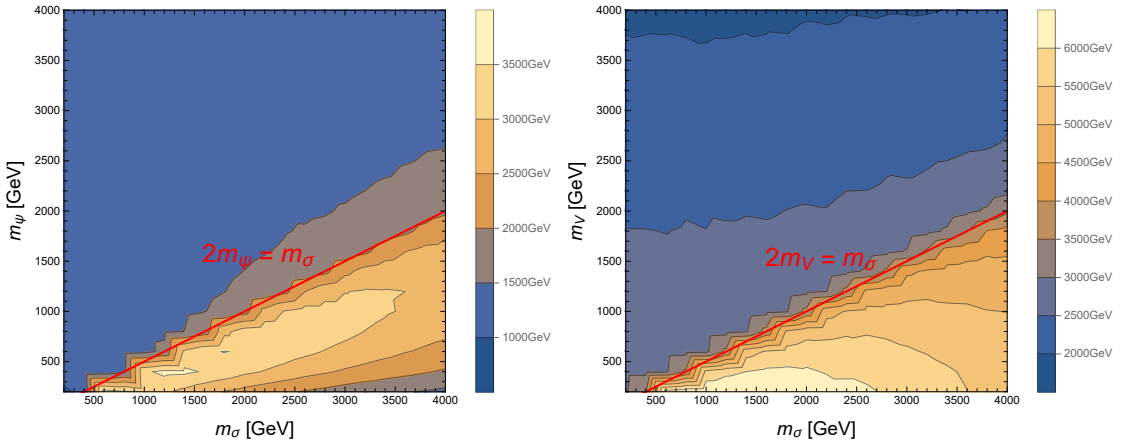

Figure 4.10: Sensitivity of a 100 TeV future proton-proton collider to the dilaton portal dark matter model considered in this work, for the case of Majorana (left panel) and vector (right panel) dark matter. The results are presented in the $(m_\sigma, m_{\Psi,V})$ plane and the colour coding indicates the expected reach on the theory cutoff scale f. These findings correspond to an integrated luminosity of 3 ab^{-1}.

signal predicted in this model. Each signal region is defined by a different missing transverse momentum selection,

$$\not{E}_T > \not{E}_T^{\text{thr.}} \qquad \text{with} \quad \not{E}_T^{\text{thr.}} \in [2-5]\ \text{TeV}\,, \tag{4.4.3}$$

so that any considered dark matter and dilaton mass configurations could be optimally covered. In the above setup, all missing transverse energy thresholds are restricted to be smaller than 5 TeV, which guarantees to avoid any potential unitarity issues. The best MET threshold value for a given mass spectrum depends on both masses, as depicted in the left and right panels of figure 4.9 for the fermionic and vector dark matter cases respectively.

For dark matter masses much larger than half the dilaton mass (i.e. far from any resonant configuration), the optimal selection enforces the missing energy to be larger than 1–3 times the dark matter mass for the two classes of models, the MET spectrum being in general flat enough to guarantee a large signal selection efficiency and a good rejection of the Z+jets background. In contrast, when dark matter production is enhanced by the existence of a dilaton resonance (i.e. for $m_\Psi < m_\sigma/2$ and $m_V < m_\sigma/2$ in the fermion and vector dark matter cases respectively), the best selection threshold is directly fixed by the dilaton mass.

Figure 4.10 shows that in contrast with the LHC, 3 ab^{-1} of proton-proton collisions at 100 TeV are sufficient to probe cutoff scales lying in the multi-TeV regime for both the fermion (left panel) and vector (right panel) dark matter cases. The results are presented in the $(m_\sigma, m_{\Psi,V})$ mass plane respectively, and the values of the f scale that are reachable for each mass spectrum are indicated by a colour code. For each configuration for which the dark matter can be produced from the decay of a resonantly produced dilaton (below the red line), scales larger than 4 TeV can be probed, providing hence complementary constraints to models allowed by cosmological considerations.

In contrast, for configurations in which the dilaton cannot decay into a pair of dark matter particles, the signal cross sections are smaller. This results in a loss of sensitivity, in particular in regions favoured by cosmology.

4.5 Conclusions

In this work, a comprehensive and up-to-date set of current and future constraints on the most interesting (heavy) dilaton-portal dark matter models is presented. While heavy scalar and unitarity constraints push the model to large masses and weak couplings, to the extent that the direct dark matter production at the LHC can only probe a light dilaton, and not reach any viable parameter space above 300 GeV, a future collider would potentially be sensitive with the same searches. It would be interesting to examine future projections for heavy scalar and dark matter searches, to see whether these will be complementary. On the other hand, the (HL) LHC reach could be enhanced if the experimental collaborations extend their published diboson limits above 3 TeV.

It was argued that vector dark matter is more promising for collider searches thanks to the dilaton's much larger branching ratio into vectors compared to fermions or scalars. Allowing mixing of the dilaton with the Higgs boson then apparently leads to a way to weaken or evade heavy scalar searches (and increase the coupling of the dark matter to the visible sector via the Higgs portal) via the opening of a 'magic window'. It has been shown that this could allow the dark matter and dilaton *below* 1 TeV in the 'minimal mixing treatment'.

However, the 'minimal mixing' of the dilaton with the Higgs boson is not gauge invariant. Including operators to restore gauge invariance to the model erases the 'magic window', and di-Higgs bounds dominate all constraints that could be imposed on the dilaton properties. It would nevertheless be interesting to explore the high-energy origin of these Higgs-dilaton mixing terms, in the context of concrete models. Similarly, the theory could have been formulated in a gauge-invariant way by including the dilaton *before electroweak symmetry breaking*, as performed in ref. [297]: it would be interesting to revisit the constraints and searches of the present work in this alternative (and inequivalent) formulation of the theory.

Chapter 5

Implementation and reinterpretation of long-lived particle searches

Among the new physics searches at the LHC, one class of physics analyses which currently benefits from increasing interest is the search for long-lived particles (LLPs), for reasons which will be exposed in the following using arguments of refs. [331, 332]. The term *long-lived particle* refers to particles with a sufficiently high lifetime to travel along observable distances from their production point until their decay, in contrast to *prompt* decays, which seemingly decay at the point at which they are produced or at a tiny distance from it.

Qualifying a particle as long-lived is *de facto* only meaningful in an experimental context, i.e. its life-time and travelled distance have to be put in relation to the length-scales present in the experiment, e.g. the dimensions of the detector. Furthermore it implies a comparison to other particles, which in turn are not said to be long-lived. On the other hand, the term *long-lived particle* is usually only used for particles which can indeed be expected to decay after some time, i.e. unstable particles. In other words, speaking of long-lived particles is a kind of jargon which should be further clarified.

The lifetime of a particle is a property which in a given quantum field theory essentially depends on its couplings to other particles as well as the masses of the particle itself and the decay products, which affects the available phase space of the allowed decay processes, but possibly also masses of mediators such as the W boson in neutron or charged pion decays [333]. Needless to say, the boost of an unstable particle also impacts the observed lifetime in the laboratory frame. In this regard, it should also be clear that the term *lifetime* mostly refers to the lifetime of a particle in its rest frame, unless the context suggests something else. Also, this word leaves implicit that it represents a mean value for a species of particles, as the lifetime of on an individual particle is unpredictable. Besides, it is common to quantify the lifetime of a particle via the proper decay length $c\tau$, i.e. the proper lifetime τ multiplied by the speed of light, instead of the lifetime τ itself. This gives a rough idea of how far a particle can travel until it decays, when its speed is close to c (for the exact result, one needs to use the exact velocity and include the γ-factor to account for the boost in the laboratory frame). It is not much of a surprise that the existence of long-lived particles is not intimately related to a particular model, but merely

a generic feature that exists in all sorts of theories, including the Standard Model.

For instance, the muon is known to be unstable, but its lifetime ($c\tau = 658.6384\,\text{m}$) is high enough for it to be considered as stable on the detector scales of collider experiments. Its decay takes place almost exclusively far outside the detector volume. The number of unstable, long-lived *elementary* particles of the Standard Model is in fact quite limited: There is one more lepton, the tau-lepton, which decays with a much smaller lifetime ($c\tau = 87.03\,\mu\text{m}$). The electron as the lightest charged lepton is stable. The massive vector-bosons $W^{\pm}$ and Z as well as the Higgs boson decay promptly, while the photon is massless and its decay is therefore forbidden. Likewise, the neutrinos are massless *in the Standard Model*. Finally, quarks and gluons do not appear as isolated particles, but are instead confined into hadrons. On the other hand, a multitude of hadrons have sufficiently high lifetimes such that state-of-the-art collider experiments are able to resolve the displacement between the production and the decay point, while some of them can even escape the detector volume. An extensive list of some unstable SM particles together with their proper decay lengths and masses is given in table 5.1. It should be emphasised that the high collision energy can give rise to high γ-factors, leading to a non-negligible enhancement of the displacement between the production and decay vertices. This displacement becomes observable above a magnitude of roughly $10\,\mu\text{m}$.

A plethora of different BSM physics scenarios predicts LLPs with diverse characteristics, which can lead to very unusual signatures in contrast to the familiar ones of the SM LLPs. Additionally, the fact that the heaviest long-lived SM particles have masses of about 5 GeV facilitates the discrimination of new heavier LLPs from SM LLPs. Exploiting the different signatures of long-lived particles is therefore a powerful method to search for hints of physics beyond the SM at colliders and provide constraints on a wide spectrum of BSM models.

Implementing the event selection criteria of existing LLP searches [334–366] into a user-friendly computer program can be highly valuable in order to unleash their potential to constrain different models, which provide the targeted signatures. In account of the growing interest in long-lived particles in the community, these searches have therefore recently become a priority in the development of MadAnalysis 5 [193, 214, 218]. This chapter reports on some of the contributions in this context, which are currently in preparation for publication, and has the following structure:
Section 5.1 gives an overview about the phenomenology of long-lived particles in different physics scenarios and experimental strategies to uncover them. A technical aspect, that is potentially relevant for LLP recasting, is the simulation of particle trajectories under the influence of a magnetic field in the detector volume. This task is handled in MadAnalysis 5 by a new module, as described in section 5.2. My contribution to the development of this module is part of the work related to this thesis. The following two sections 5.3 and 5.4 illustrate the design of two LLP analyses [348, 355] published by the CMS and ATLAS collaborations, and their implementation within MadAnalysis 5 using the SFS framework. One of these analyses is used to place bounds on the parameter space of the vector-like lepton doublet model introduced in section 1.4.1.2, as presented in section 5.5. The number of LLP searches performed in recent years reflects the high interest in LLPs and their potential to reveal new physics or constrain BSM models [331]. A list of ATLAS and CMS searches for different LLP signatures in LHC Run 1 and 2 is given in appendix F.

Particle	$c\tau$	m [MeV]
n	2.6362×10^8 km	939.6
μ	658.6384 m	105.7
K_L	15.34 m	497.6
$\pi^\pm$	7.8045 m	139.6
$K^\pm$	3.711 m	493.7
Ξ^0	8.71 cm	1315.0
Λ	7.89 cm	1115.7
Ξ^-	4.91 cm	1321.7
Σ^-	4.434 cm	1197.4
K_S	2.6844 cm	497.6
Ω^-	2.461 cm	1672.5
Σ^+	2.404 cm	1189.4
$B^\pm$	491.1 μm	5279.3
B^0	455.4 μm	5279.7
B_s^0	454.2 μm	5366.9
Λ_b^0	441.0 μm	5619.6
$D^\pm$	311.8 μm	1869.7
$D_s^\pm$	151.2 μm	1968.3
Ξ_c^+	136.6 μm	2467.9
D^0	122.9 μm	1864.8
τ	87.03 μm	1776.9
Ω_c^0	80 μm	2695.2
Λ_c^+	60.7 μm	2286.5
Ξ_c^0	45.8 μm	2470.9
π^0	25.5 nm	135.0
Σ^0	2.22×10^{-11} m	1192.6

Table 5.1: Selection of unstable SM particles, their mean proper decay lengths $c\tau$ and their masses m, ordered with decreasing lifetime. The values are extracted from ref. [367], but given without their uncertainties. For the benefit of better readability and comparison, the mass values in MeV are reduced to one non-integer digit.

5.1 Search strategies for long-lived particles

The emergence of long-lived particles in various BSM models with different properties suggests a variety of possible ways in which they could manifest themselves in experiments. A number of search strategies exist, targeting the different kinds of LLP candidates in existing and planned/proposed experiments. The purpose of this section is to give an overview of the existing search strategies. The focus of this section is on collider exper-

iments using general-purpose detectors such as ATLAS or CMS, which are discussed in section 5.1.1. Some examples of other experiments and detector proposals with the specific purpose of LLP detection are briefly explained in section 5.1.2. The option to search for LLPs produced in the atmosphere with the neutrino detectors IceCube [368] and Super-Kamiokande [369] has also been studied [370], but will not be addressed in this work.

The motivation for this section is to illustrate the main ideas behind the search strategies, without digging into too many technical details of a particular physics analysis or experiment. This concerns, for example, triggers and other selection requirements, SM background and signal models of interest, which will only be mentioned occasionally when it seems relevant. Furthermore, the section does not claim to give a complete listing of all existing or imaginable search strategies, detectors or detector proposals. Since the majority of the presented ideas have already found application, a number of existing searches are referenced.

5.1.1 Strategies for general purpose detectors

This subsection explains common strategies observable with general purpose detectors such as ATLAS and CMS. They are however not necessarily limited to these detectors. This subsection is mostly based on refs. [331, 371], but includes also information from additional sources in various places, which will be referenced explicitly.

Displaced vertices in the inner detector: The decay of a sufficiently long-lived particle into *charged* particles which traverse the inner detector (ID) can become visible as a *displaced vertex* (DV). In this case, a subset of the reconstructed charged particle trajectories (tracks) are found to be intersecting in one point (i.e. they form a *vertex*) which can be distinguished from the interaction point of the colliding particles (protons in the case of the LHC) [372]. This presupposes that the position of the interaction can also be determined successfully, which is equally inferred from the generally more numerous tracks forming a *primary vertex*. Interpreting the observation of a displaced vertex as the decay of a long-lived particle, the four-momenta associated with the tracks induce a loose lower bound on the LLP mass. This information can also be used to suppress background from long-lived SM particles (c.f. eq. (5.4.7)). More specific signatures can be defined by imposing additional requirements on the nature of the displaced vertices, i.e. the emerging particles. The ATLAS search in ref. [372], for example, distinguishes between five different DV signatures: The dilepton signature with at least two oppositely charged leptons e, μ emerging from the vertex, and the multitrack signatures DV+muon, DV+electron, DV+jets and DV+E_T^{miss} with a minimum of five charged particle tracks, where one of the objects μ, e, j must emerge from the displaced vertex along with the other tracks, or it is characterised by a certain amount of missing transverse energy.

Displaced vertices in the muon system: Decays of sufficiently long-lived particles which leave the inner detector volume might still be observable as displaced vertices thanks to the tracking capabilities of the muon spectrometer (MS) [373]. Ref. [374] is an example of a search for events with two displaced vertices of displaced hadronic jets, where each of the vertices is allowed to occur either in the inner detector or the

muon spectrometer. Different DV reconstruction algorithms are applied for the ID and the MS.

Displaced lepton pairs: While the displaced vertex signatures aim attention at intersecting tracks, interpreting the intersection point as the position of a possible LLP decay, searches for displaced particle tracks probe the displacement of the particle tracks from the primary interaction point. They intend to identify tracks which do not connect to the primary interaction vertex [353], indicating that they do not emanate directly from the colliding particles or a subsequent prompt decay, but supposably from the decay of a long-lived particle at a noticeable distance from the collision point. The displacement of the track can be quantified using the transverse and longitudinal impact parameters d_0 and d_z, which are discussed in section 5.2. Different ATLAS and CMS searches for displaced lepton pairs [353, 355, 375] are specifically based on these impact parameters, which can however also play a role in the event selection of searches using different signatures, e.g. for displaced vertices, to single out particles which were not produced at the primary vertex.

Displaced jets: Jets emerging from LLPs decaying in the inner detector can give rise to the previously discussed signatures of displaced tracks relative to the interaction point, and tracks forming a displaced vertex [362,366]. The situation can be different, when a jet is generated by a neutral long-lived particle which has already left the tracker and decays in one of the calorimeters [346]. Consequently, there are no tracks from which a decay vertex could be inferred. In addition, they are distinguishable from prompt jets, if they generate an exceptionally high ratio $E_{\mathrm{H}}/E_{\mathrm{EM}}$ of energy deposit in the hadronic calorimeter E_{H} compared to the electromagnetic one E_{EM}. This depends on the location where the decay takes place. Also, from the perspective of the reconstruction algorithms, they resemble a narrow jet, in comparison with prompt jets.

Displaced lepton jets: Lepton jets are a class of jets of highly collimated charged leptons, i.e. electrons and/or muons, which can be supplemented with pions [376, 377]. They can arise in models incorporating a hidden sector, caused by the decay of a relatively light (of the order MeV to GeV) hidden sector particle to SM particles. An example that is frequently put forward in this context is the case of a dark photon with kinetic mixing with the SM photon [334]. With the energies available in current collider experiments, the decaying hidden sector particle usually has a high boost owing to its low mass. The same is true for the SM decay products, which explains the extreme collimation. As for the composition of lepton jets, the exact mass of the decaying hidden sector particle is of course decisive for the allowed decay modes and affects the branching fractions, but they are generally composed to a large fraction of leptons. Further classifications into different types of lepton jets are possible based on the number of the different constituents. For instance, refs. [334,378] classifies lepton jets into three different types, depending on the number of muons and jets contained in a cone of a given size $\Delta R = \sqrt{(\Delta\eta)^2 + (\Delta\phi)^2}$. Type0 contains a minimum of two muons and no jet, Type1 requires at least two muons which are accompanied by one jet, and lepton jets of Type2 do not contain any muons.

Displaced lepton jets are possible, if the decaying hidden sector particle is long-lived, such that the decay and hence the lepton jet generation take place with some

displacement from the interaction point. Reconstructing lepton jets, and in particular displaced ones, is experimentally challenging: The granularity of the detector limits the capacity to discriminate between different particles of the collimated particle clusters. In addition, displaced lepton jets might not generate tracks in the inner detector, if they are highly displaced. However, the track reconstruction by the muon system can provide useful information for the identification of displaced lepton jets, if muons are involved. A way to search for decays of long-lived hidden sector particles to muons is therefore to use the muon spectrometer tracks and limit the attention to decays outside the pixel detector, i.e. requiring the absence of matching tracks in the pixel detector. Displaced lepton jets without muons can instead be searched for with the assumption that the LLP decays to electrons or pions occur in the hadronic calorimeter. For this purpose, an upper limit on the electromagnetic fraction, i.e. the ratio of energy deposited in the electromagnetic calorimeter to the total energy of the jet, can be imposed. In ref. [378], this upper value was fixed to 0.4 due to the observation that the electromagnetic fraction of lepton jets in simulated events, which originate from dark photon decays in the hadronic calorimeter, never exceed this value.

Non-pointing and delayed photons: The basic idea that trajectories of particles produced in LLP decays are in general not connected to the primary interaction point is not reserved to leptons and jets, but applied also to photons. However, since they are electrically neutral they do not generate tracks as they traverse the inner detector. A different approach is therefore necessary to determine the displacement of the extrapolated photon trajectories relative to the primary vertex and detect candidates with a significant displacement, called *non-pointing* photons. In contrast to charged particles, photons are not deflected by the magnetic field present in the detector volume, so that primarily the direction of the photon momentum is of interest. Another key difference compared to leptons and hadrons is that photons are massless and consequently always travel with the speed of light c. A photon emerging from a long-lived particle travelling with a lower velocity before its decay is therefore *delayed* in comparison with a photon produced at the primary vertex and detected at the same position. The delay of photons produced by LLPs is caused on the one hand by the finite time interval between LLP production and decay and the fact that the LLP travels with a speed lower than c during this time. On the other hand, the non-pointing implies that the path between the primary vertex and the detection in the detector is indirect and hence longer than the path of a prompt photon [363, 379]. The ATLAS searches [379, 380] exploit both the flight direction and time-of-flight information provided by the electromagnetic calorimeter to detect non-pointing and delayed photons. This search strategy is in particular suitable for electrically neutral LLPs decaying into an invisible particle and a photon.

Delayed jets: Using the time-of-flight information provided by the electromagnetic calorimeter is not limited to photons. Also massive particles travelling with a velocity close to the speed of light can be delayed when it is produced by a long-lived particle. The CMS search presented in ref. [363] searches for events with delayed jets, where the delay is measured relative to the arrival time of a massless particle coming from the interaction point on the direct way.

Disappearing tracks: Tracks of charged particles are determined as a consequence of hits in the layers of the tracker, which for particles produced at or close to the interaction point are expected to occur from smaller to larger radii from the beam axis. A *disappearing track* is the observation that hits are only observed below a certain radius within the tracker, as though the particle had ceased to exist. The absence of hits at higher radii suggests that the particle has decayed, but no charged decay product is observed, which seems in contradiction with charge conservation. This phenomenon can be explained by a long-lived particle decay with decay products remaining undetected due to low momentum or weak interaction with detector material [339, 359]. An example in anomaly-mediated supersymmetry breaking (AMSB) [381–383] is the decay of the lightest chargino $\tilde{\chi}_1^\pm$ to the lightest supersymmetric particle, the neutralino $\tilde{\chi}_1^0$ and a charged pion,

$$\tilde{\chi}_1^\pm \to \tilde{\chi}_1^0 \, \pi^\pm \,,$$

where the pion momentum is low due to a small mass difference between the supersymmetric particles $\tilde{\chi}_1^\pm$ and $\tilde{\chi}_1^0$, which is typically of the order of 160 MeV.

Kinked tracks: As similar signature to disappearing tracks are *kinked tracks*, where the charged LLP decay product is observable as a track with a different direction [384]. In this case, the tracks of the LLP and the charged decay product mimic the track of a particle that gets abruptly deflected. This signature has been searched for at ALEPH [385, 386].

Emerging jets: A signature that can be expected in theories with a QCD like dark sector, consists in *emerging jets* [387], i.e. jets which become apparent gradually during their propagation from the interaction point through the detector. They derive from dark partons produced from the colliding particles, which undergo dark parton showering and fragmentation resulting in dark hadrons, which can be clustered into jets. The emergence of detectable jets is then a consequence of the individual long-lived dark hadrons decaying into SM hadrons, which could give rise to several tracks not going back to the primary vertex or displaced vertices, which are the starting points of subjets within the entire emerging jet. The emerging jet signature has been proposed in ref. [387] and has been searched for at CMS [361].

Heavy stable charged particles: Unstable charged particles with a high mass, leading to a low velocity compared to the speed of light even at high momenta, and a lifetime that favours a decay outside of the detector volume are referred to as *heavy stable charged particle*[1] (HSCP) [356, 389]. Here, the charge can in general be different from $\pm e$, in contrast to the elementary particles and long-lived hadrons of the SM. Moreover, there are HSCP candidates which could combine, along their trajectory through the detector, with SM particles to form different composite particles. This could also imply an alteration of the electric charge. For particles produced at the LHC with masses exceeding 100 GeV, the proportion of particles with $\beta = v/c < 0.9$ becomes important. Both the low velocity and the perhaps unusual charge of HSCPs

1. Different terminologies are used in the literature, e.g. *heavy long-lived charged particle* [388] or *metastable heavy charged particle* [335]. Irrespective of the exact phrasing, the described signature applies to all particles with the described properties, i.e. charged particles which are stable on the length scale of the detectors and have a high mass.

would be reflected, according to the Bethe-Bloch formula [367], in an atypical rate of energy loss $\mathrm{d}E/\mathrm{d}x$ through ionisation, when compared to SM particles. For the latter, the energy loss rate does not show a strong momentum dependence in the for the LHC relevant range between 10 GeV and 1 TeV and is situated at approximately 3 MeV/cm. In contrast, $\mathrm{d}E/\mathrm{d}x$ for HSCPs has a much stronger momentum dependence, which is governed by the charge and mass values. Depending on the charge, an exceptionally high or low energy loss rate of particles in regions of high or low momentum could therefore indicate the presence of new heavy particles. Moreover, the comparatively low velocity can be observed by measuring the time-of-flight (ToF).

A relatively high number of HSCP searches has already been conducted at the LHC [335, 336, 356, 388–397], but also at LEP [398–401], HERA [402] and Tevatron [403–406].

Stopped particles: As mentioned earlier, the detector dimensions represent a limitation for many signatures used in LLP searches, since decays of particles having escaped the detector volume are usually not observable. This is in particular the case for particles travelling with high momentum, that is not severely altered by the detector elements. Conversely, it is worth considering the possibility that long-lived particles could come to rest within the detector, where they decay at a later time [358]. This phenomenon involves predominantly particles with a velocity below 0.5 c [407]. The loss in kinetic energy is due to nuclear interactions or ionisation within the detector material and is most likely to happen in detector regions with a high material density, especially the electromagnetic and hadronic calorimeters, but also parts of the muon system. A striking difference of stopped LLPs compared to other signatures is the fact that their decay can be completely disconnected from the production. In particular, it can take place when there is no collision activity in the detector, e.g. in the time interval between two bunch crossings. Consequently, these moments are best suited for the search of stopped particles, as the detector will only be exposed to low background which is unrelated to collision events. The decay of a stopped LLP in one of the calorimeters could be detected by the latter, if it measures the deposit of a significant amount of energy out of time with respect to the collider activity. Similarly, LLPs decaying in the muon system could lead to out-of-time tracks.

Several searches for stopped particles have been performed by the ATLAS, CMS and DØ collaborations [354, 358, 408–412], focusing on SUSY benchmark scenarios in which the stopped LLPs are R-hadrons [167, 413]. These are bound states formed after the production of strongly interacting supersymmetric particles, i.e. stops or gluinos, with quarks or gluons, such as $\tilde{g}q\bar{q}$, $\tilde{g}qqq$, $\tilde{g}g$ or $\bar{t}q$ [411].

5.1.2 Dedicated experiments

In the context of LLPs, it should be mentioned that besides the rather universal detectors, there are other detector designs developed specifically for the detection of LLPs, which are more sensitive to LLPs in some phase-space regions and/or with higher lifetimes. In this subsection, the three detectors MATHUSLA [414, 415], FASER [416, 417], and CODEX-b [418, 419] will be briefly introduced. Other detector designs are SHiP [420], AL3X [421] and ANUBIS [422].

5.1.2.1 MATHUSLA

The observability of LLP decays at general purpose collider experiments such as CMS and ATLAS is subject to the requirement that the decay occurs within the detector volume. This limits their ability to detect particles with very high lifetimes. Although even decays of very long-lived particles occur with some proportion within the detector volume, the triggers and the high background pose further limitations on the observable LLP decays and the LLP masses.

MATHUSLA [414, 415] is a detector proposal for the high-luminosity upgrade of the LHC (HL-LHC) that is currently in the process of being designed for the detection of displaced vertices of very long-lived neutral particles produced at one of the main experiments ATLAS or CMS. According to the design update given in ref. [415], it is supposed to be located at the earth's surface close to the CMS interaction point and have a decay volume with an area of 100 m × 100 m and a height of 25 m. The number of LLPs with $c\tau$ larger than about 100 m decaying in this decay volume is similar as for ATLAS or CMS. MATHUSLA has no particular trigger constraints, in contrast to ATLAS and CMS and benefits from an environment with background close to zero, the main sources of background being cosmic rays and muons generated in collision events of the HL-LHC. This makes it an interesting add-on to the existing underground collider experiment with regard to long-lived particle searches. If approved, it could start taking data around 2025 or 2026.

5.1.2.2 FASER

Supposing that long-lived particles have a low mass and interact only very weakly, they have a small production cross section and are predominantly produced with small transverse momentum p_T, i.e. in the *forward direction*. In this case they are likely to remain undetected in experiments like ATLAS and CMS, which commonly target signatures with high p_T and have not been conceived for detecting particles with very high pseudorapidities: At ATLAS and CMS, the forward calorimeters are limited to $|\eta| < 4.9$ [423] and $|\eta| < 5$ [424] respectively. The FASER experiment [416, 417], which will be part of the physics program of the Run 3 data taking period of the LHC, is devoted to the observation of decays of LLPs having these characteristics. The experiment is placed in a previously unused tunnel, at a distance of about 480 m in the direction of the beam axis from the interaction point of ATLAS. The detection of a particle with the above-mentioned properties could then be detected with FASER according to the following scheme [416]:

1. Collision event at the ATLAS interaction point:
$$pp \to \text{LLP} + X\,. \tag{5.1.1}$$
Here, X stands for all other final state particles of the event.
2. LLP propagation in the forward direction from the ATLAS interaction point towards the FASER detector.
3. LLP decay within the FASER detector volume into a pair of oppositely charged particles or photons with energies in the TeV range:
$$\text{LLP} \to e^+e^-, \mu^+\mu^-, \pi^+\pi^-, \gamma\gamma\,. \tag{5.1.2}$$

FASER vetoes charged particles entering the detector, such as muons produced at ATLAS. Magnets are used to separate the highly collimated LLP decay products, which otherwise would not be resolved by the detector as distinct tracks. A spectrometer with three tracking stations is used to determine, whether the tracks of the two oppositely charged particles can be traced back to the ATLAS interaction point. The total electromagnetic energy of the decay products is measured with an electromagnetic calorimeter, that is also used to identify electrons and photons. FASER is a relatively economical detector complementing the ATLAS experiment, which could allow to detect potentially copiously produced LLPs in a phase space region that is inaccessible to the ATLAS experiment.

5.1.2.3 CODEX-b

Another detector proposal for LLP detection purposes at the LHC is CODEX-b [418, 419]. Like MATHUSLA, it belongs to the class transverse detectors relative to the beam line. Its suggested location is in the cavern of LHCb within reach of its interaction point, at a distance of about 25 m. With a cubic fiducial volume of edge length of 10 m, it could observe decay vertices of LLPs in the pseudorapidity range $0.13 < \eta < 0.54$. To this end, it contains several tracking layers on the walls and different positions in the detector volume for the charged final state particles. Extensions of the suggested baseline design could allow, among other improvements, to observe LLP decays with neutral decay products. An existing shielding wall adjacent to CODEX-b and passive shielding near the interaction point together with active vetoes make of the fiducial volume a low-background environment.

5.2 Simulation of particle trajectories in the SFS framework

Long-lived particle searches typically rely on tracks of particles in the detector, positions of decay vertices relative to the primary interaction vertex and the track displacement variables d_0 and d_z, which are related to the point of closest approach of the track to the collision axis. Monte-Carlo generated events usually provide the exact positions of decay vertices in the decay cascades as well as the individual particle momenta of all intermediate and final state particles.

However, this *Monte-Carlo truth* information is only valid in the absence of detector effects on the quantities relevant for the physics analysis under consideration, or under the condition that these effects can be considered to be negligible. For instance, the tracks of charged particles are typically deliberately bent under the influence of a constant magnetic field in the detector volume in order to measure their momenta. This can of course also indirectly affect the trajectories of electrically neutral particles when they result from a decay chain that involves charged particles. While the effects might be negligible in many cases, the computational effort to simulate them exactly seems reasonable compared to the remaining work load in the analysis tool chain. Therefore, the Simplified fast detector simulation (SFS) framework [218], which applies smearing functions and reconstruction efficiencies to take detector effects into account, has been upgraded with a module for the re-calculation of particle trajectories in a constant magnetic field, hereafter referred to as *propagator module*. The purpose of this section is to first explain in section 5.2.1 the propagation of particles without the influence of a magnetic field and define the above-mentioned displacement variables for LLP studies, and to show in the next step in section 5.2.2 the consequences of a non-vanishing magnetic field on the tracks and these variables. Finally, a brief overview about the implementation of the effects in the propagator module is given in section 5.2.3.

5.2.1 Straight line propagation

This case applies to all electrically neutral particles or to all particles, if the magnetic field is zero or negligible. Consider a particle that is produced at the point described by the vector $\vec{x}_v = (x_v, y_v, z_v)$ in the laboratory frame, with the origin of the coordinate system at the primary interaction vertex of the particle collision and the z-axis directed along the momentum vectors of the colliding particles. The propagating particle can be unstable, in which case it is an intermediate particle of a decay chain, or it can be stable or long-lived enough to be considered stable on the length scale of the detector, i.e. it belongs to the final state of the collision event. It propagates along a straight line, i.e with a constant velocity $\vec{v} = (v_x, v_y, v_z)$ and momentum $\vec{p} = (p_x, p_y, p_z)$.

The production of the particle at the point $\vec{x}_v$ is assumed to take place at $t = 0$. For $t > 0$, the trajectory of the particle is then simply described by

$$\vec{x}(t) = \vec{x}_v + t\vec{v} = \vec{x}_v + \frac{c^2}{E} t\,\vec{p} \tag{5.2.1}$$

Here the relation between momentum and velocity, $\vec{p} = \gamma m \vec{v} = \frac{E}{c^2}\vec{v}$ was used. This parameterisation is valid until the eventual decay of the particle (or interactions with

other particles, which are not considered here). The example of a particle emerging from the decay of a neutral long-lived particle, which propagates along a straight line, is depicted in figure 5.1.

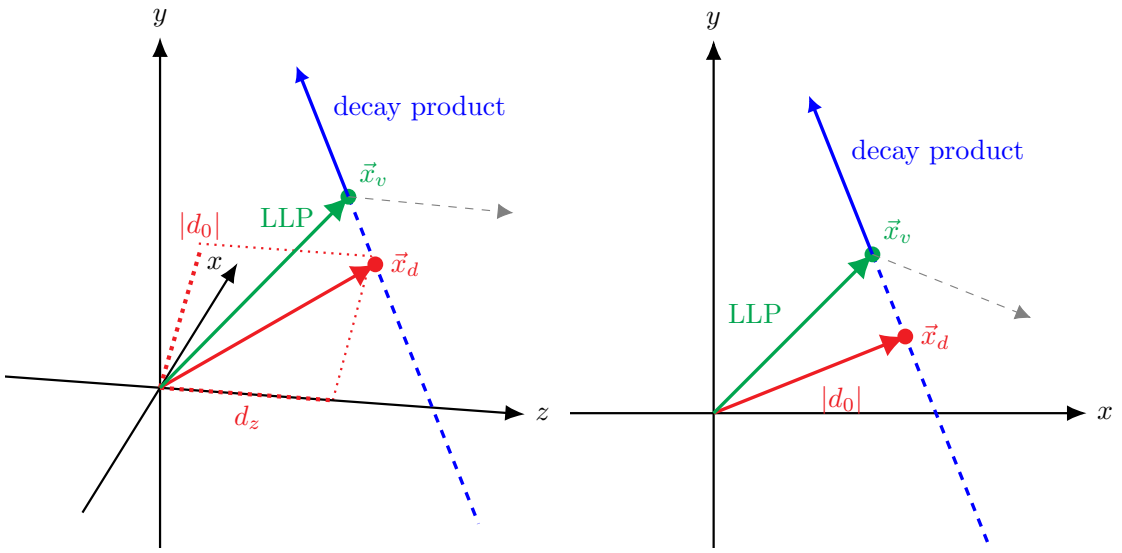

Figure 5.1: Example of a particle propagating along a straight line (blue), as described by eq. (5.2.1), in 3D (left) and a projection of the same situation on the x-y-plane (right). It is generated together with some other particle (grey) in the decay of a long-lived particle (green), which is produced at the origin and travels along the green line, until it decays at $\vec{x}_v$. The dashed blue line corresponds to the extrapolated trajectory, shown only for times preceding the production of the particle. The point of closest approach $\vec{x}_d$ (red) is the point on the extrapolated trajectory, which has the shortest distance to the z-axis, denoted by $|d_0|$. The sign of the transverse impact parameter d_0 corresponds to the sign of the z-component of the particle's angular momentum L_z. The longitudinal impact parameter d_z is the z-component of the point of closest approach $\vec{x}_d$.

5.2.1.1 Displacement variables

The *point of closest approach* $\vec{x}_d = (x_d, y_d, z_d)$ is defined from the track of the particle, described by eq. (5.2.1), pretending that it is valid for arbitrary times t, including values for times preceding the production of the particle. The term *closest approach* refers to the minimal distance to the z-axis (c.f. figure 5.1), or equivalently to the minimal magnitude of the projection of $\vec{x}(t)$ into the transverse plane,

$$\vec{x}_T(t) = \vec{x}_{v,T} + \frac{c^2}{E} t\, \vec{p}_T\,, \tag{5.2.2}$$

i.e. all vectors in this equations are two-component vectors with the x- and y-components of eq. (5.2.1). Evaluating the minimum condition of the magnitude $x_T(t) = \|\vec{x}_T(t)\|$ gives

$$\left.\frac{\mathrm{d}x_T(t)}{\mathrm{d}t}\right|_{t=t_d} = 0 \qquad \Rightarrow \quad t_d = -\frac{E}{c^2 p_T^2}\left(x_v p_x + y_v p_y\right) \tag{5.2.3}$$

and allows us to determine the corresponding point on the trajectory,

$$\vec{x}_d = \vec{x}(t = t_d) = \vec{x}_v - \frac{x_v p_x + y_v p_y}{p_T^2}\vec{p}, \tag{5.2.4}$$

in components

$$\begin{aligned} x_d &= x_v - \frac{p_x}{p_T^2}\left(x_v p_x + y_v p_y\right) , \\ y_d &= y_v - \frac{p_y}{p_T^2}\left(x_v p_x + y_v p_y\right) , \\ z_d &= z_v - \frac{p_z}{p_T^2}\left(x_v p_x + y_v p_y\right) . \end{aligned} \tag{5.2.5}$$

The *transverse impact parameter* d_0 is closely related to the distance between the point of closest approach and the z-axis, but it is defined as a signed quantity:

$$d_0 = \frac{x_v p_y - y_v p_x}{p_T} = \frac{L_z}{p_T} . \tag{5.2.6}$$

Here the numerator has been identified as the z-component of the angular momentum L_z, the sign of which takes into the corresponding sense of rotation around the z-axis. One can easily check using eqs. (5.2.4) and (5.2.6) that $|d_0| = \|\vec{x}_d\|$. It should be noted that d_0 could be calculated with the x- and y-components of any other point of the trajectory instead of x_v and y_v, since L_z is invariant along the straight line.
The *longitudinal impact parameter* d_z is simply the z-component of the point of closest approach:

$$d_z = z_d = z_v - \frac{p_z}{p_T^2}\left(x_d p_x + y_d p_y\right) . \tag{5.2.7}$$

Except for the special case where the trajectory is parallel to the z-axis, the point of closest approach, and hence also d_z are unique for a given trajectory.

5.2.2 Trajectories in a constant magnetic field

The deflection of electrically charged particles in a magnetic field goes back to the Lorentz force, given by

$$\vec{F}_L(t) = q\vec{v}(t) \times \vec{B} = \frac{qc^2}{E}\vec{p}(t) \times \vec{B} , \tag{5.2.8}$$

where q is the electric charge of the particle, $\vec{B}$ is the magnetic field, which is assumed to be constant in the following, and the velocity $\vec{v}(t)$ of the yet unknown trajectory $\vec{x}(t)$. The latter follows from the equation of motion obtained via Newton's second law:

$$\frac{\mathrm{d}\vec{p}(t)}{\mathrm{d}t} = \frac{qc^2}{E}\vec{p}(t) \times \vec{B} . \tag{5.2.9}$$

The magnetic field in the inner parts of a particle detector is usually parallel to the beam axis (here the z-axis) and constant in time. Different field configurations can be present in

other parts of the detector. For instance, the magnetic field in the ATLAS muon spectrometer is generated by toroid magnets both in the barrel and endcaps, leading to a different field configuration and bending of charged particles compared to the inner detector [425]. Here, it will be assumed for simplicity that the magnetic field is parallel to the z-axis and homogeneous over the entire space, so that it takes the form $\vec{B} = B\vec{e}_z$. Consequently, the validity of the following considerations is limited to the detector parts, where the above assumptions are fulfilled, i.e. in particular in the inner detector. However, for the purposes related to the long-lived particle searches studied in this work, this assumption seems sufficient, as will be discussed in more detail in section 5.2.4.
With this expression for $\vec{B}$, the cross product must be perpendicular to $\vec{e}_z$ and is independent of z-component of $\vec{p}(t)$. The differential equation, split into two equations for the transverse components and the z-component, reads:

$$\begin{aligned} \frac{\mathrm{d}\vec{p}_T(t)}{\mathrm{d}t} &= \frac{qc^2B}{E}\vec{p}_T(t) \times \vec{e}_z \\ &= \frac{qc^2B}{E}\left(p_y(t)\vec{e}_x - p_x(t)\vec{e}_y\right) , \\ \frac{\mathrm{d}p_z(t)}{\mathrm{d}t} &= 0 . \end{aligned} \tag{5.2.10}$$

The solution for the transverse components of the momentum describes a rotation in the transverse plane, while the z-component is a constant that is fixed by its initial value:

$$\begin{aligned} p_x(t) &= p_{0,x}\cos\omega t + p_{0,y}\sin\omega t , \\ p_y(t) &= -p_{0,x}\sin\omega t + p_{0,y}\cos\omega t , \\ p_z(t) &= p_{0,z} . \end{aligned} \tag{5.2.11}$$

Here, the *cyclotron frequency* is given by the expression

$$\omega = \frac{qc^2B}{E} . \tag{5.2.12}$$

With this result, after integrating $\vec{v}(t) = \frac{E}{c^2}\vec{p}(t)$ over time one obtains the trajectory $\vec{x}(t)$ with components

$$\begin{aligned} x(t) &= \left(x_v + \frac{p_{0,y}}{qB}\right) + \frac{1}{Bq}\left(p_{0,x}\sin\omega t - p_{0,y}\cos\omega t\right) \equiv x_h + \frac{R}{p_T}\left(p_{0,x}\sin\omega t - p_{0,y}\cos\omega t\right) , \\ y(t) &= \left(y_v - \frac{p_{0,x}}{qB}\right) + \frac{1}{Bq}\left(p_{0,x}\cos\omega t + p_{0,y}\sin\omega t\right) \equiv y_h + \frac{R}{p_T}\left(p_{0,x}\cos\omega t + p_{0,y}\sin\omega t\right) , \\ z(t) &= z_v + \frac{c^2p_z}{E}t . \end{aligned} \tag{5.2.13}$$

Projected into the transverse plane, this trajectory corresponds to a circle around the point $\vec{x}_h = (x_h, y_h)$ with radius R, where

$$x_h = x_v + \frac{p_{0,y}}{qB} , \qquad y_h = y_v - \frac{p_{0,x}}{qB} , \qquad R = \frac{p_T}{qB} , \tag{5.2.14}$$

whereas the z-component describes a uniform motion. In total, this describes a helix with a central axis parallel to the z-axis. The example, which was given for the case of straight line propagation in figure 5.1, is shown in figure 5.2 for charged decay products for particles following trajectories described by eq. (5.2.13).

Again, it is clear that this description is only valid until the particle decays or interacts, but in addition, variations of the magnetic field will have impact on the bending radius R, which is in particular the case when the particle leaves the detector and the magnetic field is no longer present. Note also that the effect of electromagnetic radiation emitted from the charged particle due to the bent trajectory (synchrotron radiation), which reduces its kinetic energy, is neglected here.

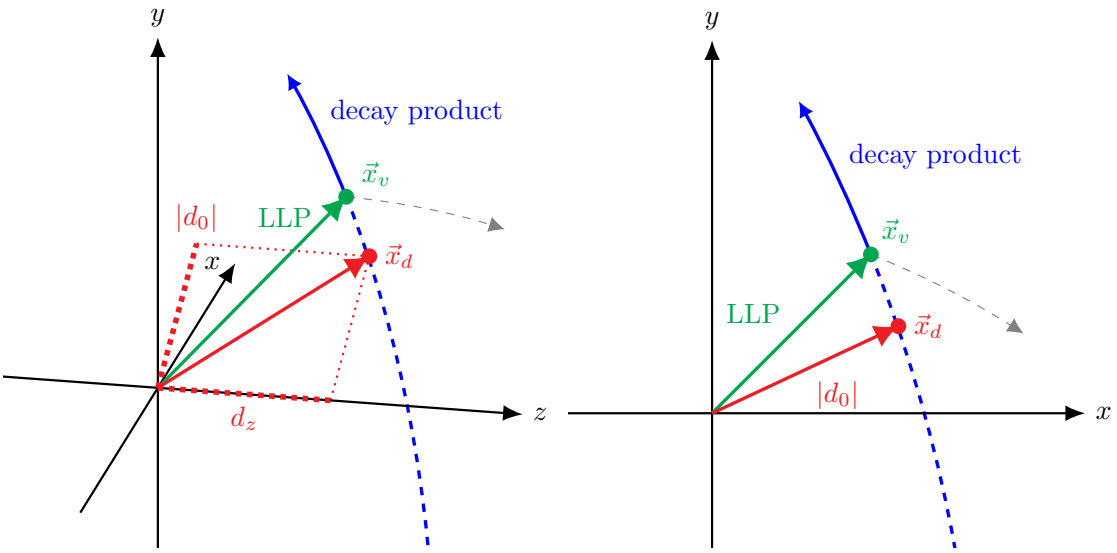

Figure 5.2: Example of a charged particle (blue), emerging from the decay of an electrically neutral long-lived particle, in correspondence to the situation in figure 5.1, propagating here under the influence of a constant magnetic field $\vec{B} = B_z\vec{e}_z$ along a bent trajectory. This situation is shown in 3D (left) and projected on the x-y-plane (right). The grey decay product is oppositely charged. Again, the extrapolation of the blue particle for the time before its creation is represented by the dashed blue line. As for the straight line propagation, the point of closest approach and the displacement variables d_0 and d_z are defined via the shortest distance in the transverse plane. In the limit of a vanishing magnetic field or high particle momenta, the trajectories approach the case of straight line propagation.

5.2.2.1 Displacement variables

As a consequence of the trajectory being a helix with an axis parallel to the z-axis, there are *in theory* infinitely many points with the smallest possible magnitude in the transverse plane $x_T(t) = \|\vec{x}_T(t)\|$, so there are infinitely many candidates for the point of closest approach with a spacing Δz between adjacent points [2]. An additional condition is

2. In the extreme case of a helix with an axis that coincides with the z-axis, *all* points would have the same magnitude R in the transverse plane and could hence be considered as possible points of closest approach. In practice, this case can safely be ignored, because it is highly unlikely that it ever occurs in

therefore needed to unambiguously define the point of closest approach.

Just as for the straight line propagation, the extremal condition on the magnitude in the transverse distance is evaluated to find a condition on the time t_d, but here it is important to insist on a positive second derivative as well to make sure that the transverse distance is indeed minimal, and not maximal. For the straight line propagation case, this was not necessary, since there is only a local minimum (unless the trajectory is parallel to the z-axis, which is highly unlikely). The condition on the first derivative constrains t_d as follows:

$$\left.\frac{\mathrm{d}x_T(t)}{\mathrm{d}t}\right|_{t=t_d} = 0 \qquad \Rightarrow \qquad \tan\omega t_d = \frac{p_{0,x}x_h + p_{0,y}y_h}{p_{0,x}y_h - p_{0,y}x_h}\,. \tag{5.2.15}$$

That this relation does not constrain t_d to imply minimum in the transverse distance from the z-axis, can be understood from the periodicity of the tangent, which is π, in contrast to the periodicity of the cosine and sine functions appearing in the parameterisation of the trajectory, which both have a periodicity of 2π. Between the maxima of the magnitude $x_T(t)$ for the circular motion in the transverse plane and the neighbouring minima, the argument of the cosine and sine functions change by a phase of π. Therefore, eq. (5.2.15) does not discriminate between maxima and minima.
Requiring in addition that the second derivative must be positive fixes rules out the local maxima of $x_T(t)$ and fixes ωt_d up to a multiple of 2π:

$$\begin{aligned} &\frac{\mathrm{d}^2x_T(t)}{\mathrm{d}t^2} > 0 \\ \Rightarrow \quad &\omega t_d = \arctan\Big(-\operatorname{sign}(R)(p_{0,x}x_h + p_{0,y}y_h), \\ &\qquad\qquad -\operatorname{sign}(R)(p_{0,x}y_h - p_{0,y}x_h)\Big) + 2\pi n\,, \qquad n \in \mathbb{Z}\,. \end{aligned} \tag{5.2.16}$$

It should be emphasised that this result does not contain the more commonly used one-argument function $\arctan(y/x)$ with return values from $(-\pi/2)$ to $\pi/2$, but instead the two-argument function $\arctan(y, x)$ [426], which is also referred to as arctan2 (or atan2) and is equivalent to the argument of a complex number $\arg(x + iy)$ [427]. Thus it returns values from $(-\pi)$ to π, according to the correct quadrant in which the complex number $z = x + iy$ is located, because it takes care of the sign of *both* arguments, whereas the one-argument function $\tan(y/x)$ uses the fraction of x and y and therefore cares only about the relative sign. Hence, eq. (5.2.16) makes sure that the trajectory reaches a *minimum* of the magnitude in the transverse plane at the time t_d, while the corresponding equation for the maxima would be obtained by either adding π or changing the sign of both arguments in the arctan function.

As explained earlier, the expression of t_d from eq. (5.2.16) together with the parameterisation of the trajectory in eq. (5.2.13) give rise to an infinite number of points of closest approach. Their x- and y-coordinates are identical, but they are separated by a temporal and spatial distance

$$\Delta t = 2\pi/\omega\,, \qquad \Delta z = \frac{2\pi c^2 p_z}{E\omega} = \frac{2\pi p_z}{qB}\,. \tag{5.2.17}$$

some event sample.

A unique definition of the point of closest approach must therefore comprise a selection criterion for t_d. Like the bending radius R, the distance Δz scales with the transverse momentum p_T, so that highly energetic particles most often have only one candidate point with minimum transverse magnitude that is in the detector volume, namely the one which is closest to the production vertex. For this reason, it seems most sensible to choose this point, rather than any of the other points potentially located far outside of the detector, which is singled out by setting $n = 0$ in eq. (5.2.16). The coordinates of the point of closest approach are then given by

$$\begin{aligned} x_d &= x_h \left(1 - \frac{|R|}{r_h}\right) , \\ y_d &= y_h \left(1 - \frac{|R|}{r_h}\right) , \\ z_d &= z_v + \frac{p_z}{qB} \arctan\Big(- \operatorname{sign}(R)(p_{0,x} x_h + p_{0,y} y_h), -\operatorname{sign}(R)(p_{0,x} y_h - p_{0,y} x_h)\Big) , \end{aligned} \tag{5.2.18}$$

where $r_h = \sqrt{x_h^2 + y_h^2}$ is the distance of the helix axis from the z-axis.

With this result, the absolute value of d_0 is easily calculated and the value of d_z is, as for the straight line propagation, equal to the z-component of the point of closest approach:

$$\begin{aligned} |d_0| &= \big||R| - r_h\big| , \\ d_z = z_d &= z_v + \frac{p_z}{qB} \arctan\Big(- \operatorname{sign}(R)(p_{0,x} x_h + p_{0,y} y_h), -\operatorname{sign}(R)(p_{0,x} y_h - p_{0,y} x_h)\Big) . \end{aligned} \tag{5.2.19}$$

Note that d_0 was previously defined as a signed quantity, which should also be the case for the propagation in a magnetic field. In particular, both definitions of d_0 ought to be consistent in the limit of a vanishing magnetic field $B_z \to 0$, in which the radius $|R|$ becomes infinitely large. Fortunately, the exact same definition of d_0 as in the straight line propagation case can be applied when the particle is placed at the point of closest approach on the helix, according to eq. (5.2.18). Obviously the result will be the same as if the particle propagated along a straight line through this point with the corresponding momentum. Inserting eq. (5.2.16) for $n = 0$ into eq. (5.2.11), the momentum at the point of closest approach, denominated as *perigee momentum* $\vec{p}^{\,(\text{perigee})}$, takes the form

$$\begin{aligned} p_x^{(\text{perigee})} &= p_x(t_d) = -\operatorname{sign}(R) \frac{y_h p_T}{r_h} , \\ p_y^{(\text{perigee})} &= p_y(t_d) = \operatorname{sign}(R) \frac{x_h p_T}{r_h} , \\ p_z^{(\text{perigee})} &= p_z(t_d) = p_{z,0} . \end{aligned} \tag{5.2.20}$$

Replacing the coordinates x_v, y_v and p_x, p_y in eq. (5.2.6) with the respective coordinates of $\vec{x}_d$ and $\vec{p}^{\,(\text{perigee})}$ yields

$$d_0 = \frac{x_d\, p_y^{(\text{perigee})} - y_d\, p_x^{(\text{perigee})}}{p_T} = \operatorname{sign}(R)\,(r_h - |R|) . \tag{5.2.21}$$

5.2.3 The propagator module of SFS

The previous subsections 5.2.1 and 5.2.2 each consider explicitly the propagation of a particle, either with or without bending of the trajectory, away from a production point $\vec{x}_v$. The possibility of the particle to decay further has already been mentioned, but not discussed extensively. A realistic simulation of a complete collision event in the detector environment of a collider experiment should in general account for complete decay chains, i.e. not only the final state particle trajectories are relevant, but also all intermediate particles. This makes a recursive procedure unavoidable. Additionally, the simulation algorithm must be able to properly handle particles of different electric charge, including neutral ones. Thus, unless the magnetic field is considered negligible, both cases of propagation, along a straight line or a bent trajectory, need to be applied in different places of the decay hierarchy. In praxis, a few simplifications with respect to the physically exact approach are appropriate, as will be explained below.

The simulation of magnetic field effects within MadAnalysis 5 using the particle propagator module is done in the following way: An event, which is part of a sample of simulated events provided by some Monte-Carlo event generator, has been read from file using the internal MadAnalysis 5 methods. It is represented by internal objects of different types, in particular for the various particles and their properties, such as four-vectors for the four-momentum and the decay vertex. The four-vectors are in general given in the laboratory frame. This information is part of the event record and was generated by the event generator under the assumption that there is no magnetic field. The role of the propagator module, in its current state, consists in modifying this information to account for a non-vanishing constant magnetic field $\vec{B} = B\vec{e}_z$, and compute corrected values of the decay vertex positions, the initial particle momenta after production, and the displacement variables d_0 and d_z, which include these effects.

The particle objects are organised in a tree-like structure that represents the decay hierarchy, in which each particle is assigned a set of parent and child particles, generically called *mothers* and *daughters*. The mother and daughter particle objects of a given particle object are accessible in the code via *pointer*[3] variables. This is used e.g. to obtain the position in space-time where the particle was produced, via the position of the decay vertex of the mother particle. A particle, which is the decay product of some other particle, has one mother, namely the decaying particle. The decay products of a particle are consequently its daughter particles. Occasionally, a particle can have more than one mother. This is possible, if it is produced directly in the hard scattering process from the colliding particles. Another possibility is the recombination of particles within hadronisation. These are special cases to the particle propagator module, which however do not introduce any additional complications, as will be explained below. Meanwhile, it shall be assumed that each particle has exactly one mother particle, except for the first particle of a decay hierarchy/tree, and some number of daughter particles, except for the particles which do not decay in the event. Each final state particle of the hard collision process is on top of such a decay tree. Apart from the particles being interconnected through mother-daughter relations, which effectively generates a tree-like structure, the whole set of particle objects

3. Pointers, a feature of the `C++` programming language [428], are a type of variable that can store the location of an object in memory [429].

is also part of a list. This list reflects the structure of the event in the event record format. While the exact details of the ordering of the particles within this list is not of interest here, it is important to remark that mother particles always come before their daughter particles. In other words, the list respects the time ordering of particle creation. It is therefore convenient and safe to perform the different calculations and the modifications of the particle properties following the order of this list of particle objects.

The central element of the propagator module is a method called `ParticlePropagator`, which takes as argument a particle object, executes the different steps in the calculations and manipulates the relevant properties of the particle object. Iterating through the list from the beginning, the first particles encountered are the initial state particles. These are the only particle objects in the list, for which the `ParticlePropagator` method is not called. The first relevant particle is one of the final state particles of the *hard event*. It is at the root of a decay tree. The production vertex of this particle is located at the origin of the coordinate system, which is defined to be the center of the particle collision, and its initial momentum is unaffected by the magnetic field. Furthermore, the time $t = 0$ coincides, per definition, with the collision. With this information, a parameterisation of the trajectory $\vec{x}(t)$ of the particle as a function of time t is known, depending on its electric charge either as a straight line through eq. (5.2.4) or as a helix through eq. (5.2.13). Also, the point of closest approach and the displacement variables are easily computed with the corresponding formulæ of the previous subsections. The variables d_0 and d_z are always computed both exactly and in the approximation of straight line propagation. Then, the new decay vertex position is computed by evaluating $\vec{x}(t)$ at the time of the decay. In principle, this is all that is needed for the current particle. However, there is one more important task, which needs to be accomplished in preparation for the computations with the daughter particles: While for the first particle in the decay tree the magnetic field has no impact on the *initial* momentum, it modifies the *final* momentum according to eq. (5.2.11), evaluated at the time of the decay, if the particle is charged. This modification is a rotation of the momentum in the x-y-plane. If the initial momenta of the daughter particles were left unchanged, momentum conservation at the decay vertex would generally be violated. For this reason, the same rotation concerns also the initial momenta of the daughter particles. In praxis, the rotation angle is determined with an existing function of MadAnalysis 5 and stored in a variable of the particle object, so that it is accessible at any moment for the calculations concerning the daughter particles.

In the subsequent iterations through the list of particle objects, there are usually other particles being produced directly in the hard process, which give rise to different decay trees and where the same procedure is applied. The remaining particle objects correspond to decay products of particles in different decay trees, i.e. they are at a lower position in the decay hierarchy. For these, the calculations can be done along the same lines with a few generalisations of the explained approach:

— The position $\vec{x}_v$ of the particle creation in the formulæ parameterising the trajectory is the point, where the mother particle decays. Likewise, the time $t = 0$ of the particle creation corresponds to the time $t_{\text{decay}}^{\text{mother}}$, at which the mother particle decays. In order for the formulæ to be valid, the time t to be used is the time relative to the decay time of the mother. Hence, for calculating the position and momentum at the decay, the formulæ must be evaluated at $t = \Delta t_{\text{prop}} = t_{\text{decay}}^{\text{particle}} - t_{\text{decay}}^{\text{mother}}$, where the

two decay times are given in the laboratory frame relative to the time of the particle collision. In the previously considered special case of particles produced in the hard process, the colliding particles are the mother particles and are considered in the algorithm as decaying particles at the origin $\vec{x}_v = \vec{0}$ at $t = 0$.

— The momentum must be rotated around the z-axis by the rotation angle stored in the corresponding variable of the mother particle object prior to proceeding with the parameterisation of the trajectory and the calculation of the related quantities. The momenta of particles at the root of a decay tree are not rotated, since the rotation angle stored in the mother particle objects (the colliding particles) is zero. For particles with more than one mother, the rotation angle of the first mother particle is used, which is a deliberate choice made in the implementation, which does not have any consequences: This situation is expected to occur only in two special cases: As mentioned above, a particle object can have the colliding particles as mothers. The other possibility can arise in the process of hadronisation, where particles are recombined into hadrons. In this case the recombining particles are the mothers of the resulting composite object. It can safely be expected that the rotation angle of the mothers is the same in these cases, as will be explained below.

— The rotation angle to be applied to the daughter particles is determined by calculating the rotation of the final momentum at the decay with respect to the initial momentum at the production and adding it to the value stored in the variable of the mother particle. In this way, a particle accumulates all the rotations of the previous particles in the decay chain.

— For particles at the end of a decay chain, i.e. without daughter particles, the calculation of the decay position is neither possible nor necessary. In this case, only the point of closest approach and the displacement variables are calculated.

Applying these principles iteratively to all particle objects in the list, the entire event can be corrected to include the effects of the magnetic field. A few more comments are in order: It has been mentioned that event records can contain particles which combine to hadrons, in which case the particle object for the hadron can have more than one mother. One could come up with the idea that the magnetic field could affect the trajectories of the combining particles and possibly alter in some way the recombination. In reality, there is no such risk, as these hadronisation processes take place on very short time scales, i.e. the lifetime of the recombining particles is zero.

If the time between creation and decay of a particle is very small (below some threshold defined in the code), the propagator module does not calculate the decay position at all, but it is simply set to its initial position. There are two reasons for this: On the one hand, there is a risk to introduce numerical instabilities, i.e. the displacement between production vertex and the calculated decay vertex can be significantly larger than the physically correct result, which is related to the precision of the types of number variables used in the calculations. This becomes particularly important, when the trajectory of a charged particle is only slightly bent. In this case, the helix radius in the parameterisation of the trajectory is huge. If the time interval Δt for the propagation is very small, then the position of the decay is $\vec{x}(t) \approx \vec{x}_v$, which according to eq. (5.2.13) requires enormous cancellations in the x- and y-components between the $p_{0,x}/(qB)$ or $p_{0,y}/(qB)$ term and the sine and cosine terms. In other words, the subtraction of a very large number from a

very large number should give a very small number. This is likely to fail due to the limited numerical precision of the calculations, i.e. the calculated distance between production and decay vertex would be much bigger than for the mathematically correct result. For this reason, it is safer in these cases to use the approximation that the particle decays where it was created, without any impact on its momentum. Another reason is the performance of the code. As a functionality which operates on practically all particles of an event, the particle propagator module should avoid putting efforts into the calculation of negligible effects, which would unnecessarily slow down the already computationally intensive analysis process of MadAnalysis 5. However, the effect of this module on the performance seems to be rather unimportant. In addition, the module is not active by default, i.e. it is irrelevant for analyses which do not need to include the effect of a magnetic field or use the displacement variables. For very small electric charges or very small magnetic fields, the bending is also negligible. Therefore, in these cases the straight line propagation is used. To illustrate the structure and of the particle propagator module, its behaviour is summarised in terms of pseudo-code in algorithm 1.

Data: Ordered list of all particle objects associated with a collision event (initial+intermediate+final)
Result: List of all particle objects with corrected initial momenta and decay vertices as well as the displacement variables d_0, d_z and the point of closest approach
for *particle in particle list* **do**
  if *particle is not initial* **then**
    rotate momentum with rotation angle of the first mother particle;
    calculate propagation time in lab frame:
      $\Delta t_{\text{prop}} = t_{\text{decay}}^{\text{particle}} - t_{\text{decay}}^{\text{parent}}$;
    calculate the point of closest approach, d_0 and d_z assuming straight line propagation;
    if $B \approxeq 0$ *or particle has charge* $|q| \ll e$ **then**
      set rotation angle equal to rotation angle of first mother;
      calculate decay vertex position in straight line propagation;
    else
      calculate helix parameters R, x_h, y_h, r_h;
      calculate the point of closest approach, d_0 and d_z assuming helix propagation (keeping the straight line values as approximate values);
      calculate momentum components p_x^{final} and p_y^{final} at the decay;
      calculate rotation angle of the particle object from components of the initial and final momentum p_x^{initial}, p_y^{initial}, p_x^{final}, p_y^{final};
      calculate decay vertex in helix propagation;
    end
  end
end

Algorithm 1: Pseudo-code for the particle propagator module of SFS in MadAnalysis 5.

5.2.4 Impact and limitations of the propagator module

The propagator module that has been described in section 5.2.3 serves essentially two purposes: On the one hand, the particle trajectories of intermediate charged particles in the presence of a magnetic field $\vec{B} = B\vec{e}_z$ are bent around an axis that is parallel to the z-axis, which would otherwise just propagate along a straight line, resulting in a correction of the decay vertex positions. On the other hand, the impact parameters d_0 and d_z are determined based on extrapolations of the particle trajectories, which also include this bending. For the analyses considered in sections 5.3 and 5.4, which rely on both the displaced vertex positions and the impact parameters, the effects simulated by the propagator module are sufficient. In these analyses, the displaced vertex positions are required to be in a fiducial volume which is part of the inner detector volume, where the assumption of a homogeneous magnetic field parallel to the z-axis is realised. Apart from these effects, another side effect is the modification of some of the final state momenta, which are rotated around the z-axis. It is important to note that the final state momenta computed by the propagator module are the momenta of the final state particles right after their production. In other words, the simulation does not include any propagation of final

state particles in the detector volume. In order for such a propagation to be meaningful, it would be necessary to specify to which point the particle propagation should end. For example, the particles could be propataged to the surface of a cylinder that could represent a simple model of the geometry of the tracker. It would be straightforward to extend the propagator module with such a feature, but it is currently restricted to the effects, which are potentially relevant for the analyses presented in this work. A possible consequence of the propagation of final state particles could be the effect that soft final state hadrons follow a helix trajectory with small radius, such that they propagate towards one of the endcaps of the tracker instead of escaping it by traversing barrel detector parts. Simulating such a behaviour could prevent these hadrons from being clustered into a jet and therefore have some effect on the jet properties.

In order to appreciate the effect of the particle propagator module on event samples and check whether it works as expected, a sample of 50 000 Monte-Carlo events of the signal process in the CMS analysis presented in section 5.3 has been used. This section contains more details on the signal model and process, which will however not be relevant here. The simulated hard process is stop pair production

$$pp \quad \rightarrow \quad \tilde{t}_1 \tilde{t}_1 \,, \tag{5.2.22}$$

where the stop $\tilde{t}_1$ is assumed to be long-lived, here with a lifetime corresponding to $c\tau = 1\,\mathrm{m}$, whereas the mass of the stop will be varied. After production, the stops are confined into R-hadrons, some of which are charged. The masses of the R-hadrons are almost equal to the stop mass. There are three stop decay modes $\tilde{t}_1 \rightarrow b\ell$ with branching ratios $\mathrm{Br}(\ell) = 1/3$ for $\ell = e, \mu, \tau$, which are responsible for the R-hadron decays. Only the electron and muon decay modes will be relevant here.

In a first step, it will be checked whether the rotation angle between the initial and final momenta of the long-lived R-hadrons, caused by the bending of the trajectories, is consistent with the expectations from the mass and lifetime of the R-hadrons. According to eq. (5.2.12), this rotation angle for a particle decaying after a time t in the lab frame (or t_0 in its rest frame) is obtained via

$$\begin{aligned} \Delta\varphi = \omega t = \frac{qc^2 B}{E} t = \frac{qc^2 B}{E} \gamma t_0 = \frac{qc^2 B}{E} \frac{E}{mc^2} t_0 \\ = qcB \frac{ct_0}{mc^2} \,, \end{aligned} \tag{5.2.23}$$

so for a given stop mass and a fixed magnetic field, the rotation angle of the momentum is proportional to the decay time in the particle's rest frame.

With a magnetic field $B = 4\,\mathrm{T}$ and a charge $q = \pm e$, the factor qcB evaluates to

$$qcB \approx \pm 3 \times 10^8 \times 4\,\mathrm{eV/m} = \pm 1.2\,\mathrm{GeV/m} \,. \tag{5.2.24}$$

Considering three different stop masses of 20, 100 and 700 GeV and supposing that the particle decays after the mean lifetime, $ct_0 = c\tau = 1\,\mathrm{m}$, one obtains a momentum rotation $\Delta\varphi$ of 0.06, 0.012 and 0.0017 rad respectively. This calculation gives a rough idea of the order of magnitude for the momentum rotation that can be expected for the given lifetime.

A more detailed comparison of the expected and observed effect can be done using histograms in $\Delta\phi$. These were generated using MadAnalysis 5 in its *expert mode* by

writing a simple analysis, which selects only events with exactly one electron and one muon in the final state. In this way, the two long-lived R-hadrons, from which they must originate, can be accessed via pointers to the mother particle objects. In particular, the analysis identifies via the PDG-codes [430] of the particles the following singly-charged R-hadrons involving the stop, and their anti-particles:

$$R^+_{\tilde{t}_1\bar{d}}\,, \quad R^+_{\tilde{t}_1\bar{s}}\,, \quad R^+_{\tilde{t}_1\bar{b}}\,, \quad R^+_{\tilde{t}_1 u d_0}\,, \quad R^+_{\tilde{t}_1 u d_1}\,, \quad R^+_{\tilde{t}_1 s u_0}\,, \quad R^+_{\tilde{t}_1 s u_1}\,.$$

Their $\Delta\varphi$ value is taken from the corresponding variable of the particle object, where it has been stored beforehand by the particle propagator module, and a corresponding histogram entry is generated.

To derive the expected shape of the histogram, the probability distribution of the decay time is needed. The probability of an unstable particle with decay constant $\Gamma = \frac{1}{\tau}$ to decay in a time interval $[t_0, t_0 + \mathrm{d}t_0]$ (where the subscript 0 indicates that the time is given in the particle's rest frame) is given by $p(t_0)\mathrm{d}t_0$, where $p(t_0)$ is a probability density of the form [431]

$$p(t_0) = \Gamma e^{-\Gamma t_0}\,. \tag{5.2.25}$$

Let $\Delta t_{0,\mathrm{bin}}$ be the time interval corresponding to the interval $\Delta\varphi$ of a bin in the histogram. Then the number of LLPs decaying within in the φ-interval of bin i is calculated via

$$\begin{aligned} N_i &= N_{\mathrm{LLPs}} \int_{t_{0,i}}^{t_{0,i}+\Delta t_{0,\mathrm{bin}}} \mathrm{d}t_0\, p(t_0) \\ &= N_{\mathrm{LLPs}} \left(e^{-\Gamma t_{0,i}} - e^{-\Gamma(t_{0,i}+\Delta t_{0,\mathrm{bin}})} \right) \end{aligned} \tag{5.2.26}$$

where N_{LLPs} is the total number of selected R-hadron decays (corresponding to twice the number of selected events).

Figure 5.3 shows the histograms for the rotation angles of the selected R-hadron decays as well as the theoretical expectations according to eq. (5.2.26). The obtained histograms are in excellent agreement with the expectations, confirming that the propagator module works as it should for the given samples.

The same samples and selected events can be used to observe the difference between the exact and approximate formuale of the impact parameters d_0 and d_z. Here, only the relative difference between the two formulae for d_0 shall be studied, given by

$$\delta d_0 = \frac{d_0 - d_{0,\mathrm{approx}}}{d_{0,\mathrm{approx}}}\,. \tag{5.2.27}$$

This quantity is evaluated for the electrons and muons produced in the selected $\tilde{t}_1/R$-hadron decays. The results are shown in figures 5.4 and 5.5. No significant difference between the electron histograms and the corresponding muon histograms can be observed. However, the mass of the long-lived R-hadrons plays an important role. The lower the LLP mass, the bigger the difference between the exact and the approximate formula. This can be understood via the fact that a low mass leads to a high relativistic gamma factor for a given total energy, which is relevant for the lifetime of the LLP in the laboratory frame and therefore for the distance of the electron or muon production vertex from the

primary vertex. As a consequence, also the difference between the two formulas for d_0 becomes more important.

Even though the histograms in figures 5.3-5.5 show effects of the propagator module, these do not necessarily have important consequences on the results of an analysis. In particular, no significant difference was observed for the analyses presented in sections 5.3 and 5.4 with and without the presence of a magnetic field.

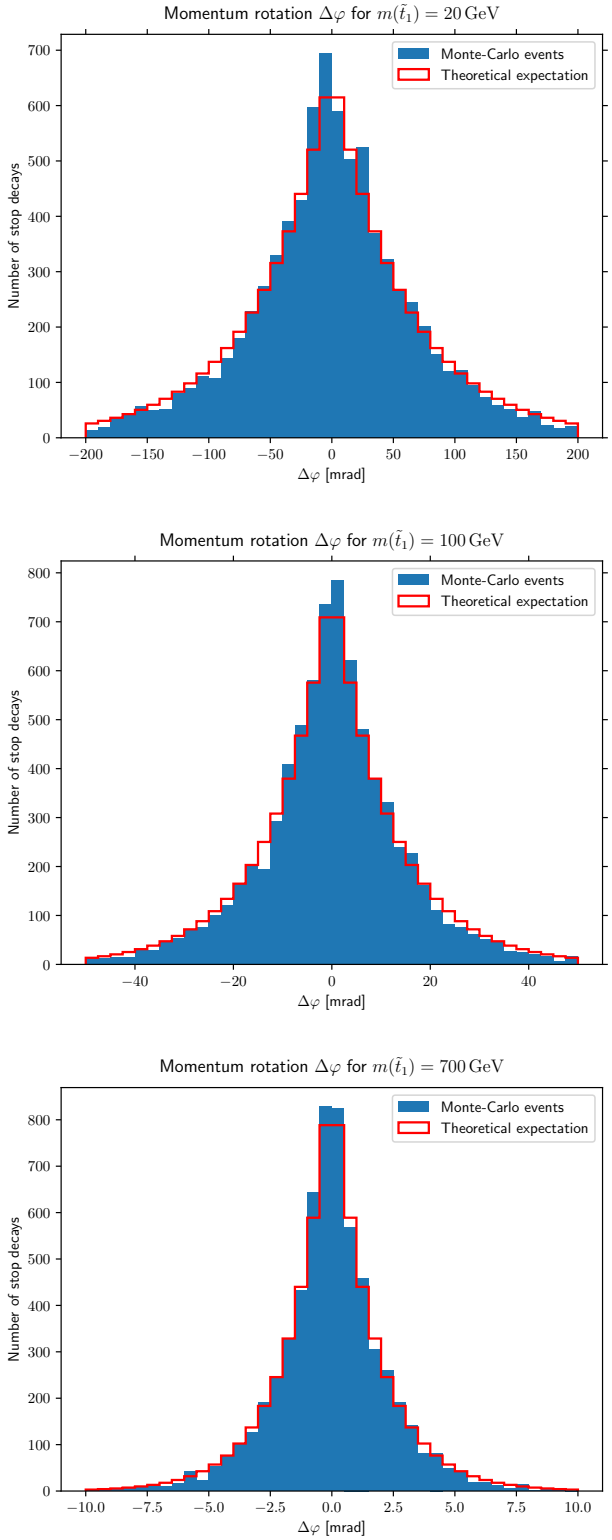

Figure 5.3: Histograms of the rotation angle between the initial and final momenta of selected singly-charged R-hadrons involving the stop $\tilde{t}_1$, which follow a bent trajectory under the influence of a magnetic field $\vec{B} = B\vec{e}_z$. The histograms were generated with Monte-Carlo event samples for three different stop masses. All selected long-lived R-hadrons have roughly the same mass as the stop.

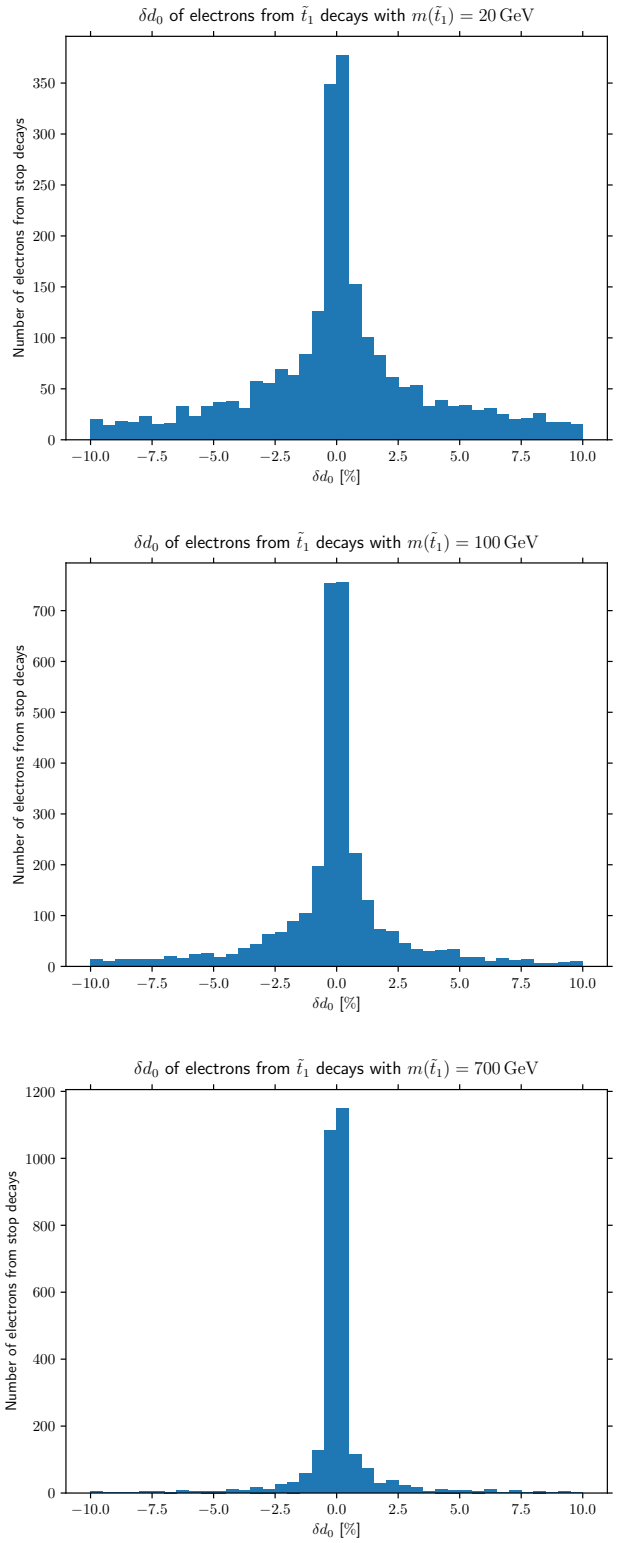

Figure 5.4: Relative difference δd_0 between the exact and approximate formulæ of d_0 for electrons originating from the decay of the selected long-lived R-hadrons for samples of three different stop masses.

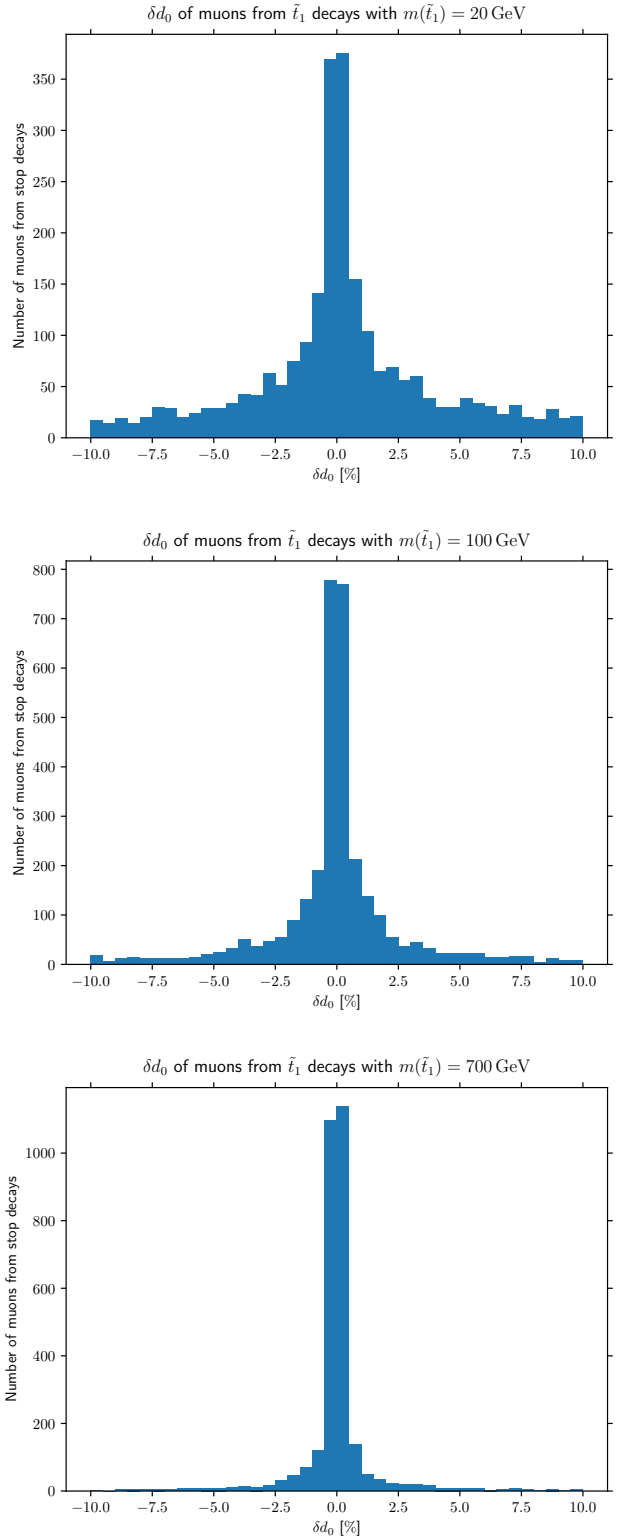

Figure 5.5: Relative difference δd_0 between the exact and approximate formulæ of d_0 for muons originating from the decay of the selected long-lived R-hadrons for samples of three different stop masses.

5.3 Displaced leptons in the $e\mu$ channel (CMS-EXO-16-022)

The analysis presented in ref. [355] is a search for long-lived particles which decay into a pair of charged leptons, precisely one electron and one muon. It has been carried out by the CMS collaboration in 2015, i.e. at the beginning of the Run-2 data-taking period of the LHC at $\sqrt{s} = 13\,\text{TeV}$ with a data-sample corresponding to an integrated luminosity of $2.6\,\text{fb}^{-1}$. This search supersedes the 8 TeV analysis described in ref. [375]. The electrons and muons, which potentially originate from LLP decays, are identified via the transverse distance of their tracks from the primary interaction vertex, i.e. via the transverse impact parameter d_0. The analysis targets events with exactly one electron-muon pair with displaced tracks. The selected events are categorised into three signal regions, depending on the two values of d_0, c.f. table 5.4. No significant excess over background has been observed in the data sample. The signal model for which the results of the analysis are interpreted is the *Displaced Supersymmetry* model [432], which goes beyond the MSSM by introducing a hidden sector that breaks R-parity via the introduction of bilinear superpotential terms of the form

$$W \supset \mu_{L,i} L_i H_u \,, \tag{5.3.1}$$

leading to mixing between the (scalar) leptonic fields and the Higgs(ino) fields. All other R-parity violating operators are assumed to be suppressed. Going to the mass eigenbasis, the bilinear terms in the previous equations generate the following superpotential terms:

$$W \supset \epsilon_i y^d_{jk} L_i Q_j D_k + \epsilon_i y^e_{jk} L_i L_j E_k \,. \tag{5.3.2}$$

Here $\epsilon_i = \frac{\mu_{L,i}}{\mu}$ is the mixing angle, with μ being the coefficient in the bilinear (R-parity conserving) superpotential term $\mu H_u H_d$. These terms violate lepton number. Constraints from proton decay are avoided by the suppression of baryon number violating operators, since both B and L must be violated for the proton decay to occur. Under the premise that $\mu_i \ll \mu$, the mixing angle is small. The new operators would allow the lightest supersymmetric particle (LSP) to decay to SM particles, leading to weaker constraints from missing energy searches. Furthermore, if the mixing angle is sufficiently small, the LSP could be long-lived such that it escapes prompt searches. In the CMS displaced leptons search it is assumed that the top squark $\tilde{t}_1$ is the LSP and is considered as the LLP candidate. The first term in eq. (5.3.2) is responsible for the decays $\tilde{t}_1 \to b\ell$ with $\ell = e, \mu, \tau$, which happen with equal branching ratio of 1/3 for all leptons, if lepton flavour universality is assumed.

An implementation of this analysis [433] is already part of the DELPHES-based Public Analysis Database (PAD) [216] of MADANALYSIS 5 and has now been adapted to the SFS framework. The details of the new implementation are documented in this section. While the selection criteria are rather straightforward to apply, the major difficulty in this search is the lack of information about the lepton detection efficiencies for highly displaced tracks. Since the CMS collaboration does not provide publicly available auxiliary material for the re-implementation of this particular analysis, we have to rely on information related to the superseded analysis [375], published in [434]. However, this rudimentary approach is not a very satisfactory solution and limits the reliability of the analysis for recasting other models. This matter will be discussed more extensively in sections 5.3.2 and 5.3.3.

5.3.1 Selection criteria

The event selection of this analysis can be divided into two stages: In a first step, the *preselection*, only events which fulfill a certain number of requirements such as the types of reconstructed objects and their kinematics as well as isolation criteria are accepted. The selected events are then distributed among different signal and control regions. Note that the transverse impact parameter d_0 is a signed quantity, but the analysis does not take into consideration the sign, so only the absolute value $|d_0|$ is used. In the following, a more detailed description of the selection criteria and the definitions of the event regions is given.

5.3.1.1 Preselection

The analysis targets events with exactly one electron and one muon in the final state, which are clearly identified as such and which fulfill all preselection cuts. The particle reconstruction is done with the particle-flow event reconstruction algorithm [435] based on information from the different detector parts of CMS, which are combined to reconstruct the stable particles, i.e. identify their types and determine the flight direction and energy. More specifically, independently reconstructed tracks from hits in the inner tracker and in the muon system are combined for the reconstruction of muon candidates [436], whereas electron candidates are reconstructed based on the combination of hits in the inner tracker and clusters of energy deposit in the electromagnetic calorimeter [437].

The electron and muons candidates must fulfill the following requirements in the preselection stage: The imposed lower bounds on the p_T values are different for electrons (42 GeV) and muons (40 GeV). In both cases, the absolute value of the pseudorapidity $|\eta|$ must not exceed the value 2.4, which is explained by the acceptance of the CMS detector. Furthermore, electrons in the overlap region of the barrel and endcap detectors ($|\eta|$ between 1.44 and 1.56 [375]) are rejected due to a lower detector performance compared to the other detector regions. In addition the leptons must satisfy isolation conditions, which impose an upper limit on an isolation variable p_T^{iso} defined as the scalar sum of p_T of all other particles reconstruction with the particle-flow algorithm within a cone with a specified size $\Delta R = \sqrt{(\Delta\eta)^2 + (\Delta\phi)^2}$ around the lepton's momentum. The limit on the isolation sum is fixed by the lepton momentum and in the case of electrons also depends on $|\eta|$, since different values are used in the barrel and endcap regions of the detector. A summary of the selection criteria of electron and muon candidates considered in the event preselection, including the relevant values for the isolation cone, is given in table 5.2.

Having identified a set of electrons and muons in the final state of an event according to the above requirements, the acceptance of the event is conditioned by the following rules:

— The set of selected leptons must contain exactly one electron and one muon.

— The leptons must carry opposite charge.

— The electron and muon momenta must be separated by $\Delta R > 0.5$.

Besides these criteria, which are given explicitly in the analysis summary, additional conditions adopted from [434] and slightly modified are imposed on the position of the

	Electrons	**Muons**
Transverse momentum	$p_T > 42\,\text{GeV}$	$p_T > 40\,\text{GeV}$
Pseudorapidity	$\lvert\eta\rvert < 1.44$ **or** $1.56 < \lvert\eta\rvert < 2.4$	$\lvert\eta\rvert < 2.4$
Isolation cone	$\Delta R < 0.3$	$\Delta R < 0.4$
Isolation variable		
barrel ($\lvert\eta\rvert < 1.44$)	$p_T^{\text{iso}} < 0.035\,p_T$	$p_T^{\text{iso}} < 0.15\,p_T$
endcaps ($\lvert\eta\rvert > 1.56$)	$p_T^{\text{iso}} < 0.065\,p_T$	

Table 5.2: Summary of selection criteria of electrons and muons imposed in the preselection.

production vertex $\vec{v}_{\text{prod}} = (v_x, v_y, v_z)$ of the leptons relative to the primary vertex. These requirements, which are identical for the electron and the muon, are:

$$v_0 = \sqrt{v_x^2 + v_y^2} < 10\,\text{cm}\,, \qquad v_z < 30\,\text{cm}\,. \tag{5.3.3}$$

The superseded analysis [375], for which the information in [434] was originally made available, give these criteria with an upper bound on v_0 of 4 cm. Even though these requirements are not explicitly justified, and are not even mentioned in the selection criteria of either of the analyses, it is likely that they are related to the reconstruction performance of the CMS tracker. Therefore, it has been decided to include them into the implementation, but with a higher upper limit on v_0. This is motivated by the design of the new analysis, which is supposed to probe values of $|d_0|$ up to 10 cm. From the definition of d_0, it follows that $|d_0| \leq v_0$. Therefore the upper bound on v_0 has been raised to 10 cm.

5.3.1.2 Control and signal regions

Several regions are defined to classify the events solely on the basis of both lepton transverse impact parameters $|d_{0,\ell}|$, as they are strongly correlated with the lifetime of the supposed long-lived particle, from which the selected leptons might originate. The regions are defined in the $(d_{0,e}, d_{0,\mu})$ space and cover absolute values $|d_{0,\ell}|$ ranging from zero to 10 cm.

The analysis note shows four different background control regions (CR), which are used to verify the consistency of the Monte-Carlo simulations carried out for the background estimates by the CMS collaboration. These regions are given here for completeness, but they are not part of the implementation in MadAnalysis 5 since they are not used to determine exclusion limits for production cross-sections of the signal process. The first control region (CR I) collects events characterised by a prompt electron-muon pair, i.e. with small transverse displacement $|d_0| < 100\,\mu$m for both, while the second control region (CR II) requires a somewhat bigger displacement of $100\,\mu\text{m} < |d_{0,\ell}| < 200\,\mu$m for both leptons. The remaining two control regions (CR III+IV) allow one of the leptons to be highly displaced, while for the other one only a small displacement is tolerated. There is

some overlap of these two regions, which corresponds to CRII. The exact definitions of all control regions are listed in table 5.3.

Control region		Defining cuts
CR I:	*Prompt Control region*	$\lvert d_0\rvert_{e,\mu} < 100\,\mu\text{m}$
CR II:	*Displaced Control Region*	$100\,\mu\text{m} < \lvert d_{0,\ell}\rvert < 200\,\mu\text{m}$ for $\ell = e, \mu$
CR III:	*Displaced Electron Region*	$100\,\mu\text{m} < \lvert d_{0,e}\rvert < 10\,\text{cm}$ $\lvert d_{0,\mu}\rvert < 200\,\mu\text{m}$
CR IV:	*Displaced Muon Region*	$100\,\mu\text{m} < \lvert d_{0,\mu}\rvert < 10\,\text{cm}$ $\lvert d_{0,e}\rvert < 200\,\mu\text{m}$

Table 5.3: Definition of the control regions conforming to table 1 of ref. [355].

The analysis uses three different signal regions (SR), which classify events according to the smaller of two absolute values $|d_{0,e}|$ and $|d_{0,\mu}|$. In other words, each region imposes a lower bound on $|d_0|$ that *both* leptons must respect. The lower bound is 200 μm for SR I, 500 μm for SR II and 1000 μm for SR III. Simultaneously, there is no overlap between the signal regions. For instance, an event that falls into SR III is excluded from SR I and SR II. The criteria for the signal regions are summarised in table 5.4. A graphical representation of both the signal and the control regions is given in figure 5.6.

Signal region		Defining cuts
SR I:	*Loose Search Region*	$\lvert d_{0,\ell}\rvert > 200\,\mu\text{m}$ for $\ell = e, \mu$ $\lvert d_{0,e}\rvert < 500\,\mu\text{m}$ **or** $\lvert d_{0,\mu}\rvert < 500\,\mu\text{m}$
SR II:	*Medium Search Region*	$\lvert d_{0,\ell}\rvert > 500\,\mu\text{m}$ for $\ell = e, \mu$ $\lvert d_{0,e}\rvert < 1000\,\mu\text{m}$ **or** $\lvert d_{0,\mu}\rvert < 1000\,\mu\text{m}$
SR III:	*Tight Search Region*	$\lvert d_{0,\ell}\rvert > 1000\,\mu\text{m}$ for $\ell = e, \mu$

Table 5.4: Definition of the signal regions conforming to table 1 of ref. [355]. In addition to the criteria listed explicitly, all regions respect the $|d_0|$ upper cut of 10 cm for both leptons.

5.3.2 Efficiencies

As mentioned earlier, no dedicated supplementary material is made public for this analysis, making it difficult to accurately model detector effects under the conditions when the data for this analysis was recorded. It is common practice to parameterise the detection efficiency of prompt leptons in terms of kinematic variables such as p_T and η. Though, the focus of this analysis is on displaced leptons and consequently builds upon the reconstruction of their tracks. The reconstruction efficiency must therefore be included into the implementation of the analysis and it is natural to expect that it depends in some way on the displacement relative to the primary vertex.

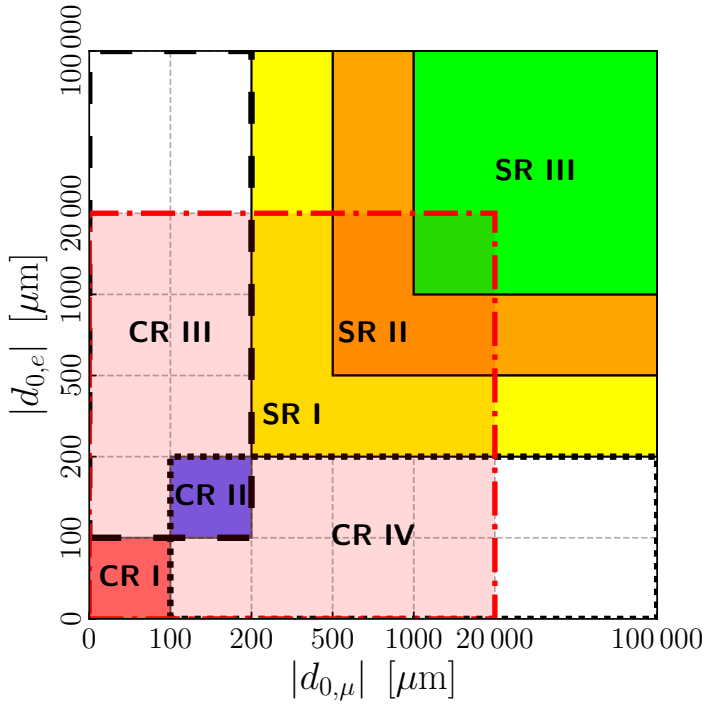

Figure 5.6: Graphical representation of the control and signal regions, generated on the basis of figure 1 in ref. [355]. The squared area enclosed by the red dash-dotted line corresponds to the range in which the d_0-dependence of the electron and muon reconstruction efficiency given by [434] (supplementary material of the superseded analysis [375]) is assumed.

Presumably the most sensible strategy to cope with the lack of information is to resort to the available contents provided for the superseded analysis [375] in [434], specifically the two plots of the $|d_0|$-dependent reconstruction efficiencies for electrons and muons (c.f. figure 5.7). Clearly, this can only serve as an approximation that introduces a systematic uncertainty into results obtained from this re-implementation. Besides the increased center-of-mass energy (13 TeV vs. 8 TeV), many modifications on hardware and software could have altered the reconstruction efficiencies, which is impossible to assess without being involved in the internal procedures of the experimental collaboration. Even more problematic is the fact that the provided efficiencies only cover the range $|d_0| < 2\,\text{cm}$, corresponding to the coverage of the signal regions of the superseded analysis. On the other hand, the Run-2 analysis which is presented here allows for higher transverse impact parameters up to 10 cm in *all* signal regions. The parts of the signal regions covered by the efficiencies from [434] is highlighted in red in figure 5.6. Outside of this region, one can only speculate about the behaviour of the $|d_0|$-dependence of the reconstruction efficiencies.

Instead of using the tabulated values for the reconstruction efficiencies, a polynomial fit was realised by the author of [433], which is also used in the new implementation and

is valid for $|d_0| < 2\,\text{cm}$:

$$\begin{aligned}\epsilon_{\text{reco},e}(|d_0|) =& 0.924921 - 0.917957\left(\frac{|d_0|}{\text{cm}}\right) + 0.522007\left(\frac{|d_0|}{\text{cm}}\right)^2 + 2.87189\left(\frac{|d_0|}{\text{cm}}\right)^3 \\ & - 4.9321\left(\frac{|d_0|}{\text{cm}}\right)^4 + 2.72756\left(\frac{|d_0|}{\text{cm}}\right)^5 - 0.506107\left(\frac{|d_0|}{\text{cm}}\right)^6 ,\end{aligned} \tag{5.3.4}$$

$$\begin{aligned}\epsilon_{\text{reco},\mu}(|d_0|) =& 0.99067 - 0.271852\left(\frac{|d_0|}{\text{cm}}\right) + 0.743217\left(\frac{|d_0|}{\text{cm}}\right)^2 - 0.611108\left(\frac{|d_0|}{\text{cm}}\right)^3 \\ & - 0.260292\left(\frac{|d_0|}{\text{cm}}\right)^4 + 0.423266\left(\frac{|d_0|}{\text{cm}}\right)^5 - 0.111279\left(\frac{|d_0|}{\text{cm}}\right)^6 .\end{aligned} \tag{5.3.5}$$

The tabulated efficiencies and the fits are shown in figure 5.7. Above transverse impact

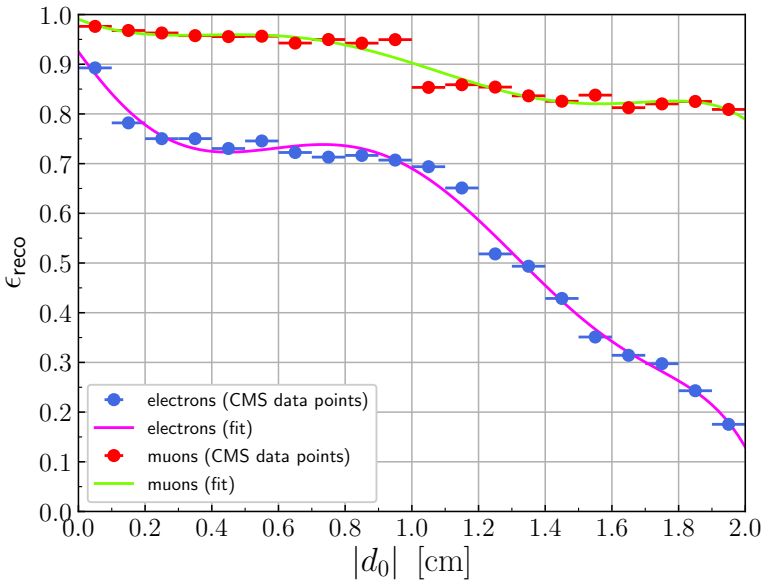

Figure 5.7: Reconstruction efficiencies of electrons and muons [434] of the superseded CMS analysis [375]. The plot was generated with data files from the corresponding HEPData entry [438, 439]. Polynomial fits for this data as described in eqs. (5.3.4) and (5.3.5) are shown, which were generated by the authors of [433] and will also be used in the new implementation of the more recent analysis.

parameters of 2 cm, it is assumed that the reconstruction efficiencies drop with a constant slopes from the approximate values at $|d_0| = 2\,\text{cm}$, which are 0.8 for muons and 0.15 for electrons. For muons, a slope of $0.1\,\text{cm}^{-1}$ is used, motivated by the observed reduction of the efficiencies below 2 cm. For electrons, it is assumed that they are reconstructable in the entire range of the transverse impact parameter below 10 cm, which is of interest in the analysis, but the efficiency is zero above this value. Thus, the efficiencies are described

by

$$\epsilon_{\text{reco},e}(|d_0|) = 0.15 - \frac{0.15}{8\,\text{cm}} \times (|d_0| - 2\,\text{cm}) \qquad \text{and} \tag{5.3.6}$$

$$\epsilon_{\text{reco},\mu}(|d_0|) = 0.8 - \frac{0.8}{8\,\text{cm}} \times (|d_0| - 2\,\text{cm}) \qquad \text{for} \qquad 2\,\text{cm} < |d_0| \leq 10\,\text{cm} \tag{5.3.7}$$

and

$$\epsilon_{\text{reco},e}(|d_0|) = \epsilon_{\text{reco},\mu}(|d_0|) = 0 \qquad \text{for} \qquad |d_0| > 10\,\text{cm}\,. \tag{5.3.8}$$

Clearly, there is no particularly good reason for these assumption other than the observation that the given efficiencies tend to decrease for higher impact parameters and that the efficiencies should not drop to zero in the relevant range. Otherwise, without any knowledge about the efficiencies, other assumptions could be just as good, and the validation procedure will have to show whether the assumptions are appropriate.

The issue of the unknown reconstruction efficiencies was also encountered by the authors of CheckMATE [236, 237], who adopted a different approach [440]. Their implementation uses the tabulated efficiencies for impact parameters below 2 cm and constant values of 0.01 for muons and 0.06 for electrons above this value. These values were certainly chosen mainly with the aim to reproduce the CMS results, but the drastic drop at $|d_0| = 2\,\text{cm}$ seems rather implausible. The CheckMATE results still deviate from CMS results for higher lifetimes in the range $c\tau > 100\,\text{mm}$ [440]. However, large deviations for these lifetimes can also be observed in the SFS implementation of the analysis.

According to the instructions in [434], the $|d_0|$-dependent reconstruction efficiencies need to be convoluted with p_T-dependent selection efficiencies, which are shown in figure 5.8, and a trigger efficiency of 95 %.

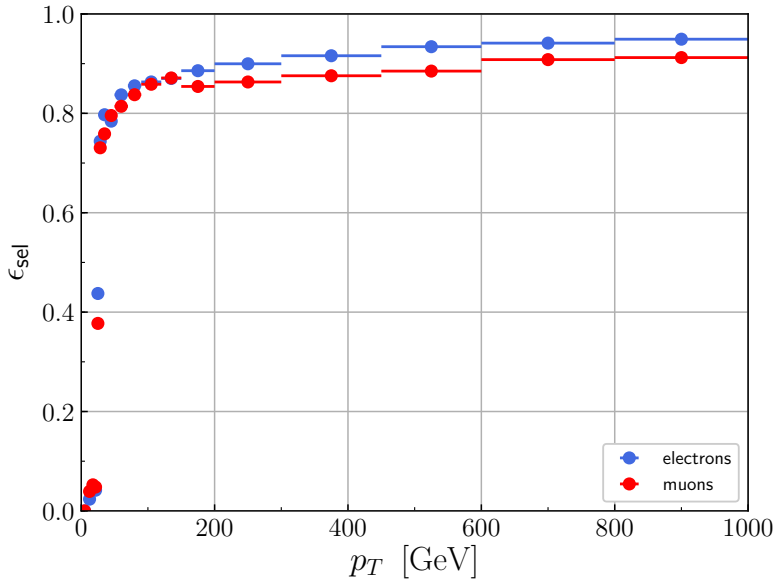

Figure 5.8: Selection efficiencies of electrons and muons [434] of the superseded CMS analysis [375]. The plot was generated with data files from the corresponding HEPData entry [438, 439].

5.3.3 Validation

The signal process considered in the analysis summary [355] is the production of a squark-antisquark pair, $pp \to \tilde{t}_1\tilde{t}_1^*$, which gives rise to the electron-muon pair through the subsequent decay of the supposed long-lived stop, $\tilde{t}_1 \to b\ell$ with $\ell = e, \mu$. For four different lifetimes ranging from 0.1 to 100 cm/c, the number of signal events in the three signal regions are given explicitly in table 4 of the analysis summary, where a stop mass value of $M_{\tilde{t}_1} = 700\,\text{GeV}$ was assumed.

To reproduce these results, samples of 400 000 events for the same four lifetimes have been generated with PYTHIA version 8.244 [280, 281]. To this end, a parameter card which is provided in the `examples` folder of PYTHIA (`sps1aNarrowStopGluino.spc`) and corresponds to the benchmark scenario (SPS 1a) [4] of minimal supergravity (mSUGRA) defined in ref. [441]. The decay table of the stop has been replaced by one that includes only the decays of interest, $\tilde{t}_1 \to b\ell$ with equal branching ratios $\text{Br}(\ell) = 1/3$ for $\ell = e, \mu, \tau$, as required by the analysis summary. Likewise, the stop mass is set to 700 GeV.

For comparison with the CMS experimental results and simulations, the overall efficiencies $\epsilon_{\text{SR}i}$ of the signal regions need to be multiplied with the expected number of events for the simulated process, i.e. its total cross section σ times the integrated luminosity L_{int}:

$$N_{\text{SR}i} = \sigma \times L_{\text{int}} \times \epsilon_{\text{SR}i} \qquad \text{with} \qquad \epsilon_{\text{SR}i} = \frac{w_{\text{final},i}}{w_{\text{initial}}}\,. \tag{5.3.9}$$

Here w_{initial} and w_{final} are the sum of weights of the sample before cuts and after the cuts of SRi. To reproduce the CMS results, the cross section for the stop production process used in the calculations for a 700 GeV stop is given at next-to-leading-order and next-to-leading-logarithm (NLO+NLL) by $\sigma \approx 67.05\,\text{fb}$ with an uncertainty of about 13 % [447]. The results are shown in table 5.5.

The table shows good agreement for the lifetimes up to $c\tau = 10\,\text{cm}$. A slightly higher deviation is observed in SR3 for the smallest lifetime. Excessively high deviations are observed for the highest lifetime with $c\tau = 100\,\text{cm}$. The deviations are probably related to the insufficient knowledge about the $|d_0|$-dependent reconstruction efficiencies, which concern especially SR3 and all signal regions for the highest lifetime. The choice of the additional requirement on v_0 could also have an effect on these numbers. Statistics might also play a role in the poorly populated regions, but is presumably less important, given the high number of generated events. In total, the results are rather satisfying for $c\tau$ up to 10 cm.

4. The *Snowmass Points and Slopes* (SPS) [441] are specific sets of parameters and lines in the parameter space of the MSSM which arise from different supersymmetry breaking mechanisms. The chosen breaking scenarios are *minimal supergravity* (mSUGRA) [442–445], *gauge-mediated SUSY breaking* (GMSB) [446] and *anomaly-mediated SUSY breaking* (AMSB) [381, 382], which all drastically reduce the number of parameters of the MSSM introduced through the most general SUSY-breaking Lagrangian. The benchmark scenarios are then specified in terms of a selected point in the remaining parameter space and possibly one free parameter on which the others can depend. The details about the scenarios can be found in ref. [441].

$c\tau$ [cm]	**SR1** MA5 / CMS	**SR2** MA5 / CMS	**SR3** MA5 / CMS
0.1	3.7 / 3.8 ± 0.2 $\delta_\epsilon = 1.7\,\%$	0.97 / 0.94 ± 0.06 $\delta_\epsilon = 3.2\,\%$	0.21 / 0.16 ± 0.02 $\delta_\epsilon = 33.8\,\%$
1	4.8 / 5.2 ± 0.4 $\delta_\epsilon = 7.6\,\%$	4.2 / 4.1 ± 0.3 $\delta_\epsilon = 2.0\,\%$	7.5 / 7.0 ± 0.3 $\delta_\epsilon = 6.7\,\%$
10	0.89 / 0.8 ± 0.1 $\delta_\epsilon = 10.8\,\%$	1.1 / 1.0 ± 0.1 $\delta_\epsilon = 7.0\,\%$	6.5 / 5.8 ± 0.2 $\delta_\epsilon = 11.8\,\%$
100	0.043 / 0.009 ± 0.005 $\delta_\epsilon = 378.4\,\%$	0.06 / 0.03 ± 0.01 $\delta_\epsilon = 86.3\,\%$	0.58 / 0.27 ± 0.03 $\delta_\epsilon = 114.1\,\%$

Table 5.5: Expected number of events passing the selection criteria of the signal regions, obtained with the SFS implementation of the analysis, compared with CMS results. The relative deviation of the efficiency is given by δ_ϵ. The numbers are given with the same number of digits as for the CMS results and uncertainties. Deviations above 15 % are highlighted in red.

The results presented in table 5.5 allow for a direct comparison between MadAnalysis 5 and CMS results for the individual signal regions. However, they are limited to a fixed mass value of the long-lived stop. Even though no similar tables are available for other stop masses, the implementation can further be tested by generating an exclusion curve in the parameter space of the stop mass and lifetime/proper decay length comparable to the one provided in the article of the analysis. For this purpose, a scan in the parameters $(m_{\tilde{t}_1}, c\tau)$ was performed in a region around the CMS exclusion curve. The latter has been reproduced from the original figure *by hand*, since no tabulated data is available to reproduce the figure. A spacing of 5 GeV in the stop mass has been chosen, according to the cross section table provided in [447], from which the cross section values have been used in order to determine whether a parameter point is excluded. The spacing in $c\tau$ corresponds to the minor ticks displayed on the vertical axis in figure 5.9, as in the original figure. For each point in this parameter space, a sample of 100 000 events has been simulated in the same manner as for the four different lifetimes in table 5.5. Upper limits on the stop production cross section were obtained separately for each signal region using the CL_s method [282], and a parameter point is considered here as excluded, if it is excluded by at least one signal region. The results of the parameter scan in comparison with CMS results is displayed in figure 5.9.

Even though the results are not in perfect agreement, one can see that the global trend of both curves is the same. In particular, one can see that for the previously tested mass value of 700 GeV the agreement is very good. It is interesting to note that in contrast to the findings in table 5.5, the best agreement is obtained for the highest lifetimes, whereas for $c\tau < 10\,\mathrm{cm}$ some significant deviations can be observed. In particular, the kink in the curve around $c\tau = 1\,\mathrm{cm}$ seems rather unusual. Nevertheless, given the low amount of material for the analysis, the obtained curve seems reasonably close to the CMS curve. Except for the lowest lifetimes, the implementation is rather more permissive, and hence more conservative, as it excludes less parameter space.

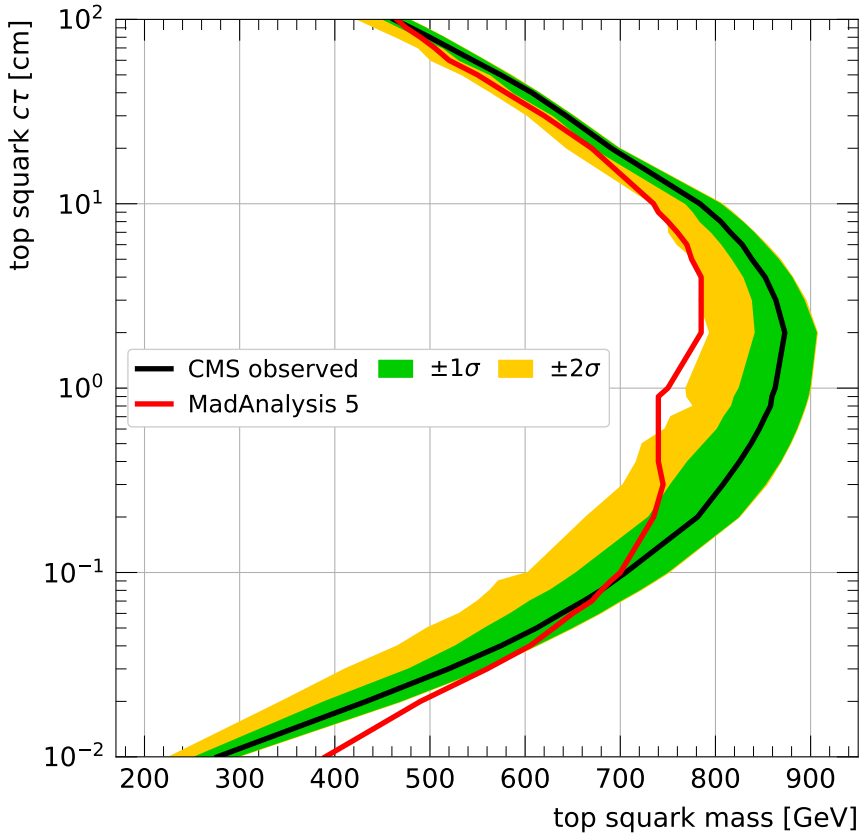

Figure 5.9: Comparison of the exclusion curve obtained using the MadAnalysis 5 (SFS) implementation of the analysis and the CMS exclusion curve. The CMS results have been extracted *by hand* from the original figure provided in the article of the analysis [355].

5.3.4 Conclusions on the analysis

The analysis is a relatively simple example of a long-lived particle search, that can easily be implemented within the MadAnalysis 5 and SFS framework. It has been useful to test the new particle propagator module and detect problems in its implementation. Its main deficit is the insufficient knowledge about the $|d_0|$-dependence of the reconstruction efficiencies. This problem has been handled using a guess of the reconstruction efficiencies in the range $2\,\text{cm} < |d_0| < 10\,\text{cm}$. With this choice, a satisfying agreement with tabulated CMS results in the signal regions with high event population can be obtained. The obtained exclusion curve is reasonably close to the CMS results and tends to be slightly less restrictive. Clearly, the implementation is not perfect, but after all the results obtained in the validation are rather satisfying.

5.4 Displaced vertices of oppositely charged leptons (ATLAS-SUSY-2017-04)

This ATLAS search [348] targets events with displaced vertices (DV) associated with a pair of leptons (ee, $e\mu$ or $\mu\mu$) with invariant mass greater than 12 GeV. It uses data samples from 2016, i.e. during then Run-2 period of the LHC at $\sqrt{s} = 13$ TeV. The value of the integrated luminosity is indicated as $32.8\,\text{fb}^{-1}$ (with an uncertainty of 2.2 %) [448,449]. Two different models with different signal processes and topologies as well as coupling scenarios are investigated, namely a simplified RPV SUSY model and a Z' toy model. The latter has merely been chosen as a prototype of a two-body LLP decay in order to obtain efficiencies which can be applied to comparable models. As stated in the article of the analysis, a long-lived Z' is not expected to be viable but excluded by searches for displaced hadronic jets, because the coupling to $q\bar{q}$ which induces its production should also contribute to the decay with a high branching fraction. As opposed to the CMS analysis presented in the previous section, this analysis requires the muons to originate from the *same* DV. Nevertheless, it allows for several DVs per event. Moreover, an event is not rejected automatically when a DV does not fulfill all of the requirements imposed by the cuts, as long as there is at least one other DV surviving the cuts. In this search, no event with a dileptonic displaced vertex compatible with all selection criteria has been observed.

An extensive amount of auxiliary material for the reinterpretation of the results of this analysis is provided in the HepData entry of the analysis [450] and in [451]. Most importantly, the auxiliary material contains information about the reconstruction efficiency of displaced vertices and the vetoes which are applied in the different detector regions and have a significant effect on the final result. Including this information into the implementation of the analysis is therefore crucial for reproducing the ATLAS results. The deficit of the reconstruction efficiencies is their model dependence which requires special attention on the user's side. Nonetheless, it can be expected that the efficiencies give accurate results when the decay topology of the signal process coincides with one of the signal processes considered in the analysis.

5.4.1 Selection criteria

The search is designed to allow for more than one displaced vertex per event. The event selection is composed of two types of cuts. In a first step, a number of cuts keep or reject events as a whole. Then, the remaining cuts perform a selection of displaced vertex candidates and do not reject events unless the number of vertex candidates has been reduced to zero.

The validity of the implementation can in principle be checked in detail against cutflow tables which are part of the auxiliary material in [451]. Currently, the comparison with these tables is essentially limited to the final numbers after all cuts due to the missing simulation of pile-up in the SFS framework, as will be detailed in section 5.4.4.2. From pile-up events, one can expect additional displaced vertices of soft hadrons, which are successively removed by imposing the different vertex selection criteria. Despite the limited reproducibility, the tables contain valuable information about the effect of the different

cuts on the number of surviving events and vertices of different kinds. In the following, the selection criteria are presented and their applicability within MadAnalysis 5 and the SFS framework is explained.

5.4.1.1 Event level requirements

Triggers: Three triggers with different requirements on the transverse momenta and pseudorapidities are used to select events with possibly displaced electron and muon candidates. A *muon trigger* requires a track in the ATLAS muon system with $p_T > 60\,\text{GeV}$ and $|\eta| < 1.05$. The MadAnalysis 5 implementation only uses muons to evaluate these criteria. Two different photon triggers are used which are sensitive to electromagnetic showers induced by potentially displaced electrons. Here, the conditions are the presence of a photon with $p_T > 140\,\text{GeV}$ for the *single photon trigger* or two photons with $p_T > 50\,\text{GeV}$ for the *diphoton trigger*. In the MadAnalysis 5 implementation, these criteria are evaluated for both photons and electrons candidates, since the latter can give rise to photons when interacting with the detector components. At least one of the three triggers must be fired in order for an event to be kept.

Preselection: An additional set of criteria is applied, depending on the trigger requirements which are fulfilled. The details are listed in table 5.6. These preselection criteria check the presence of one or two candidates of the *reconstructed* particles (e, μ, γ) with different constraints on p_T, η and in some cases the transverse impact parameter d_0. Electrons fall into two different categories: Usually they must have an impact parameter $|d_0| > 2\,\text{mm}$, but this condition is dropped if they satisfy the *loose electron* isolation criteria. These can easily be implemented following a cone isolation approach, as for the CMS analysis. Two different isolation criteria must be fulfilled for loose electrons, where different cone sizes are used [452]: Calorimeter isolation requires the sum of E_T^{cone20} in a cone around the considered electron with fixed size $\Delta R < 0.2$ to be as small as

$$\frac{E_T^{\text{cone20}}}{p_T} < 0.2\,, \tag{5.4.1}$$

whereas the track isolation restricts the scalar sum of p_T of all other tracks in a cone with variable size $\Delta R < \Delta R_{\text{max}} = 0.2$ around the electron track to

$$\frac{p_T^{\text{varcone20}}}{p_T} < 0.15 \qquad \text{with} \qquad \Delta R = \min\left(\frac{10}{p_T[\text{GeV}]}, \Delta R_{\text{max}}\right)\,. \tag{5.4.2}$$

For muons, the quality of the reconstruction determines whether a displacement of $|d_0| > 1.5\,\text{mm}$ is enforced: If a muon leaves a track both in the inner detector and the muon system and the agreement is good (such that $\chi^2/\text{DoF} < 5$), then the d_0-criterion is applied. Otherwise, only the remaining requirements are used in the preselection. Simulating such a behaviour within MadAnalysis 5 seems very difficult and in contradiction with the SFS philosophy of keeping the detector simulation simple and fast. A detailed knowledge of the detector components and the reconstruction algorithms would be needed. The implementation of the analysis

therefore includes the d_0-criterion for all muons, which does not seem to cause serious problems in the final results.

Cosmic-ray veto: A small proportion of muons in an event record might not be related to the final state of the collision event but a coincidence of a cosmic ray muon passing through the detector in the time frame while the event is recorded. Such a muon is expected to be falsely identified as two oppositely charged muons, one of which being associated with the *entering* muon, since the detector hits of the muon entering the detector would be reconstructed in the direction opposite to its true direction, leading to the interpretation of a muon that leaves the detector. Determining the charge of the particle using the bending of its trajectory in the magnetic field of the detector obviously leads to the wrong sign, when the wrong direction is assumed. Furthermore, since cosmic ray muons are unrelated to the collision events in the detector, the displacement of the oppositely charged muon pair could give rise to the reconstruction of a displaced vertex with high invariant mass. Therefore, events containing a pair of muons with nearly opposite momenta are rejected. Precisely, these are muon pairs with pseudorapidities $\eta_{1,2}$ and polar angles $\phi_{1,2}$ such that

$$\Delta R_{\cos} \equiv \sqrt{(|\phi_1 - \phi_2| - \pi)^2 + (\eta_1 + \eta_2)^2} < 0.01\,. \tag{5.4.3}$$

Primary vertex: A primary vertex must be identifiable based on at least two tracks and the highest scalar sum of p_T^2 of its tracks compared to all other vertices. The position of the primary vertex is a necessary reference point in order to specify the displacement of other vertices. This criterion is not implemented, because the collision point in Monte-Carlo events usually coincides with the origin of the coordinate system, and there is mostly enough activity related to the primary vertex so that it can be well identified.

Displaced vertex: Finally, the events must contain tracks which form at least one displaced vertex. To allow for highly displaced vertices, the ATLAS *standard tracking* algorithm is supplemented with a *large radius tracking* algorithm [453], which significantly relaxes the requirements on the tracks, e.g. it raises the $|d_0|$ upper limit from 10 mm to 300 mm and the $|d_z|$ upper limit from 250 mm to 1500 mm. The locations of displaced vertices are obtained from the reconstructed tracks with a *vertexing* algorithm via the successive combination of intersecting tracks (taking into account the uncertainties of the track reconstruction) to vertices and merging of vertices when their distance is small enough. The details of the algorithm are described in ref. [338]. In this analysis, only tracks with the following requirements are accepted in the displaced vertex reconstruction:

$$p_T > 1\,\text{GeV}\,, \qquad 2 < |d_0| < 300\,\text{mm}\,, \qquad |d_z| < 1500\,\text{mm}\,. \tag{5.4.4}$$

Monte-Carlo events already contain the information about the vertex positions, which can be slightly modified, if the magnetic field is taken into account using the particle propagator module. Again, it is not the aim to simulate in a complicated manner detector and reconstruction effects to reproduce the performance of the ATLAS detector and its various algorithms. Instead, the implementation of the analysis simply generates an object representing a displaced vertex for each external

Trigger	Cand. 1	p_T [GeV]	$\lvert\eta\rvert$	$\lvert d_0\rvert$ [mm]	Cand. 2	p_T [GeV]	$\lvert\eta\rvert$	$\lvert d_0\rvert$ [mm]
$\boldsymbol{\mu}$	μ	> 62	< 1.07	> 1.5 (**)	no candidate 2 required			
$\boldsymbol{\gamma}$	γ	> 150	< 2.5	——	γ	> 10	< 2.5	——
					e	> 10	< 2.5	> 2.0
					μ	> 10	< 2.5	> 1.5 (**)
	e	> 150	< 2.5	> 2.0	no candidate 2 required			
$\boldsymbol{\gamma\gamma}$	γ	> 55	< 2.5	——	γ	> 55	< 2.5	——
	e	> 55	< 2.5	> 2.0	e	> 55	< 2.5	> 2.0
					γ	> 55	< 2.5	——
	e (*)	> 55	< 2.5	——	γ	> 55	< 2.5	——

Table 5.6: Preselection criteria based on table 1 of ref. [348]. According to the triggers which have been fired beforehand, the presence of one or two candidate objects with the specified properties is required for at least one of the triggers. As explained in more detail in the text, electron candidates tagged with a single star (*) must fulfill the *loose electron* isolation criteria, whereas the two stars (**) indicate that the d_0-requirement for muon candidates is only enforced, if there is a good agreement between the ID and MS tracks.

final-state particle, which is compatible with the track requirements for the DV reconstruction. Then, a very simple merging is performed, which consists in replacing two DV objects of vertices separated by a distance smaller than 1 mm by a single DV object and assigning all particles associated with the vertices to the new DV object. The position assigned to the new DV object is arbitrarily set to the position of one of the two vertices. This should reproduce the merging procedure well enough, assuming that the LLP decay products are either stable or promptly decaying or sufficiently short-lived particles, such that there is no risk to end up with two displaced vertices when there should be only one.

5.4.2 Vertex level requirements

To be considered as a signal event, each of the reconstructed vertices must fulfill a set of conditions, listed below. The violation of one of the criteria by a displaced vertex candidate only leads to the rejection this vertex. Events are rejected when no displaced vertex is consistent with the full set of requirements.

Vertex fit: The vertices used in the following considerations are required to be well reconstructed, so the analysis requires that the fit of each vertex must satisfy $\chi^2/\text{DoF} < 5$. On the level of the Monte-Carlo truth, where the exact information about the positions of the vertices in space and time is exactly known, this condition is meaningless. Certainly, the imperfection of the ATLAS detector components and algorithms should be taken into account for comparing Monte-Carlo and experimental event samples. Therefore, DV reconstruction efficiencies are used, which describe the probability of a true vertex to be reconstructed, depending on the properties of the associated tracks. They are given in terms of efficiency maps for the two signal models in the auxiliary material of the analysis. More details about these efficiencies are given in section 5.4.3.

Transverse displacement: Prompt decays and decays with small displacement are

avoided by considering only displaced vertices at positions $\vec{x}_{\text{DV}} = (x_{\text{DV}}, y_{\text{DV}}, z_{\text{DV}})$, which have a transverse displacement from the collision axis of the protons colliding at $\vec{x}_{\text{pp}} = (x_{\text{pp}}, y_{\text{pp}}, z_{\text{pp}})$ that is bigger than

$$d_{xy} \equiv \sqrt{(x_{\text{DV}} - x_{pp})^2 + (y_{\text{DV}} - y_{pp})^2} > 2\,\text{mm}\,. \tag{5.4.5}$$

In the Monte-Carlo events, the protons collide at the origin, $\vec{x}_{\text{pp}} = \vec{0}$.

Fiducial volume: Only vertices in a restricted detector volume, where the track and vertex reconstruction are expected to be reliable, are taken into account. This so-called *fiducial volume* has the form of a cylinder with the beam axis as its symmetry axis and defined by the following boundaries for the position of the displaced vertices:

$$r_{xy} \equiv \sqrt{x_{\text{DV}}^2 + y_{\text{DV}}^2} < 300\,\text{mm}\,, \qquad |z_{\text{DV}}| < 300\,\text{mm}\,. \tag{5.4.6}$$

Material veto: The ATLAS detector contributes itself to the presence of displaced vertices from hadronic interactions of primary particles with detector material [338, 454, 455]. This detector effect constitutes a source of background that should be reduced. A veto is therefore applied in order to reject vertices in the *material regions*, where high contamination of this background is expected. It uses maps of the fiducial detector volume which were determined using simulated minimal-bias events by observing the distribution of secondary vertices expected from the hadronic decays $K_S \to \pi^+\pi^-$ and $\Lambda^0 \to p\,\pi$ (here p and π stand for a proton and negatively charged pion π^- or a anti-proton and a positively charged pion π^+) for a model of the detector that takes into account its geometry and material distribution [455]. In this analysis, the material veto applies to *all* vertices in the material regions, including those of possible signal events, and implies a reduction of the fiducial volume of around 42 %. Instead of a precise map of the vetoed regions, the auxiliary material, provided in [451] and the HEPData entry of the analysis [450], contains a map (figure and corresponding tabulated data) that shows the *fraction* of the volume which is covered by the material veto as a grid in the longitudinal and transverse distance $|z|$ and R. This map is given in figure 5.10. As the material distribution depends also on the polar angle ϕ, the map in $|z|$ and R gives an average over ϕ of the fraction of vetoed volume. Similarly to a detection efficiency, it can be interpreted as the probability for a displaced vertex in some region of the fiducial volume to be vetoed. The implementation of the analysis in MadAnalysis 5 therefore uses a random generator to decide on the basis of this map, whether a displaced vertex is kept or rejected. To this end, the information about the maps from the corresponding data tables has been turned into `C++` code as part of the implementation.

Disabled pixel modules veto: In a similar way as the material veto, another veto is applied to vertices, which arise in front of disabled pixel modules of the inner detector. The disabled modules would certainly affect the reliability of the track reconstruction, so the veto ensures that only well reconstructed vertices are kept. The consequence of this veto is a reduction of the fiducial volume by 2.3 %. Like in the case of the material veto, a map [348, 451] in $|z|$ and R, shown in figure 5.10, is used with an average over ϕ and the implementation of the analysis rejects vertices based on this map and pseudo random numbers.

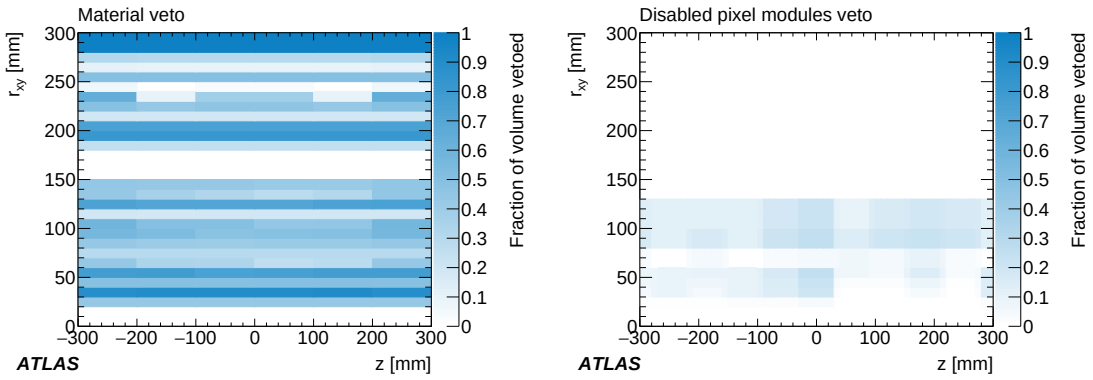

Figure 5.10: Maps of the detector volume fraction vetoed by the material veto (left) and the disabled pixel modules veto (right). The figures have been taken from [451]. The exact values are provided in a tabulated form in the HEPData entry of the analysis [438, 450] and are used in the code of the MadAnalysis 5 implementation.

Two leptonic tracks: At least two leptonic tracks must be associated with each reconstructed vertex. This is a restriction on the possible new physics scenarios for the long-lived particle, which is assumed to be at the origin of the displaced vertex. Therefore, vertices of less than two leptonic tracks are discarded.

Invariant mass: The momenta of the tracks associated with the displaced vertices give a lower bound on the mass of the decaying long-lived particle, which is required in the search to exceed 12 GeV, i.e.

$$m_{\mathrm{DV}}^2 = \left(\sum_i p_i\right)^2 \geq (12\,\mathrm{GeV})^2 \,. \tag{5.4.7}$$

Here the four-momenta p_i are the momenta of all *tracks* forming the displaced vertex, so the momenta of invisible particles produced at the location of the displaced vertex are not included. Given the mass values of long-lived SM particles (c.f. table 5.1), this lower bound allows to suppress displaced vertices of decaying Standard Model particles.

Trigger and preselection matching: The criteria of the trigger and preselection stage, previously applied to the whole set of particles, are also required to hold for the subset of particles associated with each of the displaced vertices. Once again, the choice of preselection criteria is coupled to the matching trigger criteria.

Oppositely charged lepton pair: The displaced vertices must involve at least a pair of leptons (ee, $\mu\mu$ or $e\mu$) with opposite electric charge. Of course, this restricts the search to signal models with LLP decays involving these final state particles.

5.4.3 Efficiencies

To compare simulated event samples with experimental results from ATLAS, three sorts of efficiencies need to be applied to the Monte-Carlo truth events for this analysis. Two of them were already explained in section 5.4.2 and reflect the effects of material and disabled

pixels vetoes. These are in some sense artificial, since the detector is deliberately made inefficient in specific regions to reject badly reconstructed events. Nonetheless, as these vetoes reduce the amount of events as a consequence of the presence and the imperfections of the detector, which affects also potential signal events, they deserve to be considered as efficiencies. However, they will not be reconsidered in this section.

The remaining efficiencies to be included into the implementation of this analysis, which are provided with the auxiliary material, comprehend detection and reconstruction efficiencies, i.e. they codify the performance of detector components and reconstruction algorithms. More precisely, they give the overall probability for a displaced vertex to be successfully reconstructed, based on the properties of the lepton pair that is required to be associated with the vertices considered in the analysis. Following the instructions provided with the auxiliary material, the efficiencies have to be applied to the Monte-Carlo truth information, so they should combine the performance information of all the hardware and software components of ATLAS participating contributing in some way to this analysis.

The detection efficiencies of displaced vertices should objectively, i.e. without any assumption on the underlying theory about the nature of the displaced vertices, only depend on the properties of the associated particles observed by the detector. For instance, one could think of the kinematic quantities such as the particle species, the transverse momentum p_T, the pseudorapidity η, etc. of the individual particles, but also quantities involving more than one particle of a vertex, e.g. the sum of p_T or the angles between the particles. Still, it is not necessarily straightforward to parameterise the efficiencies in terms of the relevant variables in a model-independent manner, such that it could compete with a sophisticated simulation of the detector and the reconstruction algorithms. This might explain why two different parameterisations are provided in the supplementary material for the two signal models considered in the analysis. They take the form of binned efficiencies in two or three variables:

Z' toy model: Apart from the lepton pair, no other decay products are involved in the Z' decay. The efficiencies are given for fixed masses $m(Z')$ of 100, 250, 500, 750 and 1000 GeV with a binning in the transverse distance r_{xy} between the z-axis (fixed by the momenta of the colliding partons) and the position of the displaced vertex, and the transverse momentum of the lepton pair $p_T(\ell\ell')$.

RPV SUSY model: In contrast to the Z' decay, the neutralino decay involves in addition to the two leptons a neutrino, which is not directly visible for the detector, but carries away momentum. Obviously, this has implications on the kinematics of the pair of visible leptons, since they do not have to conserve the four-momentum of the neutralino. For this reason, the mass of the neutralino cannot be determined directly from the momenta of the visible lepton pair. Unlike the Z'-efficiencies, which depend on the mass of the long-lived Z', but are only given for fixed values, the RPV SUSY efficiencies depend on the invariant mass of the lepton pair $m(\ell\ell')$, without assumption about the neutralino mass, so they have a binning in the three variables r_{xy}, $p_T(\ell\ell')$ and $m(\ell\ell')$.

The provided efficiencies lend themselves perfectly to the validation of the implementation of the analysis, as show the results produced in the validation procedure, which is documented in section 5.4.4. Yet, the ultimate goal of implementing an analysis is evidently not to validate the implementation, but to use it for the reinterpretation with event samples

of different new physics scenarios than the ones which were already investigated by the authors of the analysis. In this respect, the two parameterisations of the efficiencies are not ideal. First, they are they model-dependent, which limits the applicability of the implementation to other new physics models. Secondly, in the the case of the Z'-parameterisation, they are only given for five discrete values of the LLP mass. It would be preferable, if each of them were valid for some mass range instead, such that other masses LLP masses could be probed.

To cope with the latter issue, mass *intervals* have been defined somewhat arbitrarily around the given values, in order to allow the implementation to deal with arbitrary LLP masses. Moreover, instead of accessing the true value of the mass of the LLP, the invariant of the lepton pair is determined in the same way as for the RPV SUSY case. Clearly, this solution can only serve as an approximation, the validity of which can not even be tested, since there is no data available for different Z' masses. Alternatively, the RPV SUSY efficiencies could be used, which are defined on known mass intervals. This has been tested with the Z' model samples used in the validation, where deviations of the order 15 % in the overall selection efficiency compared to the dedicated Z' efficiencies were observed, leading to a stronger disagreement with ATLAS results. Therefore, this has not been chosen as the preferred solution, but the user will have the choice between the two efficiencies, as both are implemented.

It seems unlikely that the problem of model-dependence could be cured in a satisfying way with the available material. Perhaps a more generic parameterisation of the efficiencies in terms of a different, possibly bigger set of variables might exist. A possible choice of variables could for example involve the angle between the visible leptons or the angle between the LLP momentum and the total momentum of the lepton pair. One could attempt to determine such efficiencies by histogramming the values for the efficiencies in the new variables for samples of the two signal models and different LLP masses and combining the information from the different histograms in a sensible way. However, the resulting efficiencies could at best be tested against the known results of the two models, but the validity for other models or even samples of the same models with different LLP masses or lifetimes is not guaranteed.

In consequence, the implementation of the analysis has unfortunately a reduced applicability to other models, namely models with the same LLP decay topology as for the Z' or neutralino decay. As long as the visible decay products of the long-lived particle and the kinematics correspond to the decays probed in the analysis, the detector components and reconstruction algorithms should behave identically and the respective efficiencies should be applicable without problems.

5.4.4 Validation

A decent amount of material is provided in both the analysis note and the auxiliary material, that can be used for the validation of the implementation. It includes cutflows, plots (with tabulated data on HEPData) of per-decay and per-event signal efficiencies and exclusion cross-sections. Among this material, a number of results has been selected for the validation procedure, in which event samples for the respective physical scenarios were generated and used for the reproduction with the implemented analysis.

Cutflow tables for both models were used as a guideline during the implementation, with the intention to reproduce the efficiencies of the individual cuts. This is in fact not possible throughout the whole cutflow, because there is currently no support for pile-up in SFS, which seemingly plays a non-negligible role in intermediate steps. In spite of that, the provided cutflow tables are still useful to some extent, as they put forward the importance of the individual cuts.
For the Z' toy model, there are cutflows for in total six *different event samples*, where the Z' takes the masses 100 GeV and 1000 GeV and decays exclusively into one of the three dilepton final states ee, $e\mu$ or $\mu\mu$.
For the RPV SUSY model, the situation is different: According to the description of the provided cutflow table, the two coupling scenarios of the λ_{121} and λ_{122} couplings are combined, where the former induces the decays to ee and $e\mu$ and the latter the decays to $e\mu$ and $\mu\mu$. In analogy to the Z' cutflows, the table contains separate cutflows for each of the neutralino decay modes ee, $e\mu$ and $\mu\mu$, where an event is counted in the cutflow, if it contains at least one vertex associated with the corresponding lepton pair. Here, two different neutralino lifetimes are considered for a single configuration of the squark and neutralino masses, which leads to six different cutflows as well.

Due to the limited usefulness of the cutflows, where results from the implementation and ATLAS can only be expected to be comparable only after the final cut, it is reasonable to check the validity of the implementation with more of the available material. In particular, one should probe different regions in the relevant parameter space, i.e. the masses and lifetimes involved in the signal processes, since problems in the implementation could remain undetected in some regions of the parameter space. Therefore, a scan has been performed for the SUSY RPV model for two configurations of the quark and neutralino masses over a wide spectrum of neutralino lifetimes, considering the λ_{121} and λ_{122} couplings separately. 50 000 parton-showered and hadronised events [5] were simulated for each of the parameter points. The samples were then passed to the MadAnalysis 5 implementation of the analysis to determine selection efficiencies, including the effects of the Simplified fast detector simulation (SFS), and subsequently the resulting upper limits on the squark production cross section, with the ambition to reproduce some of the ATLAS results presented in the figures 3-5 of ref. [348].

5.4.4.1 Event generation

Pythia 8.244 [280, 281] has been used to simulate the production of the Z', which is one of its internal processes. The decay table of the Z' had to be modified to enforce the selected decay to ee, $e\mu$ or $\mu\mu$ with a branching fraction of 100 % and a proper lifetime fixed via $c\tau = 250$ mm. Each decay mode was considered for a mass $m(Z')$ of 100 GeV and 1000 GeV with 20 000 events per sample. These six cases are analysed for comparison with the cutflows provided in [451].

5. The number of events in the sample is reduced to some extent due to the application of the MLM matching scheme [456], leading to a varying number of events for the different parameters points. The same is true for all other samples generated with MadGraph5_aMC@NLO and Pythia in the validation as well as the samples of the vector-like lepton model studied in section 5.5. All event numbers given in the following refer to the initially generated number of events with MadGraph5_aMC@NLO before matching.

The various event samples of neutralino production in the RPV SUSY model have been generated using MadGraph5_aMC@NLO [235] version 2.8.3.2 and Pythia 8.244. Precisely, the simulation of neutralino ($\tilde{\chi}_1^0$) production proceeds in the following way: MadGraph5_aMC@NLO generates tree-level events for the squark-antisquark production of first and second generation squarks with up to two additional partons. Pythia8 takes care of the squark-decay to the fermionic superpartner and the neutralino, which is a prompt decay, and the following decay of the long-lived neutralino to a pair of leptons. In addition, it is used for parton showering, hadronisation and matching/merging. All event samples were generated with the NNPDF 2.3 LO [457] set of parton distribution functions and using the MLM matching scheme [456] with a matching scale of one fourth of the squark mass.
The MSSM UFO [264] model files [458] shipped with MadGraph5_aMC@NLO are used for the simulation, with the parameter card being replaced by a card provided in the HEPData entry of the analysis, which contains the relevant decay tables for the R-parity violating interactions. The squark and neutralino masses, the neutralino decay table and width were adapted to each of the cases considered in the selected validation material.
According to the explanations provided with the ATLAS cutflow tables, only two samples are needed to reproduce the tables, which combine all neutralino decay modes with equal branching ratios $\mathrm{Br}(\tilde{\chi}_1^0 \to \mathrm{ee}\nu) = \mathrm{Br}(\tilde{\chi}_1^0 \to \mathrm{e}\mu\nu) = \mathrm{Br}(\tilde{\chi}_1^0 \to \mu\mu\nu) = 1/3$. A classification of the events is then done on the level of the analysis code depending on the types of the displaced vertices present in the events to generate three different cutflow tables from each sample, as further explained below. Here, the samples were generated with 20 000 events, corresponding to the raw event number in the provided ATLAS cutflow tables.
In the remaining cases, the couplings λ_{121} and λ_{122} are considered separately, where the former induces the decays to $ee\nu$ and $e\mu\nu$ and the latter the decays to $e\mu\nu$ and $\mu\mu\nu$. Here, the branching fraction is 0.5 for each of the decay modes. To cover all cases with reasonable statistics and density of points in parameters space as well as computational effort, samples of 50 000 events for two configurations of the masses and 21 different neutralino lifetimes were generated for both of the R-parity violating couplings, i.e. in total 84 samples. The masses are $m(\tilde{q}) = 700\,\mathrm{GeV}$, $m(\tilde{\chi}_1^0) = 50\,\mathrm{GeV}$ and $m(\tilde{q}) = 1600\,\mathrm{GeV}$, $m(\tilde{\chi}_1^0) = 1300\,\mathrm{GeV}$ and the widths span from $c\tau = 1\,\mathrm{mm}$ to $c\tau = 10\,000\,\mathrm{mm}$.

5.4.4.2 Pile-up

Important differences between the ATLAS results and corresponding results from the implementation in SFS can be observed in the intermediate cuts of the cutflow tables below (tables 5.7-5.12). Apart from possible misinterpretations of the cut labelling in the table and some differences in the order of the selection criteria, a significant part of the difference seems to be related to the effect of pile-up that is not taken into account in the re-implementation of the analysis. Indeed, the ATLAS simulation includes the effect of pile-up, i.e. the presence of several proton-proton collisions in a single bunch-crossing, through the simulation of soft QCD processes using Pythia. It has been checked with an external non-public code and the `C++` code of the analysis that the sum of weights for the intermediate cuts get closer to the ATLAS results when pile-up events are included. Pile-up leads to fake displaced vertices, which are in fact primary vertices of other proton-proton collisions.

At present, MadAnalysis 5 does not have the capabilities to include pile-up events in SFS (such a feature might be added in the future, but has until now not been a priority in the development of MadAnalysis 5). Fortunately, one can observe that the final results in the cutflows agree reasonably well with the ATLAS results, both for the Z' and the RPV SUSY model, which indicates that pile-up effects are efficiently suppressed by the selection criteria of the analysis. It is therefore not necessary to worry about pile-up in this analysis. With regard to the performance of the code, it is even beneficial to avoid including pile-up events, which would roughly correspond to adding a contribution that is subtracted thereafter. Finally, it should be noted that the instructions for the reinterpretation of this analysis, which are provided in the auxiliary material [451], do *not* address pile-up. To conclude, pile-up is irrelevant for this analysis and therefore not simulated.

5.4.4.3 Cutflows

As pointed out earlier in this section, the use of the cutflows of this analysis for validation purposes is limited. They give some insight about the importance of the different cuts, but their reproduction would require to simulate pile-up and make sure that the order of all cuts is identical. In addition, it is not clear, whether the provided efficiencies for the reconstruction of displaced vertices describe purely the imperfections of the vertex reconstruction (including track reconstruction) or whether they are combined with other effects such as trigger efficiencies, in which case they could affect the event numbers at several stages of the cutflow.

Furthermore, the cutflow tables give the impression that the ATLAS simulations include the preselection criteria only at the vertex level ("Preselection matching"), which does not correspond to the description in the analysis note. The SFS implementation of the analysis applies both preselection and trigger criteria at the cut labelled as "Triggers". For these reasons, it is pointless to try to reproduce the cutflow in detail.

In spite of these concerns, the cutflow tables are given below (tables 5.7 - 5.11) to illustrate the impact of the various selection criteria on the samples in the RPV SUSY and Z' signal models. They show the sum of event weights of the remaining events after the different cuts. The ATLAS cutflows of the RPV SUSY model were reweighted to represent the expected number of events, given the squark-antisquark production cross section and the size of the data set used in the analysis, corresponding to an integrated luminosity of $32.8\,\text{fb}^{-1}$. In the cutflows of the Z' toy model, the numbers simply represent the sum of the weights attributed to the events by Pythia. For comparison with the ATLAS cutflows, the event weights in the cutflows generated with the MadAnalysis 5 implementation of the analysis were reweighted such that the initial weights before all cuts agree with the corresponding ATLAS numbers. The cuts highlighted in red are not implemented in the SFS implementation, i.e. they let pass all events without any modification on the selection of displaced vertex candidates. The first of these cuts is called "Primary vertex" has already been discussed in section 5.4.1.1. The Monte-Carlo truth events should almost always contain a primary vertex fulfilling compatible with the requirements at the origin of the coordinate system, so this cut should not have an important effect. This can also be observed on the ATLAS side of the cutflow tables below. The cuts "Lepton kinematics" and "Lepton identification"' seems to be related to the lepton reconstruction, which is

trivial in the Monte-Carlo truth, where all particles are clearly identified. The kinematic requirements of the reconstruction relevant for the particles associated with the displaced vertices should also be covered by the preselection.

	$c\tau = 30$ mm						$c\tau = 1000$ mm					
	N_{weighted} (SFS/ATLAS)						N_{weighted} (SFS/ATLAS)					
Channel	ee		$e\mu$		$\mu\mu$		ee		$e\mu$		$\mu\mu$	
No cuts	21.0	21.0	21.2	21.2	20.8	20.8	21.1	21.1	20.9	20.9	21.1	21.1
Triggers	21.0	20.6	21.0	20.5	20.2	16.6	21.1	19.1	20.9	18.5	21.0	10.9
Cosmic-ray veto	21.0	20.6	21.0	20.5	20.2	16.6	21.1	19.0	20.8	18.4	21.0	10.9
Primary vertex	21.0	20.6	21.0	20.5	20.2	16.6	21.1	19.0	20.8	18.4	21.0	10.9
$N(\text{DV}) \geq 1$	9.2	15.1	9.5	15.2	9.3	12.7	3.9	10.5	4.1	10.3	4.3	6.6
Vertex fit	9.2	15.1	9.5	15.2	9.3	12.7	3.9	10.5	4.1	10.2	4.3	6.6
d_{xy}	9.2	15.1	9.5	15.2	9.3	12.7	3.9	10.5	4.1	10.2	4.3	6.6
Fiducial volume	9.2	14.8	9.5	14.9	9.3	12.4	3.4	9.8	3.6	9.6	3.7	6.3
Dis. pixel mod. veto	9.0	14.4	9.2	14.6	9.0	12.2	3.2	9.3	3.4	9.1	3.4	5.9
Material veto	7.9	10.9	8.2	11.1	8.6	12.2	2.3	4.9	2.4	4.8	3.0	5.9
$N(l) \geq 1$	7.9	7.7	8.2	9.5	8.6	8.5	2.3	2.2	2.4	2.6	3.0	2.7
$N(l) \geq 2$	7.9	5.4	8.2	6.3	8.6	6.8	2.3	1.3	2.4	1.5	3.0	2.0
Lepton kinematics	7.9	5.3	8.2	6.3	8.6	6.8	2.3	1.2	2.4	1.5	3.0	2.0
Lepton identification	7.9	4.7	8.2	5.5	8.6	6.2	2.3	1.1	2.4	1.3	3.0	1.8
Overlap removal	7.9	4.7	8.2	5.4	8.6	6.2	2.3	1.1	2.4	1.3	3.0	1.8
Trigger matching	7.7	4.7	8.0	5.2	8.3	5.7	2.2	1.1	2.4	1.2	2.8	1.7
Presel. matching	7.7	4.7	8.0	5.2	8.3	5.7	2.2	1.1	2.4	1.2	2.8	1.7
m_{DV}	7.7	4.7	8.0	5.2	8.3	5.7	2.2	1.1	2.4	1.2	2.8	1.7
Opposite charge	4.6	4.6	5.2	5.1	5.7	5.7	1.2	1.0	1.3	1.2	2.0	1.7

Table 5.7: Cutflow tables for two samples in the RPV SUSY combining the decays induced by the λ_{121} and λ_{122} couplings, for neutralino proper decay lengths of 30 mm and 1000 mm. The numbers N_{weighted} provided by ATLAS correspond to the sum of the event weights, reweighted to match the expected event numbers in a data set obtained with the integrated luminosity of the analysis ($32.8\,\text{fb}^{-1}$). For simplicity, the corresponding numbers obtained with the SFS implementation of the analysis were reweighted to match the initial number N_{weighted} of ATLAS. The cuts highlighted in red are not implemented.

	$c\tau = 30$ mm						$c\tau = 1000$ mm					
	ϵ_{cut} (MA5 / ATLAS)						ϵ_{cut} (MA5 / ATLAS)					
Channel	ee		$e\mu$		$\mu\mu$		ee		$e\mu$		$\mu\mu$	
No cuts	1.000	1.000	1.000	1.000	1.000	1.000	1.000	1.000	1.000	1.000	1.000	1.000
Triggers	0.999	0.981	0.989	0.967	0.969	0.798	1.000	0.905	0.998	0.885	0.996	0.517
Cosmic-ray veto	1.000	1.000	1.000	1.000	1.000	1.000	1.000	0.995	1.000	0.995	1.000	1.000
Primary vertex	1.000	1.000	1.000	1.000	1.000	1.000	1.000	1.000	1.000	1.000	1.000	1.000
$N(\text{DV}) \geq 1$	0.438	0.733	0.451	0.741	0.460	0.765	0.186	0.553	0.197	0.560	0.203	0.606
Vertex fit	1.000	1.000	1.000	1.000	1.000	1.000	1.000	1.000	1.000	0.990	1.000	1.000
d_{xy}	1.000	1.000	1.000	1.000	1.000	1.000	1.000	1.000	1.000	1.000	1.000	1.000
Fiducial volume	1.000	0.980	1.000	0.980	1.000	0.976	0.870	0.933	0.868	0.941	0.867	0.955
Dis. pixel mod. veto	0.976	0.973	0.974	0.980	0.975	0.984	0.943	0.949	0.940	0.948	0.934	0.937
Material veto	0.877	0.757	0.891	0.760	0.946	1.000	0.721	0.527	0.725	0.527	0.867	1.000
$N(l) \geq 1$	1.000	0.706	1.000	0.856	1.000	0.697	1.000	0.449	1.000	0.542	1.000	0.458
$N(l) \geq 2$	1.000	0.701	1.000	0.663	1.000	0.800	1.000	0.591	1.000	0.577	1.000	0.741
Lepton kinematics	1.000	0.981	1.000	1.000	1.000	1.000	1.000	0.923	1.000	1.000	1.000	1.000
Lepton identification	1.000	0.887	1.000	0.873	1.000	0.912	1.000	0.917	1.000	0.867	1.000	0.900
Overlap removal	1.000	1.000	1.000	0.982	1.000	1.000	1.000	1.000	1.000	1.000	1.000	1.000
Trigger matching	0.982	1.000	0.975	0.963	0.971	0.919	0.968	1.000	0.972	0.923	0.949	0.944
Presel. matching	0.998	1.000	0.996	1.000	0.998	1.000	0.999	1.000	0.999	1.000	1.000	1.000
m_{DV}	0.999	1.000	1.000	1.000	1.000	1.000	1.000	1.000	1.000	1.000	1.000	1.000
Opposite charge	0.596	0.979	0.652	0.981	0.688	1.000	0.531	0.909	0.559	1.000	0.701	1.000

Table 5.8: Cut efficiency tables corresponding to the cutflow tables for the two samples combining the λ_{121} and λ_{122} couplings in the RPV SUSY model. The cuts highlighted in red are not implemented.

	$m(Z') = 100\,\text{GeV}$					
	N_{weighted} (SFS/ATLAS)					
Channel	ee		$e\mu$		$\mu\mu$	
No cuts	20000.0	20000.0	20000.0	20000.0	20000.0	20000.0
Triggers	301.4	322.7	400.5	462.1	757.9	790.8
Cosmic-ray veto	301.4	322.7	400.5	462.1	757.9	790.8
Primary vertex	301.4	322.7	400.5	462.1	757.9	790.8
$N(\text{DV}) \geq 1$	31.1	124.8	45.9	182.6	124.8	398.1
Vertex fit	31.1	124.8	45.9	182.6	124.8	398.1
d_{xy}	31.1	124.8	45.9	182.6	124.8	398.1
Fiducial volume	23.0	121.1	40.9	176.0	116.8	375.7
Dis. pixel mod. veto	23.0	120.3	39.9	164.7	102.8	362.7
Material veto	18.0	71.4	30.9	106.2	102.8	362.7
$N(l) \geq 1$	18.0	44.7	30.9	69.8	102.8	253.4
$N(l) \geq 2$	18.0	38.6	30.9	61.8	102.8	246.7
Lepton kinematics	18.0	37.7	30.9	60.0	102.8	246.2
Lepton identification	18.0	35.9	30.9	57.5	102.8	238.2
Overlap removal	18.0	35.9	30.9	57.5	102.8	238.2
Trigger matching	18.0	35.9	30.9	57.5	102.8	237.3
Presel. matching	9.0	14.8	21.0	20.1	81.8	79.5
m_{DV}	9.0	14.8	21.0	20.1	81.8	79.5
Opposite charge	9.0	14.8	21.0	20.1	81.8	79.5

Table 5.9: Cutflow tables for three samples of different decay modes in the Z' toy model for a Z' mass of 100 GeV. The numbers N_{weighted} correspond to the sum of the event weights as provided by PYTHIA, which in the SFS case were reweighted to match the initial numbers of ATLAS. The cuts highlighted in red are not used in the MADANALYSIS 5 implementation.

	$m(Z') = 100\,\text{GeV}$					
	ϵ_{cut} (MA5 / ATLAS)					
Channel	ee		$e\mu$		$\mu\mu$	
No cuts	1.000	1.000	1.000	1.000	1.000	1.000
Triggers	0.015	0.016	0.020	0.023	0.038	0.040
Cosmic-ray veto	1.000	1.000	1.000	1.000	1.000	1.000
Primary vertex	1.000	1.000	1.000	1.000	1.000	1.000
$N(\text{DV}) \geq 1$	0.103	0.387	0.115	0.395	0.165	0.503
Vertex fit	1.000	1.000	1.000	1.000	1.000	1.000
d_{xy}	1.000	1.000	1.000	1.000	1.000	1.000
Fiducial volume	0.737	0.970	0.891	0.964	0.936	0.944
Dis. pixel mod. veto	1.000	0.993	0.976	0.936	0.880	0.965
Material veto	0.783	0.594	0.775	0.645	1.000	1.000
$N(l) \geq 1$	1.000	0.626	1.000	0.657	1.000	0.699
$N(l) \geq 2$	1.000	0.864	1.000	0.885	1.000	0.974
Lepton kinematics	1.000	0.977	1.000	0.971	1.000	0.998
Lepton identification	1.000	0.952	1.000	0.958	1.000	0.968
Overlap removal	1.000	1.000	1.000	1.000	1.000	1.000
Trigger matching	1.000	1.000	1.000	1.000	1.000	0.996
Presel. matching	0.500	0.412	0.677	0.350	0.796	0.335
m_{DV}	1.000	1.000	1.000	1.000	1.000	1.000
Opposite charge	1.000	1.000	1.000	1.000	1.000	1.000

Table 5.10: Cut efficiency tables corresponding to the cutflow tables (table 5.9) for the samples of the three decay Z' decay modes of the 100 GeV Z'. The cuts highlighted in red are not used in the MadAnalysis 5 implementation.

	$m(Z') = 1000\,\text{GeV}$					
	N_{weighted} (SFS/ATLAS)					
Channel	ee		$e\mu$		$\mu\mu$	
No cuts	20000.0	20000.0	20143.6	20143.6	19608.3	19608.3
Triggers	19029.3	17871.4	18323.0	16465.8	10239.6	9657.6
Cosmic-ray veto	19024.3	17864.4	18314.9	16457.3	10239.6	9655.8
Primary vertex	19024.3	17858.5	18314.9	16453.6	10239.6	9655.0
$N(\text{DV}) \geq 1$	3255.0	6457.8	3964.7	6376.3	3208.0	4199.3
Vertex fit	3255.0	6455.9	3964.7	6373.9	3208.0	4197.6
d_{xy}	3255.0	6455.9	3964.7	6373.9	3208.0	4196.7
Fiducial volume	2343.1	5986.3	2849.8	5960.4	2401.1	3969.0
Dis. pixel mod. veto	2319.1	5759.8	2810.5	5791.1	2381.4	3858.0
Material veto	2083.2	3848.9	2514.4	4065.3	2381.4	3858.0
$N(l) \geq 1$	2083.2	2340.4	2514.4	2816.9	2381.4	2453.4
$N(l) \geq 2$	2083.2	2192.9	2514.4	2654.8	2381.4	2342.2
Lepton kinematics	2083.2	2180.9	2514.4	2645.4	2381.4	2340.9
Lepton identification	2083.2	2113.7	2514.4	2499.4	2381.4	2215.6
Overlap removal	2083.2	2113.7	2514.4	2497.1	2381.4	2215.6
Trigger matching	2083.2	2113.7	2514.4	2497.1	2381.4	2173.5
Presel. matching	2083.2	2110.8	2501.3	2480.9	2381.4	2170.1
m_{DV}	2083.2	2110.8	2500.3	2480.9	2381.4	2170.1
Opposite charge	2083.2	2088.4	2500.3	2468.4	2381.4	2166.0

Table 5.11: Cutflow tables for three samples of different decay modes in the Z' toy model for a Z' mass of 1000 GeV. The numbers N_{weighted} correspond to the sum of the event weights as provided by PYTHIA, which in the SFS case were reweighted to match the initial numbers of ATLAS. The cuts highlighted in red are not used in the MADANALYSIS 5 implementation.

	$m(Z') = 1000\,\text{GeV}$					
	ϵ_{cut} (MA5 / ATLAS)					
Channel	ee		$e\mu$		$\mu\mu$	
No cuts	1.000	1.000	1.000	1.000	1.000	1.000
Triggers	0.951	0.894	0.910	0.817	0.522	0.493
Cosmic-ray veto	1.000	1.000	1.000	0.999	1.000	1.000
Primary vertex	1.000	1.000	1.000	1.000	1.000	1.000
$N(\text{DV}) \geq 1$	0.171	0.362	0.216	0.388	0.313	0.435
Vertex fit	1.000	1.000	1.000	1.000	1.000	1.000
d_{xy}	1.000	1.000	1.000	1.000	1.000	1.000
Fiducial volume	0.720	0.927	0.719	0.935	0.748	0.946
Dis. pixel mod. veto	0.990	0.962	0.986	0.972	0.992	0.972
Material veto	0.898	0.668	0.895	0.702	1.000	1.000
$N(l) \geq 1$	1.000	0.608	1.000	0.693	1.000	0.636
$N(l) \geq 2$	1.000	0.937	1.000	0.942	1.000	0.955
Lepton kinematics	1.000	0.995	1.000	0.996	1.000	0.999
Lepton identification	1.000	0.969	1.000	0.945	1.000	0.946
Overlap removal	1.000	1.000	1.000	0.999	1.000	1.000
Trigger matching	1.000	1.000	1.000	1.000	1.000	0.981
Presel. matching	1.000	0.999	0.995	0.994	1.000	0.998
m_{DV}	1.000	1.000	1.000	1.000	1.000	1.000
Opposite charge	1.000	0.989	1.000	0.995	1.000	0.998

Table 5.12: Cut efficiency tables corresponding to the cutflow tables (table 5.11) for the samples of the three decay Z' decay modes of the 1000 GeV Z'. The cuts highlighted in red are not used in the MadAnalysis 5 implementation.

5.4.4.4 Parameter scan: Overall selection efficiencies and exclusion limits

With a parameter scan, the validity of the implementation can be tested over a wide range of lifetimes. The visualisation of the results facilitates the identification of deviations from ATLAS results and the LLP lifetimes, for which they arise. Due to the relatively high number of samples involved, problems in the implementation can clearly be distinguished from statistical effects. The analysis note provides different figures showing the lifetime dependence of the selection efficiency and the upper limits on the squark production cross section for different choices of squark and neutralino masses, where the λ_{121} and λ_{122} couplings are considered separately. In the HEPData entry of the analysis, the data points of the figures are made available, allowing the reproduction of the plots.

Here, two configurations of squark and neutralino masses were chosen for comparison, for which the scan was done in both coupling scenarios. The results of the overall selection efficiencies and cross section upper limits are shown in figures 5.11 and 5.12.

One can observe that the results are in relatively good agreement up to proper decay lengths of 1000 mm. Beyond this value the curves diverge, which seems to suggest that the implementation is missing a detail which becomes important at higher lifetimes. However, this does not seem very plausible, since an increased lifetime should only reduce the number of decays occurring in the fiducial volume, but there is no qualitatively new effect to be expected above this lifetime. An interesting observation is that the blue ATLAS curves for $m(\tilde{q}) = 1600\,\text{GeV}$ and $m(\chi_1^0) = 1300\,\text{GeV}$ contain a noticeable kink above $c\tau = 1000\,\text{mm}$, which is particularly striking in the case of the λ_{121} coupling, for which no reasonable explanation could be found in the selection criteria of the analysis. It is worth mentioning in this context that according to the analysis note, ATLAS did not generate samples for proper decay lengths above 1000 mm, but combined different samples in the $c\tau$-range between 10 mm and 1000 mm. To use these samples for different LLP lifetimes, the events were reweighted to account for the different probability of the same events to occur in a sample of different lifetime. For the validation of the MadAnalysis 5 implementation of the analysis, a different sample was generated for each value of $c\tau$. However, there is no obvious reason why the different approaches would lead to significantly different results at high lifetimes and a kink in the ATLAS results. The issue has been reported to the ATLAS SUSY conveners, who were so far not able to provide any reasonable explanation of the observed difference. The analysis has been taken over by a different group who announced to investigate on this matter in view of a new analysis, once the existing analysis code will have been integrated into a new analysis framework. Unfortunately their investigations were not completed at the time of this writing.

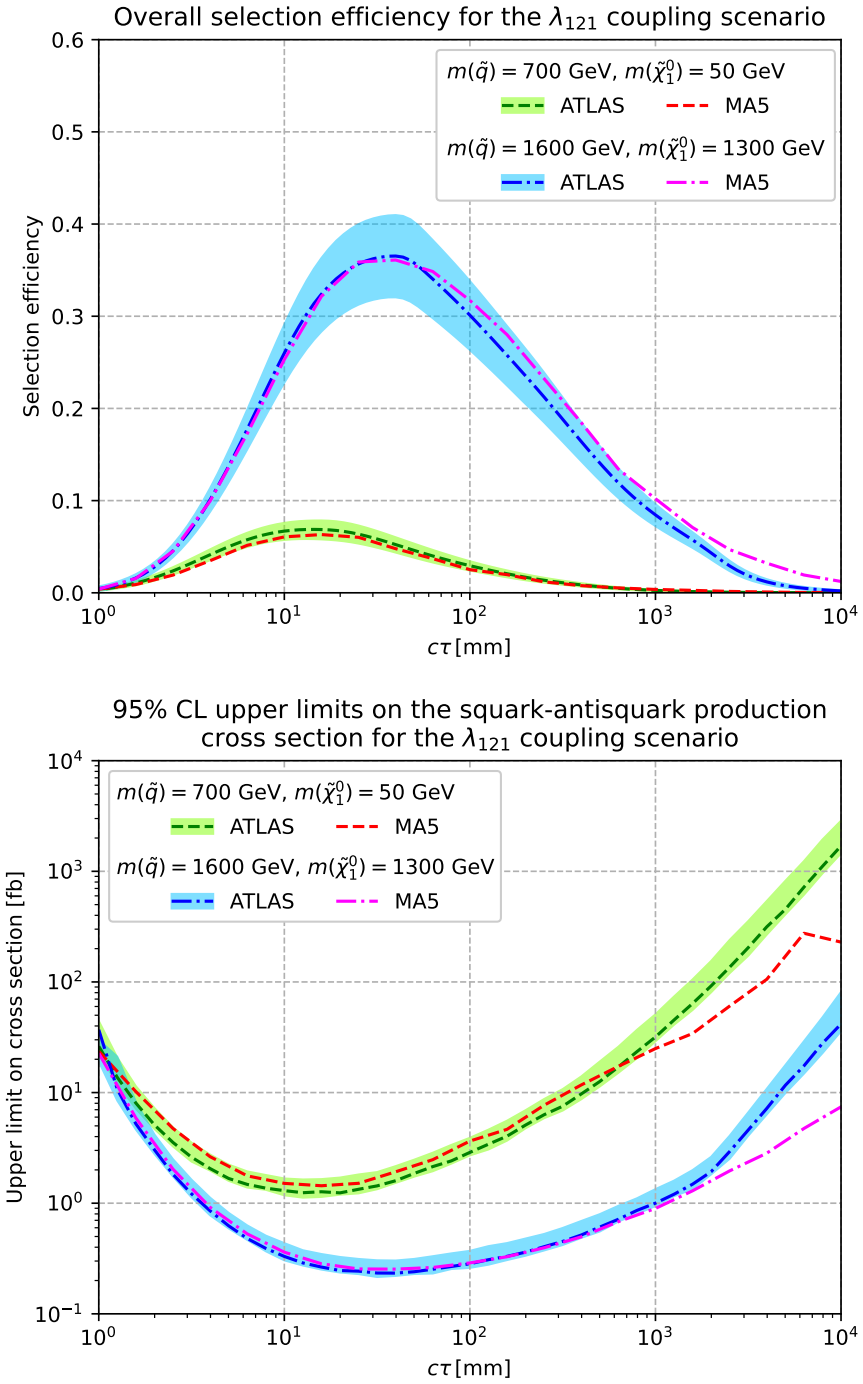

Figure 5.11: Overall selection efficiencies (top) and upper limits on the squark-antisquark production cross section (bottom) obtain with the MadAnalysis 5 implementation, in comparison with the limits and uncertainties found by the ATLAS collaboration, for two configurations of squark and neutralino masses in the λ_{121} coupling scenario.

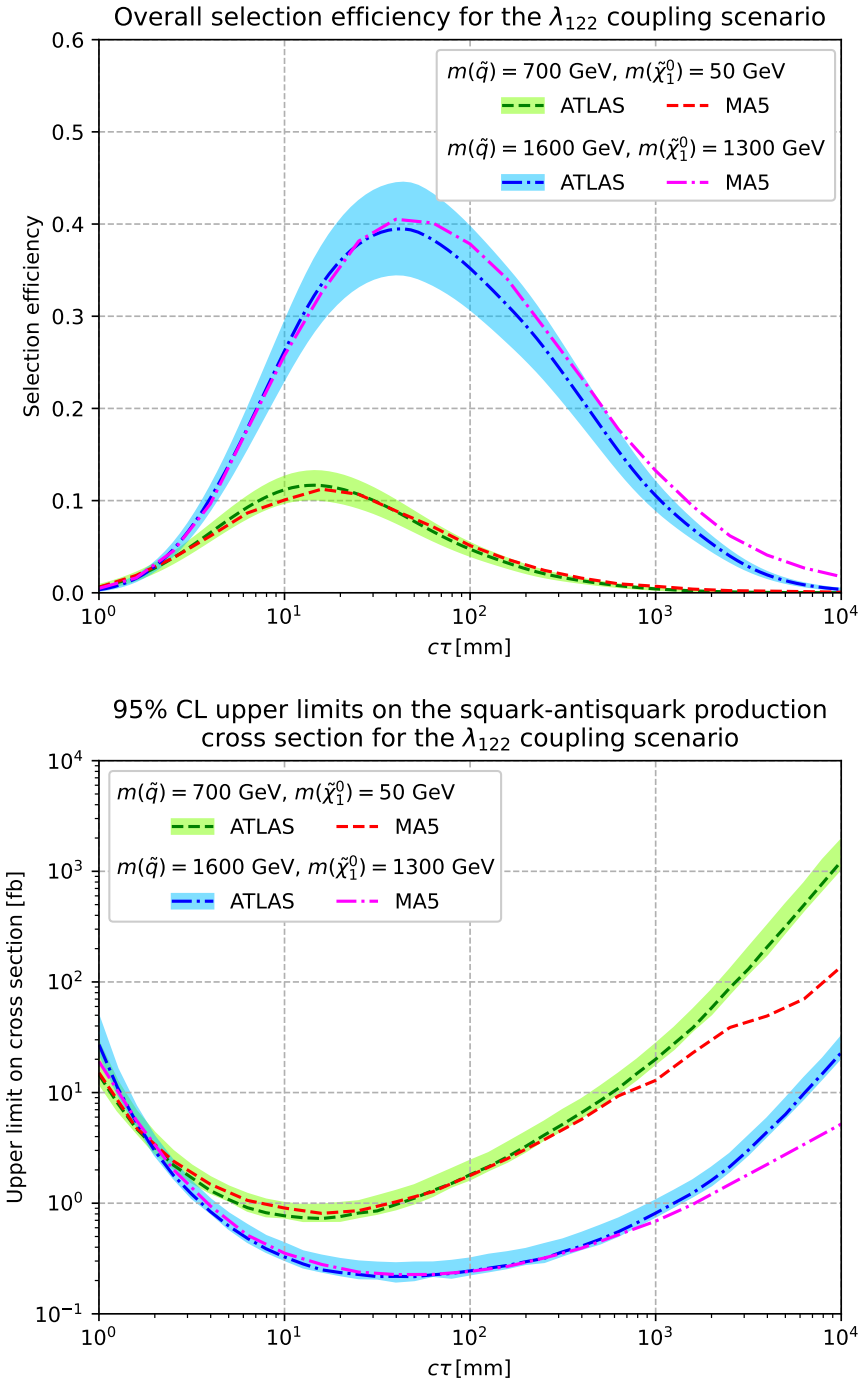

Figure 5.12: Overall selection efficiencies (top) and upper limits on the squark-antisquark production cross section (bottom) obtain with the MadAnalysis 5 implementation, in comparison with the limits and uncertainties found by the ATLAS collaboration, for two configurations of squark and neutralino masses in the λ_{121} coupling scenario.

5.4.4.5 Conclusions on the implementation

The validation process has shown, that the implementation reproduces with reasonably good agreement the final numbers of the ATLAS cutflows. A comparison of the intermediate numbers turns out to be problematic and would presumably require including the simulation of pile-up events, which is currently not possible using MadAnalysis 5 and SFS. It is also not entirely clear, which effects are included in the DV reconstruction efficiencies provided in the auxiliary material of the analysis.

To gain better insights about the validity of the implementation, a parameter scan in the lifetime of the neutralino in the RPV SUSY model for two different configurations of squark and neutralino masses were performed. Here, the agreement with ATLAS results is satisfactory for $c\tau < 1000\,\text{mm}$ but for higher lifetimes a significant difference is is observed in the results for the overall selection efficiencies. At present, the disagreement can not be explained, so that the use of the implementation is only recommended for LLP lifetimes below this value.

Another deficit is the absence of model-independent reconstruction efficiencies, which restrict the use of the implementation to models of the same decay topologies as for the Z' or χ_1^0 in the signal models used by ATLAS. In addition, the user must correctly choose the version of the analysis with the appropriate efficiencies. Nevertheless, if these conditions are respected, the implementation of the analysis can be a valuable tool to set limits on the parameter space of different models.

5.5 Application to vector-like leptons

To demonstrate the exclusion potential of the re-implementation of the ATLAS LLP search discussed in the previous section, the vector-like lepton model introduced in section 1.4.1.2 with mixing of the vector-like leptons with the electron instead of the SM τ lepton, is a suitable candidate signal model. In this model, the vector-like leptons τ' and ν' are produced via the channels (c.f. section 1.4.1.2):

$$\begin{aligned} pp &\to \nu'\overline{\nu}' \,, \\ pp &\to \nu'\tau'^{+} \,, \\ pp &\to \overline{\nu}'\tau'^{-} \,. \end{aligned} \tag{5.5.1}$$

Note that $\overline{\nu}'$ stands for the anti-particle of ν', not for one of the two-component spinor fields as in section 1.4.1.

The neutral VLL ν' decays to an electron and a W-boson, where the latter can then promptly decay to an electron or muon and a neutrino with a branching fraction $\mathrm{Br}(\mathrm{W} \to \ell\nu) \approx 11\,\%$ for $\ell = e, \mu$ [367]. This decay chain generates a vertex with two leptons and a neutrino, as in the case of the χ_1^0 decay in the RVP SUSY model, which justifies the use of the provided efficiencies in the vector-like doublet model. The decay width is proportional to the square of the mixing parameter ϵ, i.e. for small mixing ν' becomes long-lived.

Concerning the charged vector-like lepton τ', the possible decay $\tau \to Ze$ can also generate for the analysis relevant vertices, since the Z-boson decays into pairs of electrons or muons, with a branching ratio of $\mathrm{Br}(\mathrm{Z} \to \ell^+\ell^-) \approx 3.4\,\%$ for $\ell = e, \mu$. As the Z-boson is short-lived, this leads to a vertex with three associated charged leptons. This does not correspond to the topology of the neutralino decay in the RPV SUSY model, so the efficiencies are *a priori* not applicable. The implementation of the analysis can deal with such vertices, but only by applying the efficiency maps for the RPV SUSY model, which might deviate from the true reconstruction efficiencies for this kind of vertex.

Both the production cross sections of the charged and neutral vector-like leptons at the LHC and their decay widths to Z or W bosons are of comparable size [173]. However, the branching fraction into charged leptons is somewhat smaller for the Z boson than for the W boson. Nevertheless, the contribution of the charged leptons in terms of 3-lepton vertices cannot be expected to be completely negligible. Therefore, the overall selection efficiencies obtained with the implementation of this analysis for samples of the vector-like doublet model might be fudged by the application of the unsuitable efficiencies to these vertices. Using the implementation of the analysis for this model in spite of these concerns can be justified as follows: The probability of a displaced vertex to be reconstructed successfully can be expected to be higher, when the number of associated tracks is higher. In using efficiencies of 2-lepton vertex reconstruction for 3-lepton vertices, the implementation would therefore rather underestimate the selection efficiency, i.e. it predicts a smaller number of events passing the selection than the actual analysis would find. In consequence, the bounds on the production cross section of the vector-like leptons will be *weaker* than it should be. This is acceptable, because it does not falsely exclude viable parameter space, but simply places conservative bounds.

As illustrated in section 1.4.1.2, the doublet VLL model is a relatively simple extension of the Standard Model with only two additional parameters, namely the VLL mass, which is equal for τ' and ν' at leading order, and the mixing parameter ϵ. The latter is traded for the proper decay length $c\tau$ of the *neutral* VLL ν', so that a scan in $M_{\tau'}$ and $c\tau$ can be performed with the implementation of the ATLAS analysis to determine the excluded regions. The grid scan in these parameters was performed with mass values below 1600 GeV in steps of 50 GeV and proper decay lengths from 1 mm to 10 000 mm with equal spacing on a logarithmic scale, i.e. powers of 10 increased in steps of 0.5 (precisely the scan was first done with twice the spacing, which was then refined locally to determine the shape of the excluded parameter regions more precisely). In order to determine the excluded parameter points, besides the value of the integrated luminosity of the analysis, a cross section prediction is needed for every event sample to calculate the expected number of events of VLL production. A leading order value for the cross section of the LLP production processes is provided by the event generator. To estimate the effect of higher order corrections on the excluded regions, different K-factors ($^2/_3$, 1 and $^3/_2$) were used to rescale the leading order cross section, considering both possibilities of the cross section to be over- or underestimated at leading order. The upper limits on the cross section were obtained using the CL_s method [282].

5.5.1 Event generation

The events were simulated in a similar way as for the RPV SUSY samples in the validation of the analysis with MadGraph5_aMC@NLO version 2.8.3.2 together with Pythia 8.244 and UFO model files generated for the VLL model by `SARAH` [267, 459–462]. The simulated processes are the ones given in eq. (5.5.1) with up to two jets. It was generated at leading order with 50 000 events per sample, where the NNPDF 2.3 LO [457] set of parton distribution functions was used and the MLM matching scheme [456] with a matching scale of one quarter of the τ' mass was applied.

5.5.2 Results

From the results of the grid scan, exclusion regions in the τ' mass and the proper decay length $c\tau$ were determined, which are shown in figure 5.13. The lifetime $c\tau > 1000$ mm has been highlighted in red to signal that results in this region cannot be trusted due to unsatisfying results in the validation in this lifetime range.

The scan does not put any constraints on the τ' lifetime for masses below 200 GeV. One can observe that a ν' with $c\tau$ below approximately 2 mm is only relatively weakly constrained to masses above approximately 300 GeV. For higher lifetimes, this lower bound grows above 700 GeV. As mentioned earlier, these bounds are conservative.

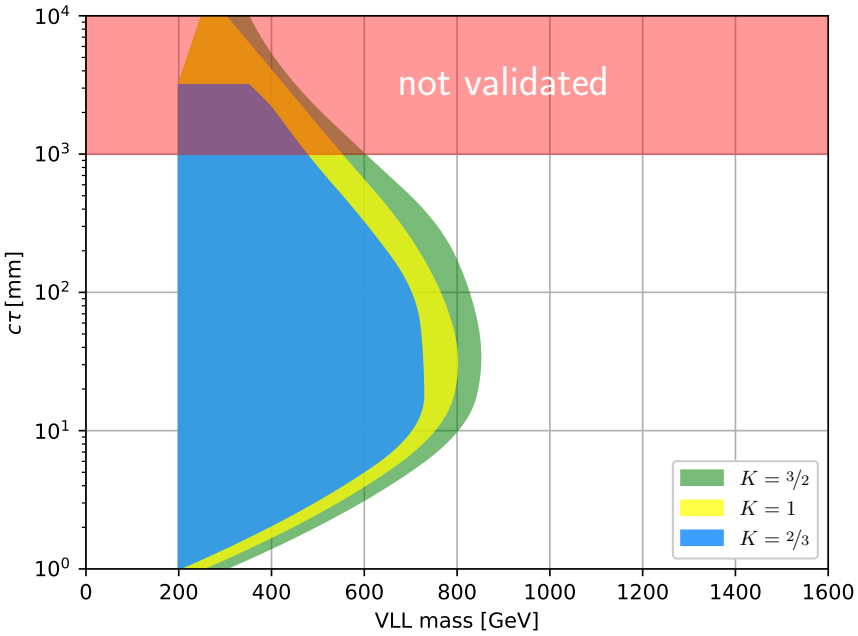

Figure 5.13: Excluded regions at 95 % CL in the parameter space of mass and proper decay length of the vector-like lepton τ' in the vector-like doublet model for cross-sections calculated with different K-factors. The red-shaded region covers the lifetime range above $c\tau = 1000\,\text{mm}$, in which doubts about the validity of the implementation exist.

5.6 Conclusions

The relevance of LLP searches in current and future collider and non-collider experiments has been motivated as an attractive search strategy for signals of new physics, which provide a new discovery potential of particles, which could escape detection within prompt searches. MadAnalysis 5 is a useful tool to fully exploit the potential of collider searches via the reinterpretation of the results to other new physics models. This chapter has presented recent work to supplement MadAnalysis 5 with new capabilities for the searches of non-prompt signatures. A technical feature has been added for the precise determination of trajectories, decay vertices and displacement variables. New physical content in terms of two new LLP analyses was added. The implementations have been validated over a significant range of lifetimes. All the same the validation process has revealed some difficulties in the re-interpretation of analyses, such as the lack of information about efficiencies of detectors and reconstruction algorithms, or the model-dependence of the provided information. The available material for analyses is a general issue in the re-interpretation of physics analyses at the LHC, and there are ongoing efforts and discussions [213] between experimentalists and theorists to communicate about the needs in recasting and the possibilities to provide the additional material of future searches in the most useful form. Finally the parameter space of the vector-like lepton doublet model was investigated with the implementation of the ATLAS search for displaced vertices of oppositely charged leptons and exclusion regions were determined. Other LLP searches are planned to be added to MadAnalysis 5 in the near future.

Conclusion

After two data taking periods of the Large Hadron Collider, the about 50 year old Standard Model is still the best description of what has so far been observed in high-energy collider experiments. This is unquestionably an enormous success for the SM, whereas in the meantime the LHC experiments have failed to tell us something new, leaving the particle physics community without any confirmed solution to the serious problems of the SM, which were discussed in 1. In spite of this unsatisfying circumstance, the LHC program carried out over the past decade is by no means a general failure. It should not be forgotten that the high number of measurements without significant deviations from the SM predictions has been a valuable input for constraining many theories of BSM physics. In the absence of new physics, using these null results to constrain BSM models will certainly remain an important strategy in the future and might provide indications where to look for new physics. The re-interpretation of search results is the purpose of recasting, which consists in the implementation of the logic of existing physics analyses, i.e. the event selection procedure, into a computer program which applies it to Monte-Carlo event samples generated for a different signal hypothesis. This technique has been discussed in some detail in chapter 2.

Chapter 3 and 4 of this thesis have presented the phenomenological study of an effective theory, which addresses one of the longstanding problems of the SM, the absence of a dark matter candidate. The model introduces a candidate for DM and establishes interactions with the SM particle content via the dilaton portal, i.e. by including an additional scalar, the dilaton. The latter is systematically embedded into the model in a procedure that is governed by spontaneously broken scale invariance. This study provides an example of how the LHC results, in combination with complementary experimental input from dark matter direct detection and the relic density as well as partial wave unitary constraints, allow us to restrict the phenomenologically viable parameter space of the model. In particular, it has been found that heavy scalar searches in Run 2 of the LHC have contributed to stronger bounds in the model parameter space. Together with unitarity constraints, they push the model to high masses and weak couplings. Different mixing scenarios have been considered, where in the 'minimal mixing' case the emergence of a 'magic window' in the parameter space of the dilaton mass and decay constant can be observed, in which the constraints on the dilaton mass disappear in a certain range of the dilaton decay constant. It was found for this scenario that the dilaton and dark matter could be lighter than 1 TeV. However, restoring gauge invariance with additional terms destroys this magic windows, since the di-Higgs bounds become dominant. Concerning the LHC dark matter searches, direct production for DM masses above 300 GeV are out of reach of the LHC, but could

be accessible at future colliders. The study is also an example of how results of collider searches can be combined with complementary experimental input, which in this case has been done via a matching of the relic density with Planck results and by the computation of dark matter direct detection cross sections and comparison with observations.

This thesis has also addressed in chapter 5 the matter of unconventional collider signatures, with a focus on searches for long-lived particles in the context of LHC recasting. It has been argued that new physics might remain undetected in searches which limit their attention to promptly decaying particles. This explains the increasing interest in searches for displaced decays of LLPs, which can give rise to a variety of different signatures, depending on the type of the LLP, some of which have been discussed in this work. The detection of such signatures is associated with some technical challenges on the experimental side, compared to prompt searches, such as the correct reconstruction of tracks and vertices. It has been pointed out that for recasting purposes, it is important to take into account the detector efficiencies in the re-implementation of an analysis, since they have implications on the signal yield of a simulated event sample. Another effect of detectors is the bending of charged particle trajectories in the magnetic field that is present in the detector volume. Part of this work has been the simulation of magnetic field effects on the trajectories of particles involved in a simulated event sample, which has been implemented as a new module of the MadAnalysis 5 framework. The latter has then been used for the implementation of two 13 TeV LHC searches for long-lived particle signatures: a CMS search for displaced leptons and an ATLAS search for displaced vertices of oppositely charged leptons. The implementation has been documented and some complications, related in particular to reconstruction efficiencies, have been pointed out. However, with the exception of the highest lifetimes used for the validation, the validity of the implementations has been confirmed by comparison with results of the experimental collaborations. An application of the re-implemented ATLAS analysis to a suitable signal model, an extension of the SM with a vector-like lepton doublet, has been presented, where an exclusion plot in the parameter space of the VLL mass and lifetime was obtained.

It is certain that long-lived particle searches will play an important role in the next years in the LHC main experiments, but also in new experimental setups. For instance, the dedicated LLP experiment FASER will be operational in the upcoming Run 3 data taking period of the LHC. There will be other technical improvements in the future, including especially the high-luminosity upgrade, which will significantly increase the amount of available data and therefore enhance the potential of the (HL-)LHC to uncover BSM physics, or alternatively further constrain BSM theories, for example with recasting. Additionally, there are proposals for future colliders. Good motivations to persue the quest for new physics exist, e.g. the recent independent confirmation of the tension concerning the anomalous magnetic moment of the muon, or the persisting B-anomalies. What is certain is that particle physics is far from being at its end, and we can hope for exciting news in upcoming years.

Appendix A

Two-component spinors

Some theories are more conveniently formulated in terms of two-components spinors rather than in the more commonly used four-component spinor notation. This appendix will briefly introduce two-component spinors based on ref. [32], showing essentially how they are related to four-component spinors and giving the expressions for their gauge covariant derivative and their gauge and Yukawa interaction terms. Nothing more will be needed in this thesis, which uses two-component spinors only in the context of vector-like fermions and Supersymmetry in section 1.4. For a very exhaustive introduction into this matter, the interested reader shall be referred to ref. [463].

Two-component spinors, also often called *Weyl-spinors* [463], are classified as either left-handed or right-handed, according to the representation of the Lorentz group under which they transform. *Left-handed* spinors transform under the $(\frac{1}{2}, 0)$-representation and *right-handed* ones under the $(0, \frac{1}{2})$-representation. To mark the difference between these two types of spinors, a different notation is conventionally used for their spinor indices. In this convention, dotted indices are used for right-handed spinors and undotted indices for left-handed spinors, with the possible values 1 and 2 in both cases. A left-handed spinor is turned into a right-handed one via Hermitian conjugation, and vice versa:

$$\psi^\dagger_{\dot\alpha} \equiv (\psi_\alpha)^\dagger \,. \tag{A.1}$$

Contraction and raising or lowering of spinor indices in a similar way as for Lorentz indices is possible with the help of an anti-symmetric symbol,

$$\epsilon^{12} = -\epsilon^{21} = \epsilon_{21} = -\epsilon_{12} = 1 \,, \tag{A.2}$$

such that the following relations hold:

$$\psi_\alpha = \epsilon_{\alpha\beta}\psi^\beta \,, \qquad \psi^\alpha = \epsilon^{\alpha\beta}\psi_\beta \,, \qquad \psi^\dagger_{\dot\alpha} = \epsilon_{\dot\alpha\dot\beta}\psi^{\dagger\dot\beta} \,, \qquad \psi^{\dagger\dot\alpha} = \epsilon^{\dot\alpha\dot\beta}\psi^\dagger_{\dot\beta} \,. \tag{A.3}$$

Four-component spinors can be expressed in terms of two left-handed spinors ξ_α and χ_α in the case of Dirac spinors or one left-handed spinor ψ_α in the case of Majorana spinors:

$$\Psi_D = \begin{pmatrix} \xi_\alpha \\ \chi^{\dagger\dot\alpha} \end{pmatrix} \,, \qquad \Psi_M = \begin{pmatrix} \psi_\alpha \\ \psi^{\dagger\dot\alpha} \end{pmatrix} \,. \tag{A.4}$$

Consequently, a theory can always be formulated by using only left-handed spinor fields instead of both left- and right-handed ones, since right-handed spinors can always be written as the hermitian conjugate of a left-handed one. Alternatively, one could do the same thing using only right-handed spinor fields.

In order to express chiral interaction, which involve only the left- or right-handed part of a spinor, in the Dirac spinor notation, the chiral projectors P_L and P_R can be used, which act on Ψ_D as

$$P_L\Psi_D = \begin{pmatrix} \xi_\alpha \\ 0 \end{pmatrix}, \qquad P_R\Psi_D = \begin{pmatrix} 0 \\ \chi^{\dagger\dot{\alpha}} \end{pmatrix}. \tag{A.5}$$

To see which form the Lagrangian takes in the two-component spinor notation, consider the free Lagrangian of a Dirac fermion:

$$\mathcal{L}_{\text{Dirac}} = i\overline{\Psi}_D\gamma^\mu\partial_\mu\Psi_D - m\overline{\Psi}_D\Psi_D\,. \tag{A.6}$$

Owing to the way in which the Dirac spinor is expressed via two Weyl-spinors, the corresponding representation of the Dirac matrices, the *Weyl-representation* [46], has to be used. In this representation, they take the form

$$\gamma^\mu = \begin{pmatrix} 0 & \sigma^\mu \\ \overline{\sigma}^\mu & 0 \end{pmatrix}, \tag{A.7}$$

containing the 2×2 matrices $\sigma^\mu = (1, \sigma^i)$ and $\overline{\sigma}^\mu = (1, -\sigma^i)$, which are explicitly given by

$$\begin{aligned} \sigma^0 = \overline{\sigma}^0 &= \begin{pmatrix} 1 & 0 \\ 0 & 1 \end{pmatrix}, \qquad \sigma^1 = -\overline{\sigma}^1 = \begin{pmatrix} 0 & 1 \\ 1 & 0 \end{pmatrix}, \\ \sigma^2 = -\overline{\sigma}^2 &= \begin{pmatrix} 0 & -i \\ i & 0 \end{pmatrix}, \qquad \sigma^3 = -\overline{\sigma}^3 = \begin{pmatrix} 1 & 0 \\ 0 & -1 \end{pmatrix}. \end{aligned} \tag{A.8}$$

Here, σ^i for $i = 1, 2, 3$ are the Pauli matrices. Therefore, the explicit form of the adjoint spinor is

$$\overline{\Psi}_D = \Psi_D^\dagger\gamma^0 = \begin{pmatrix} \chi^\alpha & \xi^\dagger_{\dot{\alpha}} \end{pmatrix}. \tag{A.9}$$

Then, the Lagrangian $\mathcal{L}_{\text{Dirac}}$ expressed in terms of the two-component spinors, is given by

$$\mathcal{L}_{\text{Dirac}} = i\xi^\dagger_{\dot{\alpha}}(\overline{\sigma}^\mu)^{\dot{\alpha}\beta}\partial_\mu\xi_\beta + i\chi^\alpha(\sigma^\mu)_{\alpha\dot{\beta}}\partial_\mu\chi^{\dagger\dot{\beta}} - m(\xi^\dagger_{\dot{\alpha}}\chi^{\dagger\dot{\alpha}} + \chi^\alpha\xi_\alpha)\,, \tag{A.10}$$

where the height of the spinor indices corresponds to the previously mentioned contraction of the spinor indices, or in a notation, where the indices are suppressed

$$\mathcal{L}_{\text{Dirac}} = i\xi^\dagger\overline{\sigma}^\mu\partial_\mu\xi + i\chi\sigma^\mu\partial_\mu\chi^\dagger - m(\xi^\dagger\chi^\dagger + \chi\xi)\,. \tag{A.11}$$

The indices can be restored with

$$\xi\chi \equiv \xi^\alpha\chi_\alpha\,, \qquad \xi^\dagger\chi^\dagger \equiv \xi^\dagger_{\dot{\alpha}}\chi^{\dagger\dot{\alpha}} \tag{A.12}$$

and

$$\xi^\dagger\overline{\sigma}^\mu\chi \equiv \xi^\dagger_{\dot{\alpha}}(\overline{\sigma}^\mu)^{\dot{\alpha}\beta}\chi_\beta\,, \qquad \xi\sigma^\mu\chi^\dagger \equiv \xi^\alpha(\sigma^\mu)_{\alpha\dot{\beta}}\chi^{\dagger\dot{\beta}}\,. \tag{A.13}$$

Using the anti-commuting nature of ξ and χ, it can be shown that

$$\xi\chi = \chi\xi\,, \qquad \xi^\dagger\chi^\dagger = \chi^\dagger\xi^\dagger\,, \qquad \xi^\dagger\overline{\sigma}^\mu\chi = -\chi\sigma^\mu\xi^\dagger\,, \tag{A.14}$$

and hence

$$\mathcal{L}_{\text{Dirac}} = i\xi^\dagger\overline{\sigma}^\mu\partial_\mu\xi + i\chi^\dagger\overline{\sigma}^\mu\partial_\mu\chi - m(\xi\chi + \xi^\dagger\chi^\dagger)\,. \tag{A.15}$$

Along the same lines, one finds for the Lagrangian of a Majorana fermion:

$$\begin{aligned}\mathcal{L}_{\text{Majorana}} &= \frac{i}{2}\overline{\Psi}_M\gamma^\mu\partial_\mu\Psi_M - \frac{1}{2}m\overline{\Psi}_M\Psi_M \\ &= i\psi^\dagger\overline{\sigma}^\mu\partial_\mu\psi - \frac{1}{2}m(\psi\psi + \psi^\dagger\psi^\dagger)\,.\end{aligned} \tag{A.16}$$

Due to the similar form of the Lagrangians, they can be summarised in a more general expression,

$$\mathcal{L} \supset i\psi^{\dagger i}\overline{\sigma}^\mu\partial_\mu\chi_i + \frac{1}{2}\left(M^{ij}\psi_i\psi_j + \text{c.c.}\right)\,, \tag{A.17}$$

which can describe both Majorana and Dirac fermions, where the indices i and j run over the various fermions of the theory.

Concerning interacting theories, the fermions can have interaction terms with scalars or vectors [463], the form of which will be given in the following. For gauge interactions, the covariant derivative will be needed, which has the general form

$$(D_\mu)_i{}^j \equiv \delta_i{}^j\partial_\mu + ig_aA_\mu^a(T^a)_i{}^j\,, \tag{A.18}$$

where A_μ^a are the gauge fields, T^a the generators and g_a the gauge coupling. For left-handed spinors ψ_i, the Lagrangian for the interaction with the gauge bosons A_a^μ is then given by

$$\mathcal{L}_{\text{gauge}} = -g_aA_\mu^a\psi^{\dagger i}\overline{\sigma}^\mu(T^a)_i{}^j\psi_j\,. \tag{A.19}$$

Yukawa interactions of the fermion fields and scalars of the theory can be expressed in the form

$$\mathcal{L}_{\text{Yukawa}} = -\frac{1}{2}Y^{Ijk}\phi_I\psi_j\psi_k - \frac{1}{2}Y_{Ijk}\phi^I\psi^{\dagger j}\psi^{\dagger k}\,, \tag{A.20}$$

where the index I runs over the scalars of the theory and the Yukawa couplings fulfill $Y_{Ijk} = (Y^{Ijk})^*$.

Appendix B

Vector-like leptons: Derivations

B.1 Mixing

The Lagrangian of the vector-like singlet model contains mass and mixing terms between the SM tau lepton and the vector-like lepton of the the form

$$\mathcal{L} \supset -\begin{pmatrix}\tau & \tau'\end{pmatrix}\mathcal{M}\begin{pmatrix}\overline{\tau}\\ \overline{\tau}'\end{pmatrix} + \text{c.c.}\,, \tag{B.1}$$

where the mass matrix is given by

$$\mathcal{M} = \begin{pmatrix}\frac{y_\tau v}{\sqrt{2}} & \frac{\epsilon v}{\sqrt{2}}\\ 0 & m_{\tau'}\end{pmatrix}\,. \tag{B.2}$$

The matrix can be diagonalised with a transformation of the field basis via unitary matrices L and R (see ref. [463, p.34 f.] for more details)

$$\begin{pmatrix}\tau\\ \overline{\tau}'\end{pmatrix} = L\begin{pmatrix}\tilde{\tau}\\ \tilde{\tau}'\end{pmatrix}\,, \qquad \begin{pmatrix}\overline{\tau}\\ \overline{\tau}'\end{pmatrix} = R\begin{pmatrix}\tilde{\overline{\tau}}\\ \tilde{\overline{\tau}}'\end{pmatrix}\,, \tag{B.3}$$

where the fields carrying an additional tilde symbol are the mass eigenstate fields, which will then have a mass matrix

$$L^T\mathcal{M}R = \mathbf{m} = \text{diag}(M_\tau, M_{\tau'})\,. \tag{B.4}$$

To find the expressions for L and R, one can make use of their unitarity to write

$$\begin{aligned}\mathbf{m}^\dagger\mathbf{m} &= \left(R^\dagger\mathcal{M}^\dagger L^*\right)\left(L^T\mathcal{M}R\right) = R^\dagger\mathcal{M}^\dagger\mathcal{M}R = \mathbf{m}^2\,,\\ \mathbf{m}\mathbf{m}^\dagger &= \left(L^T\mathcal{M}R\right)\left(R^\dagger\mathcal{M}^\dagger L^*\right) = L^T\mathcal{M}\mathcal{M}^\dagger L^* = \mathbf{m}^2\,,\end{aligned} \tag{B.5}$$

where it is obvious that $\mathbf{m}^2 = \mathbf{m}^\dagger\mathbf{m} = \mathbf{m}\mathbf{m}^\dagger$ is Hermitian and diagonal, since $\mathbf{m}$ is diagonal. Since the combinations $\mathcal{M}^\dagger\mathcal{M}$ and $\mathcal{M}\mathcal{M}^\dagger$ are Hermitian, one could follow the standard procedure for the diagonalisation of a matrix, i.e. determine matrices $U_{L,R}$, such that they diagonalise the combinations of mass matrices via $U_L^\dagger\mathcal{M}^\dagger\mathcal{M}U_L$ and $U_R^\dagger\mathcal{M}\mathcal{M}^\dagger U_R$. These

are as usual constructed from the normalised eigenvectors of $\mathcal{M}^\dagger\mathcal{M}$ and $\mathcal{M}\mathcal{M}^\dagger$. Once this is done, one can identify $L = U_L^*$ and $R = U_R$.

Here, we are only interested in the case of small mixing, which will simplify the calculation. With $\mathcal{M}$ being real, L and R are orthogonal matrices, i.e. rotations. A small amount of mixing $\epsilon \ll 1$ leads to small rotations, so that at leading order in the rotation angles α_L and α_R they take the form

$$L = \begin{pmatrix} 1 & -\alpha_L \\ \alpha_L & 1 \end{pmatrix}, \qquad R = \begin{pmatrix} 1 & -\alpha_R \\ \alpha_R & 1 \end{pmatrix}. \tag{B.6}$$

After evaluating the condition that $\mathbf{m}^2$ must be diagonal for both L and R as in eq. (B.5), i.e. requiring that the off-diagonal matrix elements vanish and neglecting terms of second order in the rotation angles, one obtains

$$\alpha_L = -\frac{\sqrt{2}\epsilon m_{\tau'} v}{2m_{\tau'}^2 - v^2 y_\tau^2}, \qquad \alpha_R = -\frac{\epsilon v^2 y_\tau}{2m_{\tau'}^2 - v^2 y_\tau^2}. \tag{B.7}$$

In the vector-like doublet model, the mass matrix of the charged leptons is given by

$$\mathcal{M} = \begin{pmatrix} \frac{y_\tau v}{\sqrt{2}} & 0 \\ \frac{\epsilon v}{\sqrt{2}} & m_{\tau'} \end{pmatrix}, \tag{B.8}$$

which is just the transposed of the above mass matrix. The procedure is exactly the same as, whereas the difference in the mass matrix leads to an interchange of the rotation angles,

$$\alpha_L = -\frac{\epsilon v^2 y_\tau}{2m_{\tau'}^2 - v^2 y_\tau^2}, \qquad \alpha_R = -\frac{\sqrt{2}\epsilon m_{\tau'} v}{2m_{\tau'}^2 - v^2 y_\tau^2}, \tag{B.9}$$

which is effectively the same as an interchange of L and R.

B.2 Gauge interactions

In this section, the gauge-covariant derivatives and the resulting interaction Lagrangians are given explicitly for the third-generation SM leptons and a vector-like lepton. Corresponding expressions for the generation one and two SM leptons are obtained in the same way as for the third generation. The expressions are obtained starting from eqs. (A.18) and (A.19). After deriving the interaction Lagrangians in the interaction basis, the physical gauge boson fields are introduced (c.f. section 1.1.3.4), using the relations [463]

$$\begin{aligned} W_\mu^1 &= \frac{1}{\sqrt{2}}\left(W_\mu^+ + W_\mu^-\right), \\ W_\mu^2 &= \frac{i}{\sqrt{2}}\left(W_\mu^+ - W_\mu^-\right), \\ W_\mu^3 &= Z_\mu c_W + A_\mu s_W, \\ B_\mu &= -Z_\mu s_W + A_\mu c_W, \end{aligned} \tag{B.1}$$

with $c_W \equiv \cos\theta_W$ and $s_W \equiv \sin\theta_W$, and the gauge coupling g' is replaced using

$$e = g s_W = g' c_W \qquad \text{and} \qquad c_W^2 + s_W^2 = 1. \tag{B.2}$$

B.2.1 Standard Model leptons

The fields associated with the SM third-generation leptons are $L = (\nu, \tau)$, which transforms under the $(\mathbf{1}, \mathbf{2}, -1/2)$ representation and $\overline{\tau}$, which transforms under the $(\mathbf{1}, \mathbf{1}, +1)$ representation.

B.2.1.1 Lepton doublet L

Covariant derivative:

$$\begin{aligned} D_\mu L &= \left(\partial_\mu + \frac{i}{2} g W_\mu^1 \sigma^1 + \frac{i}{2} g W_\mu^2 \sigma^2 + \frac{i}{2} g W_\mu^3 \sigma^3 - i\frac{g'}{2} B_\mu\right) L \\ &= \left(\partial_\mu + \frac{i}{2}\begin{pmatrix} g W_\mu^3 - g' B_\mu & g(W_\mu^1 - i W_\mu^2) \\ g(W_\mu^1 + i W_\mu^2) & -(g W_\mu^3 + g' B_\mu) \end{pmatrix}\right)\begin{pmatrix}\nu \\ \tau\end{pmatrix} \end{aligned} \tag{B.3}$$

Interaction Lagrangian:

$$\begin{aligned} \mathcal{L}^L_{\text{gauge}} &= -\frac{1}{2}(L)^i \left(g W_\mu^1 \overline{\sigma}^\mu (\sigma_1)_i{}^j + g W_\mu^2 \overline{\sigma}^\mu (\sigma_2)_i{}^j + g W_\mu^3 \overline{\sigma}^\mu (\sigma_3)_i{}^j - g' B_\mu \overline{\sigma}^\mu \delta_i{}^j\right)(L)_j \\ &= -\frac{1}{2}\begin{pmatrix}\nu^\dagger & \tau^\dagger\end{pmatrix}\begin{pmatrix} (g W_\mu^3 - g' B_\mu)\overline{\sigma}^\mu & g(W_\mu^1 - i W_\mu^2)\overline{\sigma}^\mu \\ g(W_\mu^1 + i W_\mu^2)\overline{\sigma}^\mu & (-g W_\mu^3 - g' B_\mu)\overline{\sigma}^\mu \end{pmatrix}\begin{pmatrix}\nu \\ \tau\end{pmatrix} \\ &= -\frac{1}{2}\Big[(g W_\mu^3 - g' B_\mu)\nu^\dagger \overline{\sigma}^\mu \nu + g(W_\mu^1 - i W_\mu^2)\nu^\dagger \overline{\sigma}^\mu \tau \\ &\qquad + g(W_\mu^1 + i W_\mu^2)\tau^\dagger \overline{\sigma}^\mu \nu + (-g W_\mu^3 - g' B_\mu)\tau^\dagger \overline{\sigma}^\mu \tau\Big] \end{aligned} \tag{B.4}$$

Interactions with the physical fields A_μ, Z_μ and $W_\mu^\pm$:

$$\begin{aligned} \mathcal{L}^L_{\text{gauge}} = &-\frac{g}{\sqrt{2}} W_\mu^+ \nu^\dagger \overline{\sigma}^\mu \tau - \frac{g}{\sqrt{2}} W_\mu^- \tau^\dagger \overline{\sigma}^\mu \nu + e A_\mu \tau^\dagger \overline{\sigma}^\mu \tau \\ &- \frac{g}{2 c_W} Z_\mu \nu^\dagger \overline{\sigma}^\mu \nu - \frac{g}{c_W}\left(s_W^2 - \frac{1}{2}\right) Z_\mu \tau^\dagger \overline{\sigma}^\mu \tau \end{aligned} \tag{B.5}$$

B.2.1.2 Lepton singlet $\overline{\tau}$

Covariant derivative:

$$D_\mu \overline{\tau} = \left(\partial_\mu + i g' B_\mu\right)\overline{\tau} \tag{B.6}$$

Interaction Lagrangian:

$$\mathcal{L}^{\overline{\tau}}_{\text{gauge}} = -g' B_\mu \, \overline{\tau}^\dagger \overline{\sigma}^\mu \overline{\tau} \tag{B.7}$$

Interactions with the physical fields A_μ, Z_μ and $W_\mu^\pm$:

$$\mathcal{L}^{\overline{\tau}}_{\text{gauge}} = \frac{g s_W^2}{c_W} Z_\mu \, \overline{\tau}^\dagger \overline{\sigma}^\mu \overline{\tau} - e A_\mu \, \overline{\tau}^\dagger \overline{\sigma}^\mu \overline{\tau} \tag{B.8}$$

B.2.2 Singlet vector-like lepton model

In the singlet VLL model, two left-handed fields τ' and $\overline{\tau}'$ are associated with the vector-like lepton. The field τ' transforms under the $(\mathbf{1}, \mathbf{1}, -1)$ representation and the field $\overline{\tau}'$ under the $(\mathbf{1}, \mathbf{1}, +1)$ representation.

B.2.2.1 Lepton singlet τ'

Covariant derivative:

$$D_\mu \tau' = \left(\partial_\mu - i g' B_\mu\right) \tau' \tag{B.9}$$

Interaction Lagrangian:

$$\mathcal{L}^{\tau'}_{\text{gauge}} = g' B_\mu \, \tau'^\dagger \overline{\sigma}^\mu \tau' \tag{B.10}$$

Interactions with the physical fields A_μ, Z_μ and $W^\pm_\mu$:

$$\mathcal{L}^{\overline{\tau}'}_{\text{gauge}} = -\frac{g s_W^2}{c_W} Z_\mu \, \tau'^\dagger \overline{\sigma}^\mu \tau' + e A_\mu \, \tau'^\dagger \overline{\sigma}^\mu \tau' \tag{B.11}$$

B.2.2.2 Lepton singlet $\overline{\tau}'$

Covariant derivative of $\overline{\tau}'$ (same representation as $\overline{\tau}$):

$$D_\mu \overline{\tau}' = \left(\partial_\mu + i g' B_\mu\right) \overline{\tau}' \tag{B.12}$$

Interaction Lagrangian:

$$\mathcal{L}^{\overline{\tau}'}_{\text{gauge}} = -g' B_\mu \, \overline{\tau}'^\dagger \overline{\sigma}^\mu \overline{\tau}' \tag{B.13}$$

Interactions with the physical fields A_μ, Z_μ and $W^\pm_\mu$:

$$\mathcal{L}^{\overline{\tau}'}_{\text{gauge}} = \frac{g s_W^2}{c_W} Z_\mu \, \overline{\tau}'^\dagger \overline{\sigma}^\mu \overline{\tau}' - e A_\mu \, \overline{\tau}'^\dagger \overline{\sigma}^\mu \overline{\tau}' \tag{B.14}$$

B.2.3 Doublet vector-like lepton model

The doublet VLL model contains two doublets of left-handed fields: $L' = (\nu', \tau')$ transforms under the $(\mathbf{1}, \mathbf{2}, -1/2)$ representation and $\overline{L}' = (\overline{\tau}', \overline{\nu}')$ under the $(\mathbf{1}, \mathbf{2}, +1/2)$ representation.

B.2.3.1 Lepton doublet L'

Covariant derivative (same representation as L):

$$\begin{aligned} D_\mu L' &= \left(\partial_\mu + \frac{i}{2} g W^1_\mu \sigma^1 + \frac{i}{2} g W^2_\mu \sigma^2 + \frac{i}{2} g W^3_\mu \sigma^3 - i \frac{g'}{2} B_\mu\right) L' \\ &= \left(\partial_\mu + \frac{i}{2} \begin{pmatrix} g W^3_\mu - g' B_\mu & g(W^1_\mu - i W^2_\mu) \\ g(W^1_\mu + i W^2_\mu) & -(g W^3_\mu + g' B_\mu) \end{pmatrix}\right) \begin{pmatrix} \nu' \\ \tau' \end{pmatrix} \end{aligned} \tag{B.15}$$

Interaction Lagrangian:

$$\begin{aligned}\mathcal{L}^{L'}_{\text{gauge}} = -\frac{1}{2}\Big[&(gW^3_\mu - g'B_\mu)\nu'^\dagger\overline{\sigma}^\mu\nu' + g(W^1_\mu - iW^2_\mu)\nu'^\dagger\overline{\sigma}^\mu\tau' \\ &+ g(W^1_\mu + iW^2_\mu)\tau'^\dagger\overline{\sigma}^\mu\nu' + (-gW^3_\mu - g'B_\mu)\tau'^\dagger\overline{\sigma}^\mu\tau'\Big]\end{aligned} \tag{B.16}$$

Interactions with the physical fields A_μ, Z_μ and $W^\pm_\mu$:

$$\begin{aligned}\mathcal{L}^{L'}_{\text{gauge}} = &-\frac{g}{\sqrt{2}}W^+_\mu\nu'^\dagger\overline{\sigma}^\mu\tau' - \frac{g}{\sqrt{2}}W^-_\mu\tau'^\dagger\overline{\sigma}^\mu\nu' + eA_\mu\tau'^\dagger\overline{\sigma}^\mu\tau' \\ &- \frac{g}{2c_W}Z_\mu\nu'^\dagger\overline{\sigma}^\mu\nu' - \frac{g}{c_W}\left(s^2_W - \frac{1}{2}\right)Z_\mu\tau'^\dagger\overline{\sigma}^\mu\tau'\end{aligned} \tag{B.17}$$

B.2.3.2 Lepton doublet $\overline{L}'$

Covariant derivative of $\overline{L}'$:

$$\begin{aligned}D_\mu\overline{L}' &= \left(\partial_\mu + \frac{i}{2}gW^1_\mu\sigma^1 + \frac{i}{2}gW^2_\mu\sigma^2 + \frac{i}{2}gW^3_\mu\sigma^3 + i\frac{g'}{2}B_\mu\right)\overline{L}' \\ &= \left(\partial_\mu + \frac{i}{2}\begin{pmatrix} gW^3_\mu + g'B_\mu & g(W^1_\mu - iW^2_\mu) \\ g(W^1_\mu + iW^2_\mu) & -(gW^3_\mu - g'B_\mu)\end{pmatrix}\right)\begin{pmatrix}\overline{\tau}' \\ \overline{\nu}'\end{pmatrix}\end{aligned} \tag{B.18}$$

Interaction Lagrangian:

$$\begin{aligned}\mathcal{L}^{\overline{L}'}_{\text{gauge}} &= -\frac{1}{2}(\overline{L}')^i\left(gW^1_\mu\overline{\sigma}^\mu(\sigma_1)_i{}^j + gW^2_\mu\overline{\sigma}^\mu(\sigma_2)_i{}^j + gW^3_\mu\overline{\sigma}^\mu(\sigma_3)_i{}^j + g'B_\mu\overline{\sigma}^\mu\delta_i{}^j\right)(\overline{L}')_j \\ &= -\frac{1}{2}\begin{pmatrix}\overline{\tau}'^\dagger & \overline{\nu}'^\dagger\end{pmatrix}\begin{pmatrix}(gW^3_\mu + g'B_\mu)\overline{\sigma}^\mu & g(W^1_\mu - iW^2_\mu)\overline{\sigma}^\mu \\ g(W^1_\mu + iW^2_\mu)\overline{\sigma}^\mu & (-gW^3_\mu + g'B_\mu)\overline{\sigma}^\mu\end{pmatrix}\begin{pmatrix}\overline{\tau}' \\ \overline{\nu}'\end{pmatrix} \\ &= -\frac{1}{2}\Big[(gW^3_\mu + g'B_\mu)\overline{\tau}'^\dagger\overline{\sigma}^\mu\overline{\tau}' + g(W^1_\mu - iW^2_\mu)\overline{\tau}'^\dagger\overline{\sigma}^\mu\overline{\nu}' \\ &\qquad + g(W^1_\mu + iW^2_\mu)\overline{\nu}'^\dagger\overline{\sigma}^\mu\overline{\tau}' + (-gW^3_\mu + g'B_\mu)\overline{\nu}'^\dagger\overline{\sigma}^\mu\overline{\nu}'\Big]\end{aligned} \tag{B.19}$$

Interactions with the physical fields A_μ, Z_μ and $W^\pm_\mu$:

$$\begin{aligned}\mathcal{L}^{\overline{L}'}_{\text{gauge}} = &-\frac{g}{\sqrt{2}}W^+_\mu\overline{\tau}'^\dagger\overline{\sigma}^\mu\overline{\nu}' - \frac{g}{\sqrt{2}}W^-_\mu\overline{\nu}'^\dagger\overline{\sigma}^\mu\overline{\tau}' - eA_\mu\overline{\tau}'^\dagger\overline{\sigma}^\mu\overline{\tau}' \\ &+ \frac{g}{c_W}\left(s^2_W - \frac{1}{2}\right)Z_\mu\overline{\tau}'^\dagger\overline{\sigma}^\mu\overline{\tau}' + \frac{g}{2c_W}Z_\mu\overline{\nu}'^\dagger\overline{\sigma}_\mu\overline{\nu}'\end{aligned} \tag{B.20}$$

Appendix C

Dilaton-dark-matter model: Derivation of the dilaton potential

This appendix shows how to derive the form of the dilaton potential in eq. (3.2.4), which is used in the dilaton portal dark matter model presented in chapter 3. The basic assumption on the origin of this potential is, that the underlying conformal field theory, which is the UV completion of the effective theory of chapter 3, is explicitly broken via an operator $\mathcal{O}$ with a scaling dimension $\Delta_{\mathcal{O}}$ which is nearly marginal, i.e.

$$\mathcal{L}^{\text{CFT}}_{\text{breaking}} = \lambda_{\mathcal{O}}\mathcal{O}(x)\,, \qquad |\Delta_{\mathcal{O}} - 4| \ll 1\,. \tag{C.1}$$

According to [286, 290], this leads to a potential in the low-energy effective theory of the form

$$V(\chi) = \chi^4 \sum_{n=0}^{\infty} c_n(\Delta_{\mathcal{O}}) \left(\frac{\chi}{f}\right)^{n(\Delta_{\mathcal{O}}-4)} \tag{C.2}$$

with coefficients $c_n(\Delta_{\mathcal{O}})$ being proportional to $\lambda^n_{\mathcal{O}}$. This result can be derived by promoting the parameter $\lambda_{\mathcal{O}}$ to a *spurion* [290,464] field, which transforms under scale transformations, such that it preserves the scale symmetry. After writing down all the scale invariant operators involving the spurion, it is again replaced by the constant parameter $\lambda_{\mathcal{O}}$ and the resulting terms give a potential in the form of eq. C.2.

The exact coefficients c_n of this potential are unknown and depend on the UV completion of the theory. Without these coefficients at hand, the potential is useless. However, the dependence of the potential on the coefficients c_n can be eliminated by imposing two conditions:

1. The potential has a minimum for $\chi = \langle\chi\rangle \equiv f \neq 0$, the vacuum expectation of χ:
$$\left.\frac{\mathrm{d}V(\chi)}{\mathrm{d}\chi}\right|_{\chi=f} = 0\,. \tag{C.3}$$
2. The potential is responsible for the mass term of $\overline{\chi}$ via
$$\left.\frac{\mathrm{d}^2V(\chi)}{\mathrm{d}\chi^2}\right|_{\chi=f} = m_\sigma^2\,. \tag{C.4}$$

The remaining ingredient is the aforementioned condition $|\Delta_{\mathcal{O}} - 4| \ll 1$, which will justify a first order expansion of the potential in α.

First derivative:

$$\begin{aligned}\frac{\mathrm{d}}{\mathrm{d}\chi}V(\chi)\Big|_{\chi=f} &= f^4\sum_{n=0}^{\infty}c_n(\Delta_{\mathcal{O}})(4+n\alpha)\left(\frac{\chi}{f}\right)^{3+n\alpha}\Big|_{\chi=f}\\ &= f^4\sum_{n=0}^{\infty}c_n(\Delta_{\mathcal{O}})(4+n\alpha)\\ &= 0\end{aligned} \tag{C.5}$$

Since $f \neq 0$, one obtains:

$$\sum_{n=0}^{\infty}c_n(\Delta_{\mathcal{O}}) = -\frac{1}{4}\sum_{n=0}^{\infty}c_n(\Delta_{\mathcal{O}})n\alpha\,. \tag{C.6}$$

Second derivative:

$$\begin{aligned}\frac{\mathrm{d}^2V}{\mathrm{d}\chi^2}\Big|_{\chi=f} &= f^4\sum_{n=0}^{\infty}c_n(\Delta_{\mathcal{O}})(4+n\alpha)(3+n\alpha)\left(\frac{\chi}{f}\right)^{2+n\alpha}\Big|_{\chi=f}\\ &= f^4\sum_{n=0}^{\infty}c_n(\Delta_{\mathcal{O}})(4+n\alpha)(3+n\alpha)\\ &= 12f^4\sum_{n=0}^{\infty}c_n(\Delta_{\mathcal{O}}) + 7f^4\sum_{n=0}^{\infty}c_n(\Delta_{\mathcal{O}})n\alpha + \mathcal{O}(\alpha^2)\end{aligned} \tag{C.7}$$

Here, the result of eq. (C.6) can be inserted:

$$\begin{aligned}\frac{\mathrm{d}^2V}{\mathrm{d}\chi^2}\Big|_{\chi=f} &= (-3+7)f^4\sum_{n=0}^{\infty}c_n(\Delta_{\mathcal{O}})n\alpha + \mathcal{O}(\alpha^2)\\ &= 4f^4\sum_{n=0}^{\infty}c_n(\Delta_{\mathcal{O}})n\alpha + \mathcal{O}(\alpha^2)\\ &= m^2\,.\end{aligned} \tag{C.8}$$

where the result from the first derivative was used. Therefore, one can write

$$\sum_{n=0}^{\infty}c_n(\Delta_{\mathcal{O}})n\alpha = \frac{m^2}{4f^2} + \mathcal{O}(\alpha^2)\,. \tag{C.9}$$

Expansion of V in α around $\alpha = 0$:

$$\begin{aligned} V(\chi) &= V(\chi)\Big|_{\alpha=0} + \frac{\mathrm{d}V(\chi)}{\mathrm{d}\alpha}\Big|_{\alpha=0} \alpha + \mathcal{O}(\alpha^2) \\ &= \chi^4 \sum_{n=0}^{\infty} c_n(\Delta_{\mathcal{O}}) \left[1 + \left(\frac{\chi}{f}\right)^{n\alpha} \log\left(\frac{\chi}{f}\right)\Big|_{\alpha=0} n\alpha\right] + \mathcal{O}(\alpha^2) \\ &= \chi^4 \sum_{n=0}^{\infty} c_n(\Delta_{\mathcal{O}}) \left[1 + \log\left(\frac{\chi}{f}\right) n\alpha\right] + \mathcal{O}(\alpha^2) \end{aligned} \tag{C.10}$$

Inserting the result of eq. (C.6) gives,

$$\begin{aligned} V(\chi) &= \chi^4 \sum_{n=0}^{\infty} c_n(\Delta_{\mathcal{O}}) \left[-\frac{1}{4} n\alpha + \log\left(\frac{\chi}{f}\right) n\alpha\right] + \mathcal{O}(\alpha^2) \\ &= \chi^4 \left[\log\left(\frac{\chi}{f}\right) - \frac{1}{4}\right] \sum_{n=0}^{\infty} c_n(\Delta_{\mathcal{O}}) n\alpha + \mathcal{O}(\alpha^2)\,, \end{aligned} \tag{C.11}$$

and with eq. (C.8), the result is:

$$\begin{aligned} V(\chi) &= \chi^4 \left[\log\left(\frac{\chi}{f}\right) - \frac{1}{4}\right] \frac{m^2}{4f^4} + \mathcal{O}(\alpha^2) \\ &= \frac{m^2}{16f^4}\, \chi^4 \left[4 \log\left(\frac{\chi}{f}\right) - 1\right] + \mathcal{O}(\alpha^2)\,. \end{aligned} \tag{C.12}$$

Hence, under the above assumption, the potential at leading order in α is completely determined by the parameters m and f.

Appendix D

Dilaton-dark-matter model: Perturbative unitarity constraints

Since the theory introduced in chapter 3 contains non-renormalisable operators, it must have a cutoff comparable to the scale f. This is expected to be manifest, even at tree level, in perturbative unitarity constraints on two-body scattering amplitudes. In particular, there are some couplings that could in principle be large compared to f since they are enhanced by additional massive factors involving the masses of the theory vector bosons (especially in the dark matter case). In this appendix, the calculation of the unitarity constraints involving massive vectors is described. For simplicity, only the case of no mixing between the dilaton and the Higgs is examined, and the Higgs boson is neglected entirely. For references on the calculation of unitarity constraints, and in particular including vector bosons, see refs. [465–469].

D.1 Scattering to dark matter

First, the scattering of vector bosons amongst themselves and into pairs of dilatons, as well as dilaton self-scattering shall be considered. The relevant terms in the Lagrangian read

$$\mathcal{L}_{\sigma V} = \frac{m_V^2}{f}\sigma V_\mu V^\mu + \frac{m_V^2}{2f^2}\sigma^2 V_\mu V^\mu - \xi\frac{m_\sigma^2}{f}\sigma^3 - \frac{\zeta}{24}\frac{m_\sigma^2}{f^2}\sigma^4\,, \tag{D.1}$$

where ξ and ζ are model-dependent and usually taken to be 5/6 and 11 respectively [298].

Since the model has a $\mathbb{Z}_2$ symmetry, states with odd numbers of vectors can only scatter to states with odd numbers of vectors, so that the only scattering amplitudes to

be considered are $\mathcal{M}_{\sigma\sigma\to\sigma\sigma}$, $\mathcal{M}_{\sigma\sigma\to VV}$, $\mathcal{M}_{VV\to\sigma\sigma}$ and $\mathcal{M}_{VV\to VV}$. These are given by

$$\begin{aligned}
i\mathcal{M}_{\sigma\sigma\to\sigma\sigma} =& -36i\xi^2\frac{m_\sigma^4}{f^2}\left[\frac{1}{s-m_\sigma^2}+\frac{1}{t-m_\sigma^2}+\frac{1}{u-m_\sigma^2}\right]-\zeta i\frac{m_\sigma^2}{f^2}\,,\\
i\mathcal{M}_{VV\to\sigma\sigma} =& \, i\frac{2m_V^2}{f^2}\epsilon_1\cdot\epsilon_2+6i\xi\epsilon_1\cdot\epsilon_2\frac{m_V^2m_\sigma^2}{f^2(s-m_\sigma^2)}\\
&+i\left(\frac{2m_V^2}{f}\right)^2\epsilon_1^\mu\epsilon_2^\nu\left[\frac{1}{t-m_V^2}\left(\eta^{\mu\nu}+\frac{k_1^\mu k_2^\nu}{m_V^2}\right)+\frac{1}{u-m_V^2}\left(\eta^{\mu\nu}+\frac{k_2^\mu k_1^\nu}{m_V^2}\right)\right],\\
i\mathcal{M}_{VV\to VV} =& -i\frac{4m_V^4}{f^2}\epsilon_1^\mu\epsilon_2^\nu\tilde{\epsilon}_1^\rho\tilde{\epsilon}_2^\kappa\left[\frac{\eta_{\mu\nu}\eta_{\rho\kappa}}{s-m_\sigma^2}+\frac{\eta_{\mu\rho}\eta_{\nu\kappa}}{t-m_\sigma^2}+\frac{\eta_{\mu\kappa}\eta_{\nu\rho}}{u-m_\sigma^2}\right],
\end{aligned}\tag{D.2}$$

where $\epsilon_{1,2}$ denote the incoming polarisation vectors and $\tilde{\epsilon}_{1,2}$ the outgoing ones. Note that in all of the amplitudes $s/t/u$ channel poles are not possible, and so it is possible to search over all scattering momenta up to some potential cutoff without needing to excise singular regions or submatrices as required in the general case [467, 469].

Since there are three initial polarisations possible for each vector, the scattering matrix (including the dilaton-dilaton state) is in principle of rank 10. However, it breaks into irreducible blocks under the Lorentz algebra, and in particular one can separate off the symmetric and antisymmetric states of $\epsilon_i^\mu\epsilon_j^\nu$ for $i\neq j$.

Typically, only the high-energy limit is considered, where only longitudinal gauge bosons are retained. It turns out, however, that even the transverse components can contribute in this limit. In fact, in the low-energy regime relevant for dark matter scattering, it is the contribution of the transverse components that dominates. So, a suitable basis of polarisation vectors can be chosen, such as $(0,1,0,0)$, $(0,0,1,0)$, $(p_V/m_V,0,0,E_V/m_V)$ for a vector aligned along the third spatial component and inserted into the above amplitudes. Then, the zeroth moment of the scattering matrix is extracted

$$T^0_{ij}=\frac{1}{64\pi}\sqrt{\frac{4|\mathbf{p}_{\rm in}|\;|\mathbf{p}_{\rm out}|}{s}}\int_{-1}^{1}d(\cos\theta)\mathcal{M}_{ij}\,,\tag{D.3}$$

where appropriate symmetry factors have been included for the incoming and outgoing states to be identical pairs, and $\mathbf{p}_{\rm in}$ and $\mathbf{p}_{\rm out}$ are the three-momenta in the centre-of-mass frame for the incoming and outgoing states respectively.

To find the limit from unitarity, and since the incoming and outgoing states may be related by a unitary rotation which is not of interest here, the square root of the eigenvalues of the T^0 matrix is taken and the maximum of these is compared to $1/2$,

$$|a_0^{\rm max}|\equiv\sqrt{\max\left[\text{eigenvalues}\left(T^0(T^0)^\dagger\right)\right]}\;<\frac{1}{2}\,.\tag{D.4}$$

It will be convenient to define

$$T^0_{ij}\equiv\frac{1}{16\pi f^2}\tilde{T}^0_{ij}\,.\tag{D.5}$$

The full expressions are too cumbersome to list here, but can be made available in `Mathematica` format or in a `C` program. In the following sections, different regions of parameter space of interest will be identified and approximate formulæ will be derived for those cases.

D.2 Scattering at high energy

In the limit of large s, the following expressions are found for the scattering of longitudinal gauge bosons and the dilaton,

$$\begin{aligned}
\tilde{T}^0_{(V_LV_L)(V_LV_L)} &\to -\frac{3}{2}m_\sigma^2\,,\\
\tilde{T}^0_{(V_LV_L)(\sigma\sigma)} &\to \frac{1}{4}\left[4m_V^2+(6\xi-4)m_\sigma^2-8m_V^2\log\frac{s}{m_V^2}\right],\\
\tilde{T}^0_{(\sigma\sigma)(\sigma\sigma)} &\to -\frac{11}{2}m_\sigma^2\,.
\end{aligned} \tag{D.1}$$

At this level, scattering involving the transverse modes is also relevant, and the scattering matrix can be rotated into

$$\tilde{T}^0 = \begin{pmatrix} 0 & 0 & 0 & 0\\ 0 & 0 & -\sqrt{2}m_V^2 & \sqrt{2}m_V^2\\ 0 & -\sqrt{2}m_V^2 & \tilde{T}^0_{(V_LV_L)(V_LV_L)} & \tilde{T}^0_{(V_LV_L)(\sigma\sigma)}\\ 0 & \sqrt{2}m_V^2 & \tilde{T}^0_{(\sigma\sigma)(V_LV_L)} & \tilde{T}^0_{(\sigma\sigma)(\sigma\sigma)} \end{pmatrix}. \tag{D.2}$$

In the limit that m_V^2 is small and the scattering energy is large, the amplitude is dominated by dilaton-dilaton scattering. One obtains

$$a_0^{\max} = \frac{m_\sigma^2}{64\pi f^2}\sqrt{261+28\sqrt{65}}\,. \tag{D.3}$$

This is essentially the constraint originating from dilaton self-scattering,

$$\frac{11m_\sigma^2}{16\pi f^2} \lesssim 1 \to m_\sigma \lesssim 2f\,, \tag{D.4}$$

that is considerably stronger than the one from pure longitudinal vector scattering.

f (TeV)	$p_{V,\max}$ (TeV)	Approx. max(m_V) (TeV)
1	5	1.9
1	20	1.4
2	10	3.8
2	20	3.1

Table D.1: Bounds on the vector dark matter mass m_V for given illustrative cutoff values f and typical maximum centre-of-mass vector momentum $p_{V,\max}$.

The above result *can* be used in the limit that $s \gg m_V^2$, so that the logarithmic term appearing in the second relation of eq. (D.1) is large. For reasonable values, it is found that the obtained constraint on m_σ is comparable or slightly stronger than the above. For the limit $m_V \gg m_\sigma$,

$$\frac{1}{8\pi f^2}m_V^2\log\frac{s}{m_V^2} < \frac{1}{2}\,, \tag{D.5}$$

which bounds m_V for a given cutoff. This can be directly compared with the values shown in figure 4.6 and which are reported in table D.1. These approximate values agree with the maximum values of m_V found numerically, although the high-energy limit is generally found not to be a very good approximation for the full scattering matrix.

Finally, while separate constraints from the symmetric/antisymmetric scattering of the transverse and longitudinal vector modes have been computed, in the large momentum limit these all reduce to

$$\sqrt{2}\frac{m_V^2}{16\pi f^2} < \frac{1}{2}\,. \tag{D.6}$$

D.3 Scattering at low energy

When $m_V \gg m_\sigma$, the amplitude is largest at low momenta and dominated by the scattering of *transverse* vectors of the type that obey $\epsilon \cdot k_{3,4} = 0$. It turns out that the other modes reduce the scattering amplitude and mix little with the other states. The largest eigenvalue is well approximated by the $(11) \leftrightarrow (11)$ scattering, and largest when $p_V = m_\sigma$,

$$\begin{aligned} a_0 =& \frac{m_V^4}{16\pi f^2 E_V}\left[\frac{1}{p_V}\log\left(1+\frac{4p_V^2}{m_\sigma^2}\right) - \frac{2p_V}{4m_V^2+4p_V^2-m_\sigma^2}\right] \\ \simeq& \frac{m_V^3}{16\pi m_\sigma f^2}\log 5\,. \end{aligned} \tag{D.1}$$

This places a constraint on the minimum dilaton mass,

$$m_\sigma \gtrsim \frac{m_V^3}{8\pi f^2}\log 5\,. \tag{D.2}$$

This can correspondingly be considered the point at which Sommerfeld enhancement of the amplitudes is significant, as clearly seen in figure 4.5.

D.4 Scattering to gluons

In this work, vector dark matter is of interest partly because it can be more copiously produced than fermions or scalars via the dilaton portal. It should not be a surprise then that a unitarity limit on the theory arises from the scattering of gluons into vector bosons via the dilaton. The corresponding scattering amplitude is given by

$$i\mathcal{M}_{gg\to VV} = \left(i\frac{\alpha_s b_3}{4\pi f}\epsilon_1^g\cdot\epsilon_2^g s\right)\frac{i}{s-m_\sigma^2}\left(i\frac{2m_V^2}{f}\tilde{\epsilon}_1\cdot\tilde{\epsilon}_2\right), \tag{D.1}$$

where $\epsilon_{1,2}^g$ are the gluon polarisation vectors and b_3 denotes the QCD beta function. For the longitudinal modes,

$$\tilde{\epsilon}_1\cdot\tilde{\epsilon}_2 = \frac{1}{m_V^2}(p^2+E^2) = \frac{s}{2m_V^2}\,, \tag{D.2}$$

so that in the $s \gg 4m_V^2$ limit, one has

$$i\mathcal{M}_{gg\to VV} \to -i\frac{\alpha_s b_3}{4\pi f^2}\frac{s^2}{s-m_S^2}\,. \tag{D.3}$$

Now $|T^0_{(gg),(V_LV_L)}| = \frac{|M|}{32\pi}$, but there are 2 incoming spins, and 8 incoming pairs of colours that give non-zero results. So the scattering matrix looks like

$$T^0 = \begin{pmatrix} 0 & T^0_{(gg),(V_LV_L)} & \cdots \\ T^0_{(gg),(V_LV_L)} & 0 & 0 \\ \vdots & 0 & 0 \end{pmatrix}, \tag{D.4}$$

so

$$T^0(T^0)^\dagger = \begin{pmatrix} 16|T^0_{(gg),(V_LV_L)}|^2 & 0 & \cdots \\ 0 & 0 & 0 \\ \vdots & 0 & 0 \end{pmatrix}. \tag{D.5}$$

Therefore, one finally obtains

$$a_0^{\max} = \sqrt{16}\times\frac{\alpha_s b_3}{128\pi^2 f^2}s\,. \tag{D.6}$$

However, this is only for scattering into *one* vector boson species. After accounting for the contributions of the Z and W bosons (which act as the equivalent of three individual vectors), one obtains an additional factor of two in the limit,

$$\sqrt{4}\times\sqrt{16}\times\frac{\alpha_s b_3}{128\pi^2 f^2}s < 1/2 \to s < \frac{8\pi^2 f^2}{7\alpha_s}\,. \tag{D.7}$$

Similar constraints on the maximal scattering energy via gluon fusion were found long ago in ref. [466].

Appendix E

Dilaton-dark-matter model: Constraints from heavy scalar searches

This appendix gives a more detailed picture of the heavy scalar constraints on the dilaton-dark-matter model presented in section 4.2.2. These were generated with HiggsBounds [315], which in each run (i.e. for each parameter point) provides an output file that contains a listing of the most sensitive channels. In the following, the excluded regions dominated by these different channels are displayed separately, together with the description of the channel as given in the output file. Only channels which cover a significant part of the excluded parameter space have been included.

E.1 Minimal mixing scenario

In the minimal mixing scenario, the most important constraints are provided by diboson searches [470–472]. As argued in section 4.2.2, the couplings of the heavy scalar to massive gauge bosons and fermions vanish for $v/f = \sin\alpha$, so that a 'magic window' appears in the minimal mixing scenario, in which the heavy scalar mass is unconstrained (see figures E.2 and E.3). This is explained by the vanishing of the couplings of the heavy scalar to the massive gauge bosons (as well as fermions). The gap gets closed for higher mixing angles α. For instance, HiggsBounds provides constraints on the *light*, SM-like scalar [473], which cover this gap for $\sin\alpha = 0.13$, as can be seen in figure E.4. Here, the coupling of the light scalar to gluons becomes too large, leading to an overabundant production of the light scalar.

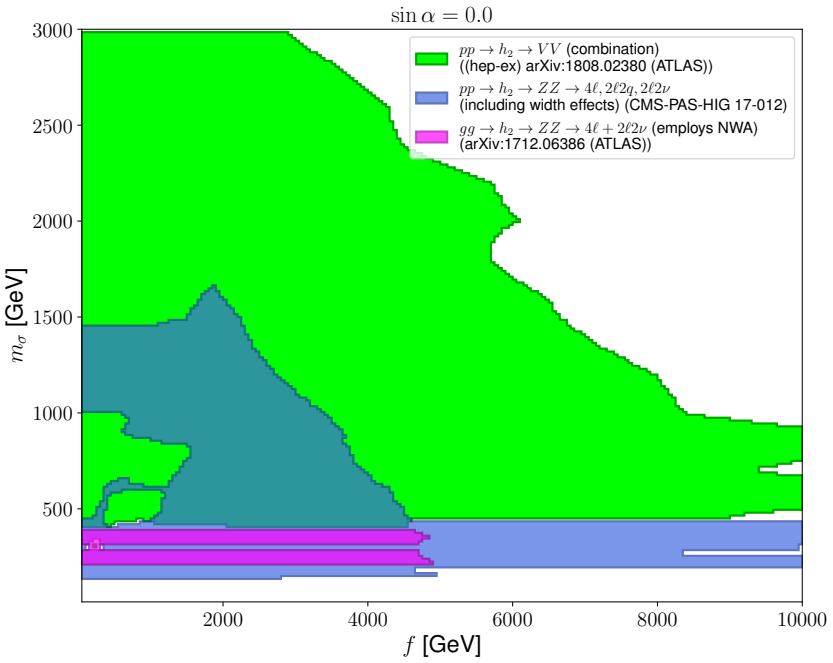

Figure E.1: Constraints obtained with HiggsBounds for the zero mixing case, dominated by di-boson searches [470–472].

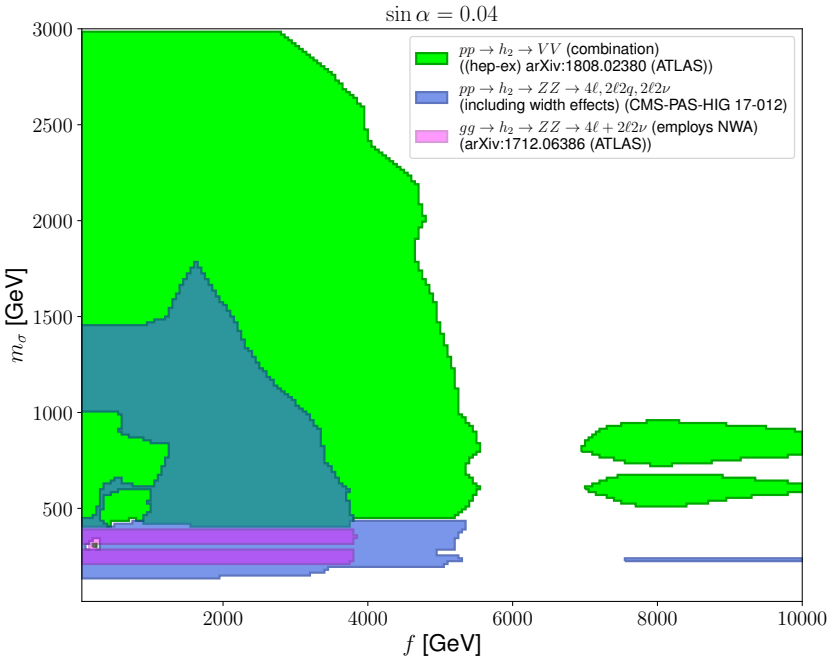

Figure E.2: Constraints obtained with HiggsBounds for the minimal mixing scenario with $\sin\alpha = 0.04$, dominated by di-boson searches [470–472]. A 'magic window' appears around $f = 6145\,\text{GeV}$.

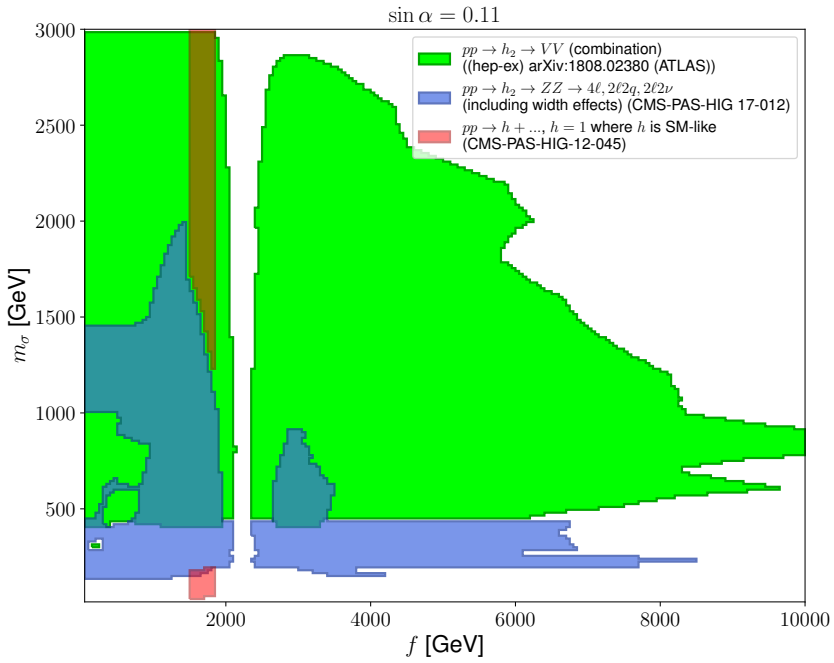

Figure E.3: Constraints obtained with HiggsBounds for the minimal mixing scenario with $\sin\alpha = 0.11$, still dominated by di-boson searches [470, 471]. A 'magic window' appears around $f = 2223\,\text{GeV}$. In addition, for this mixing angle also constraints from the light scalar [473] become relevant.

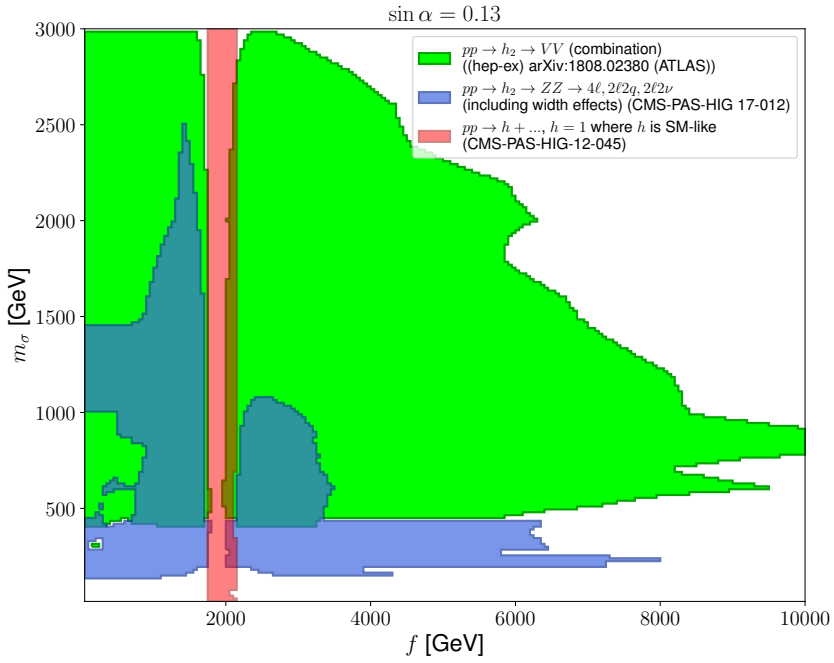

Figure E.4: Constraints obtained with HiggsBounds for the minimal mixing scenario with $\sin\alpha = 0.13$, still dominated by di-boson searches [470, 471]. The 'magic window', expected here at $f = 1876\,\text{GeV}$, is covered with constraints from the light scalar [473].

E.2 Gauge invariant mixing scenario

As explained in section 4.2.2, including additional terms in order to write the Lagrangian in a gauge invariant way leads to an enhanced coupling $\lambda_{\sigma hh}$ of the heavy scalar to the light ones, c.f. eqs. (4.2.15) and (4.2.16). The 'magic window' observed in the minimal mixing scenario is therefore covered with constraints from searches for pairs of SM-like scalars [474, 475], as can be seen in figure E.5 for $\sin\alpha = 0.11$. In addition, the constraints on the SM-like scalar [473] observed already in the minimal mixing scenario are still present both for $\sin\alpha = 0.11$ and $\sin\alpha = 0.15$.

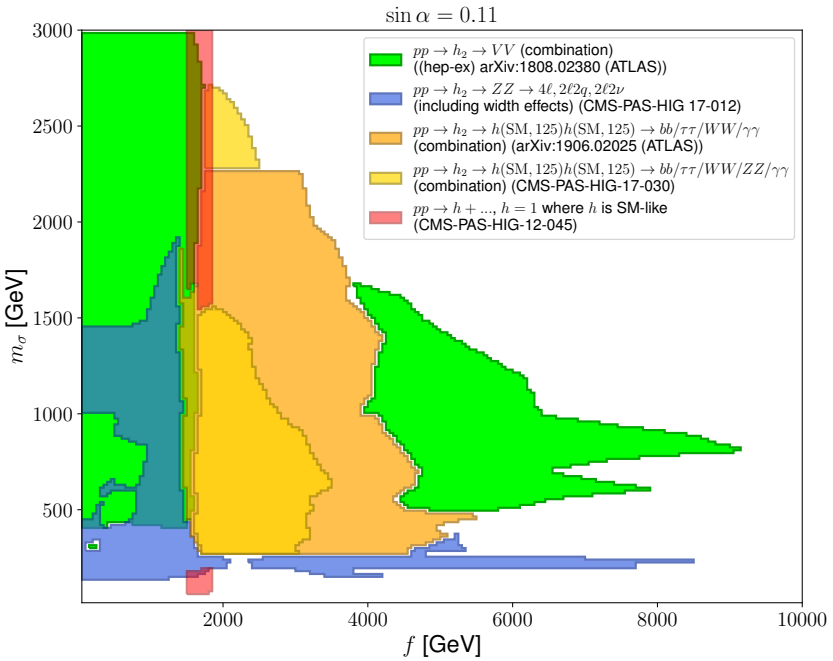

Figure E.5: Constraints obtained with HiggsBounds for the gauge invariant mixing scenario with $\sin\alpha = 0.11$, where in addition to the constraints from di-boson searches [470, 471], additional constraints from searches for pairs of SM-like scalars [474, 475] exclude a significant part of the parameter space. The latter prohibit the emergence of a 'magic window', which is observed for the same mixing angle in the minimal mixing scenario. Also, the constraints on the SM-like scalar [473] are still present.

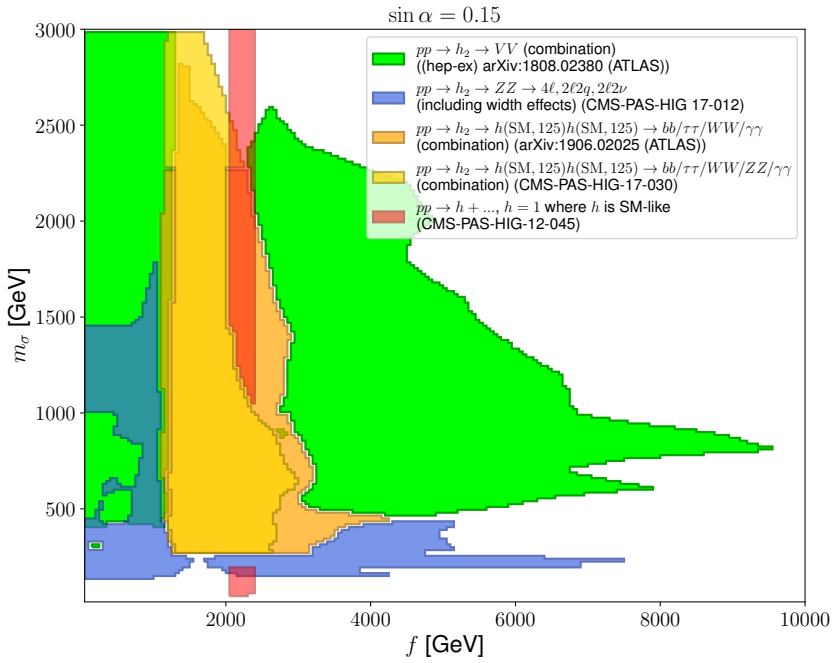

Figure E.6: Constraints obtained with HiggsBounds for the gauge invariant mixing scenario with $\sin\alpha = 0.11$. As in figure E.5, these involve constraints from diboson [470, 471] and di-Higgs [474, 475] searches as well as constraints on the SM-like scalar [473].

Appendix F

List of long-lived particle searches at ATLAS and CMS

This appendix gives a non-exhaustive list of searches for different signatures of long-lived particles, which have been conducted in the past at the LHC experiments ATLAS and CMS.

ATLAS 7 and 8 TeV searches

— *Search for Massive Long-lived Highly Ionising Particles with the ATLAS Detector at the LHC* [392]

— *Search for stable hadronising squarks and gluinos with the ATLAS experiment at the LHC* [391]

— *Search for heavy long-lived charged particles with the ATLAS detector in pp collisions at* $\sqrt{s} = 7$ *TeV* [390]

— *Search for displaced muonic lepton jets from light Higgs boson decay in proton-proton collisions at* $\sqrt{s} = 7$ *TeV with the ATLAS detector* [377]

— *Searches for heavy long-lived sleptons and R-Hadrons with the ATLAS detector in pp collisions at* $\sqrt{s} = 7$ *TeV* [393]

— *Search for long-lived, multi-charged particles in pp collisions at* $\sqrt{s}$=7 *TeV using the ATLAS detector* [394]

— *Search for nonpointing photons in the diphoton and* E_T^{miss} *final state in* $\sqrt{s}$=7 *TeV proton-proton collisions using the ATLAS detector* [379]

— *Search for charginos nearly mass degenerate with the lightest neutralino based on a disappearing-track signature in pp collisions at* $\sqrt{s}$=8 *TeV with the ATLAS detector* [476]

— *Search for long-lived stopped R-hadrons decaying out-of-time with pp collisions using the ATLAS detector* [411]

— *Search for long-lived neutral particles decaying into lepton jets in proton-proton collisions at* $\sqrt{s} = 8$ *TeV with the ATLAS detector* [378]

— *Search for nonpointing and delayed photons in the diphoton and missing transverse momentum final state in 8 TeV pp collisions at the LHC using the ATLAS detector* [380]

— *Searches for heavy long-lived charged particles with the ATLAS detector in proton-proton collisions at* $\sqrt{s} = 8$ *TeV* [388]

— *Search for long-lived, weakly interacting particles that decay to displaced hadronic jets in proton-proton collisions at* $\sqrt{s} = 8$ *TeV with the ATLAS detector* [374]

— *Search for massive, long-lived particles using multitrack displaced vertices or displaced lepton pairs in pp collisions at* $\sqrt{s} = 8$ *TeV with the ATLAS detector* [372]

CMS 7 and 8 TeV searches

— *Search for Stopped Gluinos in pp collisions at* $\sqrt{s} = 7$ *TeV* [410]

— *Search for Stopped HSCP in pp collisions at Sqrt(s)=7 TeV* [408]

— *Search for Heavy Stable Charged Particles in pp collisions at* $\sqrt{s} = 7$ *TeV* [395]

— *Search for heavy long-lived charged particles in pp collisions at* $\sqrt{s} = 7$ *TeV* [397]

— *Search for Fractionally Charged Particles in pp Collisions at* $\sqrt{s} = 7$ *TeV* [396]

— *Searches for Long-Lived Charged Particles in pp Collisions at* $\sqrt{s}$*=7 and 8 TeV* [389]

— *Search for Displaced Supersymmetry in events with an electron and a muon with large impact parameters* [375]

— *Search for Decays of Stopped Long-Lived Particles Produced in Proton–Proton Collisions at* $\sqrt{s} = 8$ *TeV* [412]

ATLAS 13 TeV searches

— *Search for long-lived neutral particles decaying into displaced lepton jets in proton–proton collisions at* $\sqrt{s} = 13$ *TeV with the ATLAS detector* [334]

— *Search for metastable heavy charged particles with large ionization energy loss in pp collisions at* $\sqrt{s} = 13$ *TeV using the ATLAS experiment* [335]

— *Search for heavy long-lived charged R-hadrons with the ATLAS detector in 3.2* fb^{-1} *of proton–proton collision data at* $\sqrt{s} = 13$ *TeV* [336]

— *Search for long-lived neutral particles decaying into Lepton-Jets with the ATLAS detector in proton-proton collision data at 13 TeV* [337]

— *Search for long-lived, massive particles in events with displaced vertices and missing transverse momentum in* $\sqrt{s} = 13$ *TeV pp collisions with the ATLAS detector* [338]

— *Search for long-lived charginos based on a disappearing-track signature in pp collisions at* $\sqrt{s} = 13$ *TeV with the ATLAS detector* [339]

— *Search for long-lived particles in final states with displaced dimuon vertices in pp collisions at* $\sqrt{s} = 13$ *TeV with the ATLAS detector* [340]

— *Search for heavy charged long-lived particles in proton-proton collisions at* $\sqrt{s} = 13$ *TeV using an ionisation measurement with the ATLAS detector* [341]

— *Search for the Production of a Long-Lived Neutral Particle Decaying within the ATLAS Hadronic Calorimeter in Association with a Z Boson from pp Collisions at* $\sqrt{s} = 13$ *TeV* [342]

— *Search for long-lived particles produced in pp collisions at* $\sqrt{s} = 13$ *TeV that decay into displaced hadronic jets in the ATLAS muon spectrometer* [343]

— *Search for heavy long-lived multicharged particles in proton-proton collisions at* $\sqrt{s}$ *= 13 TeV using the ATLAS detector* [344]

— *Search for heavy charged long-lived particles in the ATLAS detector in 36.1* fb^{-1} *of proton-proton collision data at* $\sqrt{s} = 13$ *TeV* [345]

— *Search for long-lived neutral particles in pp collisions at* $\sqrt{s}$ *= 13 TeV that decay into displaced hadronic jets in the ATLAS calorimeter* [346]

— *Search for heavy neutral leptons in decays of W bosons produced in 13 TeV pp collisions using prompt and displaced signatures with the ATLAS detector* [347]

— *Search for displaced vertices of oppositely charged leptons from decays of long-lived particles in pp collisions at* $\sqrt{s}$ *=13 TeV with the ATLAS detector* [348]

— *Search for light long-lived neutral particles produced in pp collisions at* $\sqrt{s} = 13$ *TeV and decaying into collimated leptons or light hadrons with the ATLAS detector* [349]

— *Search for long-lived neutral particles produced in pp collisions at* $\sqrt{s} = 13$ *TeV decaying into displaced hadronic jets in the ATLAS inner detector and muon spectrometer* [350]

— *Search for long-lived, massive particles in events with a displaced vertex and a muon with large impact parameter in pp collisions at* $\sqrt{s} = 13$ *TeV with the ATLAS detector* [351]

— *Search for displaced leptons in* $\sqrt{s} = 13$ *TeV pp collisions with the ATLAS detector* [352, 353]

— *A search for the decays of stopped long-lived particles at* $\sqrt{s} = 13$ *TeV with the ATLAS detector* [354]

CMS 13 TeV searches

— *Search for displaced leptons in the e-mu channel* [355]

— *Search for long-lived charged particles in proton-proton collisions at* $\sqrt{s} = 13$ *TeV* [356]

— *Search for new long-lived particles at* $\sqrt{s} = 13$ *TeV* [357]

— *Search for decays of stopped exotic long-lived particles produced in proton-proton collisions at* $\sqrt{s} = 13$ *TeV* [358]

— *Search for disappearing tracks as a signature of new long-lived particles in proton-proton collisions at* $\sqrt{s} = 13$ *TeV* [359]

— *Search for long-lived particles with displaced vertices in multijet events in proton-proton collisions at* $\sqrt{s}$ *=13 TeV* [360]

— *Search for new particles decaying to a jet and an emerging jet* [361]

— *Search for long-lived particles decaying into displaced jets in proton-proton collisions at* $\sqrt{s} = 13$ *TeV* [362]

— *Search for long-lived particles using nonprompt jets and missing transverse momentum with proton-proton collisions at* $\sqrt{s} = 13$ *TeV* [363]

— *Search for long-lived particles using delayed photons in proton-proton collisions at* $\sqrt{s} = 13$ *TeV* [364]

— *Search for disappearing tracks in proton-proton collisions at* $\sqrt{s} = 13$ *TeV* [365]

— *Search for long-lived particles using displaced jets in proton-proton collisions at* $\sqrt{s} = 13$ *TeV* [366]

Bibliography

[1] W. Buchmuller & C. Ludeling; "Field Theory and Standard Model"; in "2005 European School of High-Energy Physics," (2006); arXiv:hep-ph/0609174. 1, 5, 8, 24

[2] O. Brandt; "Supersymmetry Searches at the LHC"; (2008); arXiv:0808.2934 [hep-ex]. 1

[3] N. Craig, P. Draper, K. Kong, Y. Ng & D. Whiteson; "The unexplored landscape of two-body resonances"; Acta Phys. Polon. B **50**, p. 837 (2019). arXiv:1610.09392 [hep-ph]. 2

[4] J. Haller, A. Hoecker, R. Kogler, K. Mönig, T. Peiffer & J. Stelzer; "Update of the global electroweak fit and constraints on two-Higgs-doublet models"; Eur. Phys. J. C **78**, p. 675 (2018). arXiv:1803.01853 [hep-ph]. 5, 24, 68, 69

[5] J. Kretzschmar; *Standard Model physics at the LHC* (2019); arXiv:1803.10800 [hep-ex]. 5, 24

[6] (ATLAS Collaboration); "Summary plots from the ATLAS Standard Model physics group"; https://atlas.web.cern.ch/Atlas/GROUPS/PHYSICS/CombinedSummaryPlots/SM/index.html (visited on 22 August 2021) (2021). 5, 24

[7] (CMS Collaboration); "Summaries of CMS cross section measurements"; https://twiki.cern.ch/twiki/bin/view/CMSPublic/PhysicsResultsCombined (visited on 22 August 2021) (2021). 5, 24

[8] M. Bustamante, L. Cieri & J. Ellis; "Beyond the Standard Model for Montaneros"; in "5th CERN - Latin American School of High-Energy Physics," (2009); arXiv:0911.4409 [hep-ph]. 5, 25

[9] G. ALTARELLI; "The Standard model of particle physics"; (2005)arXiv:hep-ph/0510281. 5, 22

[10] G. Altarelli; "Collider Physics within the Standard Model: a Primer"; (2013)arXiv:1303.2842 [hep-ph]. 5, 16

[11] P. Ramond; "The Five Instructions"; in "Theoretical Advanced Study Institute in Elementary Particle Physics: The Dark Secrets of the Terascale," (2012); arXiv:1201.0396 [hep-ph]. 5

[12] S. F. Novaes; "Standard model: An Introduction"; in "10th Jorge Andre Swieca Summer School: Particle and Fields," (1999); arXiv:hep-ph/0001283. 5

[13] Y. Grossman; "Introduction to flavor physics"; in "2009 European School of High-Energy Physics," (2010); arXiv:1006.3534 [hep-ph]. 5, 6

[14] P. Langacker; "Introduction to the Standard Model and Electroweak Physics"; in "Theoretical Advanced Study Institute in Elementary Particle Physics: The Dawn of the LHC Era," (2009); arXiv:0901.0241 [hep-ph]. 5, 14, 22

[15] M. Herrero; "The Standard model"; NATO Sci. Ser. C **534**, pp. 1–59 (1999). arXiv:hep-ph/9812242. 5

[16] A. Maas; "Brout-Englert-Higgs physics: From foundations to phenomenology"; Prog. Part. Nucl. Phys. **106**, pp. 132–209 (2019). arXiv:1712.04721 [hep-ph]. 5

[17] C. Quigg; "The Electroweak Theory"; in "Theoretical Advanced Study Institute in Elementary Particle Physics (TASI 2000): Flavor Physics for the Millennium," (2002); arXiv:hep-ph/0204104. 5

[18] M. E. Peskin; "Lectures on the Theory of the Weak Interaction"; in "2016 European School of High-Energy Physics," (2017); arXiv:1708.09043 [hep-ph]. 5

[19] K. Freese; "Status of Dark Matter in the Universe"; Int. J. Mod. Phys. **1**, pp. 325–355 (2017). arXiv:1701.01840 [astro-ph.CO]. 5

[20] G. Bertone & D. Hooper; "History of dark matter"; Rev. Mod. Phys. **90**, p. 045002 (2018). arXiv:1605.04909 [astro-ph.CO]. 5

[21] N. A. Nilsson & M.-I. Park; "Tests of Standard Cosmology in Horava Gravity"; (2021)arXiv:2108.07986 [hep-th]. 5

[22] D. Scott; "The standard model of cosmology: A skeptic's guide"; Proc. Int. Sch. Phys. Fermi **200**, pp. 133–153 (2020). arXiv:1804.01318 [astro-ph.CO]. 5

[23] H. Baer, K.-Y. Choi, J. E. Kim & L. Roszkowski; "Dark matter production in the early Universe: beyond the thermal WIMP paradigm"; Phys. Rept. **555**, pp. 1–60 (2015). arXiv:1407.0017 [hep-ph]. 5

[24] S. K. Vempati; "Physics beyond the Standard Model (Mostly Supersymmetry)"; CERN Yellow Rep. School Proc. **2**, pp. 87–128 (2018). 5

[25] R. Bousso; "The Cosmological Constant Problem, Dark Energy, and the Landscape of String Theory"; Pontif. Acad. Sci. Scr. Varia **119**, pp. 129–151 (2011)arXiv:1203.0307 [astro-ph.CO]. 5, 26

[26] (Muon g-2 Collaboration); B. Abi *et al.*; "Measurement of the Positive Muon Anomalous Magnetic Moment to 0.46 ppm"; Phys. Rev. Lett. **126**, p. 141801 (2021). arXiv:2104.03281 [hep-ex]. 5, 27

[27] A. Pomarol; "Beyond the Standard Model"; in "2010 European School of High Energy Physics," (2012); arXiv:1202.1391 [hep-ph]. 5

[28] B. Gripaios; "Lectures on Physics Beyond the Standard Model"; (2015)arXiv:1503.02636 [hep-ph]. 5

[29] K. S. Babu; "TASI Lectures on Flavor Physics"; in "Theoretical Advanced Study Institute in Elementary Particle Physics: The Dawn of the LHC Era," (2009); arXiv:0910.2948 [hep-ph]. 5, 28

[30] M. McCullough; "Lectures on Physics Beyond the Standard Model." in "6th Tri-Institute Summer School on Elementary Particles," (2018). 5

[31] V. Peralta; *Phenomenology of Vector-like Fermions in Physics Beyond the Standard Model*; Ph.D. thesis; Sao Paulo U. (2017); arXiv:1712.06193 [hep-ph]. 5

[32] S. P. Martin; "TASI 2011 lectures notes: two-component fermion notation and supersymmetry"; in "Theoretical Advanced Study Institute in Elementary Particle Physics: The Dark Secrets of the Terascale," (2012); arXiv:1205.4076 [hep-ph]. 5, 153

[33] Y. Grossman & P. Tanedo; "Just a Taste: Lectures on Flavor Physics"; in "Theoretical Advanced Study Institute in Elementary Particle Physics: Anticipating the Next Discoveries in Particle Physics," (2017); arXiv:1711.03624 [hep-ph]. 6, 14

[34] E. Witten; "Symmetry and Emergence"; Nature Phys. **14**, pp. 116–119 (2018). arXiv:1710.01791 [hep-th]. 6

[35] J. Goldstone; "Field Theories with Superconductor Solutions"; Nuovo Cim. **19**, pp. 154–164 (1961). 6

[36] J. Goldstone, A. Salam & S. Weinberg; "Broken Symmetries"; Phys. Rev. **127**, pp. 965–970 (1962). 6

[37] F. Englert & R. Brout; "Broken Symmetry and the Mass of Gauge Vector Mesons"; Phys. Rev. Lett. **13**, pp. 321–323 (1964). 6, 16

[38] P. W. Higgs; "Broken Symmetries and the Masses of Gauge Bosons"; Phys. Rev. Lett. **13**, pp. 508–509 (1964). 6, 16

[39] P. W. Higgs; "Broken symmetries, massless particles and gauge fields"; Phys. Lett. **12**, pp. 132–133 (1964). 6, 16

[40] P. W. Higgs; "Spontaneous Symmetry Breakdown without Massless Bosons"; Phys. Rev. **145**, pp. 1156–1163 (1966). 6, 16

[41] G. S. Guralnik, C. R. Hagen & T. W. B. Kibble; "Global Conservation Laws and Massless Particles"; Phys. Rev. Lett. **13**, pp. 585–587 (1964). 6, 16

[42] T. W. B. Kibble; "Symmetry breaking in nonAbelian gauge theories"; Phys. Rev. **155**, pp. 1554–1561 (1967). 6, 16

[43] F. Englert, R. Brout & M. F. Thiry; "Vector mesons in presence of broken symmetry"; Nuovo Cim. A **43**, pp. 244–257 (1966). 6, 16

[44] J. C. Romao & J. P. Silva; "A resource for signs and Feynman diagrams of the Standard Model"; Int. J. Mod. Phys. A **27**, p. 1230025 (2012). arXiv:1209.6213 [hep-ph]. 7

[45] J. Iliopoulos; "Introduction to the Standard Model of the Electro-Weak Interactions"; in "8th CERN–Latin-American School of High-Energy Physics," (2013); arXiv:1305.6779 [hep-ph]. 8, 9, 24

[46] M. E. Peskin & D. V. Schroeder; *An Introduction to quantum field theory* (Addison-Wesley, Reading, USA) (1995); ISBN 978-0-201-50397-5. 17, 20, 21, 55, 59, 154

[47] M. Kobayashi & T. Maskawa; "CP Violation in the Renormalizable Theory of Weak Interaction"; Prog. Theor. Phys. **49**, pp. 652–657 (1973). 22, 26

[48] J. L. Hewett; "The Standard model and why we believe it"; in "Theoretical Advanced Study Institute in Elementary Particle Physics (TASI 97): Supersymmetry, Supergravity and Supercolliders," (1997); arXiv:hep-ph/9810316. 23, 24

[49] G. P. Salam; "Elements of QCD for hadron colliders"; in "2009 European School of High-Energy Physics," (2010); arXiv:1011.5131 [hep-ph]. 24

[50] P. Skands; "Introduction to QCD"; in "Theoretical Advanced Study Institute in Elementary Particle Physics: Searching for New Physics at Small and Large Scales," (2012); arXiv:1207.2389 [hep-ph]. 24

[51] S. Weinberg; "The Making of the standard model"; Eur. Phys. J. C **34**, pp. 5–13 (2004). arXiv:hep-ph/0401010. 24

[52] A. B. Arbuzov; "Quantum Field Theory and the Electroweak Standard Model"; (2017). arXiv:1801.05670 [hep-ph]. 24

[53] G. 't Hooft; "Renormalization of Massless Yang-Mills Fields"; Nucl. Phys. B **33**, pp. 173–199 (1971). 24

[54] G. 't Hooft; "Renormalizable Lagrangians for Massive Yang-Mills Fields"; Nucl. Phys. B **35**, pp. 167–188 (1971). 24

[55] F. Zwicky; "Die Rotverschiebung von extragalaktischen Nebeln"; Helv. Phys. Acta **6**, pp. 110–127 (1933). 25

[56] F. Zwicky; "On the Masses of Nebulae and of Clusters of Nebulae"; Astrophys. J. **86**, pp. 217–246 (1937). 25

[57] K. Lundmark; "The Motions and the Distances of Spiral Nebulœ.: (Plates 18, 19.)"; Monthly Notices of the Royal Astronomical Society **85**, pp. 865–894 (1925). ISSN 0035-8711. https://doi.org/10.1093/mnras/85.8.865; https://academic.oup.com/mnras/article-pdf/85/8/865/3685291/mnras85-0865.pdf. 25

[58] K. Lundmark; "Über die Bestimmung der Entfernungen, Dimensionen, Massen und Dichtigkeit fur die nächstgelegenen anagalacktischen Sternsysteme." Meddelanden fran Lunds Astronomiska Observatorium Serie I **125**, pp. 1–13 (1930). 25

[59] E. Holmberg; "A Study of Double and Multiple Galaxies Together with Inquiries into some General Metagalactic Problems"; Annals of the Observatory of Lund **6**, pp. 1–173 (1937). 25

[60] H. W. Babcock; "The rotation of the Andromeda Nebula"; Lick Observatory Bulletin **498**, pp. 41–51 (1939). 25

[61] M. Schwarzschild; "Mass distribution and mass-luminosity ratio in galaxies"; Astronomical Journal**59**, p. 273 (1954). 25

[62] H. C. van de Hulst, E. Raimond & H. van Woerden; "Rotation and density distribution of the Andromeda nebula derived from observations of the 21-cm line"; Bull. Astron. Inst. Netherlands**14**, p. 1 (1957). 25

[63] M. S. Roberts; "A High-Resolution 21-CM Hydrogen-Line Survey of the Andromeda Nebula"; Astrophysical Journal**144**, p. 639 (1966). 25

[64] V. C. Rubin & W. K. Ford, Jr.; "Rotation of the Andromeda Nebula from a Spectroscopic Survey of Emission Regions"; Astrophys. J. **159**, pp. 379–403 (1970). 25

[65] K. C. Freeman; "On the Disks of Spiral and S0 Galaxies"; Astrophysical Journal**160**, p. 811 (1970). 25

[66] F. Wilczek; "Problem of Strong P and T Invariance in the Presence of Instantons"; Phys. Rev. Lett. **40**, pp. 279–282 (1978). https://link.aps.org/doi/10.1103/PhysRevLett.40.279. 25

[67] M. S. Roberts & A. H. Rots; "Comparison of Rotation Curves of Different Galaxy Types"; Astronomy and Astrophysics**26**, pp. 483–485 (1973). 25

[68] S. Refsdal; "On the possibility of determining Hubble's parameter and the masses of galaxies from the gravitational lens effect"; Monthly Notices of the RAS**128**, p. 307 (1964). 25

[69] S. Refsdal; "The gravitational lens effect"; Monthly Notices of the RAS**128**, p. 295 (1964). 25

[70] Y. G. Klimov; "The Use in Extragalactic Astronomy of the Deviation of Light Rays in Galactic Gravitational Fields"; Soviet Physics Doklady **8**, p. 431 (1963). 25

[71] Y. G. Klimov; "The Deflection of Light Rays in the Gravitational Fields of Galaxies"; Soviet Physics Doklady **8**, p. 119 (1963). 25

[72] Y. G. Klimov; "Occulted Galaxies and an Experimental Verification of the General Theory of Relativity"; Astronomicheskii Zhurnal**40**, p. 874 (1963). 25

[73] S. Liebes; "Gravitational Lenses"; Physical Review **133**, pp. 835–844 (1964). 25

[74] D. Walsh, R. F. Carswell & R. J. Weymann; "0957+561 A, B: twin quasistellar objects or gravitational lens?" Nature**279**, pp. 381–384 (1979). 25

[75] K. Chang & S. Refsdal; "Flux variations of QSO 0957 + 561 A, B and image splitting by stars near the light path"; Nature**282**, pp. 561–564 (1979). 25

[76] B. Paczynski; "Gravitational Microlensing by the Galactic Halo"; Astrophysical Journal**304**, p. 1 (1986). 25

[77] R. J. Nemiroff; *Prediction and Analysis of Basic Gravitational Microlensing Phenomena*; Ph.D. thesis; Pennsylvania Univ., Philadelphia. (1987). 25

[78] M. J. Irwin, R. L. Webster, P. C. Hewett, R. T. Corrigan & R. I. Jedrzejewski; "Photometric Variations in the Q2237+0305 System: First Detection of a Microlensing Event"; Astronomical Journal**98**, p. 1989 (1989). 25

[79] (Supernova Cosmology Project Collaboration); C. Alcock *et al.*; "Possible Gravitational Microlensing of a Star in the Large Magellanic Cloud"; Nature **365**, pp. 621–623 (1993). arXiv:astro-ph/9309052. 25

[80] E. Aubourg, P. Bareyre, S. Bréhin, M. Gros, M. Lachièze-Rey, B. Laurent, E. Lesquoy, C. Magneville, A. Milsztajn, L. Moscoso, F. Queinnec, J. Rich, M. Spiro, L. Vigroux, S. Zylberajch, R. Ansari, F. Cavalier, M. Moniez, J. P. Beaulieu, R. Ferlet, P. Grison, A. Vidal-Madjar, J. Guibert, O. Moreau, F. Tajahmady, E. Maurice, L. Prévôt & C. Gry; "Evidence for gravitational microlensing by dark objects in the Galactic halo"; Nature**365**, pp. 623–625 (1993). 25

[81] (MACHO Collaboration); C. Alcock *et al.*; "The MACHO project: Microlensing results from 5.7 years of LMC observations"; Astrophys. J. **542**, pp. 281–307 (2000). arXiv:astro-ph/0001272. 25

[82] (EROS Collaboration); T. Lasserre; "Not enough stellar mass machos in the galactic halo"; Astron. Astrophys. **355**, pp. L39–L42 (2000)arXiv:astro-ph/0002253. 25

[83] (EROS-2 Collaboration); P. Tisserand *et al.*; "Limits on the Macho Content of the Galactic Halo from the EROS-2 Survey of the Magellanic Clouds"; Astron. Astrophys. **469**, pp. 387–404 (2007). arXiv:astro-ph/0607207. 25

[84] U. G. Briel & J. P. Henry; "An x-ray temperature map of coma"; (1997)arXiv:astro-ph/9711237. 25

[85] (WMAP Collaboration); J. Dunkley *et al.*; "Five-Year Wilkinson Microwave Anisotropy Probe (WMAP) Observations: Likelihoods and Parameters from the WMAP data"; Astrophys. J. Suppl. **180**, pp. 306–329 (2009). arXiv:0803.0586 [astro-ph]. 25

[86] (WMAP Collaboration); E. Komatsu *et al.*; "Five-Year Wilkinson Microwave Anisotropy Probe (WMAP) Observations: Cosmological Interpretation"; Astrophys. J. Suppl. **180**, pp. 330–376 (2009). arXiv:0803.0547 [astro-ph]. 25

[87] P. J. E. Peebles; "Primordial Helium Abundance and the Primordial Fireball. II"; Astrophysical Journal**146**, p. 542 (1966). 25

[88] R. V. Wagoner, W. A. Fowler & F. Hoyle; "On the Synthesis of Elements at Very High Temperatures"; Astrophysical Journal**148**, p. 3 (1967). 25

[89] M. Fukugita, C. J. Hogan & P. J. E. Peebles; "The Cosmic baryon budget"; Astrophys. J. **503**, p. 518 (1998). arXiv:astro-ph/9712020. 25

[90] G. Hinshaw, D. Larson, E. Komatsu, D. N. Spergel, C. L. Bennett, J. Dunkley, M. R. Nolta, M. Halpern, R. S. Hill, N. Odegard & et al.; "NINE-YEAR WILKINSON MICROWAVE ANISOTROPY PROBE (WMAP) OBSERVATIONS: COSMOLOGICAL PARAMETER RESULTS"; The Astrophysical Journal Supplement Series **208**, p. 19 (2013). ISSN 1538-4365. http://dx.doi.org/10.1088/0067-0049/208/2/19. 25

[91] (Planck Collaboration); P. A. R. Ade *et al.*; "Planck 2015 results. XIII. Cosmological parameters"; Astron. Astrophys. **594**, p. A13 (2016). arXiv:1502.01589 [astro-ph.CO]. 25

[92] A. Friedman; "On the Curvature of space"; Z. Phys. **10**, pp. 377–386 (1922). 25

[93] G. Lemaitre; "A Homogeneous Universe of Constant Mass and Growing Radius Accounting for the Radial Velocity of Extragalactic Nebulae"; Annales Soc. Sci. Bruxelles A **47**, pp. 49–59 (1927). 25

[94] (Supernova Search Team Collaboration); A. G. Riess *et al.*; "Observational evidence from supernovae for an accelerating universe and a cosmological constant"; Astron. J. **116**, pp. 1009–1038 (1998). arXiv:astro-ph/9805201. 25

[95] C. Gross, A. Polosa, A. Strumia, A. Urbano & W. Xue; "Dark Matter in the Standard Model?" Phys. Rev. D **98**, p. 063005 (2018). arXiv:1803.10242 [hep-ph]. 26

[96] M. Milgrom; "A Modification of the Newtonian dynamics as a possible alternative to the hidden mass hypothesis"; Astrophys. J. **270**, pp. 365–370 (1983). 26

[97] M. Milgrom; "A Modification of the Newtonian dynamics: Implications for galaxies"; Astrophys. J. **270**, pp. 371–383 (1983). 26

[98] M. Milgrom; "A modification of the Newtonian dynamics: implications for galaxy systems"; Astrophys. J. **270**, pp. 384–389 (1983). 26

[99] J. Bekenstein & M. Milgrom; "Does the missing mass problem signal the breakdown of Newtonian gravity?" Astrophys. J. **286**, pp. 7–14 (1984). 26

[100] M. Milgrom; "Solutions for the modified Newtonian dynamics field equation"; Astrophys. J. **302**, pp. 617–625 (1986). 26

[101] J. D. Bekenstein; "Phase Coupling Gravitation: Symmetries and Gauge Fields"; Phys. Lett. B **202**, pp. 497–500 (1988). 26

[102] J. D. Bekenstein; "Relativistic gravitation theory for the MOND paradigm"; Phys. Rev. D **70**, p. 083509 (2004). [Erratum: Phys.Rev.D 71, 069901 (2005)]; arXiv:astro-ph/0403694. 26

[103] R. H. Sanders; "From dark matter to MOND"; in "20th Rencontres de Blois on Challenges in Particle Astrophysics," (2008); arXiv:0806.2585 [astro-ph]. 26

[104] A. Einstein; "Kosmologische Betrachtungen zur allgemeinen Relativitätstheorie"; Sitzungsberichte der Königlich Preußischen Akademie der Wissenschaften (Berlin pp. 142–152 (1917). 26

[105] E. Komatsu, K. M. Smith, J. Dunkley, C. L. Bennett, B. Gold, G. Hinshaw, N. Jarosik, D. Larson, M. R. Nolta, L. Page & et al.; "SEVEN-YEAR WILKINSON MICROWAVE ANISOTROPY PROBE (WMAP) OBSERVATIONS: COSMOLOGICAL INTERPRETATION"; The Astrophysical Journal Supplement Series **192**, p. 18 (2011). ISSN 1538-4365. http://dx.doi.org/10.1088/0067-0049/192/2/18. 26

[106] L. Canetti, M. Drewes & M. Shaposhnikov; "Matter and Antimatter in the Universe"; New J. Phys. **14**, p. 095012 (2012). arXiv:1204.4186 [hep-ph]. 26

[107] M. Shaposhnikov; "Baryon asymmetry of the universe and neutrinos"; Prog. Theor. Phys. **122**, pp. 185–203 (2009). 26

[108] G. Steigman; "Observational tests of antimatter cosmologies"; Ann. Rev. Astron. Astrophys. **14**, pp. 339–372 (1976). 26

[109] A. D. Sakharov; "Violation of CP Invariance, C asymmetry, and baryon asymmetry of the universe"; Pisma Zh. Eksp. Teor. Fiz. **5**, pp. 32–35 (1967). 26

[110] G. Elor, J. Harz, S. Ipek & B. Shakya; "Snowmass 2021 Letter of Interest: The Baryon Asymmetry Of The Universe"; (2020). https://www.snowmass21.org/docs/files/summaries/TF/SNOWMASS21-TF8_TF9-EF9_EF0-NF3_NF0-RF4_RF0-CF7_CF0-024.pdf. 26

[111] C. Balazs; "Baryogenesis: A small review of the big picture"; (2014)arXiv:1411.3398 [hep-ph]. 26

[112] M. B. Gavela, P. Hernandez, J. Orloff & O. Pene; "Standard model baryogenesis"; in "29th Rencontres de Moriond: Electroweak Interactions and Unified Theories," (1994); arXiv:hep-ph/9407403. 26

[113] G. 'T HOOFT; "Symmetry Breaking Through Bell-Jackiw Anomalies"; Phys. Rev. Lett. **37**, pp. 8–11 (1976). 26

[114] G. 'T HOOFT; "Computation of the Quantum Effects Due to a Four-Dimensional Pseudoparticle"; Phys. Rev. D **14**, pp. 3432–3450 (1976). [Erratum: Phys.Rev.D 18, 2199 (1978)]. 26

[115] N. S. MANTON; "Topology in the Weinberg-Salam Theory"; Phys. Rev. D **28**, p. 2019 (1983). 26

[116] F. R. KLINKHAMER & N. S. MANTON; "A Saddle Point Solution in the Weinberg-Salam Theory"; Phys. Rev. D **30**, p. 2212 (1984). 26

[117] A. D. LINDE; "On the Vacuum Instability and the Higgs Meson Mass"; Phys. Lett. B **70**, pp. 306–308 (1977). 26

[118] V. A. KUZMIN, V. A. RUBAKOV & M. E. SHAPOSHNIKOV; "On the Anomalous Electroweak Baryon Number Nonconservation in the Early Universe"; Phys. Lett. B **155**, p. 36 (1985). 26

[119] R. ZUKANOVICH FUNCHAL, B. SCHMAUCH & G. GIESEN; "The Physics of Neutrinos"; (2013)arXiv:1308.1029 [hep-ph]. 27

[120] (Kamiokande-II Collaboration); K. S. HIRATA *et al.*; "Experimental Study of the Atmospheric Neutrino Flux"; Phys. Lett. B **205**, p. 416 (1988). 27

[121] (Kamiokande Collaboration); Y. FUKUDA *et al.*; "Atmospheric muon-neutrino / electron-neutrino ratio in the multiGeV energy range"; Phys. Lett. B **335**, pp. 237–245 (1994). 27

[122] (Kamiokande-II Collaboration); K. S. HIRATA *et al.*; "Observation of a small atmospheric muon-neutrino / electron-neutrino ratio in Kamiokande"; Phys. Lett. B **280**, pp. 146–152 (1992). 27

[123] R. BECKER-SZENDY *et al.*; "The Electron-neutrino and muon-neutrino content of the atmospheric flux"; Phys. Rev. D **46**, pp. 3720–3724 (1992). 27

[124] W. W. M. ALLISON *et al.*; "Measurement of the atmospheric neutrino flavor composition in Soudan-2"; Phys. Lett. B **391**, pp. 491–500 (1997). arXiv:hep-ex/9611007. 27

[125] (Super-Kamiokande Collaboration); Y. FUKUDA *et al.*; "Evidence for oscillation of atmospheric neutrinos"; Phys. Rev. Lett. **81**, pp. 1562–1567 (1998). arXiv:hep-ex/9807003. 27

[126] (Super-Kamiokande Collaboration); Y. FUKUDA *et al.*; "Study of the atmospheric neutrino flux in the multi-GeV energy range"; Phys. Lett. B **436**, pp. 33–41 (1998). arXiv:hep-ex/9805006. 27

[127] (Super-Kamiokande Collaboration); Y. ASHIE *et al.*; "Evidence for an oscillatory signature in atmospheric neutrino oscillation"; Phys. Rev. Lett. **93**, p. 101801 (2004). arXiv:hep-ex/0404034. 27

[128] (Super-Kamiokande Collaboration); K. ABE *et al.*; "A Measurement of atmospheric neutrino flux consistent with tau neutrino appearance"; Phys. Rev. Lett. **97**, p. 171801 (2006). arXiv:hep-ex/0607059. 27

[129] (Super-Kamiokande Collaboration); K. Abe *et al.*; "Search for Matter-Dependent Atmospheric Neutrino Oscillations in Super-Kamiokande"; Phys. Rev. D **77**, p. 052001 (2008). arXiv:0801.0776 [hep-ex]. 27

[130] S. M. Bilenky & B. Pontecorvo; "Lepton Mixing and Neutrino Oscillations"; Phys. Rept. **41**, pp. 225–261 (1978). 27

[131] B. Pontecorvo; "Neutrino Experiments and the Problem of Conservation of Leptonic Charge"; Zh. Eksp. Teor. Fiz. **53**, pp. 1717–1725 (1967). 27

[132] (KATRIN Collaboration); M. Aker *et al.*; "Improved Upper Limit on the Neutrino Mass from a Direct Kinematic Method by KATRIN"; Phys. Rev. Lett. **123**, p. 221802 (2019). arXiv:1909.06048 [hep-ex]. 27

[133] (Muon g-2 Collaboration); G. W. Bennett *et al.*; "Final Report of the Muon E821 Anomalous Magnetic Moment Measurement at BNL"; Phys. Rev. D **73**, p. 072003 (2006). arXiv:hep-ex/0602035. 27

[134] (ATLAS, CMS, LHCb Collaboration); E. Graverini; "Flavour anomalies: a review"; J. Phys. Conf. Ser. **1137**, p. 012025 (2019). arXiv:1807.11373 [hep-ex]. 27

[135] (LHCb Collaboration); R. Aaij *et al.*; "Differential branching fractions and isospin asymmetries of $B \to K^{(*)}\mu^+\mu^-$ decays"; JHEP **06**, p. 133 (2014). arXiv:1403.8044 [hep-ex]. 27

[136] (LHCb Collaboration); R. Aaij *et al.*; "Differential branching fraction and angular analysis of $\Lambda_b^0 \to \Lambda\mu^+\mu^-$ decays"; JHEP **06**, p. 115 (2015). [Erratum: JHEP 09, 145 (2018)]; arXiv:1503.07138 [hep-ex]. 27

[137] (LHCb Collaboration); R. Aaij *et al.*; "Angular analysis and differential branching fraction of the decay $B_s^0 \to \phi\mu^+\mu^-$"; JHEP **09**, p. 179 (2015). arXiv:1506.08777 [hep-ex]. 27

[138] (LHCb Collaboration); R. Aaij *et al.*; "Measurements of the S-wave fraction in $B^0 \to K^+\pi^-\mu^+\mu^-$ decays and the $B^0 \to K^*(892)^0\mu^+\mu^-$ differential branching fraction"; JHEP **11**, p. 047 (2016). [Erratum: JHEP 04, 142 (2017)]; arXiv:1606.04731 [hep-ex]. 27

[139] (LHCb Collaboration); R. Aaij *et al.*; "Test of lepton universality using $B^+ \to K^+\ell^+\ell^-$ decays"; Phys. Rev. Lett. **113**, p. 151601 (2014). arXiv:1406.6482 [hep-ex]. 27

[140] (Belle Collaboration); J. T. Wei *et al.*; "Measurement of the Differential Branching Fraction and Forward-Backword Asymmetry for $B \to K^{(*)}\ell^+\ell^-$"; Phys. Rev. Lett. **103**, p. 171801 (2009). arXiv:0904.0770 [hep-ex]. 27

[141] (BaBar Collaboration); J. P. Lees *et al.*; "Measurement of Branching Fractions and Rate Asymmetries in the Rare Decays $B \to K^{(*)}l^+l^-$"; Phys. Rev. D **86**, p. 032012 (2012). arXiv:1204.3933 [hep-ex]. 27

[142] (LHCb Collaboration); R. Aaij *et al.*; "Test of lepton universality with $B^0 \to K^{*0}\ell^+\ell^-$ decays"; JHEP **08**, p. 055 (2017). arXiv:1705.05802 [hep-ex]. 27

[143] (LHCb Collaboration); R. Aaij *et al.*; "Angular analysis of the $B^0 \to K^{*0}\mu^+\mu^-$ decay using 3 fb^{-1} of integrated luminosity"; JHEP **02**, p. 104 (2016). arXiv:1512.04442 [hep-ex]. 27

[144] (Belle Collaboration); S. Wehle *et al.*; "Lepton-Flavor-Dependent Angular Analysis of $B \to K^* \ell^+ \ell^-$"; Phys. Rev. Lett. **118**, p. 111801 (2017). arXiv:1612.05014 [hep-ex]. 27

[145] (ATLAS Collaboration); M. Aaboud *et al.*; "Angular analysis of $B_d^0 \to K^* \mu^+ \mu^-$ decays in pp collisions at $\sqrt{s} = 8$ TeV with the ATLAS detector"; JHEP **10**, p. 047 (2018). arXiv:1805.04000 [hep-ex]. 27

[146] (CMS Collaboration); A. M. Sirunyan *et al.*; "Measurement of angular parameters from the decay $\mathrm{B}^0 \to \mathrm{K}^{*0} \mu^+ \mu^-$ in proton-proton collisions at $\sqrt{s} = 8$ TeV"; Phys. Lett. B **781**, pp. 517–541 (2018). arXiv:1710.02846 [hep-ex]. 27

[147] (BaBar Collaboration); J. P. Lees *et al.*; "Evidence for an excess of $\bar{B} \to D^{(*)} \tau^- \bar{\nu}_\tau$ decays"; Phys. Rev. Lett. **109**, p. 101802 (2012). arXiv:1205.5442 [hep-ex]. 27

[148] (BaBar Collaboration); J. P. Lees *et al.*; "Measurement of an Excess of $\bar{B} \to D^{(*)} \tau^- \bar{\nu}_\tau$ Decays and Implications for Charged Higgs Bosons"; Phys. Rev. D **88**, p. 072012 (2013). arXiv:1303.0571 [hep-ex]. 27

[149] (Belle Collaboration); M. Huschle *et al.*; "Measurement of the branching ratio of $\bar{B} \to D^{(*)} \tau^- \bar{\nu}_\tau$ relative to $\bar{B} \to D^{(*)} \ell^- \bar{\nu}_\ell$ decays with hadronic tagging at Belle"; Phys. Rev. D **92**, p. 072014 (2015). arXiv:1507.03233 [hep-ex]. 27

[150] A. Abdesselam *et al.*; "Measurement of the branching ratio of $\bar{B}^0 \to D^{*+} \tau^- \bar{\nu}_\tau$ relative to $\bar{B}^0 \to D^{*+} \ell^- \bar{\nu}_\ell$ decays with a semileptonic tagging method"; in "51st Rencontres de Moriond on EW Interactions and Unified Theories," (2016); arXiv:1603.06711 [hep-ex]. 27

[151] (Belle Collaboration); S. Hirose *et al.*; "Measurement of the τ lepton polarization and $R(D^*)$ in the decay $\bar{B} \to D^* \tau^- \bar{\nu}_\tau$"; Phys. Rev. Lett. **118**, p. 211801 (2017). arXiv:1612.00529 [hep-ex]. 27

[152] (LHCb Collaboration); R. Aaij *et al.*; "Measurement of the ratio of branching fractions $\mathcal{B}(\bar{B}^0 \to D^{*+} \tau^- \bar{\nu}_\tau) / \mathcal{B}(\bar{B}^0 \to D^{*+} \mu^- \bar{\nu}_\mu)$"; Phys. Rev. Lett. **115**, p. 111803 (2015). [Erratum: Phys.Rev.Lett. 115, 159901 (2015)]; arXiv:1506.08614 [hep-ex]. 27

[153] (LHCb Collaboration); R. Aaij *et al.*; "Measurement of the ratio of the $B^0 \to D^{*-} \tau^+ \nu_\tau$ and $B^0 \to D^{*-} \mu^+ \nu_\mu$ branching fractions using three-prong τ-lepton decays"; Phys. Rev. Lett. **120**, p. 171802 (2018). arXiv:1708.08856 [hep-ex]. 27

[154] M. Mondragon; "Beyond the Standard Model"; CERN Yellow Rep. School Proc. **4**, pp. 101–124 (2018). 27

[155] M. D. Schwartz; *Quantum Field Theory and the Standard Model* (Cambridge University Press) (2014); ISBN 978-1-107-03473-0, 978-1-107-03473-0. 27

[156] C. Csáki, S. Lombardo & O. Telem; *TASI Lectures on Non-supersymmetric BSM Models* (WSP) (2018); arXiv:1811.04279 [hep-ph]. 27

[157] M. J. G. Veltman; "The Infrared - Ultraviolet Connection"; Acta Phys. Polon. B **12**, p. 437 (1981). 27

[158] L. Susskind; "Dynamics of Spontaneous Symmetry Breaking in the Weinberg-Salam Theory"; Phys. Rev. D **20**, pp. 2619–2625 (1979). 27

[159] E. Gildener; "Gauge Symmetry Hierarchies"; Phys. Rev. D **14**, p. 1667 (1976). 27

[160] J. D. Wells; "Lectures on Higgs Boson Physics in the Standard Model and Beyond"; in "38th British Universities Summer School in Theoretical Elementary Particle Physics," (2009); arXiv:0909.4541 [hep-ph]. 28

[161] D.-d. Wu; "A Brief Introduction to the Strong CP Problem"; Z. Naturforsch. A **52**, pp. 179–181 (1997). 28

[162] R. D. Peccei & H. R. Quinn; "CP Conservation in the Presence of Instantons"; Phys. Rev. Lett. **38**, pp. 1440–1443 (1977). 28

[163] R. D. Peccei & H. R. Quinn; "Constraints Imposed by CP Conservation in the Presence of Instantons"; Phys. Rev. D **16**, pp. 1791–1797 (1977). 28

[164] P. Fayet; "Supersymmetry and Weak, Electromagnetic and Strong Interactions"; Phys. Lett. B **64**, p. 159 (1976). 29

[165] P. Fayet; "Spontaneously Broken Supersymmetric Theories of Weak, Electromagnetic and Strong Interactions"; Phys. Lett. B **69**, p. 489 (1977). 29

[166] P. Fayet; "Relations Between the Masses of the Superpartners of Leptons and Quarks, the Goldstino Couplings and the Neutral Currents"; Phys. Lett. B **84**, p. 416 (1979). 29

[167] G. R. Farrar & P. Fayet; "Phenomenology of the Production, Decay, and Detection of New Hadronic States Associated with Supersymmetry"; Phys. Lett. B **76**, pp. 575–579 (1978). 29, 94

[168] D. Das, A. Kundu & I. Saha; "Higgs data does not rule out a sequential fourth generation with an extended scalar sector"; Phys. Rev. D **97**, p. 011701 (2018). arXiv:1707.03000 [hep-ph]. 29

[169] S. Bar-Shalom, S. Nandi & A. Soni; "Two Higgs doublets with 4th generation fermions - models for TeV-scale compositeness"; Phys. Rev. D **84**, p. 053009 (2011). arXiv:1105.6095 [hep-ph]. 29

[170] S. Bar-Shalom, M. Geller, S. Nandi & A. Soni; "Two Higgs doublets, a 4th generation and a 125 GeV Higgs: A review." Adv. High Energy Phys. **2013**, p. 672972 (2013). arXiv:1208.3195 [hep-ph]. 29

[171] X.-G. He & G. Valencia; "An extended scalar sector to address the tension between a fourth generation and Higgs searches at the LHC"; Phys. Lett. B **707**, pp. 381–384 (2012). arXiv:1108.0222 [hep-ph]. 29

[172] S. Chamorro-Solano, A. Moyotl & M. A. Pérez; "Lepton flavor changing Higgs Boson decays in a Two Higgs Doublet Model with a fourth generation of fermions"; J. Phys. G **45**, p. 075003 (2018). arXiv:1707.00100 [hep-ph]. 29

[173] N. Kumar & S. P. Martin; "Vectorlike Leptons at the Large Hadron Collider"; Phys. Rev. D **92**, p. 115018 (2015). arXiv:1510.03456 [hep-ph]. 29, 30, 32, 34, 146

[174] P. N. Bhattiprolu & S. P. Martin; "Prospects for vectorlike leptons at future proton-proton colliders"; Phys. Rev. D **100**, p. 015033 (2019). arXiv:1905.00498 [hep-ph]. 29, 30, 32

[175] A. Djouadi & A. Lenz; "Sealing the fate of a fourth generation of fermions"; Phys. Lett. B **715**, pp. 310–314 (2012). arXiv:1204.1252 [hep-ph]. 29

[176] A. Lenz; "Constraints on a fourth generation of fermions from Higgs Boson searches"; Adv. High Energy Phys. **2013**, p. 910275 (2013). 29

[177] O. Eberhardt, G. Herbert, H. Lacker, A. Lenz, A. Menzel, U. Nierste & M. Wiebusch; "Impact of a Higgs boson at a mass of 126 GeV on the standard model with three and four fermion generations"; Phys. Rev. Lett. **109**, p. 241802 (2012). arXiv:1209.1101 [hep-ph]. 29

[178] M. Schmaltz & D. Tucker-Smith; "Little Higgs review"; Ann. Rev. Nucl. Part. Sci. **55**, pp. 229–270 (2005). arXiv:hep-ph/0502182. 30

[179] N. Arkani-Hamed, A. G. Cohen, E. Katz, A. E. Nelson, T. Gregoire & J. G. Wacker; "The Minimal moose for a little Higgs"; JHEP **08**, p. 021 (2002). arXiv:hep-ph/0206020. 30

[180] M. Perelstein; "Little Higgs models and their phenomenology"; Prog. Part. Nucl. Phys. **58**, pp. 247–291 (2007). arXiv:hep-ph/0512128. 30

[181] R. Contino; "The Higgs as a Composite Nambu-Goldstone Boson"; in "Theoretical Advanced Study Institute in Elementary Particle Physics: Physics of the Large and the Small," (2010); arXiv:1005.4269 [hep-ph]. 30

[182] G. Panico & A. Wulzer; *The Composite Nambu-Goldstone Higgs*; volume 913 (Springer) (2016); arXiv:1506.01961 [hep-ph]. 30

[183] G. Burdman, P. Ormonde & V. Peralta; "Fermion Resonances in Quiver Theories with a pNGB Higgs"; JHEP **11**, p. 045 (2014). arXiv:1408.1320 [hep-ph]. 30

[184] G. Burdman, N. Fonseca & L. de Lima; "Full-hierarchy Quiver Theories of Electroweak Symmetry Breaking and Fermion Masses"; JHEP **01**, p. 094 (2013). arXiv:1210.5568 [hep-ph]. 30

[185] C. Csáki & P. Tanedo; "Beyond the Standard Model"; in "2013 European School of High-Energy Physics," (2015); arXiv:1602.04228 [hep-ph]. 34

[186] S. P. Martin; "A Supersymmetry primer"; Adv. Ser. Direct. High Energy Phys. **18**, pp. 1–98 (1998). arXiv:hep-ph/9709356. 34, 36

[187] S. R. Coleman & J. Mandula; "All Possible Symmetries of the S Matrix"; Phys. Rev. **159**, pp. 1251–1256 (1967). 34

[188] R. Haag, J. T. Lopuszanski & M. Sohnius; "All Possible Generators of Supersymmetries of the s Matrix"; Nucl. Phys. B **88**, p. 257 (1975). 34

[189] M. D. Schwartz; *TASI Lectures on Collider Physics* (2018); arXiv:1709.04533 [hep-ph]. 39, 42

[190] E. Halkiadakis; "Introduction to the LHC Experiments"; in "Theoretical Advanced Study Institute in Elementary Particle Physics: Physics of the Large and the Small," (2010); arXiv:1004.5564 [hep-ex]. 39

[191] A. Buckley, D. Kar & K. Nordström; "Fast simulation of detector effects in Rivet"; SciPost Phys. **8**, p. 025 (2020). arXiv:1910.01637 [hep-ph]. 39, 47, 49

[192] J. Kvapil *et al.*; "ALICE Central Trigger System for LHC Run 3"; in "25th International Conference on Computing in High-Energy and Nuclear Physics," (2021); arXiv:2106.08353 [physics.ins-det]. 39

[193] E. Conte & B. Fuks; "Confronting new physics theories to LHC data with MADANALYSIS 5"; Int. J. Mod. Phys. **A33**, p. 1830027 (2018). arXiv:1808.00480 [hep-ph]. 39, 45, 47, 49, 50, 75, 88

[194] "LHC Machine"; JINST **3**, p. S08001 (2008). 39

[195] R. Bruce *et al.*; "New physics searches with heavy-ion collisions at the CERN Large Hadron Collider"; J. Phys. G **47**, p. 060501 (2020). arXiv:1812.07688 [hep-ph]. 40

[196] M. Benedikt & F. Zimmermann; "Proton Colliders at the Energy Frontier"; Nucl. Instrum. Meth. A **907**, pp. 200–208 (2018). arXiv:1803.09723 [physics.acc-ph]. 40

[197] C. E. Gerber; "LHC Highlights and Prospects"; CERN Yellow Rep. School Proc. **2**, p. 161 (2021). arXiv:1909.10919 [hep-ex]. 40

[198] V. Shiltsev & F. Zimmermann; "Modern and Future Colliders"; Rev. Mod. Phys. **93**, p. 15006 (2021). arXiv:2003.09084 [physics.acc-ph]. 40

[199] J. Nielsen; "Fundamentals of LHC Experiments"; in "Theoretical Advanced Study Institute in Elementary Particle Physics: String theory and its Applications: From meV to the Planck Scale," (2011); arXiv:1106.2516 [hep-ex]. 40

[200] J. T. Boyd; "LHC Run-2 and Future Prospects"; in "2019 European School of High-Energy Physics," (2020); arXiv:2001.04370 [hep-ex]. 40

[201] (CMS Collaboration); A. M. Sirunyan *et al.*; "Particle-flow reconstruction and global event description with the CMS detector"; JINST **12**, p. P10003 (2017). arXiv:1706.04965 [physics.ins-det]. 41

[202] (ATLAS Collaboration); A. Airapetian *et al.*; "ATLAS: Detector and physics performance technical design report. Volume 1"; (1999). 41

[203] (CMS Collaboration); G. L. Bayatian *et al.*; "CMS Physics: Technical Design Report Volume 1: Detector Performance and Software"; (2006). 41

[204] (ATLAS Collaboration); "ATLAS inner detector: Technical design report. Vol. 1"; (1997). 41

[205] J. Pequenao; "Event Cross Section in a computer generated image of the ATLAS detector." (2008). https://cds.cern.ch/record/1096081. 41, 215

[206] G. Soyez; "Pileup mitigation at the LHC: A theorist's view"; Phys. Rept. **803**, pp. 1–158 (2019). arXiv:1801.09721 [hep-ph]. 41

[207] A. Hoecker; "Physics at the LHC Run-2 and Beyond"; in "2016 European School of High-Energy Physics," (2016); arXiv:1611.07864 [hep-ex]. 42

[208] M. Cacciari, G. P. Salam & G. Soyez; "The anti-k_t jet clustering algorithm"; JHEP **04**, p. 063 (2008). arXiv:0802.1189 [hep-ph]. 42, 75

[209] R. Kogler *et al.*; "Jet Substructure at the Large Hadron Collider: Experimental Review"; Rev. Mod. Phys. **91**, p. 045003 (2019). arXiv:1803.06991 [hep-ex]. 42

[210] (ATLAS Collaboration); M. Aaboud *et al.*; "Jet reconstruction and performance using particle flow with the ATLAS Detector"; Eur. Phys. J. C **77**, p. 466 (2017). arXiv:1703.10485 [hep-ex]. 42

[211] (NNPDF Collaboration); R. D. Ball *et al.*; "Parton distributions for the LHC Run II"; JHEP **04**, p. 040 (2015). arXiv:1410.8849 [hep-ph]. 42

[212] M. Perelstein; "Introduction to Collider Physics"; in "Theoretical Advanced Study Institute in Elementary Particle Physics: Physics of the Large and the Small," (2010); arXiv:1002.0274 [hep-ph]. 43

[213] (LHC Reinterpretation Forum Collaboration); W. Abdallah *et al.*; "Reinterpretation of LHC Results for New Physics: Status and Recommendations after Run 2"; SciPost Phys. **9**, p. 022 (2020). arXiv:2003.07868 [hep-ph]. 44, 49, 149

[214] E. Conte, B. Fuks & G. Serret; "MadAnalysis 5, A User-Friendly Framework for Collider Phenomenology"; Comput. Phys. Commun. **184**, pp. 222–256 (2013). arXiv:1206.1599 [hep-ph]. 45, 75, 88

[215] E. Conte & B. Fuks; "MadAnalysis 5: status and new developments"; J. Phys. Conf. Ser. **523**, p. 012032 (2014). arXiv:1309.7831 [hep-ph]. 45

[216] B. Dumont, B. Fuks, S. Kraml, S. Bein, G. Chalons, E. Conte, S. Kulkarni, D. Sengupta & C. Wymant; "Toward a public analysis database for LHC new physics searches using MADANALYSIS 5"; Eur. Phys. J. C **75**, p. 56 (2015). arXiv:1407.3278 [hep-ph]. 45, 47, 50, 75, 115

[217] E. Conte, B. Dumont, B. Fuks & T. Schmitt; "New features of MadAnalysis 5 for analysis design and reinterpretation"; J. Phys. Conf. Ser. **608**, p. 012054 (2015). arXiv:1410.2785 [hep-ph]. 45

[218] J. Y. Araz, B. Fuks & G. Polykratis; "Simplified fast detector simulation in MADANALYSIS 5"; Eur. Phys. J. C **81**, p. 329 (2021). arXiv:2006.09387 [hep-ph]. 45, 47, 49, 50, 88, 97

[219] S. Kraml, S. Kulkarni, U. Laa, A. Lessa, V. Magerl, W. Magerl, D. Proschofsky-Spindler, M. Traub & W. Waltenberger; "SModelS v1.0: a short user guide"; (2014)arXiv:1412.1745 [hep-ph]. 47

[220] (LHC New Physics Working Group Collaboration); D. Alves; "Simplified Models for LHC New Physics Searches"; J. Phys. G **39**, p. 105005 (2012). arXiv:1105.2838 [hep-ph]. 47

[221] (DELPHES 3 Collaboration); J. de Favereau, C. Delaere, P. Demin, A. Giammanco, V. Lemaître, A. Mertens & M. Selvaggi; "DELPHES 3, A modular framework for fast simulation of a generic collider experiment"; JHEP **02**, p. 057 (2014). arXiv:1307.6346 [hep-ex]. 47, 48, 75

[222] J. Allison *et al.*; "Geant4 developments and applications"; IEEE Trans. Nucl. Sci. **53**, p. 270 (2006). 48

[223] K. Edmonds, S. Fleischmann, T. Lenz, C. Magass, J. Mechnich & A. Salzburger; "The fast ATLAS track simulation (FATRAS)"; (2008). 48

[224] S. Hamilton, E. Kneringer, W. Lukas, E. Ritsch, A. Salzburger, K. Sliwa, S. Todorova, J. Wetter & S. Zimmermann; "The ATLAS Fast Track Simulation Project"; (2011). 48

[225] W. Lukas; "Fast Simulation for ATLAS: Atlfast-II and ISF"; J. Phys. Conf. Ser. **396**, p. 022031 (2012). 48

[226] R. Rahmat, R. Kroeger & A. Giammanco; "The fast simulation of the CMS experiment"; J. Phys. Conf. Ser. **396**, p. 062016 (2012). 48

[227] (CMS Collaboration); S. Abdullin, P. Azzi, F. Beaudette, P. Janot & A. Perrotta; "The fast simulation of the CMS detector at LHC"; J. Phys. Conf. Ser. **331**, p. 032049 (2011). 48

[228] (CMS Collaboration); "Comparison of the Fast Simulation of CMS with the first LHC data"; (2010). 48

[229] S. Ovyn, X. Rouby & V. Lemaitre; "DELPHES, a framework for fast simulation of a generic collider experiment"; (2009)arXiv:0903.2225 [hep-ph]. 48

[230] M. Cacciari, G. P. Salam & G. Soyez; "FastJet User Manual"; Eur. Phys. J. **C72**, p. 1896 (2012). arXiv:1111.6097 [hep-ph]. 48, 75

[231] J. Y. Araz *et al.*; "Proceedings of the second MadAnalysis 5 workshop on LHC recasting in Korea"; Mod. Phys. Lett. A **36**, p. 2102001 (2021). arXiv:2101.02245 [hep-ph]. 49

[232] S. Kraml; "Public tools for recasting LHC searches"; (2017). https://twiki.cern.ch/twiki/bin/view/LHCPhysics/RecastingTools. 49

[233] F. Ambrogi, S. Kraml, S. Kulkarni, U. Laa, A. Lessa, V. Magerl, J. Sonneveld, M. Traub & W. Waltenberger; "SModelS v1.1 user manual: Improving simplified model constraints with efficiency maps"; Comput. Phys. Commun. **227**, pp. 72–98 (2018). arXiv:1701.06586 [hep-ph]. 49, 50

[234] I. Antcheva *et al.*; "ROOT: A C++ framework for petabyte data storage, statistical analysis and visualization"; Comput. Phys. Commun. **180**, pp. 2499–2512 (2009). arXiv:1508.07749 [physics.data-an]. 49

[235] J. Alwall, R. Frederix, S. Frixione, V. Hirschi, F. Maltoni, O. Mattelaer, H. S. Shao, T. Stelzer, P. Torrielli & M. Zaro; "The automated computation of tree-level and next-to-leading order differential cross sections, and their matching to parton shower simulations"; JHEP **07**, p. 079 (2014). arXiv:1405.0301 [hep-ph]. 49, 51, 75, 134

[236] M. Drees, H. Dreiner, D. Schmeier, J. Tattersall & J. S. Kim; "CheckMATE: Confronting your Favourite New Physics Model with LHC Data"; Comput. Phys. Commun. **187**, pp. 227–265 (2015). arXiv:1312.2591 [hep-ph]. 50, 121

[237] D. Dercks, N. Desai, J. S. Kim, K. Rolbiecki, J. Tattersall & T. Weber; "CheckMATE 2: From the model to the limit"; Comput. Phys. Commun. **221**, pp. 383–418 (2017). arXiv:1611.09856 [hep-ph]. 50, 121

[238] A. Buckley, J. Butterworth, D. Grellscheid, H. Hoeth, L. Lonnblad, J. Monk, H. Schulz & F. Siegert; "Rivet user manual"; Comput. Phys. Commun. **184**, pp. 2803–2819 (2013). arXiv:1003.0694 [hep-ph]. 50

[239] C. Bierlich *et al.*; "Robust Independent Validation of Experiment and Theory: Rivet version 3"; SciPost Phys. **8**, p. 026 (2020). arXiv:1912.05451 [hep-ph]. 50

[240] (GAMBIT Collaboration); P. Athron *et al.*; "GAMBIT: The Global and Modular Beyond-the-Standard-Model Inference Tool"; Eur. Phys. J. C **77**, p. 784 (2017). [Addendum: Eur.Phys.J.C 78, 98 (2018)]; arXiv:1705.07908 [hep-ph]. 50

[241] (GAMBIT Collaboration); C. Balázs *et al.*; "ColliderBit: a GAMBIT module for the calculation of high-energy collider observables and likelihoods"; Eur. Phys. J. C **77**, p. 795 (2017). arXiv:1705.07919 [hep-ph]. 50

[242] J. M. Butterworth, D. Grellscheid, M. Krämer, B. Sarrazin & D. Yallup; "Constraining new physics with collider measurements of Standard Model signatures"; JHEP **03**, p. 078 (2017). arXiv:1606.05296 [hep-ph]. 50

[243] J. Butterworth, D. Grellscheid, M. Krämer & D. Yallup; "Constraining BSM (Simplified) models with SM measurements"; (2016). https://indico.cern.ch/event/525142/contributions/2173705/attachments/1293517/1927668/contur.pdf; cERN workshop on (re)interpreting the results of new physics searches at the LHC. 50

[244] S. Kraml, S. Kulkarni, U. Laa, A. Lessa, W. Magerl, D. Proschofsky-Spindler & W. Waltenberger; "SModelS: a tool for interpreting simplified-model results from the LHC and its application to supersymmetry"; Eur. Phys. J. C **74**, p. 2868 (2014). arXiv:1312.4175 [hep-ph]. 50

[245] F. Ambrogi *et al.*; "SModelS v1.2: long-lived particles, combination of signal regions, and other novelties"; Comput. Phys. Commun. **251**, p. 106848 (2020). arXiv:1811.10624 [hep-ph]. 50

[246] G. Alguero, J. Heisig, C. K. Khosa, S. Kraml, S. Kulkarni, A. Lessa, P. Neuhuber, H. Reyes-González, W. Waltenberger & A. Wongel; "New developments in SModelS"; PoS **TOOLS2020**, p. 022 (2021). arXiv:2012.08192 [hep-ph]. 50

[247] P. Bechtle, O. Brein, S. Heinemeyer, G. Weiglein & K. E. Williams; "HiggsBounds: Confronting Arbitrary Higgs Sectors with Exclusion Bounds from LEP and the Tevatron"; Comput. Phys. Commun. **181**, pp. 138–167 (2010). arXiv:0811.4169 [hep-ph]. 50

[248] P. Bechtle, O. Brein, S. Heinemeyer, G. Weiglein & K. E. Williams; "HiggsBounds 2.0.0: Confronting Neutral and Charged Higgs Sector Predictions with Exclusion Bounds from LEP and the Tevatron"; Comput. Phys. Commun. **182**, pp. 2605–2631 (2011). arXiv:1102.1898 [hep-ph]. 50

[249] P. Bechtle, O. Brein, S. Heinemeyer, O. Stal, T. Stefaniak, G. Weiglein & K. Williams; "Recent Developments in HiggsBounds and a Preview of HiggsSignals"; PoS **CHARGED2012**, p. 024 (2012). arXiv:1301.2345 [hep-ph]. 50

[250] P. Bechtle, O. Brein, S. Heinemeyer, O. Stål, T. Stefaniak, G. Weiglein & K. E. Williams; "HiggsBounds – 4: Improved Tests of Extended Higgs Sectors against Exclusion Bounds from LEP, the Tevatron and the LHC"; Eur. Phys. J. C **74**, p. 2693 (2014). arXiv:1311.0055 [hep-ph]. 50

[251] P. Bechtle, S. Heinemeyer, O. Stal, T. Stefaniak & G. Weiglein; "Applying Exclusion Likelihoods from LHC Searches to Extended Higgs Sectors"; Eur. Phys. J. C **75**, p. 421 (2015). arXiv:1507.06706 [hep-ph]. 50

[252] D. Barducci, A. Belyaev, M. Buchkremer, J. Marrouche, S. Moretti & L. Panizzi; "XQCAT: eXtra Quark Combined Analysis Tool"; Comput. Phys. Commun. **197**, pp. 263–275 (2015). arXiv:1409.3116 [hep-ph]. 50

[253] M. Papucci, K. Sakurai, A. Weiler & L. Zeune; "Fastlim: a fast LHC limit calculator"; Eur. Phys. J. C **74**, p. 3163 (2014). arXiv:1402.0492 [hep-ph]. 50

[254] P. Bechtle, S. Heinemeyer, O. Stål, T. Stefaniak & G. Weiglein; "*HiggsSignals*: Confronting arbitrary Higgs sectors with measurements at the Tevatron and the LHC"; Eur. Phys. J. C **74**, p. 2711 (2014). arXiv:1305.1933 [hep-ph]. 50

[255] O. Stål & T. Stefaniak; "Constraining extended Higgs sectors with HiggsSignals"; PoS **EPS-HEP2013**, p. 314 (2013). arXiv:1310.4039 [hep-ph]. 50

[256] P. Bechtle, S. Heinemeyer, O. Stål, T. Stefaniak & G. Weiglein; "Probing the Standard Model with Higgs signal rates from the Tevatron, the LHC and a future ILC"; JHEP **11**, p. 039 (2014). arXiv:1403.1582 [hep-ph]. 50, 67, 69

[257] J. Bernon & B. Dumont; "Lilith: a tool for constraining new physics from Higgs measurements"; Eur. Phys. J. C **75**, p. 440 (2015). arXiv:1502.04138 [hep-ph]. 50, 67, 68

[258] S. Kraml, T. Q. Loc, D. T. Nhung & L. D. Ninh; "Constraining new physics from Higgs measurements with Lilith: update to LHC Run 2 results"; SciPost Phys. **7**, p. 052 (2019). arXiv:1908.03952 [hep-ph]. 50, 67, 69

[259] K. Cranmer & I. Yavin; "RECAST: Extending the Impact of Existing Analyses"; JHEP **04**, p. 038 (2011). arXiv:1010.2506 [hep-ex]. 50

[260] A. Schuy, L. Heinrich, K. Cranmer & S.-C. Hsu; "Extending RECAST for Truth-Level Reinterpretations"; in "Meeting of the Division of Particles and Fields of the American Physical Society," (2019); arXiv:1910.10289 [physics.data-an]. 50

[261] B. Fuks; "LHC recasting in a nutshell"; (2017). https://indico.cern.ch/event/637941/contributions/2606073/attachments/1510177/2354693/fuks_recasting.pdf; 1st MADANALYSIS 5 workshop on LHC recasting @ High 1, Gangwon Province, Korea. 50

[262] A. Alloul, N. D. Christensen, C. Degrande, C. Duhr & B. Fuks; "FeynRules 2.0 - A complete toolbox for tree-level phenomenology"; Comput. Phys. Commun. **185**, pp. 2250–2300 (2014). arXiv:1310.1921 [hep-ph]. 50, 51, 67, 75

[263] W. R. Inc.; "Mathematica, Version 12.0"; Champaign, IL, 2019. 51

[264] C. Degrande, C. Duhr, B. Fuks, D. Grellscheid, O. Mattelaer & T. Reiter; "UFO - The Universal FeynRules Output"; Comput. Phys. Commun. **183**, pp. 1201–1214 (2012). arXiv:1108.2040 [hep-ph]. 51, 75, 134

[265] A. V. Semenov; "LanHEP: A Package for automatic generation of Feynman rules in gauge models"; (1996)arXiv:hep-ph/9608488. 51

[266] A. Semenov; "LanHEP — A package for automatic generation of Feynman rules from the Lagrangian. Version 3.2"; Comput. Phys. Commun. **201**, pp. 167–170 (2016). arXiv:1412.5016 [physics.comp-ph]. 51

[267] F. Staub; "SARAH"; (2008)arXiv:0806.0538 [hep-ph]. 51, 147

[268] F. Staub; "Exploring new models in all detail with SARAH"; Adv. High Energy Phys. **2015**, p. 840780 (2015). arXiv:1503.04200 [hep-ph]. 51

[269] A. Buckley *et al.*; "General-purpose event generators for LHC physics"; Phys. Rept. **504**, pp. 145–233 (2011). arXiv:1101.2599 [hep-ph]. 51

[270] R. Frederix, S. Frixione, V. Hirschi, D. Pagani, H. S. Shao & M. Zaro; "The automation of next-to-leading order electroweak calculations"; JHEP **07**, p. 185 (2018). arXiv:1804.10017 [hep-ph]. 51

[271] T. Gleisberg, S. Hoeche, F. Krauss, A. Schalicke, S. Schumann & J.-C. Winter; "SHERPA 1. alpha: A Proof of concept version"; JHEP **02**, p. 056 (2004). arXiv:hep-ph/0311263. 51

[272] T. Gleisberg, S. Hoeche, F. Krauss, M. Schonherr, S. Schumann, F. Siegert & J. Winter; "Event generation with SHERPA 1.1"; JHEP **02**, p. 007 (2009). arXiv:0811.4622 [hep-ph]. 51

[273] (Sherpa Collaboration); E. Bothmann *et al.*; "Event Generation with Sherpa 2.2"; SciPost Phys. **7**, p. 034 (2019). arXiv:1905.09127 [hep-ph]. 51

[274] W. Kilian, T. Ohl & J. Reuter; "WHIZARD: Simulating Multi-Particle Processes at LHC and ILC"; Eur. Phys. J. C **71**, p. 1742 (2011). arXiv:0708.4233 [hep-ph]. 51

[275] M. Moretti, T. Ohl & J. Reuter; "O'Mega: An Optimizing matrix element generator"; (2001)arXiv:hep-ph/0102195. 51

[276] P. Stienemeier, S. Brass, P. Bredt, W. Kilian, N. Kreher, T. Ohl, J. Reuter, V. Rothe & T. Striegl; "WHIZARD 3.0: Status and News"; in "International Workshop on Future Linear Colliders," (2021); arXiv:2104.11141 [hep-ph]. 51

[277] M. Bahr *et al.*; "Herwig++ Physics and Manual"; Eur. Phys. J. C **58**, pp. 639–707 (2008). arXiv:0803.0883 [hep-ph]. 51

[278] J. Bellm *et al.*; "Herwig 7.2 release note"; Eur. Phys. J. C **80**, p. 452 (2020). arXiv:1912.06509 [hep-ph]. 51

[279] T. Sjostrand, P. Eden, C. Friberg, L. Lonnblad, G. Miu, S. Mrenna & E. Norrbin; "High-energy physics event generation with PYTHIA 6.1"; Comput. Phys. Commun. **135**, pp. 238–259 (2001). arXiv:hep-ph/0010017. 51

[280] T. Sjostrand, S. Mrenna & P. Z. Skands; "PYTHIA 6.4 Physics and Manual"; JHEP **05**, p. 026 (2006). arXiv:hep-ph/0603175. 51, 75, 122, 133

[281] T. Sjöstrand, S. Ask, J. R. Christiansen, R. Corke, N. Desai, P. Ilten, S. Mrenna, S. Prestel, C. O. Rasmussen & P. Z. Skands; "An introduction to PYTHIA 8.2"; Comput. Phys. Commun. **191**, pp. 159–177 (2015). arXiv:1410.3012 [hep-ph]. 51, 75, 122, 133

[282] A. L. Read; "Presentation of search results: The CL(s) technique"; J. Phys. **G28**, pp. 2693–2704 (2002). [,11(2002)]. 51, 75, 123, 147

[283] W. A. Bardeen, C. N. Leung & S. T. Love; "The Dilaton and Chiral Symmetry Breaking"; Phys. Rev. Lett. **56**, p. 1230 (1986). 53

[284] W. Buchmuller & N. Dragon; "Scale Invariance and Spontaneous Symmetry Breaking"; Phys. Lett. B **195**, pp. 417–422 (1987). 53

[285] W. Buchmuller & N. Dragon; "Dilatons in Flat and Curved Space-time"; Nucl. Phys. B **321**, pp. 207–231 (1989). 53

[286] R. Rattazzi & A. Zaffaroni; "Comments on the holographic picture of the Randall-Sundrum model"; JHEP **04**, p. 021 (2001). arXiv:hep-th/0012248 [hep-th]. 53, 57, 163

[287] C. Csaki, M. L. Graesser & G. D. Kribs; "Radion dynamics and electroweak physics"; Phys. Rev. D **63**, p. 065002 (2001). arXiv:hep-th/0008151. 53

[288] D. Dominici, B. Grzadkowski, J. F. Gunion & M. Toharia; "The Scalar sector of the Randall-Sundrum model"; Nucl. Phys. B **671**, pp. 243–292 (2003). arXiv:hep-ph/0206192. 53

[289] C. Csaki, J. Hubisz & S. J. Lee; "Radion phenomenology in realistic warped space models"; Phys. Rev. **D76**, p. 125015 (2007). arXiv:0705.3844 [hep-ph]. 53

[290] W. D. Goldberger, B. Grinstein & W. Skiba; "Distinguishing the Higgs boson from the dilaton at the Large Hadron Collider"; Phys. Rev. Lett. **100**, p. 111802 (2008). arXiv:0708.1463 [hep-ph]. 53, 57, 58, 163

[291] Y. Bai, M. Carena & J. Lykken; "Dilaton-assisted Dark Matter"; Phys. Rev. Lett. **103**, p. 261803 (2009). arXiv:0909.1319 [hep-ph]. 53, 63

[292] B. Grzadkowski, J. F. Gunion & M. Toharia; "Higgs-Radion interpretation of the LHC data?" Phys. Lett. B **712**, pp. 70–80 (2012). arXiv:1202.5017 [hep-ph]. 53

[293] Z. Chacko & R. K. Mishra; "Effective Theory of a Light Dilaton"; Phys. Rev. **D87**, p. 115006 (2013). arXiv:1209.3022 [hep-ph]. 53

[294] B. Bellazzini, C. Csaki, J. Hubisz, J. Serra & J. Terning; "A Higgslike Dilaton"; Eur. Phys. J. **C73**, p. 2333 (2013). arXiv:1209.3299 [hep-ph]. 53

[295] A. Ahmed, B. M. Dillon, B. Grzadkowski, J. F. Gunion & Y. Jiang; "Implications of the absence of high-mass radion signals"; Phys. Rev. D **95**, p. 095019 (2017). arXiv:1512.05771 [hep-ph]. 53

[296] A. Ahmed, A. Mariotti & S. Najjari; "A light dilaton at the LHC"; (2019)arXiv:1912.06645 [hep-ph]. 53

[297] D.-W. Jung & P. Ko; "Higgs-dilaton(radion) system confronting the LHC Higgs data"; Phys. Lett. B **732**, pp. 364–372 (2014). arXiv:1401.5586 [hep-ph]. 53, 59, 63, 86

[298] K. Blum, M. Cliche, C. Csaki & S. J. Lee; "WIMP Dark Matter through the Dilaton Portal"; JHEP **03**, p. 099 (2015). arXiv:1410.1873 [hep-ph]. 53, 58, 63, 167

[299] A. Efrati, E. Kuflik, S. Nussinov, Y. Soreq & T. Volansky; "Constraining the Higgs-Dilaton with LHC and Dark Matter Searches"; Phys. Rev. **D91**, p. 055034 (2015). arXiv:1410.2225 [hep-ph]. 53, 60, 62, 68, 70

[300] M. Kim, S. J. Lee & A. Parolini; "WIMP Dark Matter in Composite Higgs Models and the Dilaton Portal"; (2016)arXiv:1602.05590 [hep-ph]. 53

[301] B. Fuks, M. D. Goodsell, D. W. Kang, P. Ko, S. J. Lee & M. Utsch; "Heavy dark matter through the dilaton portal"; JHEP **10**, p. 044 (2020). arXiv:2007.08546 [hep-ph]. 54

[302] W. D. Goldberger, B. Grinstein & W. Skiba; "Distinguishing the Higgs boson from the dilaton at the Large Hadron Collider"; Phys. Rev. Lett. **100**, p. 111802 (2008). arXiv:0708.1463 [hep-ph]. 54

[303] C. G. Callan, Jr., S. R. Coleman & R. Jackiw; "A New improved energy - momentum tensor"; Annals Phys. **59**, pp. 42–73 (1970). 55

[304] H.-C. Cheng & I. Low; "TeV symmetry and the little hierarchy problem"; JHEP **09**, p. 051 (2003). arXiv:hep-ph/0308199 [hep-ph]. 63

[305] A. Birkedal, A. Noble, M. Perelstein & A. Spray; "Little Higgs dark matter"; Phys. Rev. **D74**, p. 035002 (2006). arXiv:hep-ph/0603077 [hep-ph]. 63

[306] O. Lebedev, H. M. Lee & Y. Mambrini; "Vector Higgs-portal dark matter and the invisible Higgs"; Phys. Lett. **B707**, pp. 570–576 (2012). arXiv:1111.4482 [hep-ph]. 63

[307] G. Arcadi, A. Djouadi & M. Kado; "The Higgs-portal for vector Dark Matter and the Effective Field Theory approach: a reappraisal"; (2020)arXiv:2001.10750 [hep-ph]. 63

[308] T. Hambye; "Hidden vector dark matter"; JHEP **01**, p. 028 (2009). arXiv:0811.0172 [hep-ph]. 63

[309] S. Baek, P. Ko, W.-I. Park & E. Senaha; "Higgs Portal Vector Dark Matter : Revisited"; JHEP **05**, p. 036 (2013). arXiv:1212.2131 [hep-ph]. 63

[310] S. Baek, P. Ko & W.-I. Park; "Invisible Higgs Decay Width vs. Dark Matter Direct Detection Cross Section in Higgs Portal Dark Matter Models"; Phys. Rev. D **90**, p. 055014 (2014). arXiv:1405.3530 [hep-ph]. 63

[311] P. Ko & H. Yokoya; "Search for Higgs portal DM at the ILC"; JHEP **08**, p. 109 (2016). arXiv:1603.04737 [hep-ph]. 63

[312] T. Kamon, P. Ko & J. Li; "Characterizing Higgs portal dark matter models at the ILC"; Eur. Phys. J. C **77**, p. 652 (2017). arXiv:1705.02149 [hep-ph]. 63

[313] B. Dutta, T. Kamon, P. Ko & J. Li; "Prospects for discovery and spin discrimination of dark matter in Higgs portal DM models and their extensions at 100 TeV *pp* collider"; Eur. Phys. J. C **78**, p. 595 (2018). arXiv:1712.05123 [hep-ph]. 63

[314] M. E. Peskin & T. Takeuchi; "Estimation of oblique electroweak corrections"; Phys. Rev. D **46**, pp. 381–409 (1992). 66, 67, 68

[315] P. Bechtle, D. Dercks, S. Heinemeyer, T. Klingl, T. Stefaniak, G. Weiglein & J. Wittbrodt; "HiggsBounds-5: Testing Higgs Sectors in the LHC 13 TeV Era"; (2020)arXiv:2006.06007 [hep-ph]. 67, 173

[316] D. Barducci, G. Belanger, J. Bernon, F. Boudjema, J. Da Silva, S. Kraml, U. Laa & A. Pukhov; "Collider limits on new physics within micrOMEGAs_4.3"; Comput. Phys. Commun. **222**, pp. 327–338 (2018). arXiv:1606.03834 [hep-ph]. 67

[317] G. Bélanger, F. Boudjema, A. Goudelis, A. Pukhov & B. Zaldivar; "micrOMEGAs5.0 : Freeze-in"; Comput. Phys. Commun. **231**, pp. 173–186 (2018). arXiv:1801.03509 [hep-ph]. 67

[318] M. Baak, M. Goebel, J. Haller, A. Hoecker, D. Ludwig, K. Moenig, M. Schott & J. Stelzer; "Updated Status of the Global Electroweak Fit and Constraints on New Physics"; Eur. Phys. J. C **72**, p. 2003 (2012). arXiv:1107.0975 [hep-ph]. 67

[319] K. Hagiwara, S. Matsumoto, D. Haidt & C. Kim; "A Novel approach to confront electroweak data and theory"; Z. Phys. C **64**, pp. 559–620 (1994). [Erratum: Z.Phys.C 68, 352 (1995)]; arXiv:hep-ph/9409380. 68

[320] (NNPDF Collaboration); R. D. Ball *et al.*; "Parton distributions for the LHC Run II"; JHEP **04**, p. 040 (2015). arXiv:1410.8849 [hep-ph]. 75

[321] P. Artoisenet, R. Frederix, O. Mattelaer & R. Rietkerk; "Automatic spin-entangled decays of heavy resonances in Monte Carlo simulations"; JHEP **03**, p. 015 (2013). arXiv:1212.3460 [hep-ph]. 75

[322] J. Alwall, C. Duhr, B. Fuks, O. Mattelaer, D. G. Öztürk & C.-H. Shen; "Computing decay rates for new physics theories with FeynRules and MadGraph 5 _- aMC@NLO"; Comput. Phys. Commun. **197**, pp. 312–323 (2015). arXiv:1402.1178 [hep-ph]. 75

[323] (CMS Collaboration); A. M. Sirunyan *et al.*; "Search for new physics in final states with an energetic jet or a hadronically decaying W or Z boson and transverse momentum imbalance at $\sqrt{s} = 13$ TeV"; Phys. Rev. D **97**, p. 092005 (2018). arXiv:1712.02345 [hep-ex]. 75

[324] (ATLAS Collaboration); The ATLAS collaboration; "Search for squarks and gluinos in final states with jets and missing transverse momentum using 139 fb^{-1} of $\sqrt{s}$ =13 TeV pp collision data with the ATLAS detector"; (2019). 75, 77, 216

[325] E. Conte, B. Dumont, B. Fuks & C. Wymant; "Designing and recasting LHC analyses with MadAnalysis 5"; Eur. Phys. J. C **74**, p. 3103 (2014). arXiv:1405.3982 [hep-ph]. 75

[326] J. Y. Araz, M. Frank & B. Fuks; "Reinterpreting the results of the LHC with MadAnalysis 5: uncertainties and higher-luminosity estimates"; Eur. Phys. J. C **80**, p. 531 (2020). arXiv:1910.11418 [hep-ph]. 76

[327] S. Banerjee, D. Barducci, G. Bélanger, B. Fuks, A. Goudelis & B. Zaldivar; "Cornering pseudoscalar-mediated dark matter with the LHC and cosmology"; JHEP **07**, p. 080 (2017). arXiv:1705.02327 [hep-ph]. 76

[328] (Planck Collaboration); N. Aghanim *et al.*; "Planck 2018 results. VI. Cosmological parameters"; (2018)arXiv:1807.06209 [astro-ph.CO]. 78

[329] M. Schumann; "Direct Detection of WIMP Dark Matter: Concepts and Status"; J. Phys. G **46**, p. 103003 (2019). arXiv:1903.03026 [astro-ph.CO]. 81

[330] T. Han, S. Mukhopadhyay & X. Wang; "Electroweak Dark Matter at Future Hadron Colliders"; Phys. Rev. D **98**, p. 035026 (2018). arXiv:1805.00015 [hep-ph]. 84

[331] J. Alimena *et al.*; "Searching for long-lived particles beyond the Standard Model at the Large Hadron Collider"; J. Phys. G **47**, p. 090501 (2020). arXiv:1903.04497 [hep-ex]. 87, 88, 90

[332] R. G. Suarez; "Long-Lived Particles at Future Colliders"; in "27th Cracow Epiphany Conference on Future of particle physics ," (2021); arXiv:2102.07597 [hep-ex]. 87

[333] B. Shuve; "THEORY OVERVIEW OF LONG-LIVED PARTICLES"; (2018). https://indico.cern.ch/event/714087/contributions/2985914/attachments/1650488/2641192/LHC-LLP_Shuve.pdf; lHC-LLP Workshop. 87

[334] (ATLAS Collaboration); "Search for long-lived neutral particles decaying into displaced lepton jets in proton–proton collisions at $\sqrt{s} = 13$ TeV with the ATLAS detector"; (2016). 88, 91, 180

[335] (ATLAS Collaboration); M. Aaboud *et al.*; "Search for metastable heavy charged particles with large ionization energy loss in pp collisions at $\sqrt{s} = 13$ TeV using the ATLAS experiment"; Phys. Rev. D **93**, p. 112015 (2016). arXiv:1604.04520 [hep-ex]. 88, 93, 94, 180

[336] (ATLAS Collaboration); M. Aaboud *et al.*; "Search for heavy long-lived charged R-hadrons with the ATLAS detector in 3.2 fb^{-1} of proton–proton collision data at $\sqrt{s} = 13$ TeV"; Phys. Lett. B **760**, pp. 647–665 (2016). arXiv:1606.05129 [hep-ex]. 88, 94, 180

[337] (ATLAS Collaboration); D. Salvatore; "Search for long-lived neutral particles decaying into Lepton-Jets with the ATLAS detector in proton-proton collision data at 13 TeV"; (2017)arXiv:1708.07625 [hep-ex]. 88, 180

[338] (ATLAS Collaboration); M. Aaboud *et al.*; "Search for long-lived, massive particles in events with displaced vertices and missing transverse momentum in $\sqrt{s} = 13$ TeV pp collisions with the ATLAS detector"; Phys. Rev. D **97**, p. 052012 (2018). arXiv:1710.04901 [hep-ex]. 88, 127, 129, 180

[339] (ATLAS Collaboration); M. Aaboud *et al.*; "Search for long-lived charginos based on a disappearing-track signature in pp collisions at $\sqrt{s} = 13$ TeV with the ATLAS detector"; JHEP **06**, p. 022 (2018). arXiv:1712.02118 [hep-ex]. 88, 93, 180

[340] (ATLAS Collaboration); M. Aaboud *et al.*; "Search for long-lived particles in final states with displaced dimuon vertices in pp collisions at $\sqrt{s} = 13$ TeV with the ATLAS detector"; Phys. Rev. D **99**, p. 012001 (2019). arXiv:1808.03057 [hep-ex]. 88, 180

[341] (ATLAS Collaboration); M. Aaboud *et al.*; "Search for heavy charged long-lived particles in proton-proton collisions at $\sqrt{s} = 13$ TeV using an ionisation measurement with the ATLAS detector"; Phys. Lett. B **788**, pp. 96–116 (2019). arXiv:1808.04095 [hep-ex]. 88, 180

[342] (ATLAS Collaboration); M. Aaboud *et al.*; "Search for the Production of a Long-Lived Neutral Particle Decaying within the ATLAS Hadronic Calorimeter in Association with a Z Boson from pp Collisions at $\sqrt{s} = 13$ TeV"; Phys. Rev. Lett. **122**, p. 151801 (2019). arXiv:1811.02542 [hep-ex]. 88, 181

[343] (ATLAS Collaboration); M. Aaboud *et al.*; "Search for long-lived particles produced in pp collisions at $\sqrt{s} = 13$ TeV that decay into displaced hadronic jets in the ATLAS muon spectrometer"; Phys. Rev. D **99**, p. 052005 (2019). arXiv:1811.07370 [hep-ex]. 88, 181

[344] (ATLAS Collaboration); M. Aaboud *et al.*; "Search for heavy long-lived multi-charged particles in proton-proton collisions at $\sqrt{s} = 13$ TeV using the ATLAS detector"; Phys. Rev. D **99**, p. 052003 (2019). arXiv:1812.03673 [hep-ex]. 88, 181

[345] (ATLAS Collaboration); M. Aaboud *et al.*; "Search for heavy charged long-lived particles in the ATLAS detector in 36.1 fb^{-1} of proton-proton collision data at $\sqrt{s} = 13$ TeV"; Phys. Rev. D **99**, p. 092007 (2019). arXiv:1902.01636 [hep-ex]. 88, 181

[346] (ATLAS Collaboration); M. Aaboud *et al.*; "Search for long-lived neutral particles in pp collisions at $\sqrt{s} = 13$ TeV that decay into displaced hadronic jets in the ATLAS calorimeter"; Eur. Phys. J. C **79**, p. 481 (2019). arXiv:1902.03094 [hep-ex]. 88, 91, 181

[347] (ATLAS Collaboration); G. Aad *et al.*; "Search for heavy neutral leptons in decays of W bosons produced in 13 TeV pp collisions using prompt and displaced signatures with the ATLAS detector"; JHEP **10**, p. 265 (2019). arXiv:1905.09787 [hep-ex]. 88, 181

[348] (ATLAS Collaboration); G. Aad *et al.*; "Search for displaced vertices of oppositely charged leptons from decays of long-lived particles in pp collisions at $\sqrt{s}$ =13 TeV with the ATLAS detector"; Phys. Lett. B **801**, p. 135114 (2020). arXiv:1907.10037 [hep-ex]. 88, 125, 128, 129, 133, 181

[349] (ATLAS Collaboration); G. Aad *et al.*; "Search for light long-lived neutral particles produced in pp collisions at $\sqrt{s} = 13$ TeV and decaying into collimated leptons or light hadrons with the ATLAS detector"; Eur. Phys. J. C **80**, p. 450 (2020). arXiv:1909.01246 [hep-ex]. 88, 181

[350] (ATLAS Collaboration); G. Aad *et al.*; "Search for long-lived neutral particles produced in pp collisions at $\sqrt{s} = 13$ TeV decaying into displaced hadronic jets in the ATLAS inner detector and muon spectrometer"; Phys. Rev. D **101**, p. 052013 (2020). arXiv:1911.12575 [hep-ex]. 88, 181

[351] (ATLAS Collaboration); G. Aad *et al.*; "Search for long-lived, massive particles in events with a displaced vertex and a muon with large impact parameter in pp collisions at $\sqrt{s} = 13$ TeV with the ATLAS detector"; Phys. Rev. D **102**, p. 032006 (2020). arXiv:2003.11956 [hep-ex]. 88, 181

[352] (ATLAS Collaboration); "Search for displaced leptons in $\sqrt{s} = 13$ TeV pp collisions with the ATLAS detector"; (2020). 88, 181

[353] (ATLAS Collaboration); G. Aad *et al.*; "Search for displaced leptons in $\sqrt{s} = 13$ TeV pp collisions with the ATLAS detector"; (2020)arXiv:2011.07812 [hep-ex]. 88, 91, 181

[354] (ATLAS Collaboration); G. Aad *et al.*; "A search for the decays of stopped long-lived particles at $\sqrt{s} = 13$ TeV with the ATLAS detector"; (2021)arXiv:2104.03050 [hep-ex]. 88, 94, 181

[355] C. Collaboration; "Search for displaced leptons in the e-mu channel"; Technical Report CMS-PAS-EXO-16-022; CERN; Geneva (2016). https://cds.cern.ch/record/2205146. 88, 91, 115, 118, 119, 122, 124, 181, 218

[356] (CMS Collaboration); V. Khachatryan *et al.*; "Search for long-lived charged particles in proton-proton collisions at $\sqrt{s} = 13$ TeV"; Phys. Rev. D **94**, p. 112004 (2016). arXiv:1609.08382 [hep-ex]. 88, 93, 94, 181

[357] (CMS Collaboration); A. M. Sirunyan *et al.*; "Search for new long-lived particles at $\sqrt{s} = 13$ TeV"; Phys. Lett. B **780**, pp. 432–454 (2018). arXiv:1711.09120 [hep-ex]. 88, 181

[358] (CMS Collaboration); A. M. Sirunyan *et al.*; "Search for decays of stopped exotic long-lived particles produced in proton-proton collisions at $\sqrt{s} = 13$ TeV"; JHEP **05**, p. 127 (2018). arXiv:1801.00359 [hep-ex]. 88, 94, 181

[359] (CMS Collaboration); A. M. Sirunyan *et al.*; "Search for disappearing tracks as a signature of new long-lived particles in proton-proton collisions at $\sqrt{s} = 13$ TeV"; JHEP **08**, p. 016 (2018). arXiv:1804.07321 [hep-ex]. 88, 93, 181

[360] (CMS Collaboration); A. M. Sirunyan *et al.*; "Search for long-lived particles with displaced vertices in multijet events in proton-proton collisions at $\sqrt{s}$ =13 TeV"; Phys. Rev. D **98**, p. 092011 (2018). arXiv:1808.03078 [hep-ex]. 88, 181

[361] (CMS Collaboration); A. M. Sirunyan *et al.*; "Search for new particles decaying to a jet and an emerging jet"; JHEP **02**, p. 179 (2019). arXiv:1810.10069 [hep-ex]. 88, 93, 181

[362] (CMS Collaboration); A. M. Sirunyan *et al.*; "Search for long-lived particles decaying into displaced jets in proton-proton collisions at $\sqrt{s} = 13$ TeV"; Phys. Rev. D **99**, p. 032011 (2019). arXiv:1811.07991 [hep-ex]. 88, 91, 182

[363] (CMS Collaboration); A. M. Sirunyan *et al.*; "Search for long-lived particles using nonprompt jets and missing transverse momentum with proton-proton collisions at $\sqrt{s} = 13$ TeV"; Phys. Lett. B **797**, p. 134876 (2019). arXiv:1906.06441 [hep-ex]. 88, 92, 182

[364] (CMS Collaboration); A. M. Sirunyan *et al.*; "Search for long-lived particles using delayed photons in proton-proton collisions at $\sqrt{s} = 13$ TeV"; Phys. Rev. D **100**, p. 112003 (2019). arXiv:1909.06166 [hep-ex]. 88, 182

[365] (CMS Collaboration); A. M. Sirunyan *et al.*; "Search for disappearing tracks in proton-proton collisions at $\sqrt{s} = 13$ TeV"; Phys. Lett. B **806**, p. 135502 (2020). arXiv:2004.05153 [hep-ex]. 88, 182

[366] (CMS Collaboration); A. M. Sirunyan *et al.*; "Search for long-lived particles using displaced jets in proton-proton collisions at $\sqrt{s} = 13$ TeV"; (2020)arXiv:2012.01581 [hep-ex]. 88, 91, 182

[367] (Particle Data Group Collaboration); P. A. Zyla *et al.*; "Review of Particle Physics"; PTEP **2020**, p. 083C01 (2020). 89, 94, 146

[368] (IceCube Collaboration); R. Abbasi *et al.*; "The IceCube Data Acquisition System: Signal Capture, Digitization, and Timestamping"; Nucl. Instrum. Meth. A **601**, pp. 294–316 (2009). arXiv:0810.4930 [physics.ins-det]. 90

[369] (Super-Kamiokande Collaboration); Y. Fukuda *et al.*; "The Super-Kamiokande detector"; Nucl. Instrum. Meth. A **501**, pp. 418–462 (2003). 90

[370] C. Argüelles, P. Coloma, P. Hernández & V. Muñoz; "Searches for Atmospheric Long-Lived Particles"; JHEP **02**, p. 190 (2020). arXiv:1910.12839 [hep-ph]. 90

[371] K. F. DiPetrillo; "Long lived particle searches in ATLAS"; (2017). https://indico.cern.ch/event/649760/contributions/2689324/attachments/1542622/2420051/kdpATLASLPP.2017.pdf; second LHC Long-lived Particle Workshop. 90

[372] (ATLAS Collaboration); G. Aad *et al.*; "Search for massive, long-lived particles using multitrack displaced vertices or displaced lepton pairs in pp collisions at $\sqrt{s}$ = 8 TeV with the ATLAS detector"; Phys. Rev. D **92**, p. 072004 (2015). arXiv:1504.05162 [hep-ex]. 90, 180

[373] (ATLAS Collaboration); G. Aad *et al.*; "Standalone vertex finding in the ATLAS muon spectrometer"; JINST **9**, p. P02001 (2014). arXiv:1311.7070 [physics.ins-det]. 90

[374] (ATLAS Collaboration); G. Aad *et al.*; "Search for long-lived, weakly interacting particles that decay to displaced hadronic jets in proton-proton collisions at $\sqrt{s}$ = 8 TeV with the ATLAS detector"; Phys. Rev. D **92**, p. 012010 (2015). arXiv:1504.03634 [hep-ex]. 90, 180

[375] (CMS Collaboration); V. Khachatryan *et al.*; "Search for Displaced Supersymmetry in events with an electron and a muon with large impact parameters"; Phys. Rev. Lett. **114**, p. 061801 (2015). arXiv:1409.4789 [hep-ex]. 91, 115, 116, 117, 119, 120, 121, 180, 218

[376] (D0 Collaboration); V. M. Abazov *et al.*; "Search for Events with Leptonic Jets and Missing Transverse Energy in $\mathbf{p\bar{p}}$ Collisions at $\sqrt{\mathbf{s}} = \mathbf{1.96}$ TeV"; Phys. Rev. Lett. **105**, p. 211802 (2010). arXiv:1008.3356 [hep-ex]. 91

[377] (ATLAS Collaboration); G. Aad *et al.*; "Search for displaced muonic lepton jets from light Higgs boson decay in proton-proton collisions at $\sqrt{s}$ = 7 TeV with the ATLAS detector"; Phys. Lett. B **721**, pp. 32–50 (2013). arXiv:1210.0435 [hep-ex]. 91, 179

[378] (ATLAS Collaboration); G. Aad *et al.*; "Search for long-lived neutral particles decaying into lepton jets in proton-proton collisions at $\sqrt{s}$ = 8 TeV with the ATLAS detector"; JHEP **11**, p. 088 (2014). arXiv:1409.0746 [hep-ex]. 91, 92, 179

[379] (ATLAS Collaboration); G. Aad *et al.*; "Search for nonpointing photons in the diphoton and E_T^{miss} final state in $\sqrt{s}$=7 TeV proton-proton collisions using the ATLAS detector"; Phys. Rev. D **88**, p. 012001 (2013). arXiv:1304.6310 [hep-ex]. 92, 179

[380] (ATLAS Collaboration); G. Aad *et al.*; "Search for nonpointing and delayed photons in the diphoton and missing transverse momentum final state in 8 TeV *pp* collisions at the LHC using the ATLAS detector"; Phys. Rev. D **90**, p. 112005 (2014). arXiv:1409.5542 [hep-ex]. 92, 180

[381] G. F. Giudice, M. A. Luty, H. Murayama & R. Rattazzi; "Gaugino mass without singlets"; JHEP **12**, p. 027 (1998). arXiv:hep-ph/9810442. 93, 122

[382] L. Randall & R. Sundrum; "Out of this world supersymmetry breaking"; Nucl. Phys. B **557**, pp. 79–118 (1999). arXiv:hep-th/9810155. 93, 122

[383] A. Pomarol & R. Rattazzi; "Sparticle masses from the superconformal anomaly"; JHEP **05**, p. 013 (1999). arXiv:hep-ph/9903448. 93

[384] S. Jung & H.-S. Lee; "Constraining Higgsino Kink Tracks from Existing LHC Searches"; Int. J. Mod. Phys. A **32**, p. 1750070 (2017). arXiv:1503.00414 [hep-ph]. 93

[385] (ALEPH Collaboration); R. Barate *et al.*; "Search for sleptons in e+ e- collisions at center-of-mass energies up to 184-GeV"; Phys. Lett. B **433**, pp. 176–194 (1998). 93

[386] (ALEPH Collaboration); R. Barate *et al.*; "Search for gauge mediated SUSY breaking topologies at $S^{(1/2)}$ similar to 189-GeV"; Eur. Phys. J. C **16**, pp. 71–85 (2000). 93

[387] P. Schwaller, D. Stolarski & A. Weiler; "Emerging Jets"; JHEP **05**, p. 059 (2015). arXiv:1502.05409 [hep-ph]. 93

[388] (ATLAS Collaboration); G. Aad *et al.*; "Searches for heavy long-lived charged particles with the ATLAS detector in proton-proton collisions at $\sqrt{s} = 8$ TeV"; JHEP **01**, p. 068 (2015). arXiv:1411.6795 [hep-ex]. 93, 94, 180

[389] (CMS Collaboration); S. Chatrchyan *et al.*; "Searches for Long-Lived Charged Particles in *pp* Collisions at $\sqrt{s}$=7 and 8 TeV"; JHEP **07**, p. 122 (2013). arXiv:1305.0491 [hep-ex]. 93, 94, 180

[390] (ATLAS Collaboration); G. Aad *et al.*; "Search for heavy long-lived charged particles with the ATLAS detector in *pp* collisions at $\sqrt{s} = 7$ TeV"; Phys. Lett. B **703**, pp. 428–446 (2011). arXiv:1106.4495 [hep-ex]. 94, 179

[391] (ATLAS Collaboration); G. Aad *et al.*; "Search for stable hadronising squarks and gluinos with the ATLAS experiment at the LHC"; Phys. Lett. B **701**, pp. 1–19 (2011). arXiv:1103.1984 [hep-ex]. 94, 179

[392] (ATLAS Collaboration); G. Aad *et al.*; "Search for Massive Long-lived Highly Ionising Particles with the ATLAS Detector at the LHC"; Phys. Lett. B **698**, pp. 353–370 (2011). arXiv:1102.0459 [hep-ex]. 94, 179

[393] (ATLAS Collaboration); G. Aad *et al.*; "Searches for heavy long-lived sleptons and R-Hadrons with the ATLAS detector in *pp* collisions at $\sqrt{s} = 7$ TeV"; Phys. Lett. B **720**, pp. 277–308 (2013). arXiv:1211.1597 [hep-ex]. 94, 179

[394] (ATLAS Collaboration); G. Aad *et al.*; "Search for long-lived, multi-charged particles in pp collisions at $\sqrt{s}$=7 TeV using the ATLAS detector"; Phys. Lett. B **722**, pp. 305–323 (2013). arXiv:1301.5272 [hep-ex]. 94, 179

[395] (CMS Collaboration); V. Khachatryan *et al.*; "Search for Heavy Stable Charged Particles in *pp* collisions at $\sqrt{s} = 7$ TeV"; JHEP **03**, p. 024 (2011). arXiv:1101.1645 [hep-ex]. 94, 180

[396] (CMS Collaboration); S. Chatrchyan *et al.*; "Search for Fractionally Charged Particles in *pp* Collisions at $\sqrt{s} = 7$ TeV"; Phys. Rev. D **87**, p. 092008 (2013). arXiv:1210.2311 [hep-ex]. 94, 180

[397] (CMS Collaboration); S. Chatrchyan *et al.*; "Search for heavy long-lived charged particles in *pp* collisions at $\sqrt{s} = 7$ TeV"; Phys. Lett. B **713**, pp. 408–433 (2012). arXiv:1205.0272 [hep-ex]. 94, 180

[398] (ALEPH Collaboration); R. Barate *et al.*; "Search for pair production of longlived heavy charged particles in e+ e- annihilation"; Phys. Lett. B **405**, pp. 379–388 (1997). arXiv:hep-ex/9706013. 94

[399] (DELPHI Collaboration); P. Abreu *et al.*; "Search for heavy stable and longlived particles in e+ e- collisions at s**(1/2) = 189-GeV"; Phys. Lett. B **478**, pp. 65–72 (2000). arXiv:hep-ex/0103038. 94

[400] (L3 Collaboration); P. Achard *et al.*; "Search for heavy neutral and charged leptons in e^+e^- annihilation at LEP"; Phys. Lett. B **517**, pp. 75–85 (2001). arXiv:hep-ex/0107015. 94

[401] (OPAL Collaboration); G. Abbiendi *et al.*; "Search for stable and longlived massive charged particles in e+ e- collisions at s**(1/2) = 130-GeV to 209-GeV"; Phys. Lett. B **572**, pp. 8–20 (2003). arXiv:hep-ex/0305031. 94

[402] (H1 Collaboration); A. Aktas *et al.*; "Measurement of anti-deuteron photoproduction and a search for heavy stable charged particles at HERA"; Eur. Phys. J. C **36**, pp. 413–423 (2004). arXiv:hep-ex/0403056. 94

[403] (CDF Collaboration); T. Aaltonen *et al.*; "Search for Long-Lived Massive Charged Particles in 1.96 TeV $\bar{p}p$ Collisions"; Phys. Rev. Lett. **103**, p. 021802 (2009). arXiv:0902.1266 [hep-ex]. 94

[404] (D0 Collaboration); V. M. Abazov *et al.*; "Search for Long-Lived Charged Massive Particles with the D0 Detector"; Phys. Rev. Lett. **102**, p. 161802 (2009). arXiv:0809.4472 [hep-ex]. 94

[405] (D0 Collaboration); V. M. Abazov *et al.*; "A Search for charged massive long-lived particles"; Phys. Rev. Lett. **108**, p. 121802 (2012). arXiv:1110.3302 [hep-ex]. 94

[406] (D0 Collaboration); V. M. Abazov *et al.*; "Search for charged massive long-lived particles at $\sqrt{s} = 1.96$ TeV"; Phys. Rev. D **87**, p. 052011 (2013). arXiv:1211.2466 [hep-ex]. 94

[407] A. Arvanitaki, S. Dimopoulos, A. Pierce, S. Rajendran & J. G. Wacker; "Stopping gluinos"; Phys. Rev. D **76**, p. 055007 (2007). arXiv:hep-ph/0506242. 94

[408] (CMS Collaboration); "Search for Stopped HSCP in pp collisions at Sqrt(s)=7 TeV"; (2011). 94, 180

[409] (D0 Collaboration); V. M. Abazov *et al.*; "Search for Stopped Gluinos from $p\bar{p}$ Collisions at $\sqrt{s} = 1.96$-TeV"; Phys. Rev. Lett. **99**, p. 131801 (2007). arXiv:0705.0306 [hep-ex]. 94

[410] (CMS Collaboration); V. Khachatryan *et al.*; "Search for Stopped Gluinos in pp collisions at $\sqrt{s} = 7$ TeV"; Phys. Rev. Lett. **106**, p. 011801 (2011). arXiv:1011.5861 [hep-ex]. 94, 180

[411] (ATLAS Collaboration); G. Aad *et al.*; "Search for long-lived stopped R-hadrons decaying out-of-time with pp collisions using the ATLAS detector"; Phys. Rev. D **88**, p. 112003 (2013). arXiv:1310.6584 [hep-ex]. 94, 179

[412] (CMS Collaboration); V. Khachatryan *et al.*; "Search for Decays of Stopped Long-Lived Particles Produced in Proton–Proton Collisions at $\sqrt{s} = 8$ TeV"; Eur. Phys. J. C **75**, p. 151 (2015). arXiv:1501.05603 [hep-ex]. 94, 180

[413] R. Barbier *et al.*; "R-parity violating supersymmetry"; Phys. Rept. **420**, pp. 1–202 (2005). arXiv:hep-ph/0406039. 94

[414] (MATHUSLA Collaboration); H. Lubatti *et al.*; "Explore the lifetime frontier with MATHUSLA"; JINST **15**, p. C06026 (2020). arXiv:1901.04040 [hep-ex]. 94, 95

[415] (MATHUSLA Collaboration); C. Alpigiani *et al.*; "An Update to the Letter of Intent for MATHUSLA: Search for Long-Lived Particles at the HL-LHC"; (2020)arXiv:2009.01693 [physics.ins-det]. 94, 95

[416] (FASER Collaboration); A. Ariga *et al.*; "FASER's physics reach for long-lived particles"; Phys. Rev. D **99**, p. 095011 (2019). arXiv:1811.12522 [hep-ph]. 94, 95

[417] (FASER Collaboration); A. Ariga *et al.*; "FASER: ForwArd Search ExpeRiment at the LHC"; (2019)arXiv:1901.04468 [hep-ex]. 94, 95

[418] V. V. Gligorov, S. Knapen, M. Papucci & D. J. Robinson; "Searching for Long-lived Particles: A Compact Detector for Exotics at LHCb"; Phys. Rev. D **97**, p. 015023 (2018). arXiv:1708.09395 [hep-ph]. 95, 96

[419] G. Aielli *et al.*; "Expression of interest for the CODEX-b detector"; Eur. Phys. J. C **80**, p. 1177 (2020). arXiv:1911.00481 [hep-ex]. 95, 96

[420] (SHiP Collaboration); M. Anelli *et al.*; "A facility to Search for Hidden Particles (SHiP) at the CERN SPS"; (2015)arXiv:1504.04956 [physics.ins-det]. 95

[421] V. V. Gligorov, S. Knapen, B. Nachman, M. Papucci & D. J. Robinson; "Leveraging the ALICE/L3 cavern for long-lived particle searches"; Phys. Rev. D **99**, p. 015023 (2019). arXiv:1810.03636 [hep-ph]. 95

[422] M. Bauer, O. Brandt, L. Lee & C. Ohm; "ANUBIS: Proposal to search for long-lived neutral particles in CERN service shafts"; (2019)arXiv:1909.13022 [physics.ins-det]. 95

[423] A. Artamonov *et al.*; "The ATLAS forward calorimeters"; JINST **3**, p. P02010 (2008). 95

[424] G. Bayatian *et al.*; "Design, performance and calibration of the CMS forward calorimeter wedges"; Eur. Phys. J. C **53**, pp. 139–166 (2008). 95

[425] (ATLAS Muon Collaboration); K. Ishii; "The ATLAS muon spectrometer"; PoS **HEP2001**, p. 253 (2001). 100

[426] W. Research; "ArcTan"; https://reference.wolfram.com/language/ref/ArcTan.html (visited on 21 April 2021) (1988). 102

[427] cppreference.com; "std::atan2, std::atan2f, std::atan2l"; https://en.cppreference.com/w/cpp/numeric/math/atan2 (visited on 21 April 2021) (2020). 102

[428] ISO; *ISO/IEC 14882:2017 Information technology — Programming languages — C++*; 5th edition (2017). https://www.iso.org/standard/68564.html. 104

[429] G. M. Seed; *Pointers*; pp. 377–483 (Springer London, London) (1996); ISBN 978-1-4471-3378-0. https://doi.org/10.1007/978-1-4471-3378-0_12. 104

[430] L. Garren, C. J. Lin, S. Navas, P. Richardson, T. Sjöstrand & T. G. Trippe; "Monte Carlo particle numbering scheme"; (2008). 110

[431] C. Anastopoulos; "Decays of Unstable Quantum Systems"; International Journal of Theoretical Physics **58**, p. 890–930 (2018). ISSN 1572-9575. http://dx.doi.org/10.1007/s10773-018-3984-z. 110

[432] P. W. Graham, D. E. Kaplan, S. Rajendran & P. Saraswat; "Displaced Supersymmetry"; JHEP **07**, p. 149 (2012). arXiv:1204.6038 [hep-ph]. 115

[433] J. Chang; "Madanalysis5 implementation of CMS-EXO-16-022"; (2018). doi :10.7484/INSPIREHEP.DATA.UFU4.99E3. 115, 119, 120, 218

[434] (CMS Collaboration); "DisplacedSusyParametrisationStudyForUser"; https://twiki.cern.ch/twiki/bin/view/CMSPublic/DisplacedSusyParametrisationStudyForUser (visited on 20 March 2021) (2016). 115, 116, 117, 119, 120, 121, 218

[435] (CMS Collaboration); "Particle-Flow Event Reconstruction in CMS and Performance for Jets, Taus, and MET"; (2009). 116

[436] (CMS Collaboration); S. Chatrchyan *et al.*; "Performance of CMS Muon Reconstruction in *pp* Collision Events at $\sqrt{s} = 7$ TeV"; JINST **7**, p. P10002 (2012). arXiv:1206.4071 [physics.ins-det]. 116

[437] (CMS Collaboration); V. Khachatryan *et al.*; "Performance of Electron Reconstruction and Selection with the CMS Detector in Proton-Proton Collisions at $\sqrt{s}$ = 8 TeV"; JINST **10**, p. P06005 (2015). arXiv:1502.02701 [physics.ins-det]. 116

[438] E. Maguire, L. Heinrich & G. Watt; "HEPData: a repository for high energy physics data"; J. Phys. Conf. Ser. **898**, p. 102006 (2017). arXiv:1704.05473 [hep-ex]. 120, 121, 130, 218, 219

[439] (CMS Collaboration); "HEPData entry of CMS-B2G-12-024, CERN-PH-EP-2014-219"; https://www.hepdata.net/record/ins1317640 (visited on 20 March 2021) (2015). 120, 121, 218

[440] Z. S. Wang; "Update on CheckMATE: recasting LHC searches for long-lived particles"; (Talk presented at the Workshop (Re)interpreting the results of new physics searches at the LHC, February 16, 2021) (2021). 121

[441] B. C. Allanach *et al.*; "The Snowmass Points and Slopes: Benchmarks for SUSY Searches"; Eur. Phys. J. C **25**, pp. 113–123 (2002). arXiv:hep-ph/0202233. 122

[442] H. P. Nilles; "Dynamically Broken Supergravity and the Hierarchy Problem"; Phys. Lett. B **115**, p. 193 (1982). 122

[443] H. P. Nilles; "Supergravity Generates Hierarchies"; Nucl. Phys. B **217**, pp. 366–380 (1983). 122

[444] A. H. Chamseddine, R. L. Arnowitt & P. Nath; "Locally Supersymmetric Grand Unification"; Phys. Rev. Lett. **49**, p. 970 (1982). 122

[445] R. Barbieri, S. Ferrara & C. A. Savoy; "Gauge Models with Spontaneously Broken Local Supersymmetry"; Phys. Lett. B **119**, p. 343 (1982). 122

[446] G. F. Giudice & R. Rattazzi; "Theories with gauge mediated supersymmetry breaking"; Phys. Rept. **322**, pp. 419–499 (1999). arXiv:hep-ph/9801271. 122

[447] A. Kulesza, C. Borschensky, A. Mann & S. Padhi; "Stop-antistop (sbottom-antisbottom) production cross sections in proton-proton collisions at 13 TeV, computed at NLO+NLL and NNLOapprox+NNLL." https://twiki.cern.ch/twiki/bin/view/LHCPhysics/SUSYCrossSections13TeVstopsbottom (visited on 2 July 2021) (2021). 122, 123

[448] (ATLAS Collaboration); "Luminosity determination in pp collisions at $\sqrt{s} = 13$ TeV using the ATLAS detector at the LHC"; (2019). 125

[449] G. Avoni *et al.*; "The new LUCID-2 detector for luminosity measurement and monitoring in ATLAS"; JINST **13**, p. P07017 (2018). 125

[450] (ATLAS Collaboration); "HEPData entry of ATLAS-SUSY-2017-04, CERN-EP-2019-139"; https://www.hepdata.net/record/ins1745920 (visited on 24 March 2021) (2019). 125, 129, 130, 219

[451] (ATLAS Collaboration); "Auxiliary material for ATLAS-SUSY-2017-04"; https://atlas.web.cern.ch/Atlas/GROUPS/PHYSICS/PAPERS/SUSY-2017-04/ (visited on 24 March 2021) (2019). 125, 129, 130, 133, 135, 219

[452] (ATLAS Collaboration); G. Aad *et al.*; "Electron and photon performance measurements with the ATLAS detector using the 2015–2017 LHC proton-proton collision data"; JINST **14**, p. P12006 (2019). arXiv:1908.00005 [hep-ex]. 126

[453] (ATLAS Collaboration); "Performance of the reconstruction of large impact parameter tracks in the ATLAS inner detector"; (2017). 127

[454] (ATLAS Collaboration); M. Aaboud *et al.*; "A measurement of material in the ATLAS tracker using secondary hadronic interactions in 7 TeV pp collisions"; JINST **11**, p. P11020 (2016). arXiv:1609.04305 [hep-ex]. 129

[455] (ATLAS Collaboration); M. Aaboud *et al.*; "Study of the material of the ATLAS inner detector for Run 2 of the LHC"; JINST **12**, p. P12009 (2017). arXiv:1707.02826 [hep-ex]. 129

[456] M. L. Mangano; "The so-called MLM prescription for ME/PS matching"; (Talk presented at the Fermilab ME/MC Tuning Workshop, October 4, 2002) (2002). 133, 134, 147

[457] R. D. Ball *et al.*; "Parton distributions with LHC data"; Nucl. Phys. B **867**, pp. 244–289 (2013). arXiv:1207.1303 [hep-ph]. 134, 147

[458] C. Duhr & B. Fuks; "A superspace module for the FeynRules package"; Comput. Phys. Commun. **182**, pp. 2404–2426 (2011). arXiv:1102.4191 [hep-ph]. 134

[459] F. Staub; "From Superpotential to Model Files for FeynArts and CalcHep/CompHep"; Comput. Phys. Commun. **181**, pp. 1077–1086 (2010). arXiv:0909.2863 [hep-ph]. 147

[460] F. Staub; "Automatic Calculation of supersymmetric Renormalization Group Equations and Self Energies"; Comput. Phys. Commun. **182**, pp. 808–833 (2011). arXiv:1002.0840 [hep-ph]. 147

[461] F. Staub; "SARAH 3.2: Dirac Gauginos, UFO output, and more"; Comput. Phys. Commun. **184**, pp. 1792–1809 (2013). arXiv:1207.0906 [hep-ph]. 147

[462] F. Staub; "SARAH 4 : A tool for (not only SUSY) model builders"; Comput. Phys. Commun. **185**, pp. 1773–1790 (2014). arXiv:1309.7223 [hep-ph]. 147

[463] H. K. Dreiner, H. E. Haber & S. P. Martin; "Two-component spinor techniques and Feynman rules for quantum field theory and supersymmetry"; Phys. Rept. **494**, pp. 1–196 (2010). arXiv:0812.1594 [hep-ph]. 153, 155, 157, 158

[464] R. Penco; "An Introduction to Effective Field Theories"; (2020)arXiv:2006.16285 [hep-th]. 163

[465] C. Itzykson & J. Zuber; *Quantum Field Theory*; International Series In Pure and Applied Physics (McGraw Hill) (1980). 167

[466] D. Dusedau, D. Lust & D. Zeppenfeld; "UNITARITY BOUNDS ON THE PRODUCTION OF (PSEUDO)SCALAR PARTICLES IN p anti-p COLLISIONS"; Phys. Lett. B **148**, pp. 234–238 (1984). 167, 171

[467] A. Schuessler & D. Zeppenfeld; "Unitarity constraints on MSSM trilinear couplings"; in "15th International Conference on Supersymmetry and the Unification of Fundamental Interactions (SUSY07)," pp. 236–239 (2007); arXiv:0710.5175 [hep-ph]. 167, 168

[468] L. Di Luzio, J. F. Kamenik & M. Nardecchia; "Implications of perturbative unitarity for scalar di-boson resonance searches at LHC"; Eur. Phys. J. C **77**, p. 30 (2017). arXiv:1604.05746 [hep-ph]. 167

[469] M. D. Goodsell & F. Staub; "Unitarity constraints on general scalar couplings with SARAH"; Eur. Phys. J. C **78**, p. 649 (2018). arXiv:1805.07306 [hep-ph]. 167, 168

[470] (ATLAS Collaboration); M. Aaboud *et al.*; "Combination of searches for heavy resonances decaying into bosonic and leptonic final states using 36 fb^{-1} of proton-proton collision data at $\sqrt{s} = 13$ TeV with the ATLAS detector"; Phys. Rev. D **98**, p. 052008 (2018). arXiv:1808.02380 [hep-ex]. 173, 174, 175, 176, 177, 219, 220

[471] (CMS Collaboration); "Search for a new scalar resonance decaying to a pair of Z bosons in proton-proton collisions at $\sqrt{s} = 13$ TeV"; (2017). 173, 174, 175, 176, 177, 219, 220

[472] (ATLAS Collaboration); M. Aaboud *et al.*; "Search for heavy ZZ resonances in the $\ell^+\ell^-\ell^+\ell^-$ and $\ell^+\ell^-\nu\bar{\nu}$ final states using proton–proton collisions at $\sqrt{s} = 13$ TeV with the ATLAS detector"; Eur. Phys. J. C **78**, p. 293 (2018). arXiv:1712.06386 [hep-ex]. 173, 174, 219

[473] (CMS Collaboration); "Combination of standard model Higgs boson searches and measurements of the properties of the new boson with a mass near 125 GeV"; (2012). 173, 175, 176, 177, 219, 220

[474] (ATLAS Collaboration); G. Aad *et al.*; "Combination of searches for Higgs boson pairs in *pp* collisions at $\sqrt{s}$ =13 TeV with the ATLAS detector"; Phys. Lett. B **800**, p. 135103 (2020). arXiv:1906.02025 [hep-ex]. 176, 177, 219, 220

[475] (CMS Collaboration); "Combination of searches for Higgs boson pair production in proton-proton collisions at $\sqrt{s} = 13$ TeV"; (2018). 176, 177, 219, 220

[476] (ATLAS Collaboration); G. Aad *et al.*; "Search for charginos nearly mass degenerate with the lightest neutralino based on a disappearing-track signature in pp collisions at $\sqrt{s}$=8 TeV with the ATLAS detector"; Phys. Rev. D **88**, p. 112006 (2013). arXiv:1310.3675 [hep-ex]. 179

List of Figures